DOCTORAL DISSERTATION

Design and Characterization of Supramolecular Materials Displaying Enhanced Circularly Polarized Luminescence and Mechanofluorochromism

Nara Institute of Science and Technology
Division of Materials Science
and
École normale supérieure Paris-Saclay
Sciences Chimiques : Molécules, Matériaux, Instrumentation et Biosystèmes (2MIB)

JOY ANN OSORIO PANIS

THÈSE DE DOCTORAT

NNT : 2020UPASA001

Design and Characterization of Supramolecular Materials Displaying Enhanced Circularly Polarized Luminescence and Mechanoflurochromism

Conception, synthèse et caractérisation de matériaux supramoléculaires pour la luminescence polarisée circulairement et mécanofluorochromisme

Thèse de doctorat de l'université Paris-Saclay et Institut des sciences et technologies de Nara

École doctorale n° S71, Sciences Chimiques : Molécules, Matériaux, Instrumentation et Biosystèmes (2MIB)
Spécialité de doctorat: Chimie
Graduate School: Chimie. Référent: ENS-Paris Saclay

Thèse préparée dans la (ou les) unité(s) de recherche PPSM (Université Paris-Saclay, ENS Paris-Saclay, CNRS) and Photonic and Reactive Molecular Science Laboratory (Division of Material Science, NAIST), sous la direction de **Clémence ALLAIN**, Directeur de recherche, la co-direction de **Tsuyoshi KAWAI**, Professeur.

Thèse soutenue au NAIST, le 20 Juillet 2022, par

Joy Ann PANIS

Composition du Jury

Gwénaël RAPENNE Professeur des universités, NAIST et Université de Toulouse	Examinateur
Michel SLIWA Directeur de recherche, Université de Lille,	Rapporteur
Jeanne CRASSOUS Directrice de recherche, Université Rennes 1	Rapporteur
Shun HIROTA Professeur, Nara Institute of Science and Technology	Examinateur
Rémi MÉTIVIER Directeur de recherche, Université Paris-Saclay / GS Chimie	Examinateur
Takuya NAKASHIMA Professeur, Osaka Metropolitan University	Examinateur
Clémence ALLAIN Directeur de recherche, Université Paris-Saclay GS Chimie	Directrice de thèse
Tsuyoshi KAWAI Professeur, Nara Institute of Science and Technology	Co-Directeur de thèse

Contents

Abstract i

1. Introduction: Circularly Polarized Luminescence and Mechanofluorochromism 1

1.1Circularly Polarized Luminescence of Small Organic Molecules 3

1.1.1 Circularly Polarized Luminescence based on Organoborons 4

1.1.2. Enhancing Chiroptical Properties: Supramolecular Assembly 9

1.1.3. Responsive CPL-active Organic Molecules 12

1.2. Mechanofluorochromism of Small Organic Molecules 17

1.3 Objective and Scope of the Studies 22

1.4 References 24

2. Circularly Polarized Luminescence and Circular Dichroism of Bichromophoric Difluoroboron-β-diketonates 31

2.1 Synthesis 32

2.2 Monomeric form of Para and Meta (S/R)-CyDFB 35

2.2.1 Photophysical Properties in Solution and Time-Correlated Single Photon Counting 35

2.2.2 Density Functional Theory (DFT) and Time-dependent DFT (TD-DFT) Calculations 37

2.3 Chiroptical Properties of Monomeric and Aggregated Bichromophores 42

2.4 Supramolecular Assembly 46

2.5 Photophysical Properties and Chiroptical Properties of Supramolecular Assembly 51

2.6 Conclusions 53

2.7 References 54

3. Energy Transfer and Sensitivity to UV Light of Supramolecular Nanowires based on Bichromophoric DFB compound 56

3.1 Synthesis 57

3.2 Photophysical Properties in Solution 58

3.3 Density Functional Theory (DFT) and Time-dependent DFT Calculations 60

3.4 Self-Assembled Nanowires 62

3.4.1 Energy Transfer in Supramolecular Assembly 62

3.5 Responsiveness to UV Light 65

3.5.1 Photobleaching and Emission shift 65
3.5.2 AFM Image Analysis 71
3.6 Conclusion 74
3.7 References 75
4. Mechanofluorochromic Properties of Bichromophoric difluoroboron β-Diketonate . 77
4.1 Synthesis 78
4.2 Photophysical Properties in Solution and Density functional theory (DFT) Calculations 79
4.3 Single Crystal Structures and Hirshfeld Surface Analysis 82
4.4 Mechanofluorochromic Property 90
4.4.1 Mechanofluorochromism of Cydiamine mono-DFB 92
4.4.2 Mechanofluorochromism of Cydiamine di-DFB 96
4.4.3 Mechanofluorochromism of Cydiester di-DFB 100
4.5 Intermolecular Interaction Energy in Crystals: Energy Framework 104
4.6 Conclusion 110
4.7 References 111
5. Conclusion and Prospects 114
6. Methods and Supplementary Information 119
6.1 General Synthesis and Characterizations 119
6.1.1 Synthesis of Compounds in Chapter 2 119
6.1.2 Synthesis of Compounds in Chapter 3 127
6.1.3 Synthesis of Compounds in Chapter 4 131
6.2 Time-resolved Fluorescence Measurements 133
6.3 DFT and TDDFT Calculations 142
6.4 Crystal Analysis 148
6.5 Thermogravimetric 151
6.6 Hirshfeld Surface Analysis 152
6.7 Circularly Polarized Luminescence (CPL) 155
Acknowledgement
Scientific Production

Abstract

Circularly polarized light (CPL) has promising application in the development of future 3D display and organic light emitting diode (OLEDs). The challenge now is to design and synthesize a small organic CPL active molecule that has high g_{CPL} values to make it suitable for the demands in device fabrications. As one of the most promising fluorophores for the supramolecular approaches, we have been recently focusing on difluoroboron-β-diketonate (DFB) complexes because of the high quantum yield in both solid and solution states, high Stokes shift and sensitivity to stimuli such as mechanical stress (mechanofluorochromism). It has been previously reported that DFB complex bearing chiral amido group displays a good CPL signal and response to mechanical stress in solid state but showed weak CPL signals in monomeric state. However, supramolecular aggregates of long range self-assembly based on this chromophore remain to be investigated. In this study, bichromophore DFB units with varying connectivity in para and meta positions were synthesized. The bichromophore DFB displayed an inversion of chirality based on spatial arrangement of chromophores and enhanced chiroptical property was observed in supramolecular self-assembled nanowire with g_{CPL} value of 0.015. In the second part of the study, energy transfer was investigated using anisotropy measurements. This showed a highly efficient energy transfer in supramolecular assembly as compared to monomeric form of both mono and di-substituted DFB. Moreover, self-assembled nanowires exhibit sensitivity through emission shift after exposure to UV. Finally, solid-state spectroscopic measurements were conducted to understand the mechanofluorochromic properties of mono and di-substituted DFB. Using time-resolve spectroscopy measurements and single crystal XRD analysis, it was found that the small changes in spacers such as the amide and esters highly influenced the mechanofluorochromic properties of bichromophore DFB through the strength of intermolecular interactions and molecular packing.

CHAPTER 1

Introduction: Circularly Polarized Luminescence and Mechanofluorochromism

Chiral active materials are widely existing in nature such as our DNA, and biomolecular components from living organism.[1–3] Such chirality of molecules is due to the non-superimposable and mirror image structures of molecules which behaves differently from its enantiomer. Early study of stereochemistry was rooted in first half of 19th century with the discovery of *Hemidrism* of crystals, and series of exploration such as circularly polarized light, the response of natural compound with circularly polarized light and Pasteur's efforts in deducing structure of enantiomers of *paratartaric acid*[4,5] (see Figure 1). This has initiated the growth of study and interest in molecular chirality on traditional medicine and natural products.[4] Fundamental and in-depth understanding of molecular chirality and its interaction with light was the foundation of chiral optics or chiroptics and this field of study has taken important parts in biology, toxicology, and medicine especially drug discovery and synthesis.

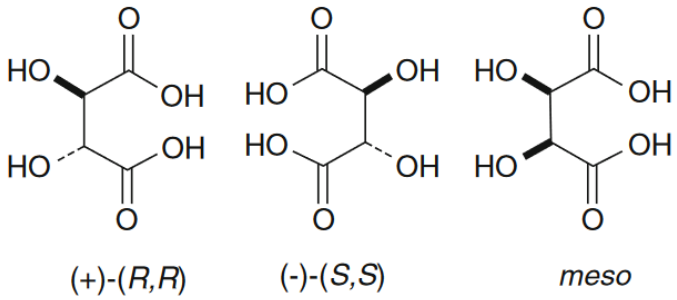

Figure 1.1. Tartaric acid (+), (-) and meso. Reprinted from ref. 4 with permission from *Springer Nature.*

Chiroptical properties of molecules can be measured through circular dichroism or the difference in the absorption of left and right circularly polarized light[6] and through the circularly polarized luminescence (CPL) or difference in the emission of left and right circularly polarized light.[7–9] CPL active materials has become appealing as it provides more application in state-of-the-art fabrication of light harvesting devices, 3D-displays, information storage and optical sensors.[10] This can be quantified with luminescence dissymmetry factors (g_{lum}) which can be calculated using the equation:

$$g_{\mathrm{lum}} = \frac{2(I_L - I_R)}{(I_L + I_R)}$$

where I_L and I_R are the intensities of left and right CPL. Theoretically, it can also be calculated with the following equation:

$$g_{\mathrm{lum}} = 4 \times cos\theta \frac{|m||\mu|}{|m|^2 + |\mu|^2}$$

where $|\mu|$and $|m|$ are the electric and magnetic dipole transition moment, θ is the angle between them and the highest theoretical value for g_{lum} is 2. Meanwhile, the difference in absorbance of the left and right circularly polarized light in ground state was defined as circular dichroism (CD= A^L-A^R) where A^L and A^R are the absorbances from left and right circularly polarized light. Useful quantity called dissymmetry factor (g_{abs}) can be derived from this equation and can be calculated as follows:

$g_{abs} = \frac{\Delta\varepsilon}{\varepsilon} = \frac{A^L - A^R}{A}$ where $\Delta\varepsilon = \varepsilon^L - \varepsilon^R$ is difference in molar quantity; A^L and A^R are the absorbances from left and right circularly polarized light and A is absorbance in non-polarized light.

From the equation, it was clear that the luminescence dissymmetry factors are highly dependent on molecular structure with magnetic allowed transition and electronic dipole forbidden transitions.[11–13] Several early studies on lanthanide complexes have been reported to exhibit high g_{lum} values because of favorable f-f transitions.[14,15] On the other hand, studies on CPL active small organic molecules (SOMs) have gained interest because of advantages over lanthanide complexes such as tunability, wider emission range and processibility in some device manufacturing processes.[14] However, obtaining high g_{lum} values with high quantum yield for organic compounds is still a challenge.

Another interesting property of luminescent compounds is mechanofluorochromism or the changes of emission after application of mechanical stress such as smearing, shearing, and grinding. The first induced emission through mechanical force was reported in 1904 when Francis Bacon showed that lumps of sugars emitted light after crushing.[16,17] However, because of complexity of studies with the molecular structures it was not sustained until in 2000s where the advances in mechanofluorochromic materials were explored.[18] Molecular re-arrangement, intermolecular interactions, chemical reactions and formation of excimers or combination of those upon application of mechanical stress are the main reasons for mechanofluorochromism.[19–23] The mechanofluorochromic compounds are gaining interest for applications in optoelectronics, security ink and papers and mechanosensors.[24–26]

Several mechanofluorochromic compounds were published in the last 10 years such as oligophenylenevinylenes[27,28] pyrene[29–31] metal complexes[32–34] tetrathiazolylthiophene,[35,36] and organoboron.[37–40] Of all the organoboron-based mechanofluorochromic compounds, we mainly focused with difluoroboron β-diketonate

(DFB) because of high quantum yield in solution and solid state as well as its promising mechanofluorochromic properties.[22,39,41–43]

As we have realized the importance of molecular design in improving CPL and mechanofluorochromism, this thesis therefore explores the techniques in improving the properties from molecular design and synthesis to formation of supramolecular assembly and finally its responsiveness. The design and synthesis of organic compounds with multiple functionalities are of great interest as it expands the use of the material in different applications. It goes beyond the borderline of specific application limited only with either CPL or mechanofluorochromism thus, unique design of compounds can be revolutionary and may contribute to expansion of perspectives for single molecules design with multiple functionalities.

This introductory chapter discuss early studies with isolated CPL active SOMs with a special focus on organoboron compounds. Molecular design approaches in improving chiroptical properties such supramolecular assemblies and aggregates are then discussed. Moreover, this also covers the mechanofluorochromism of organic molecules and the recent studies divulging the factors affecting the sensitivity and its reversibility. We also stated the objectives and scope of the study to impart our efforts in contributing for the future direction in the field of CPL and mechanofluorochromism.

1.1 Circularly Polarized Luminescence of Small Organic Molecules

Discovery of CPL active compounds has been instrumental for advances in the field of study in biomolecules, drug development and modern opto-electronics. So far, circularly polarized luminescence (CPL) active compounds with highest luminescence (g_{lum}) dissymmetry were reported for lanthanide complexes because of favorable transition satisfying the magnetic dipole selection rule. This was owed with the f-f transitions for lanthanide complexes and d-d transition for transition metals which satisfied the magnetic (m) allowed and electric (μ) forbidden transition.[44] The highest g_{lum} reported was Eu (III) complex with g_{lum} value of 1.38 from transition of $^5D_0 \rightarrow {}^7F_1$, however low ϕ_F is limiting its applications.[15,45] On the other hand, organic molecules have low g_{lum} values because of overwhelming electronic allowed transition (μ) and usually displays g_{lum} values in the range of 10^{-5} to 10^{-3} for isolated organic molecules.[9,14,45] Despite low g_{lum} values compared with lanthanide complexes, the quest for CPL active SOMs was boosted by advantages in terms of tunability of the emission wavelength, responsiveness to stimuli, biocompatibility, and processability in device fabrication.[10,46]

The early study of CPL active organic compound was reported in 1967 where Emeis and Oosterhof presented the chirality of *trans* β-hydrindanone, which displayed intrinsically chiral ketones.[47] During this time, most of the studies with CPL active

compounds was focused on chiral ketones displaying g_{lum} values in the range of 10^{-3} to 10^{-2} owing to the n-π* and satisfying the electronic forbidden and magnetic allowed transitions. Some of the cyclic ketones displaying CPL activity that were explored during 1960s are listed in Figure 1.1.

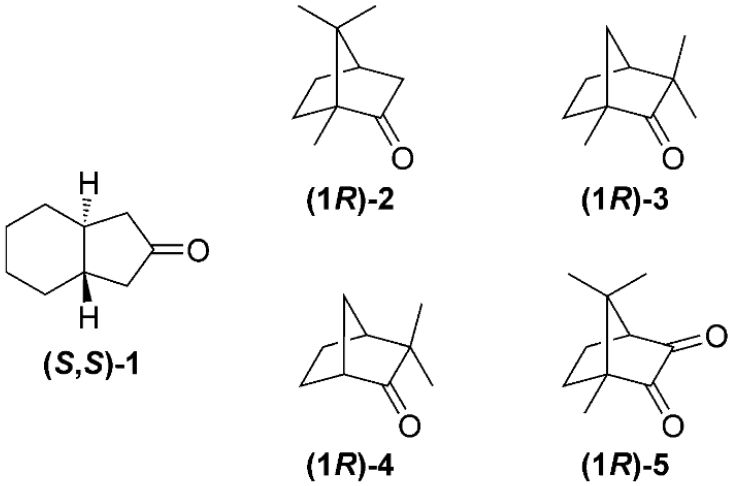

Figure 1.1. (++)-(*S,S*)-trans-b-hydrindanone (**(*S,S*)-1**), (1*R*)-camphor (**(1 *R*)-2**), (1*R*)-fenchone (**(1 *R*)-3**), (1*R*)-camphenilone (**(1 *R*)-4**), or (1*R*)-camphorquinone (**(1 *R*)-5**). Reprinted from ref. 14 with permission from *John Wiley and Sons.*

Since most of the chiral carbonyl compounds based on ketones have low ϕ_F, the research has shifted to molecular compounds with extended aromatic groups. SOMs with extended aromatic groups may display higher ϕ_F and g_{lum} values that will make them suitable for different applications in opto-electronics. One of the earliest conjugated aromatic CPL active compounds was reported by Drake et al, in 1979 displaying g_{lum} values of glum = $+8x10^{-3}$ for C2-symmetric calycanthine.[14] From CPL-active SOMs emitting in UV region, the interest in the development of molecules has shifted to emissive compounds in visible region. One of the interesting dyes are organoboron because of simpler synthetic pathways, high fluorescence emission quantum yield, high molar absorptivity and photostability. Moreover, most emission and absorption of organoboron are within near IR and visible region making it a promising compound for various applications.[48,49] However, most of these organoboron compounds such as BODIPY are achiral thus, the inclusion or embedding of dyes to chiral molecules has been the primary techniques to gain significant chirality.[50] There are many reported studies on CPL active small organic fluorescent dyes but in the next section, we focused the discussion on organoboron based CPL active molecules.

1.1.1 Circularly Polarized Luminescence based on Organoborons

The early molecular designs of chiral BODIPY was the covalently bonded asymmetric phenyls including the urobilin derivatives shown in Figure 1.2-a and 1.2-b.[49,51] Most of these molecular design of mono-BODIPY displayed low g_{lum} values (~10^{-3}) hence, to improve the chiroptical properties axial chiral compounds were introduced. Binaphthyls are one of the most used axial chiral inducers in the early study of CPL-active BODIPY. The perturbation of achiral BODIPY was demonstrated in the study of Beer et al., (2000) where they synthesized mono and bis-BODIPY shown in Figure 1.2-c and 1.2-d.[49] Although axial chiral binaphthyl was introduced in BODIPY, g_{lum} value remains weak (10^{-3}). An attempt to increase the CPL signal by changing the fluorophores from BODIPY to dimesytilboron was performed however, no significant improvement in the g_{lum} values was observed. This indicated that the chirality of compounds is mainly dependent on the nature of chiral source and not in the fluorophores attached.[44,52]

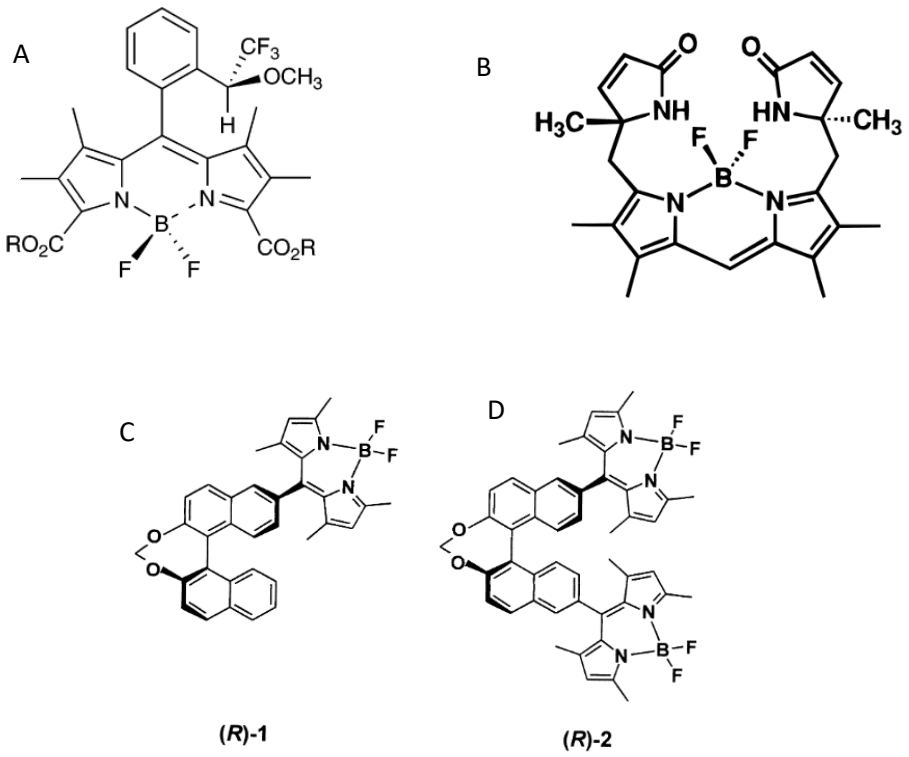

Figure 1.2. Mono chiral BODIPY attached with chiral phenyl (a), BODIPY with urobilin derivative (b)[51], mono-BODIPY in binaphthyl (c) and bis-BODIPY in binaphthyl (d).[49] Reprinted from ref. 49 and 51 with permission from *John Wiley and Sons* and *American Chemical Society*.

Efforts in improving chiroptical properties through molecular design continues and another simple functionalization of BODIPY was demonstrated by the group of de la Moya when they synthesized chiral *O*-BODIPY dyes. It was the first demonstration of structural design to obtain spiranic structures of *O*-BODIPYs where the BODIPY and 1'1-binaphthyl derivative is orthogonally arranged. This study showed that the simple complexation with chiral binaphthyl can cause perturbation of achiral fluorophores. The chiral perturbation of inherently achiral BODIPY was shown to enable CPL activity through absorption visible light. While the CPL of *O*-BODIPY dyes exhibited the usual g_{lum} values in the range of 10^{-5} – 10^{-3}, they showed that the simple and straight forward functionalization of BODIPY moiety can easily induces chirality to achiral fluorophores.[48]

With continuous search for chiral active organic compounds displaying high g_{lum} and ϕ_F, researchers gained interest with helicenes as potential CPL active compounds because of their promising g_{lum} values and high quantum yield.[44,53] In 2001, aggregating heterocyclic helicenes were reported by Phillips et al., unfortunately the g_{lum} values reported are limited for the aggregated form with g_{lum} value of 0.01.[54] Two years later, Venkataraman et al, (2003) reported the first triarylamine based with g_{lum} value of 0.01 for aggregating helicenes. In that same paper, they compared shorter helicene (M-1) with longer conjugated helicene (P-2) in isolated form shown in Figure 1.3. The shorter helicene showed g_{lum} value of |0.001| while the longer conjugated helicene displayed g_{lum} value of |0.0008| indicating that the increase in helicity of molecular geometry is not the only function to consider in obtaining high g_{lum} values.[55]

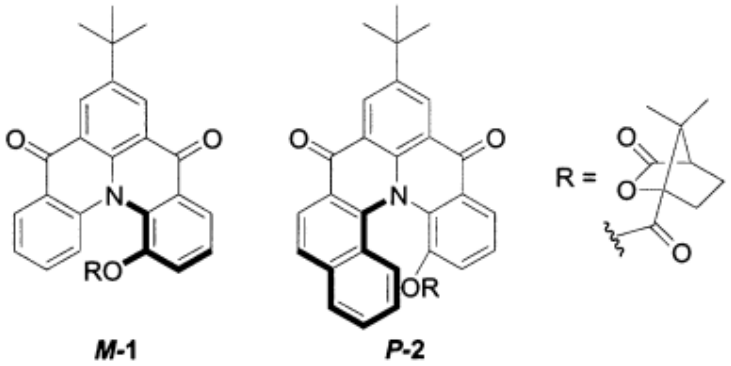

Figure 1.3. Hetero-helicenes based on triarylamines. Reprinted from ref. 55 with permission from *American Chemical Society*.

Helicenes as promising CPL-active compound was utilized as chiral platform for organoboron compounds to impart the chirality in fluorophores. Azahelicenes with BODIPY was demonstrated by the group of Maeda forming a unique molecular design of carbazole based-helicenes.[56] Series of carbazole-helicenes were synthesized with tunable

emission targeting NIR-responsive CPL dyes, and through structure analysis it was revealed that the chirality of helicenes were imparted to the organoboron moieties. These series of isolated carbazole based-helicenes displayed g_{lum} values in the range of $|7.0x10^{-4}|$ to $|1.9x10^{-3}|$. The group of Crassous demonstrated the influence of helicene sizes and the number of boron atoms in azabora[n]helicenes as well as with corresponding platina[n]helicenes analogues (see Figure 1.4).[57]

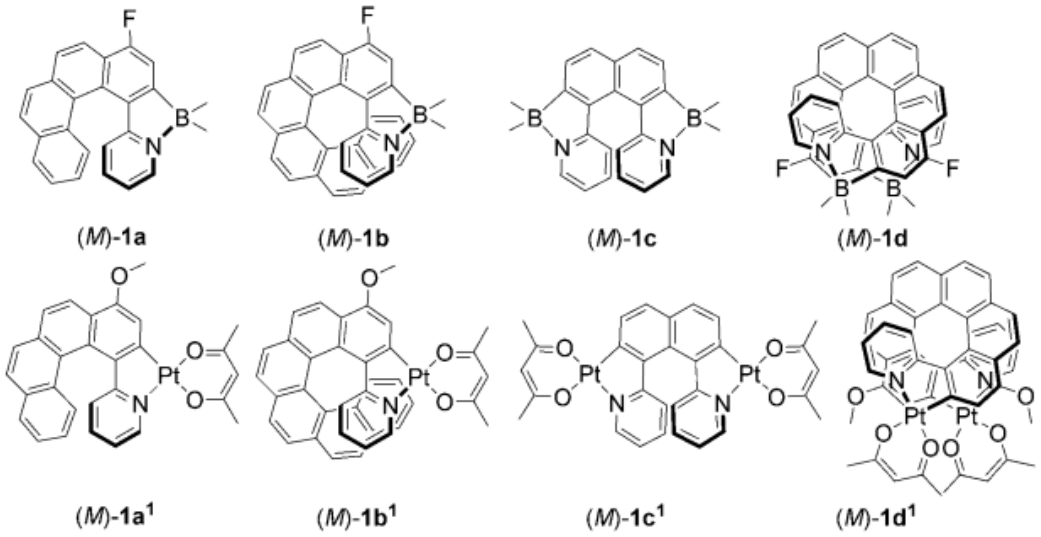

Figure 1.4. Structures of azabora[n]helicenes (1a to 1d) and the corresponding platina[n]helicenes ($1a^1$ to $1d^1$). Reprinted from ref. 57 with permission from *John Wiley and Sons.*

The g_{lum} for platina[n]helicences displayed values in the order of 10^{-3} to 10^{-4} which is typical with SOMs, but these complexes exhibit higher quantum yields. Interestingly, the g_{lum} values for azabora[n]helicences displayed g_{lum} values as high as 10^{-2} with red phosphorescence showing that these compounds are potential materials for CPL-OLEDs. Moreover, sign of CPL signals for *M* and *P* for the compounds 1a-1c are opposite of what was obtained with the bis azabora[10] helicene (structure 1d). Meanwhile, the corresponding platina complex (structure $1d^1$) showed no CPL signal due to planarity of geometry of platinum, hence it clearly shows that the Boron influenced the geometry hence optical chirality in helicenes.[57]

The direction of the studies and perspectives was then focused on the perturbation of achiral organoboron complex to induce chirality through molecular designs. One example is the unique boron fused double-helicenes synthesized by Hatakeyama et al, (2016).[58] They demonstrated boron complexation and introduction of bulky alkyl group such as tert-butyl caused distorted racemic structure. The structure of

the compound and stacked arrangement was shown in Figure 1.4-B. This has formed chiral helicenes which exhibited g_{lum} value of 1.7 x 10^{-3} (see Figure 1.5).

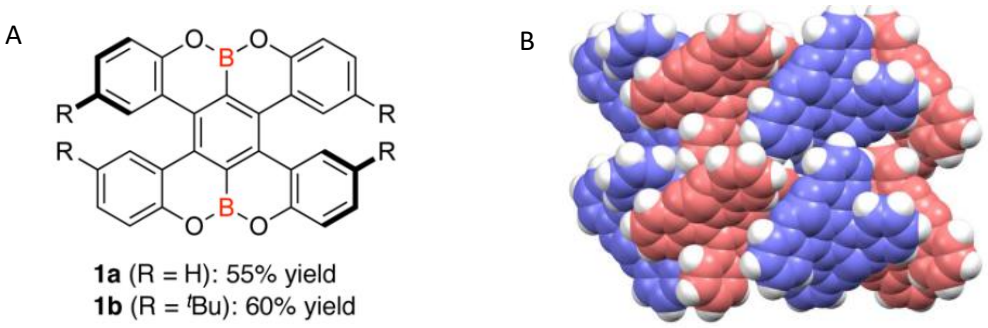

Figure 1.5. Boron fused double-helicenes structure (a) and packing (b). Reprinted from ref. 58 with permission from *American Chemical Society*.

Another example of molecular structure manipulation in inducing chirality was the synthesis of figure-of-eight helicity. The group of Nabeshima designed synthesized macrocyclic bis-BODIPY (bis(boron-dipyrromethene)) complex [1B2] shown in Figure 1.6. [59] In their work, they introduced BODIPY units into a macrocyclic ring framework that has induced the chirality of macromolecule. This compound exhibits g_{lum} value of 9 x10^{-3} and ϕ_F = 0.58. Moreover, the emission of this figure-of-eight macromolecule was far red shifted which is very useful in bioimaging applications.

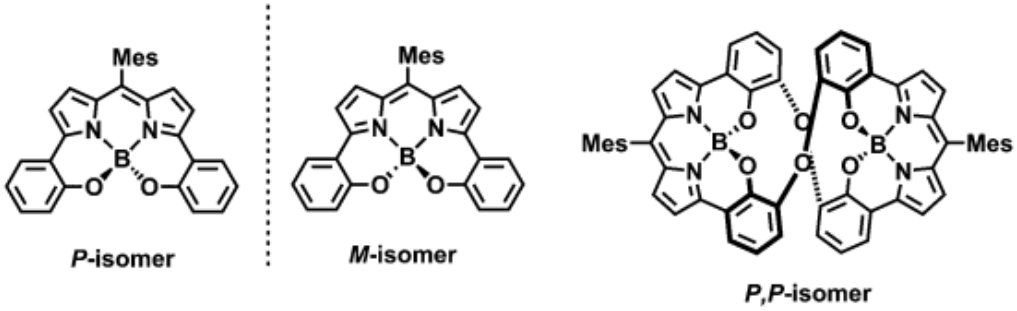

Figure 1.6. Figure-of-eight helicity of N_2O_2 dipyrrins boron complex. Reprinted from ref. 59 as permitted by *Royal Society of Chemistry*.

So far, this figure-of-eight macromolecule bis-BODIPY boron complex is one of the isolated organic molecules that exhibits high g_{lum} values (~10^{-2}) in red region (663nm). The comparison of chiroptical property with reference monomer revealed that bis-BODIPY boron has g_{lum} values more than three times of reference monomer. This is an

indication of synergistic effect of multichromophoric groups which is responsible for enhanced CPL in figure-of-eight conformation.[59]

1.1.2. Enhancing Chiroptical Properties: Supramolecular Assembly

From the early studies on molecular manipulation of the isolated small organic molecules, it is still noticeable that CPL signals are far lower than the lanthanide complexes and obtaining higher g_{lum} values for SOMs remains a challenge for researchers. In the previous section, it was discussed that the perturbation of achiral molecules can be achieved through manipulation of molecular structure and inducing chirality to fluorophore. The synergy between fluorophores in multichromophoric isolated organic molecule has also enhanced the g_{lum} values. Another way of modulating the electronic states of organic molecules in through supramolecular assembly. The first observed enhancement of chiroptical properties through aggregation was in 2001. The helicenes synthesized by the group of Turro showed that the monomeric form ($2x10^{-6}$M) did not display any CPL signals, while increase in concentration to $1x10^{-3}$M caused appearance of emission at 600nm and 700nm accompanied by enhanced CPL signals (g_{lum} = 0.01). The group of Takeuchi developed a helicene containing phthalhydrazide forming trimeric disk through hydrogen bonding that eventually forms 1D nanofibers as shown in Figure 1.7. [60]

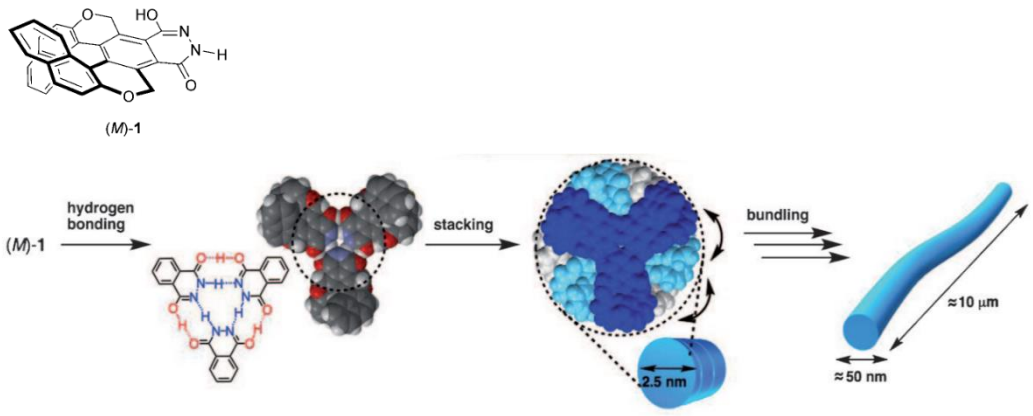

Figure 1.7. Structure of M-1 and self-assembly of helicene containing phthalhydrazide. Reprinted from ref. 60 with permission from *John Wiley and Sons.*

The 1D fibrous self-assembled trimeric disk was found to form in non-polar solvents and the self-assembly is highly dependent on the purity of the enantiomer. This system exhibits promising CPL with g_{lum} value =0.035, which is one of the highest values obtain for compounds without any chiral platforms.[60] On the other hand, the group of

Haino studied supramolecular assembly of tris(phenylisoxazolyl)benzenes. They revealed that supramolecular assembly of this compound is driven by π-π, and dipole-dipole interaction while the alkyl side chains highly affect its stability. Moreover, this compound formed both achiral and chiral supramolecular assembly, the helical assemblies being responsible for the chiroptical properties in both solution and gel forms.[61] This was followed with another study of tris(phenylisoxazolyl)benzenes bearing perylenebisimide moiety. Herein, they showed the helical stacking of both *S* and *R* enantiomers is favorable in decalin and was not formed in chloroform. The helical structure of tris(phenylisoxazolyl)benzenes bearing perylenebisimide displayed g_{lum} value of 0.007. They also showed in this study that the chiroptical properties can be controlled with temperature, wherein they demonstrated the increase in CD of *S* enantiomer at low temperature 293k (g_{abs} value of 0.0014).[62]

Axial chiral platform is also commonly used to induce chirality in achiral fluorophore and in 2013, the group of Kawai demonstrated the first study on enhanced chirality of supramolecular assembled bichromophore system. They covalently attached achiral fluorophore perylene bisimides in enantiopure cyclohexane diamine and formed nanowires which enhance g_{lum} value of monomers ($8x10^{-3}$ at 630 nm) to g_{lum} value of $2.5x10^{-2}$ (at 650 nm) in nanowires formed in methylcyclohexane.[11] Kawai's group continues to evaluate the effect of supramolecular assemblies by comparing the CPL signals from spherical and nanowires of bichromophore perylene bisimides using binaphthyl as chiral bridge (see Figure 1.8). They revealed that the g_{lum} values are highly dependent on the morphologies of supramolecular assembly wherein spherical aggregates display g_{lum} values 0.01 while the 1D nanowires has g_{lum} values 0.02 and lastly, the monomer has g_{lum} values of $3.0x10^{-3}$. This only shows that the chiroptical properties of SOMs can be modulated with the morphology.[63]

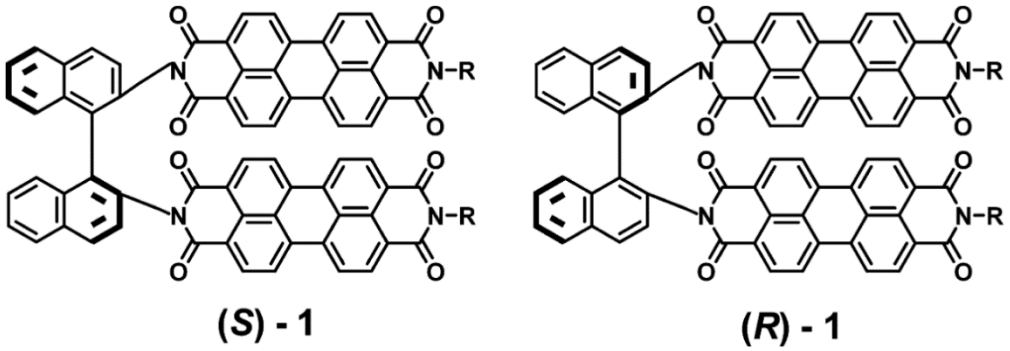

Figure 1.8. Structures of bichromophore perylene bisimides using binaphthyl as chiral bridge where R = $CH(C_6H_{13})_2$. Reprinted from ref. 63 with permission from *American Chemical Society.*

Another example of helical aggregates exhibiting enhanced g_{lum} values upon formation of supramolecular assembly is chiral pyrene derivatives shown in Figure 1.9. In

the study conducted by the group of Akutagawa, chiral alkylamide pyrene derivatives formed 1D nano helical π-stacked formed in different solvents such as methylcyclohexane (MCH) and toluene.[64] The formation of supramolecular assembly was governed not only with π-π stacking but also with the formation of H-bond which was highly affected by the solvent polarity. Using THF and chloroform as solvents, the organogels formation was not observed owing to the destabilized hydrogen bonding, while the supramolecular assembly formed in MCH displayed the most stable and largest excitonic coupling. This has resulted to high g_{lum} value of 0.003. Moreover, the CPL signals of 1D nanowires formed in chloroform and THF was inverted compared to the supramolecular assembly formed in MCH and toluene because of hydrogen bonding modification in self-assembly through solvent polarity.

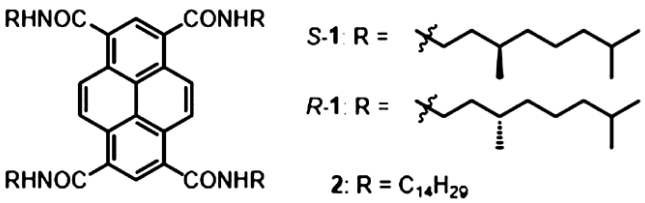

Figure 1.9. Structures of chiral alkylamide pyrene derivatives (*R-1* and *S-1*).[64] Reprinted with permission form *American Chemical Society*.

Although the formation of supramolecular assembly has evidently enhanced the chiroptical properties, most of these compounds showed decrease in quantum yield upon aggregation. This was mainly caused by the increasing non-radiative pathways that was promoted within the aggregated chromophores. Compounds exhibiting aggregation induced emissions (AIE) were shown to counter the challenges in fluorescence quenching upon self-assembly. In 2001, the group of Tang ed the aggregation induced emission (AIE) in 1-methyl-1,2,3,4,5-pentaphenylsilole which exhibits an increase in emission by more than two orders of magnitude.[65] They extended the studies in combing AIE compound with chiral pendants to develop CPL active compound with high fluorescence and g_{lum} values in condensed phase. They designed and synthesized the AIE chromophore (silole) attached to chiral sugars which was shown in Figure 1.10a. Initially, this compound did not exhibit CD signals in monomeric form (low ϕ_F =0.6%). Upon formation of aggregates, silole compound self-assembled into right-handed nano helical wires with high quantum yield (ϕ_F =81.3%) and high g_{lum} values ranging from 0.08-0.32 in cast film, suspension, in PMMA and microfluidic channel (see Figure 1.10b).

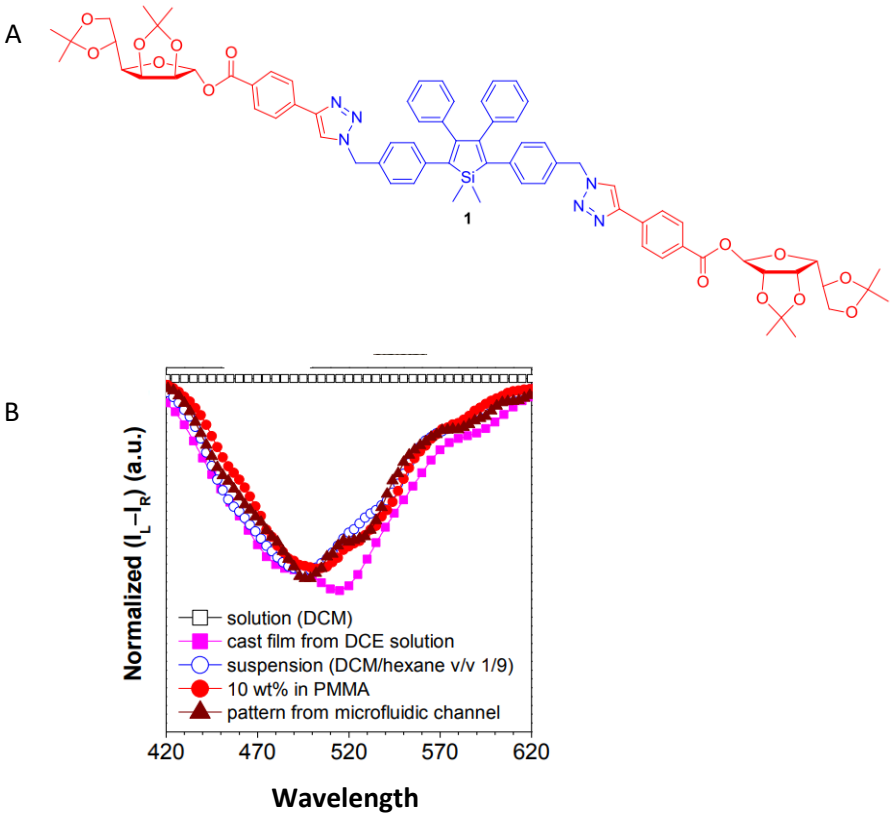

Figure 1.10. Structures AIE silole attached to chiral sugars (a) and the CPL signals at different experimental conditions (b). Image from ref. 6 as permitted by *Royal Chemical Society*.

1.1.3. Responsive CPL-active Organic Molecules

As discussed in the previous section, self-assembled SOMs were shown to enhance the CPL signals as compared with isolated molecules and interestingly, some of these are found to be responsive with different stimuli. Organic molecules which are both CPL-active and responsive with different stimuli are gaining interest for multiple applications. In the past few years, several responsive CPL-active molecules have been developed. This responsivity is based on the fact that the formation of stacked molecules is driven by different intermolecular interactions (π-π stacking, hydrogen bonding formation, and dipole-dipole interactions) which are often sensitive to different stimuli. One example is the dependence of the morphology of the supramolecular assembly with the polarity of solvent which was previously discussed in the study of Kawai's group.[63] Another example is the formation of 0D nanospheres, 2D flake, 3D nanoflakes of *R* and *S* SPAn[9] (see Figure 1.11) at different solvent compositions. By varying the water fraction of the solvent system various aggregates with different morphologies and g_{lum} values were observed, wherein highest g_{lum} values were obtained from 3D nanoflakes (~10^{-2}).

The enhanced g_{lum} values at 3D nanoflakes were attributed to formation of excimers through the molecular packing in this arrangement.

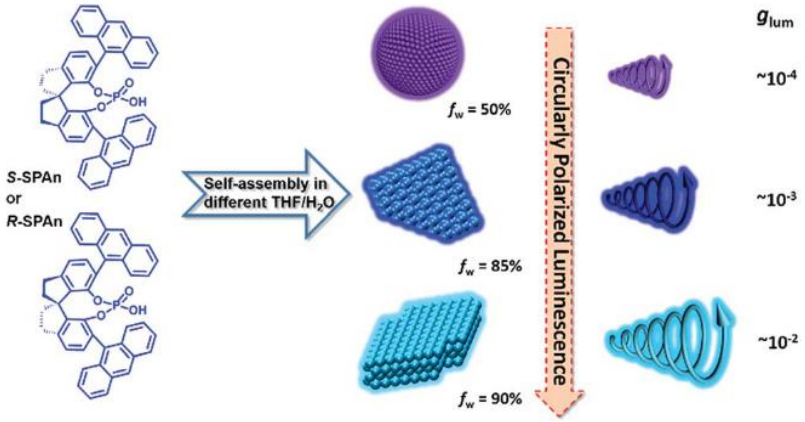

Figure 1.11. Structures of *S* and *R* SPAn and the different morphologies with corresponding g_{lum} values obtained at different THF/water ratio. Image from ref. 9 as permitted by *Royal Society of Chemistry*.

CPL inversion was also reported as an effect of variation in pH of the environment. In the study of Liu's group, they showed that the proton-deprotonation has highly affected the molecular orientation and packing of CPL active compounds through suppression of hydrogen bonding. This was the main reason for the inversion of chirality of the histidine π-gel (PyC_3H).[67] The cycle of protonation-deprotonation is highly efficient for at least five cycles and this system was the first reported bio-inspired histidine proton shuttle. The structure and CPL signals including the reversibility was shown in Figure 1.12. Aside from the pH, light is also a good stimulus in modulating the CPL signals from organic chromophores. While the previous examples of CPL-active organic compounds sensitive to pH and solvent polarity are mostly from supramolecular assembly, light sensitive CPL active SOMs are reported from isolated molecules. Most common examples of light sensitive isolated CPL-active molecules are based on photochromic materials. In one of the studies of Kawai's group, a CPL switch (CPL signals can be turn on or off) was developed based on pyrene-bearing helical tetrathiazole.

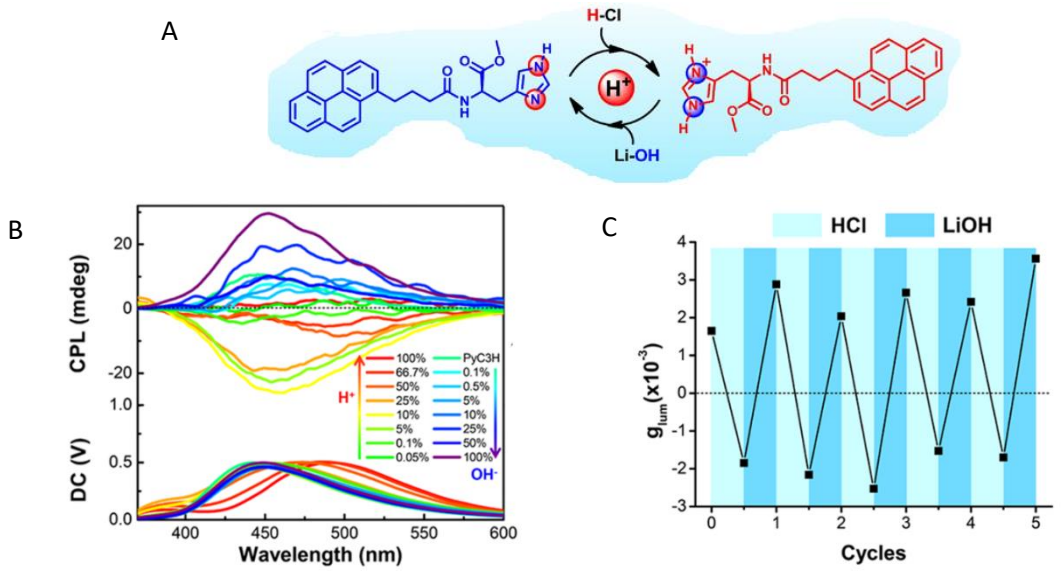

Figure 1.12. Structures of histidine π-gel (PyC_3H) protonated-deprotonated (a) CPL signals at different proton ratios (b) and the cycles of CPL inversion (c).[67] Reprinted with permission from *American Chemical Society*.

The switching of the CPL signals is owed to geometrical changes upon photoisomerization (see Figure 1.13). The open and closed form of tetrathiazole moiety causes large structural changes which induce or prevent the excimers formation from intermolecular interaction of two pyrenes. Formation of hydrogen bonding and π-π stacking between interacting pyrenes were evident in the NMR structures. Moreover, the chirality of the pyrene derivatives was also influenced by the conformation of pyrenes of 1D-o. This has induced excimer formation with enhanced CPL signals and was found to have sign as with the cotton effect observed in CD spectra.[68]

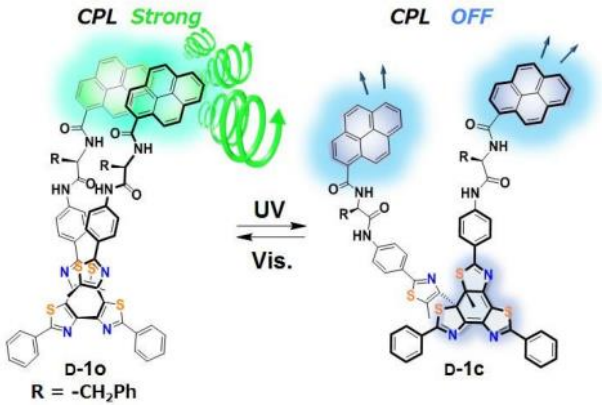

Figure 1.13. Photoswitching (open and close form) of chiral pyrene stack with tetrathiazole D-1. Reprinted from ref. 68 with permission from *Royal Society of Chemistry*.

CPL switches was also reported for supramolecular assembly. In the study from the group of Liu, enantiomeric glutamate spiropyran moiety gels were found to display reversible changes in morphology of the supramolecular assembly from fibers to helical structures after exposure to UV and visible light.[69] The structural changes are responsible for the CPL-switching characteristic of the glutamate spiropyran gels. Packing of gels were investigated to understand the structural changes of supramolecular assembly. They found that the interchangeable zwitterion merocyanine and ring closed state of spiropyran influencing the distortion of aromatic rings out of plane was the reason for chiral arrangement (see Figure 1.14). Isolated molecules in solution did not exhibit chiroptical properties, however upon formation of gels the compound display both CD and CPL signals. The glutamic gelator has chiral center while the fluorophores are achiral, hence chiroptical properties obtained after the formation of supramolecular assembly only proves that the chirality was transferred from gelator to the spiropyran.[69]

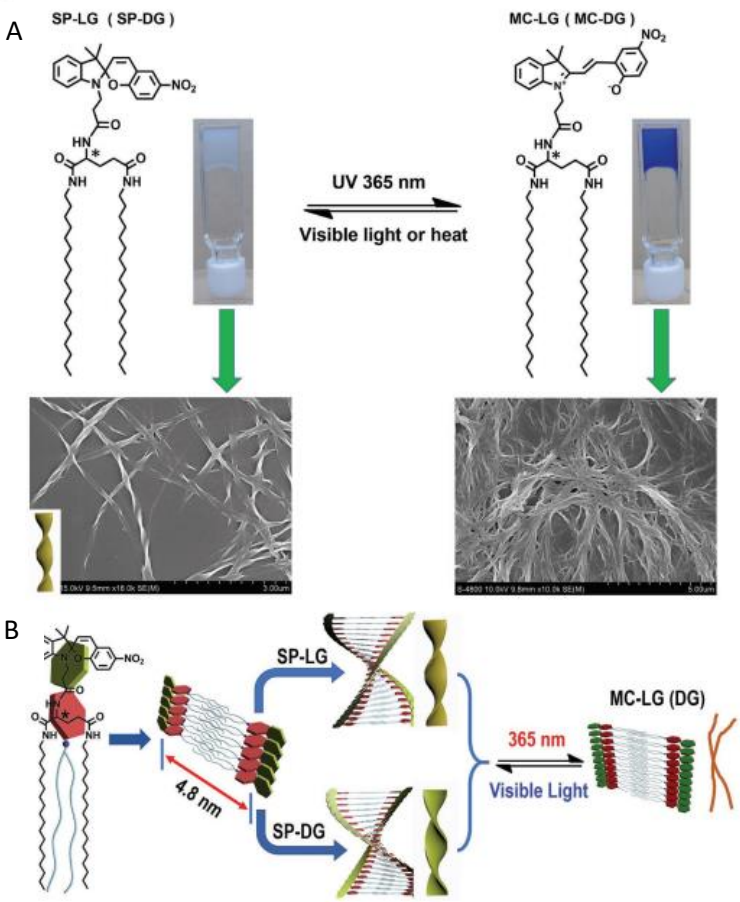

Figure 1.14. Structures of enantiomeric glutamate spiropyran moiety in zwitterionic merocyanine (MC) and closed ring form including the SEM images (a) and schematic diagram of structural changes after exposure to UV and visible light.[69]

From the discussed studies on responsive CPL active compounds, it was shown that most of the changes in chiroptical properties are rooted from the structure changes with stimuli. Hence, application of mechanical force which highly affect the molecular packing of compounds was also reported to cause CPL signal changes. Several studies on CPL sensitivity after applying mechanical stress were reported on metal-organic frameworks.[10] On the other hand, only few studies on solid state SOMs and the sensitivity of its CPL signal to mechanical stress have been reported. In 2019, the group of Allain and Métivier revealed the mechano-CPL (changes in CPL signal upon application of mechanical stress) of difluoro-boron β-diketonate (DFB) complexes attached to chiral amido groups shown in Figure 1.15.

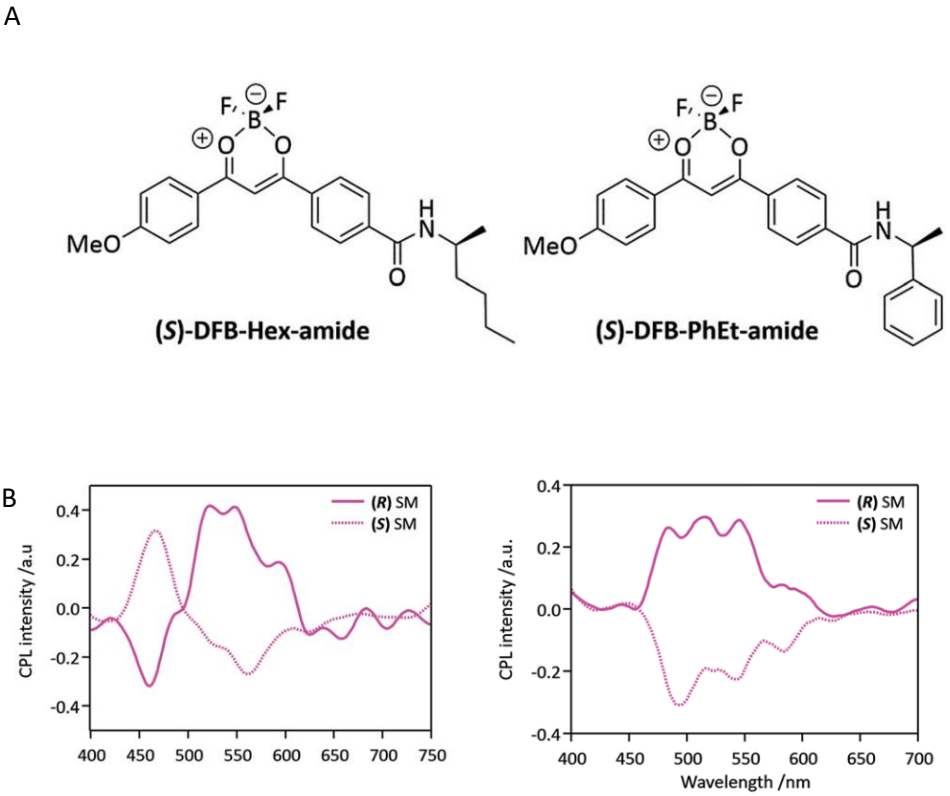

Figure 1.15. Structures of DFB-Hex-amide and DFB-Phet-amide (a) and the CPL signals of thermal annealed and smeared samples (b).[70]

These chiral difluoro-boron β-diketonate (DFB) complexes display low g_{lum} values ($<10^{-3}$) in monomeric form. Solutions DFB-Hex-amide and DFB-Phet-amide were deposited in paper which also exhibited low CPL signals however, after thermal annealing the deposited samples the CPL signals increased with g_{lum} values in the range of 10^{-2}. The thermal annealed samples were smeared displaying CPL signal inversion in DFB-Hex-amide accompanied with appearance of emission at longer wavelength. The red shifted emission and CPL signals including its inversion was mainly due to the exciton-coupling induced after smearing. On the other hand, the DFB-Phet-amide did not show inversion of CPL signals and promotes the formation of amorphous form. The differences in the

behavior of these two chiral DFB compounds lies behind the conformational freedom brought by their structures in crystalline form. It is also the first reported signal inversion of CPL in solid state after application of mechanical stress.[70]

1.2. Mechanofluorochromism of Small Organic Molecules

The last example of CPL active compounds based on DFB was displaying CPL signals sensitive to mechanical stress. Moreover, these compounds display mechanofluorochromism or the shift in emission brought by application of mechanical force. Mechanofluorochromic compounds have been capturing the interest of researchers for the past 10years because of their potential use in development of advanced smart materials and sensors. Mechanofluorochromism exhibited by organic molecules has some advantages such as tunability of its emission through molecular structure manipulation. One of the early studies in mechanofluorochromism of organic dyes was in 2002 when Weder demonstrated the mechanofluorochromism of oligo (p-phenylene vinylene) (OPVs) derivatives deposited in LLDPE blend films (see Figure 1.16a).

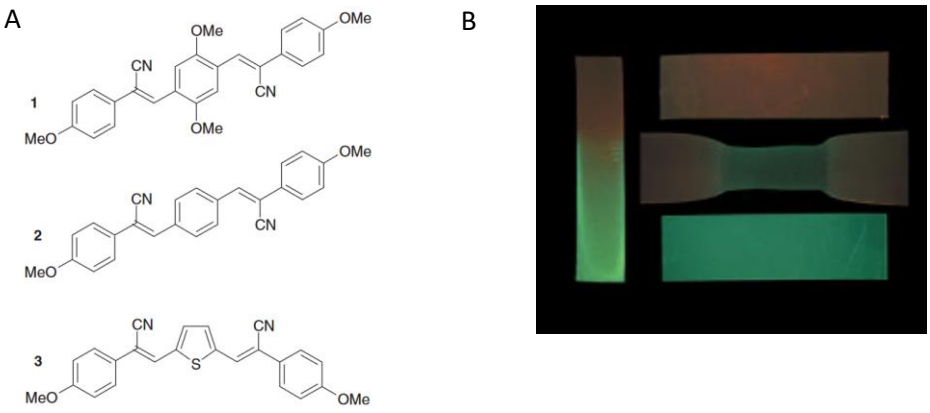

Figure 1.16. Structures of oligo (p-phenylene vinylene) (OPVs) derivatives (a) and the emissions of LDDPE dyed with (OPVs) derivatives before and after stretching (b).[27] Reprinted with permission from *John Wiley and Sons.*

Years before Weder's experiment, cyano-OPVs were already known to display emission from induced excimer formation in compounds owing on different crystallinity and pronounced π-π stacking of OVPs. It was shown in Weder's work that the emission of OPVs derivatives deposited in host polymer can be controlled through the extent of aggregation with varying concentrations. Most importantly, changes in emission were observed after uniaxial tensile stretching mainly caused by suppressed excimer formation and dominant contribution from monomers in stretched films. The images of dyed polymer films before and after stretching were shown in Figure 1.16b.[27] This study was

believed to be the first demonstration of mechanofluorochromism of organic molecules deposited in polymer hosts. To further intensify the emission shift, organic dyes are then covalently attached in polymer. Herein, they showed the more intense mechanofluorochromic effect caused by the higher forces directly experienced by OPVs after applying mechanical stress. This method induced smaller aggregate of dyes which was seldom observed in physical blending. The application of mechanical stress caused the destruction of molecular arrangement of these small aggregates triggering more pronounced changes in emission.[71] In a similar study by the group Pucci, they used bis(benzoxazolyl)stilbene in poly(propylene) film and similar emission shifts due to suppressed excimer formation were obtained after stretching the film.[72] From these series of studies, it was then suggested that the mechanoflurochromism was highly dependent on molecular packings and aggregation of dye in the polymer platforms. These can be modulated with varying concentrations as well as the molecular structure of dyes.

From the embedded or covalently bonded organic dyes in polymers platforms, studies were shifted to pure solid-state materials displaying mechanofluorochromism. Several factors affecting the mechanofluorochromic properties in organic compounds such as intermolecular interactions, molecular structures, crystal packing and aggregation was explored in later years after discovering mechanofluorochromism. The group of Akari showed the importance of hydrogen bonding sites specifically of amide group (C_6TPPy) in mechanofluorochomism of pyrenes.[73] They demonstrated that the presence of amide helped to stabilize the columnar stacking of these pyrene units exhibiting blue emissive powder (B-form) shown in Figure 1.17b.

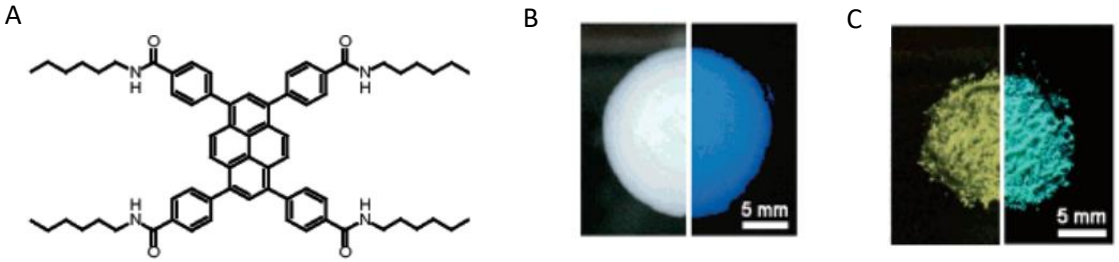

Figure 1.17. Structures of pyrene derivative with C_6TPPy (a) the B-form (b) and G-form (c) under ambient light (left) and UV (right).[73] Reprinted with permission from *American Chemical Society*.

On the other hand, smearing B-form pyrenes lead to distortion of molecular stacking causing emission shift with green emissions (G-form) shown in Figure 1.17c. The structural investigation through XRD and IR revealed that the green emissive powder has weaker hydrogen bonding, hence proves the impact of intermolecular interaction in mechanofluorochromic properties. This is also the first reported study of mechanofluorochromism of organic compound in pure solid-state form.[18]

The continuation of study with pyrene derivatives by Akari's group evaluated the effect hydrogen bonding in mechanofluorochromism through replacement of the amide groups with esters. The strength of hydrogen bonding in pyrenes with four amide groups are responsible for the formation of molecular stacking with blue emission, while the ester derivative was shown to form slip stacking causing the red shifted emission. It was also discovered that these compounds are displaying reversible emission. The recovery of the initial state for pyrene with amide groups is achievable when lower pressure was exerted in smearing the compound. High-pressured smearing displayed irreversible mechanofluorochromic effect caused by complete destruction of hydrogen bonds. On the other hand, ester derivative requires higher pressure to observe mechanofluorochromic effect. This demonstrates that intermolecular interactions are not only crucial with emission shift after smearing, but also playing significant role in recovery of emissions.

Recovery of emission from smeared to initial state was attained with series of thermal annealing-smearing cycles. The effect of bulkiness of side chains was revealed to affect the reversibility of the emission. In the same study of Akari's group, shortest alkyl chains did not show any reversibility, while the intermediated length of alkyls (C_6-C_{14}) showed reversibility. This is indicating that side chains support the rearrangement of molecules. Finally, the bulkiest side chain 2-ethylhexyl prevented the molecular arrangement resulting to partially reversed emission.[74] Another study of mechanofluorochromism in pyrene derivatives bearing bulky sidechains was reported by the group of Métivier and Allain (see Figure 1.18).[29] Similar observations from Akari's group were observed wherein the pyrene derivative with bulky sidechain (3) displayed partial emission recovery indicating hindered re-arrangement while the less bulky side chain (2) exhibits recovery after thermal annealing. Lastly, the structure of (1) promotes formation of polymorphs exhibiting hypsochromic and bathochromic shift with monomer-like and dynamic excimer behaviors. For both polymorphs, only partial recovery was observed owing to the formation of meta-stable state after thermal annealing.

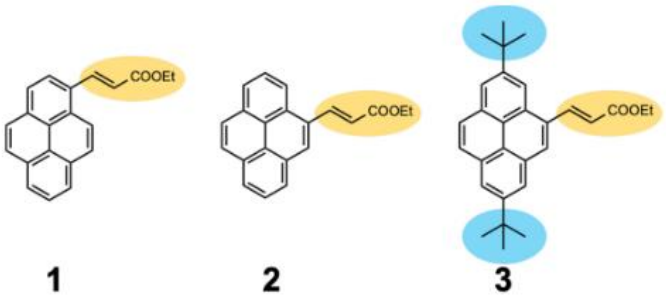

Figure 1.17. Structures of pyrene derived acrylates (1-3).[29]
Reprinted with permission from *Elsevier.*

One of the fastest emission recoveries after smearing the crystals has been observed in difluoro-boron β-diketonate (DFB) derivatives. The group of Fraser demonstrated that the dendritic blue emissive crystals of DFB Avobenzone (BF_2AVB) turned to yellow emissive powder after smearing. It recovers its blue emission after few seconds of annealing. The possibility of multiple interactions such as hydrogen bonding, arene stacking, and fluorine interactions was the suggested cause of such reversibility in emission.[75] Moreover, they also demonstrated in this work that emissions are tunable through different solid-state morphologies. Herein, they exhibited green crystals, blue crystals, and dendritic crystals arranged in different molecular packings (see Figure 1.18).

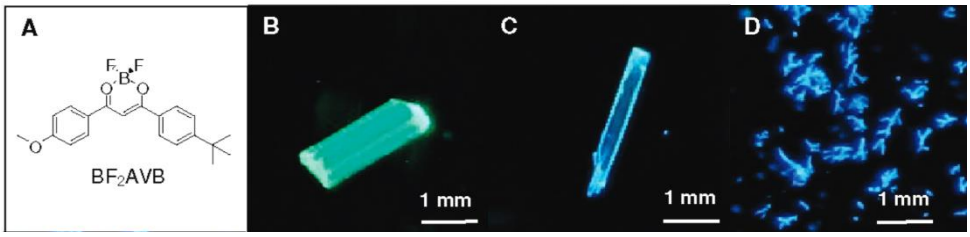

Figure 1.18. Structures BF_2AVB (a) and the images of green crystals (b), blue crystal (c) and dendritic crystals (d).[75] Reprinted with permission from *American Chemical Society.*

Although several studies prior to the paper of Fraser were published explaining the emission shift through excimer formation, the reversibility of the emission after smearing are not well understood. Two years later, Fraser together with the group Reddy explained the mechanofluorochromic property of two polymorphs BF_2AVB (cyan and green emitting crystals) through molecular structure and properties of crystals. In depth crystal analysis and nanoindentation measurements revealed that the cyan emitting crystals contains weak slip planes which tends to recover after thermal annealing and was easily deformed as compared to green emitting crystal which is harder (see Figure 1.19).[76]

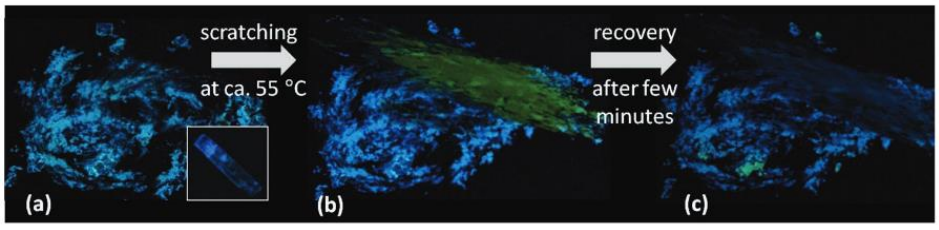

Figure 1.19. Powder film from crushed cyan BF_2AVB (a) after smearing showing yellow emission (b), recovery after few minutes of exposure in heating gun (c).[76] Reprinted with permission from *John Wiley and Sons*.

The findings in the study of Reddy's group hence recommends designing of mechanofluorochromic compounds where the crystal structures contain many slip planes for it was expected to display promising emission shift and recovery.

To further understand the mechanofluorochromism in difluoro-boron β-diketonate (DFB) compounds, the group of Allain and Métivier conducted an in-depth study on the polymorphism and thermal back reaction of DFB-Ester through combination of spectroscopic and photophysico-chemical measurements. They revealed in this study that DFB-Ester formed green crystals and yellows emissive crystals which mainly differs in the degree of overlap and π-π stacking among its aromatic groups. Smearing or depositing the solution forms amorphous state with yellow orange emission. The thermal back reactions from yellow orange to green was explained through residual crystals that re-grow after thermal annealing. However, since two crystals may co-exist, the process of thermal annealing causes competitive formation of yellow crystals (meta-stable) and green crystals (thermal stable). Increasing the annealing temperature favors formation of more thermally stable crystals (green crystals).[77] A scheme summarizing the different processes is shown in Figure 1.20.

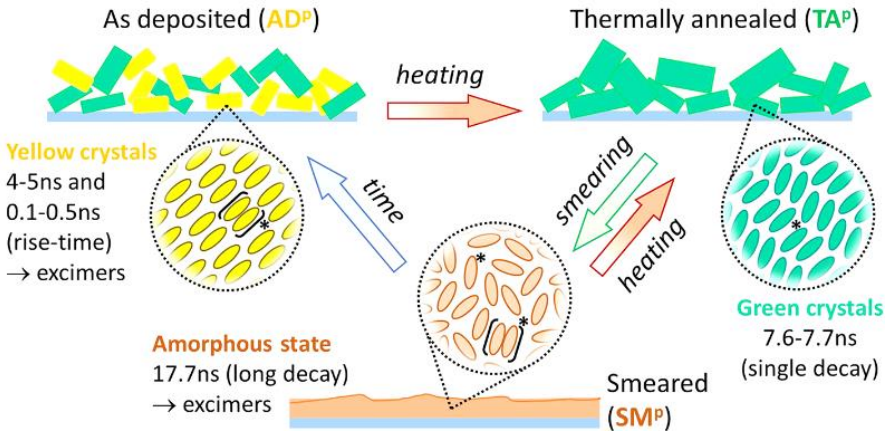

Figure 1.20. The schematic diagram showing the morphologies, photophysical processes of the emitting species including the decay times.[77] Reprinted with permission from publisher *American Chemical Society.*

Although studies on in-depth studies on mechanofluorochromism and its emission recovery were reported, efforts were still exerted by different groups to unveil the effects of molecular structures on solid state properties of DFB derivatives. Some of

these are the variation in alkoxy length of side chain in DFB revealing the threshold length of n=6 in reversibility of ordered structure.[22] Also, the effect of chelating group in β-diketonates such as phenyl group instead of fluorine were explored. This revealed the fluorescence quenching, and poor mechanofluorochromism with phenyl owing to the non-radiative relaxation pathway and bulky groups.[78]

1.3 Objective and Scope of the Studies

In this chapter, the early studies and discovery of CPL-active materials of small organic molecules were discussed. The different molecular designs from mono-chromophore, helicenes, spiranic fluorophores, to synergistic multi-chromophores twisted macromolecules in isolated form have given its contribution in enhancing the chiroptical properties of organic molecules. Moreover, supramolecular assembly introduced an elevated strategy to enhance the g_{lum} values of small organic molecules while avoiding the challenges in synthesizing large molecules. It was also introduced some of the CPL-responsive compounds to different stimuli like mechanical stress. Development of such materials has become more appealing for continuous study of single molecules with multiple functionalities; therefore, this thesis aims to contribute to design and synthesis of a unique small organic displays which displays both CPL-activity and mechanofluorochromism. Specifically, we aim: (1) to synthesize a bichromophore DFB compound and explore its chiroptical properties in solution and supramolecular assembly; (2) to study the photophysical properties of supramolecular assembly and its sensitivity to stimuli; and finally (3) to study the mechanofluorochromism of bichromophore DFBs.

The synthesis of bichromophoric DFB was discussed in the first part of the study and, we extended the investigation on the effect of connectivity in meta and para position of β-diketonate. Photophysical properties as well as the theoretical calculations using DFT and TD-DFT were executed to further understand the nature of the bichromophores bearing two DFB in para and meta positions. Supramolecular assembly was attempted for both compounds using different solvent system followed by CD and CPL spectroscopy measurements to investigate the effect of aggregation to the chiroptical properties. Structural analysis using XRD, and molecular modelling were carried out to understand the molecular packing in supramolecular assembly.

In second part, the research focused on the comparison of photophysical properties of mono and bichromophoric DFB as well as its ability to form supramolecular assembly. We then proceeded in the energy migration property of mono-substituted compared to di-substituted DFB and finally the supramolecular assembly. In the later part

of the chapter 3, we discussed the responsiveness of the supramolecular self-assembled nanowires to UV light, and we investigated the primary reasons for such responsiveness through combination of photophysical measurements and microscopy.

The last part of the research was focused on the solid-state measurements wherein the mechanofluorochromic properties of mono-DFB and bichromophore DFB was compared. Moreover, we studied the mechanofluorochromism of bichromophore bearing amide and ester bridges to determine the impact of intermolecular interactions such as hydrogen bonding. To gain insights and understanding to the mechanofluorochromic properties of these compounds, we did single crystal analysis and time-resolved fluorescence spectroscopy. The reversibility of the emission was also investigated, and some calculations were performed to understand the intermolecular interactions within the crystal system. In the last chapter, the conclusions and perspectives for the study was discussed.

1.4 References

(1) Inaki, M.; Liu, J.; Matsuno, K. Cell Chirality: Its Origin and Roles in Left–Right Asymmetric Development. *Phil. Trans. R. Soc. B.* 2016, *371* (1710), 20150403.

(2) McDermott, G.; Prince, S. M.; Freer, A. A.; Hawthornthwaite-Lawless, A. M.; Papiz, M. Z.; Cogdell, R. J.; Isaacs, N. W. Crystal Structure of an Integral Membrane Light-Harvesting Complex from Photosynthetic Bacteria. *Nature.* 1995, *374* (6522), 517–521.

(3) Umair, M.; Jabbar, S.; Sultana, T.; Ayub, Z.; Abdelgader, S. A.; Xiaoyu, Z.; Chong, Z.; Fengxia, L.; Xiaomei, B.; Zhaoxin, L. Chirality of the Biomolecules Enhanced Its Stereospecific Action of Dihydromyricetin Enantiomers. *Food Sci. Nutr.* 2020, *8* (9), 4843–4856.

(4) Gal J, Cintas P. Early History of the Recognition of Molecular Biochirality. *Top Curr. Chem.* 2013; 333:1-40.

(5) Gal, J. Molecular Chirality in Chemistry and Biology: Historical Milestones. *Helv. Chim. Acta.* 2013, *96* (9), 1617–1657.

(6) Berova, N.; Bari, L. D.; Pescitelli, G. Application of Electronic Circular Dichroism in Configurational and Conformational Analysis of Organic Compounds. *Chem. Soc. Rev*., 2007,36, 914-931.

(7) Saleh, N.; Moore, B.; Srebro, M.; Vanthuyne, N.; Toupet, L.; Williams, J. A. G.; Roussel, C.; Deol, K. K.; Muller, G.; Autschbach, J.; Crassous, J. Acid/Base-Triggered Switching of Circularly Polarized Luminescence and Electronic Circular Dichroism in Organic and Organometallic Helicenes. *Chem. Eur. J.* 2015, *21* (4), 1673–1681.

(8) Wan, S.-P.; Lu, H.-Y.; Li, M.; Chen, C.-F. Advances in Circularly Polarized Luminescent Materials Based on Axially Chiral Compounds. *J. Photochem. Photobiol. C.* 2022, *50*, 100500.

(9) Ma, K.; Chen, W.; Jiao, T.; Jin, X.; Sang, Y.; Yang, D.; Zhou, J.; Liu, M.; Duan, P. Boosting the Circularly Polarized Luminescence of Small Organic Molecules *via* Multi-Dimensional Morphology Control. *Chem. Sci.* 2019, *10* (28), 6821–6827.

(10) Deng, Y.; Wang, M.; Zhuang, Y.; Liu, S.; Huang, W.; Zhao, Q. Circularly Polarized Luminescence from Organic Micro-/Nanostructures. *Light Sci. Appl.* 2021, *10* (1), 76.

(11) Kumar, J.; Nakashima, T.; Tsumatori, H.; Mori, M.; Naito, M.; Kawai, T. Circularly Polarized Luminescence in Supramolecular Assemblies of Chiral Bichromophoric Perylene Bisimides. *Chem. Eur. J.* 2013, *19* (42), 14090–14097.

(12) Song, F.; Zhao, Z.; Liu, Z.; Lam, J. W. Y.; Tang, B. Z. Circularly Polarized Luminescence from AIEgens. *J. Mater. Chem. C* 2020, *8* (10), 3284–3301.

(13) Riehl, J. P.; Richardson, F. S. Circularly Polarized Luminescence Spectroscopy. *Chem. Rev*. 1986, 86, 1, 1–16.

(14) Sánchez-Carnerero, E. M.; Agarrabeitia, A. R.; Moreno, F.; Maroto, B. L.; Muller, G.; Ortiz, M. J.; de la Moya, S. Circularly Polarized Luminescence from Simple Organic Molecules. *Chem. Eur. J.* 2015, *21* (39), 13488–13500.

(15) Lunkley, J. L.; Shirotani, D.; Yamanari, K.; Kaizaki, S.; Muller, G. Extraordinary Circularly Polarized Luminescence Activity Exhibited by Cesium Tetrakis(3-Heptafluoro-Butylryl-(+)-Camphorato) Eu(III) Complexes in EtOH and $CHCl_3$ Solutions. *J. Am. Chem. Soc.* 2008, *130* (42), 13814–13815.

(16) Eddingsaas, N. C.; Suslick, K. S. Intense Mechanoluminescence and Gas Phase Reactions from the Sonication of an Organic Slurry. *J. Am. Chem. Soc.* 2007, *129* (21), 6718–6719.

(17) Tsuchiya, Y.; Yamaguchi, K.; Miwa, Y.; Kutsumizu, S.; Minoura, M.; Murai, T. *N* , *N* -Diarylthiazol-5-Amines: Structure-Specific Mechanofluorochromism and White Light Emission in the Solid State. *Bull. Chem. Soc. Jpn.* 2020, *93* (7), 927–935.

(18) Chi, Z.; Zhang, X.; Xu, B.; Zhou, X.; Ma, C.; Zhang, Y.; Liu, S.; Xu, J. Recent Advances in Organic Mechanofluorochromic Materials. *Chem. Soc. Rev.* 2012, *41* (10), 3878.

(19) Louis, M.; Piñero García, C.; Brosseau, A.; Allain, C.; Métivier, R. Mechanofluorochromism of a Difluoroboron-β-Diketonate Derivative at the Nanoscale. *J. Phys. Chem. Lett.* 2019, *10* (16), 4758–4762.

(20) Krishna, G. R.; Devarapalli, R.; Prusty, R.; Liu, T.; Fraser, C. L.; Ramamurty, U.; Reddy, C. M. Structure–Mechanical Property Correlations in Mechanochromic Luminescent Crystals of Boron Difluoride Dibenzoylmethane Derivatives. *IUCrJ.* 2015, *2* (6), 611–619.

(21) Morris, W. A.; Liu, T.; Fraser, C. L. Mechanochromic Luminescence of Halide-Substituted Difluoroboron β-Diketonate Dyes. *J. Mater. Chem. C.* 2015, *3* (2), 352–363.

(22) Nguyen, N. D.; Zhang, G.; Lu, J.; Sherman, A. E.; Fraser, C. L. Alkyl Chain Length Effects on Solid-State Difluoroboron β-Diketonate Mechanochromic Luminescence. *J. Mater. Chem.*, 2011,21, 8409-8415.

(23) Ito, F.; Naganawa, R.; Fujimoto, Y.; Takimoto, M.; Mochiduki, Y.; Katsumi, S. Real‐Time Fluorescence Visualization of Nanoparticle Aggregation and the Polymorph‐Transition Process of a Mechanofluorochromic Difluoroboron‐β‐Diketone Derivative. *ChemPhysChem.* 2021, cphc.202100370.

(24) Calupitan, J. P.; Brosseau, A.; Josse, P.; Cabanetos, C.; Roncali, J.; Métivier, R.; Allain, C. Mechanofluorochromic Material toward a Recoverable Microscale Force Sensor. *Adv. Mater. Interfaces.* 2022, 9, 2102246.

(25) Josse, P.; Allain, M.; Calupitan, J. P.; Jiang, Y.; Cabanetos, C.; Roncali, J. Structural Control of the Molecular Packing and Dynamics of Mechanofluorochromic Materials Based on Small Donor‐Acceptor Systems with Turn‐On Luminescence. *Adv. Optical Mater.* 2020, *8* (13), 2000420.

(26) Liu, M.; Zhai, L.; Sun, J.; Xue, P.; Gong, P.; Zhang, Z.; Sun, J.; Lu, R. Multi-Color Solid-State Luminescence of Difluoroboron β-Diketonate Complexes Bearing Carbazole with Mechanofluorochromism and Thermofluorochromism. *Dyes and Pigments* 2016, *128*, 271–278.

(27) Löwe, C.; Weder, C. Oligo(p-Phenylene Vinylene) Excimers as Molecular Probes: Deformation-Induced Color Changes in Photoluminescent Polymer Blends. *Adv. Mater.* 2002, *14* (22), 1625–1629.

(28) Hulvat, J. F.; Sofos, M.; Tajima, K.; Stupp, S. I. Self-Assembly and Luminescence of Oligo(*p* -Phenylene Vinylene) Amphiphiles. *J. Am. Chem. Soc.* 2005, *127* (1), 366–372.

(29) Hirai, Y.; Wrona-Piotrowicz, A.; Zakrzewski, J.; Brosseau, A.; Métivier, R.; Allain, C. Mechanofluorochromism of pyrenyl acrylates with different substitutional position and steric hindrance. *J. Photochem. Photobiol.* Vol. 405,2021, 112972.

(30) Hirai, Y.; Laize‐Générat, L.; Wrona‐Piotrowicz, A.; Zakrzewski, J.; Makal, A.; Brosseau, A.; Michely, L.; Versace, D.; Allain, C.; Métivier, R. Multi‐Directional Mechanofluorochromism of Acetyl Pyrenes and Pyrenyl Ynones. *ChemPhysChem* 2021, *22* (15), 1638–1644.

(31) Zhao, J.; Li, L.; Wang, W.; Guan, X.; Rong, J.; Zhang, C. Modulation of Mechanofluorochromism Based on Carboxylic Acid Esters Compounds Bearing Triphenylamine and Pyrene with Different Substituents. *J. Lumin.* 2022, *241*, 118495.

(32) Genovese, D.; Aliprandi, A.; Prasetyanto, E. A.; Mauro, M.; Hirtz, M.; Fuchs, H.; Fujita, Y.; Uji‐I, H.; Lebedkin, S.; Kappes, M.; De Cola, L. Mechano‐ and Photochromism from Bulk to Nanoscale: Data Storage on Individual Self‐Assembled Ribbons. *Adv. Funct. Mater.* 2016, *26* (29), 5271–5278.

(33) Yu, X.; Li, X.; Cai, Z.; Sun, L.; Wang, C.; Rao, H.; Wei, C.; Bian, Z.; Jin, Q.; Liu, Z. Mechanochromic Properties in a Mononuclear Cu(Ⅰ) Complex without Cuprophilic Interactions. *Chem. Commun.* 2021, *57* (41), 5082–5085.

(34) Jia, J.; Zhao, H. A Multi-Responsive AIE-Active Tetraphenylethylene-Functioned Salicylaldehyde-Based Schiff Base for Reversible Mechanofluorochromism and Zn2+ and CO32− Detection. *Org. Electron.* 2019, *73*, 55–61.

(35) Nagura, K.; Saito, S.; Yusa, H.; Yamawaki, H.; Fujihisa, H.; Sato, H.; Shimoikeda, Y.; Yamaguchi, S. Distinct Responses to Mechanical Grinding and Hydrostatic Pressure in Luminescent Chromism of Tetrathiazolylthiophene. *J. Am. Chem. Soc.* 2013, *135* (28), 10322–10325.

(36) Mosca, S.; Milani, A.; Peña-Álvarez, M.; Yamaguchi, S.; Hernández, V.; Ruiz Delgado, M. C.; Castiglioni, C. Mechanochromic Luminescent Tetrathiazolylthiophenes: Evaluating the Role of Intermolecular Interactions through Pressure and Temperature-Dependent Raman Spectroscopy. *J. Phys. Chem. C.* 2018, *122* (30), 17537–17543.

(37) Zhou, L.; Xu, D.; Gao, H.; Han, A.; Liu, X.; Zhang, C.; Li, Z.; Yang, Y. Triphenylamine Functionalized β-Ketoiminate Boron Complex Exhibiting Aggregation-Induced Emission and Mechanofluorochromism. *Dyes Pigm.* 2017, *137*, 200–207.

(38) Zhao, J.; Peng, J.; Chen, P.; Wang, H.; Xue, P.; Lu, R. Mechanofluorochromism of Difluoroboron β-Ketoiminate Boron Complexes Functionalized with Benzoxazole and Benzothiazole. *Dyes Pigm.* 2018, *149*, 276–283.

(39) Tanaka, K.; Chujo, Y. Recent Progress of Optical Functional Nanomaterials Based on Organoboron Complexes with β-Diketonate, Ketoiminate and Diiminate. *NPG Asia Mater.* 7, e223 2015.

(40) Yoshii, R.; Suenaga, K.; Tanaka, K.; Chujo, Y. Mechanofluorochromic Materials Based on Aggregation-Induced Emission-Active Boron Ketoiminates: Regulation of

the Direction of the Emission Color Changes. *Chem. Eur. J.* 2015, *21* (19), 7231–7237.

(41) Zhang, H.; Chen, P.-Z.; Niu, L.-Y.; Yang, Q.-Z. A Difluoroboron B-Diketonate-Based Luminescent Material with Tunable Solid-State Emission and Thermally Activated Delayed Fluorescence. *Mater. Chem. Front*., 2020,4, 285-291.

(42) Xu, S.; Evans, R. E.; Liu, T.; Zhang, G.; Demas, J. N.; Trindle, C. O.; Fraser, C. L. Aromatic Difluoroboron β-Diketonate Complexes: Effects of π-Conjugation and Media on Optical Properties. *Inorg. Chem.* 2013, *52* (7), 3597–3610.

(43) Qi, Y.; Wang, Y.; Yu, Y.; Liu, Z.; Zhang, Y.; Du, G.; Qi, Y. High-Contrast Mechanochromism and Polymorphism-Dependent Fluorescence of Difluoroboron β-Diketonate Complexes Based on the Effects of AIEE and Halogen. *RSC Adv.* 2016, *6* (40), 33755–33762.

(44) Gong, J.; Zhang, X. Coordination-Based Circularly Polarized Luminescence Emitters: Design Strategy and Application in Sensing. *Coord. Chem. Rev.* 2022, *453*, 214329.

(45) Greenfield, J. L.; Wade, J.; Brandt, J. R.; Shi, X.; Penfold, T. J.; Fuchter, M. J. Pathways to Increase the Dissymmetry in the Interaction of Chiral Light and Chiral Molecules. *Chem. Sci.* 2021, *12* (25), 8589–8602.

(46) Liao, P.; Zang, S.; Wu, T.; Jin, H.; Wang, W.; Huang, J.; Tang, B. Z.; Yan, Y. Generating Circularly Polarized Luminescence from Clusterization‐triggered Emission Using Solid Phase Molecular Self-Assembly. *Nat. Commun.* 2021, *12* (1), 5496.

(47) C.A. Emeis, L.J. Oosterhoff. Emission of circularly polarized radiation by optically active compounds, *Chem. Phys. Lett*. 1, (4),1967,129-13.

(48) Sánchez-Carnerero, E.M.; Moreno, F.; Maroto, B.L.; Agarrabeitia, A.R.; Ortiz, M.J.; Vo, B.G.; Muller, G.; and de la Moya, S. Circularly Polarized Luminescence by Visible-Light Absorption in a Chiral O-BODIPY Dye: Unprecedented Design of CPL Organic Molecules from Achiral Chromophores. *J. Am. Chem. Soc.* 2014 136 (9), 3346-3349.

(49) Beer, G.; Niederalt, C.; Grimme, S.; Daub, J. Redox Switches with Chiroptical Signal Expression Based on Binaphthyl Boron Dipyrromethene Conjugates. *Angew. Chem., Int. Ed. Engl.* 2000;39(18):3252-3255.

(50) Lu, H.; Mack, J.; Nyokong, T.; Kobayashi, N.; Shen, Z. Optically active BODIPYs, *Coord. Chem. Rev.* 318,2016, 1-15,

(51) Gossauer, A.; Fehr, F.; Nydegger, F.; Stöckli-Evans, H. Synthesis and Conformational Studies of Urobilin Difluoroboron Complexes. Unprecedented Solvent-Dependent Chiroptical Properties of the BF_2 Chelate of an Urobilinoid Analogue. *J. Am. Chem. Soc.* 1997, *119* (7), 1599–1608.

(52) Jiang, Z.; Gao, T.; Liu, H.; Shaibani, M. S. S.; Liu, Z. Easily Accessible Axial Chiral Binaphthalene-Triarylborane Dyes Displaying Intense Circularly Polarized Luminescence Both in Solution and in Solid-State. *Dyes Pigm.* 2020, *175*, 108168.

(53) Norel, L.; Rudolph, M.; Vanthuyne, N.; Williams, J.A.G.; Lescop, C.; Roussel, C.; Autschbach, J.; Crassous, J. and Réau, R. Metallahelicenes: Easily Accessible Helicene Derivatives with Large and Tunable Chiroptical Properties. *Angew. Chem. Int. Ed*. 2010, 49, 99 –102

(54) Phillips, K. E. S.; Katz, T. J.; Jockusch, S.; Lovinger, A. J.; Turro, N. J. Synthesis and Properties of an Aggregating Heterocyclic Helicene. *J. Am. Chem. Soc.* 2001, *123* (48), 11899–11907.
(55) Field, J. E.; Muller, G.; Riehl, J. P.; Venkataraman, D. Circularly Polarized Luminescence from Bridged Triarylamine Helicenes. *J. Am. Chem. Soc.* 2003, *125* (39), 11808–11809.
(56) Maeda, C.; Nagahata, K.; Shirakawa, T.; Ema, T. Azahelicene - Fused BODIPY Analogues Showing Circularly Polarized Luminescence. *Angew. Chem.* 2020, *132* (20), 7887–7891.
(57) Shen, C.; Srebro-Hooper, M.; Jean, M.; Vanthuyne, N.; Toupet, L.; Williams, J. A. G.; Torres, A. R.; Riives, A. J.; Muller, G.; Autschbach, J.; Crassous, J. Synthesis and Chiroptical Properties of Hexa-, Octa-, and Deca-Azaborahelicenes: Influence of Helicene Size and of the Number of Boron Atoms. *Chem. Eur. J.* 2017, *23* (2), 407–418.
(58) Katayama, T.; Nakatsuka, S.; Hirai, H.; Yasuda, N.; Kumar, J.; Kawai, T.; Hatakeyama, T. Two-Step Synthesis of Boron-Fused Double Helicenes. *J. Am. Chem. Soc.* 2016, *138* (16), 5210–5213.
(59) Saikawa, M.; Nakamura, T.; Uchida, J.; Yamamura, M.; Nabeshima, T. Synthesis of Figure-of-Eight Helical BisBODIPY Macrocycles and Their Chiroptical Properties. *Chem. Commun.* 2016, *52* (71), 10727–10730.
(60) Kaseyama, T.; Furumi, S.; Zhang, X.; Tanaka, K.; Takeuchi, M. Hierarchical Assembly of a Phthalhydrazide-Functionalized Helicene. *Angew. Chem. Int. Ed.* 2011, *50* (16), 3684–3687.
(61) Tanaka, M.; Ikeda, T.; Mack, J.; Kobayashi, N.; Haino, T. Self-Assembly and Gelation Behavior of Tris(Phenylisoxazolyl)Benzenes. *J. Org. Chem.* 2011, *76* (12), 5082–5091.
(62) Ikeda, T.; Masuda, T.; Hirao, T.; Yuasa, J.; Tsumatori, H.; Kawai, T.; Haino, T. Circular Dichroism and Circularly Polarized Luminescence Triggered by Self-Assembly of Tris(Phenylisoxazolyl)Benzenes Possessing a Perylenebisimide Moiety. *Chem. Commun.*, 2012,48, 6025-6027
(63) Kumar, J.; Nakashima, T.; Tsumatori, H.; Kawai, T. Circularly Polarized Luminescence in Chiral Aggregates: Dependence of Morphology on Luminescence Dissymmetry. *J. Phys. Chem. Lett.* 2014, 5, 2, 316–321.
(64) Anetai, H.; Takeda, T.; Hoshino, N.; Araki, Y.; Wada, T.; Yamamoto, S.; Mitsuishi, M.; Tsuchida, H.; Ogoshi, T.; Akutagawa, T. Circular Polarized Luminescence of Hydrogen-Bonded Molecular Assemblies of Chiral Pyrene Derivatives. *J. Phys. Chem. C* 2018, *122* (11), 6323–6331.
(65) Luo, J.; Xie, Z.; Lam, J.; Cheng, L.; Chen, H.; Qiu, C.; Kwok, H.S.; Zhan, X.; Liu, Y.; Zhuc, D. and Tang, B. Z. Aggregation-induced emission of 1-methyl-1,2,3,4,5-pentaphenylsilole. *Chem. Commun.*, 2001, 1740-1741
(66) Liu, J.; Su, H.; Meng, L.; Zhao, Y.; Deng, C.; Ng, J. C. Y.; Lu, P.; Faisal, M.; Lam, J. W. Y.; Huang, X.; Wu, H.; Wong, K. S.; Tang, B. Z. What Makes Efficient Circularly Polarised Luminescence in the Condensed Phase: Aggregation-Induced Circular Dichroism and Light Emission. *Chem. Sci.* 2012, *3* (9), 2737.

(67) Niu, D.; Ji, L.; Ouyang, G.; Liu, M. Histidine Proton Shuttle-Initiated Switchable Inversion of Circularly Polarized Luminescence. *ACS Appl. Mater. Interfaces* 2020, *12* (15), 18148–18156.
(68) Hashimoto, Y.; Nakashima, T.; Shimizu, D.; Kawai, T. Photoswitching of an Intramolecular Chiral Stack in a Helical Tetrathiazole. *Chem. Commun.* 2016, *52* (29), 5171–5174.
(69) Miao, W.; Wang, S.; Liu, M. Reversible Quadruple Switching with Optical, Chiroptical, Helicity, and Macropattern in Self-Assembled Spiropyran Gels. *Adv. Funct. Mater.* 2017, *27* (29), 1701368.
(70) Louis, M.; Sethy, R.; Kumar, J.; Katao, S.; Guillot, R.; Nakashima, T.; Allain, C.; Kawai, T.; Métivier, R. Mechano-Responsive Circularly Polarized Luminescence of Organic Solid-State Chiral Emitters. *Chem. Sci.* 2019, *10* (3), 843–847.
(71) Kunzelman, J.; Gupta, M.; Crenshaw, B. R.; Schiraldi, D. A.; Weder, C. Pressure-Sensitive Chromogenic Polyesters. *Macromol. Mater. Eng.* 2009, *294* (4), 244–249.
(72) Pucci, A.; Bertoldo, M.; Bronco, S. Luminescent Bis(Benzoxazolyl)Stilbene as a Molecular Probe for Poly(Propylene) Film Deformation. *Macromol. Rapid Commun.* 2005, *26* (13), 1043–1048.
(73) Sagara, Y.; Mutai, T.; Yoshikawa, I.; Araki, K. Material Design for Piezochromic Luminescence: Hydrogen-Bond-Directed Assemblies of a Pyrene Derivative. *J. Am. Chem. Soc.* 2007, *129* (6), 1520–1521.
(74) Sase, M.; Yamaguchi, S.; Sagara, Y.; Yoshikawa, I.; Mutai, T.; Araki, K. Piezochromic Luminescence of Amide and Ester Derivatives of Tetraphenylpyrene—Role of Amide Hydrogen Bonds in Sensitive Piezochromic Response. *J. Mater. Chem.* 2011, *21* (23), 8347.
(75) Zhang, G.; Lu, J.; Sabat, M.; Fraser, C. L. Polymorphism and Reversible Mechanochromic Luminescence for Solid-State Difluoroboron Avobenzone. *J. Am. Chem. Soc.* 2010, *132* (7), 2160–2162.
(76) Krishna, G. R.; Kiran, M. S. R. N.; Fraser, C. L.; Ramamurty, U.; Reddy, C. M. The Relationship of Solid-State Plasticity to Mechanochromic Luminescence in Difluoroboron Avobenzone Polymorphs. *Adv. Funct. Mater.* 2013, *23* (11), 1422–1430.
(77) Louis, M.; Brosseau, A.; Guillot, R.; Ito, F.; Allain, C.; Métivier, R. Polymorphism, Mechanofluorochromism, and Photophysical Characterization of a Carbonyl Substituted Difluoroboron-β-Diketone Derivative. *J. Phys. Chem. C* 2017, *121* (29), 15897–15907.
(78) Louis, M.; Guillot, R.; Métivier, R.; Allain, C. β-Diketone Derivatives: Influence of the Chelating Group on the Photophysical and Mechanofluorochromic Properties. *Photochem. Photobiol. Sci.* 2018, *17* (6), 822–828.

CHAPTER 2

Circularly Polarized Luminescence and Circular Dichroism of Bichromophoric Difluoroboron-β-diketonates

CPL nature of organic molecules and coordination substances in self-organized supramolecular aggregates have been extensively studied, in which long-range exciton coupling is expected to enhance chiroptical activity.[1–3] Aggregation induced emission (AIE) of some chiral organic molecules has also been reported for enhanced CPL capability.[4,5] As one of the most promising fluorophores for the supramolecular approaches, we have been recently focusing on difluoroboron-β-diketonate (DFB) complexes because of the high quantum yield in both solid and solution states,[6] high Stokes shift and sensitivity to stimuli such as mechanical stress[7–10] and presence of organic vapors.[10] Typical BF_2 units may promote specific inter-molecular association. It has been previously reported that DFB complex bearing chiral amido group displays a good CPL signal and response to mechanical stress in solid state but showed weak CPL signals in monomeric state.[11]However, supramolecular aggregates of long range self-assembly based on this chromophore remain to be investigated.

In this chapter, we report two new bichromophoric DFB compounds with chiral cyclohexane diamine bridge (Figure 2.1). Different solvents systems lead to different aggregated forms and photophysical and chiroptical properties. We show that both the geometry of the bichromophore (relative orientations of the DFB units toward the chiral diamine, see figure 1) and the solvent systems strongly influence the chiroptical properties. The results of this chapter were already submitted for publication:

Circularly Polarized Luminescence and Circular Dichroism of Bichromophoric Difluoroboron-β-diketonates: Inversion and Enhanced Chirality based on Spatial Arrangements and Self-assembly

J.A. Panis, M. Louis, A. Brosseau, S. Katao, F.D.L. Reyes, T. Nakashima, R. Métivier, C. Allain and T. Kawai (Chemistry- A European Journal: https://doi.org/10.1002/chem.202201012)

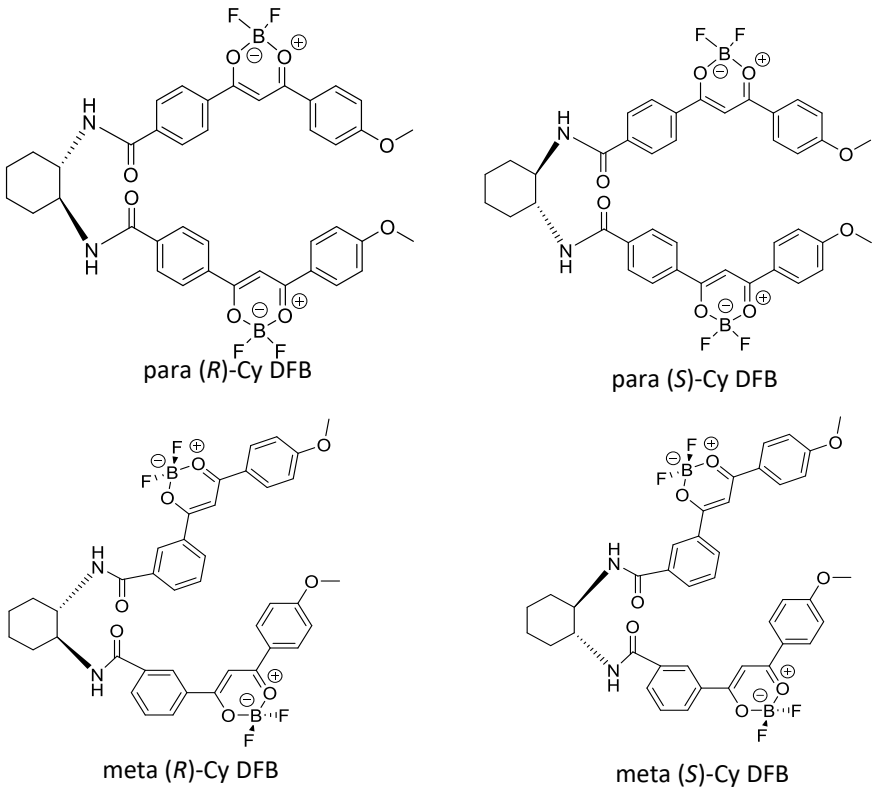

Figure 2.1. Chemical Structures of DFB derivatives studied here.

2.1 Synthesis

The target compound **para (*R/S*)-CyDFB** was synthesized by Claisen condensation reaction of 4-methoxy acetophenone and dimethyl terephthalate forming β-keto enol. Herein, para and meta (*R/S*) were referring to 1*R*,2*R* and *1S,2S(-)*-1,2-cyclohexanediamine enantiopure compounds. Saponification with LiOH converts ester to carboxylic group,[12] and this step was followed by peptidic coupling of para (*R/S*) cyclohexane diamine forming the bichromophoric ligand[13]. Finally, complexation of the bichromophore ligand using $BF_3(OEt)_2$ yields a yellow powder of **para (*R/S*)-CyDFB** after purification. Characterizations with ^1H, ^{13}C NMR, and Spiral TOF mass spectrometry confirms the target compound. The same steps were used to synthesize the **meta (*R/S*)-CyDFB** but using dimethyl isophthalate in Claisen condensation reaction instead of dimethyl terephthalate as shown in Scheme 2.1 and Scheme 2.2. The complete synthesis procedures are written in Chapter 6.

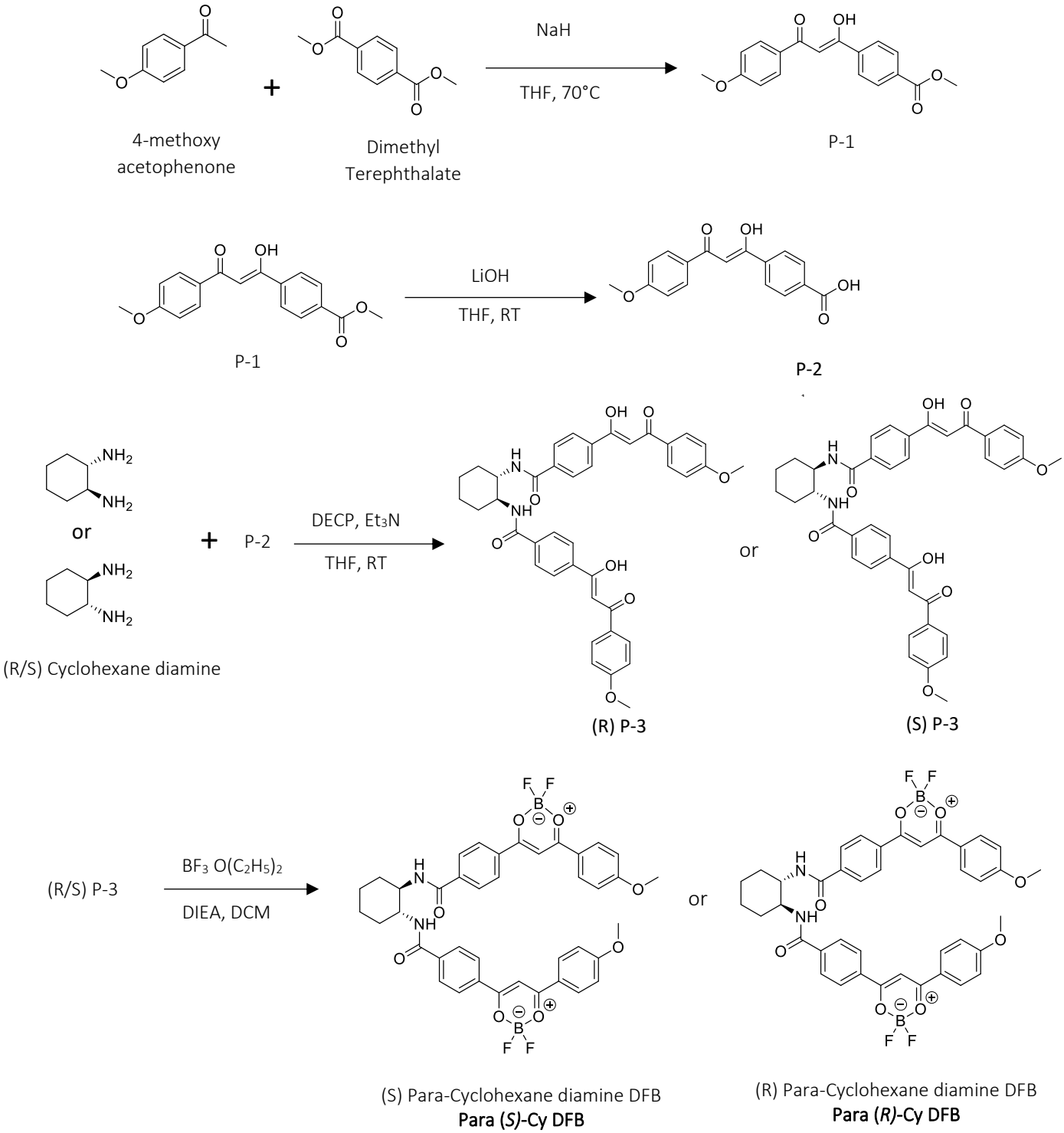

Scheme 2.1. Synthetic route for synthesis of Para (*S/R)*-CyDFB.

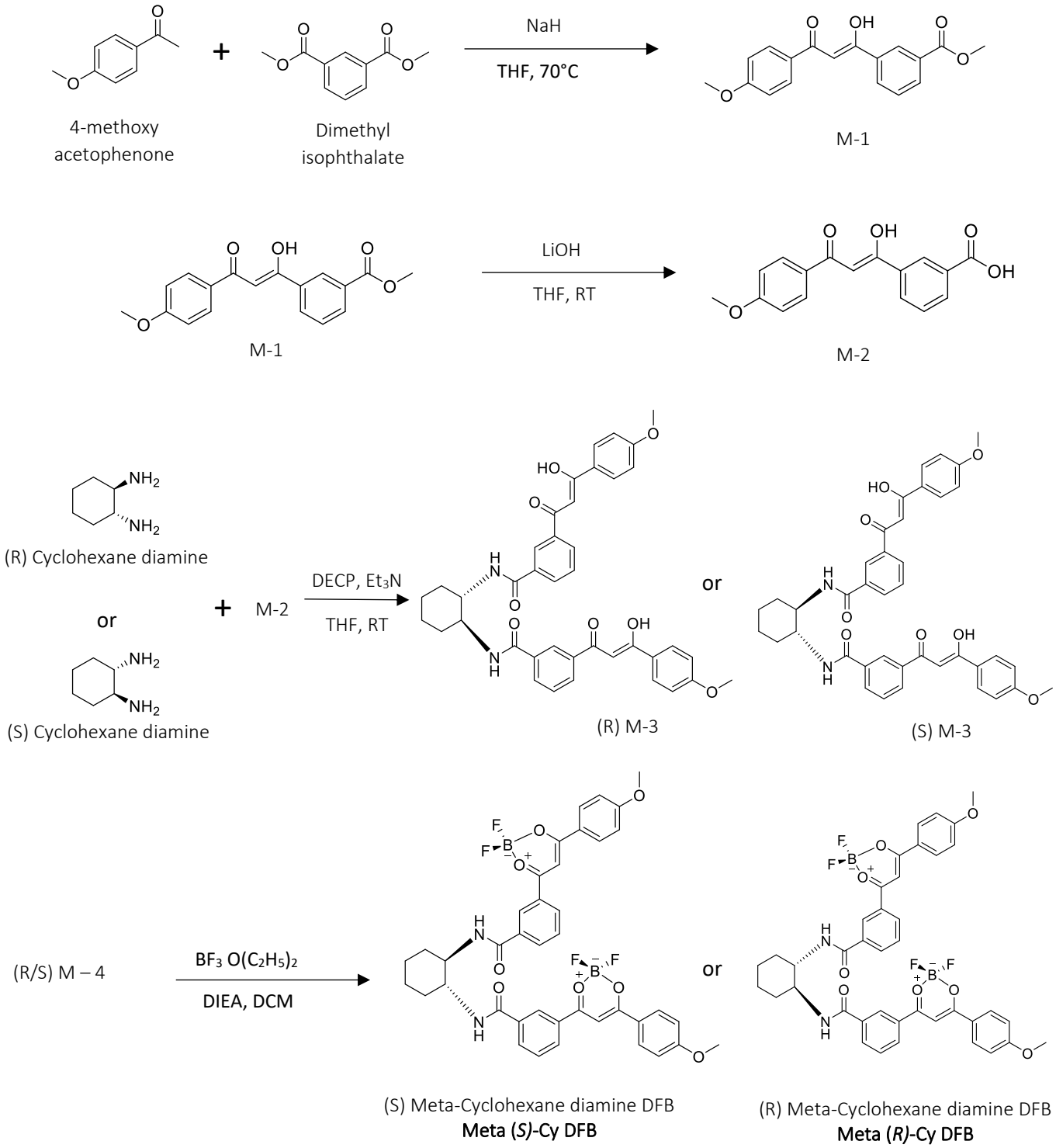

Scheme 2.2. Synthetic route for synthesis of Meta (*S/R*)-CyDFB

2.2 Monomeric form of Para and Meta (*S/R*)-CyDFB

We first measure the photophysical properties of **para** and **meta (*S*)-CyDFB** in dichloromethane (DCM) wherein the compounds displayed a good solubility. Both compounds display a broad and intense absorption band centered at 390nm. The molar absorption coefficient (ε) of **para (*S*)-CyDFB** was higher (105,000 M cm^{-1}) than **meta (*S*)-CyDFB** (72,000 M cm^{-1}) indicating a higher energy harvesting property. The fluorescence quantum yield of **para** and **meta (*S*)-CyDFB** in DCM are 0.67 and 0.64 respectively.

2.2.1 Photophysical Properties in Solution and Time-Correlated Single Photon Counting

The absorption and emission spectra of **para** and **meta (*S*)-CyDFB** were measured with different solvent polarities as shown in Figure 2.2 and Figure 2.3. Absorption spectra for both compounds do not significantly shift ranging from 389nm to 398nm for **para (*S*)-CyDFB** and 385nm to 393nm for **meta (*S*)-CyDFB** indicating less interactions of their ground state to solvent molecules.[14] Emissions for **para (*S*)-CyDFB** displayed maximum wavelength at 440nm, 446nm 443nm and 444nm in chloroform, DCM, THF and toluene while **meta (*S*)-CyDFB** displayed at 436nm, 442nm, 436nm and 440nm respectively. However, there are noticeable shifts of emissions in polar solvents such as DMF and acetonitrile indicating a weak intramolecular charge transfer nature in the excited state with the presence of methoxy as electron donating group.[15] Lippert-Mataga plot (see Tables 2.1-2.2 and Figure 2.4) showed a linear correlation between the solvent orientation polarizability and the Stokes shift, excluding toluene for which specific aromatic solute to solvent interactions may occur.[16] Lippert-Mataga equation is as follows:

$$\nu_F - \nu_A = \frac{2}{hc}\left(\frac{\varepsilon - 1}{2\varepsilon + 1} - \frac{n^2 - 1}{2n^2 + 1}\right)\frac{(\mu_E - \mu_G)^2}{a^3} + C$$

where $\nu_A - \nu_F$ are the wavenumbers (cm^{-1}) of the absorption and emission

h is Planck's constant (=6.6256 x 10^{-27} ergs)

c is speed of light (3.0 x 10^{10}/cm)

ε is dielectric constant of solvent

n is refractive index of solvent

μ_G is dipole moment in ground state

μ_E is dipole moment in excited state

a is cavity radius

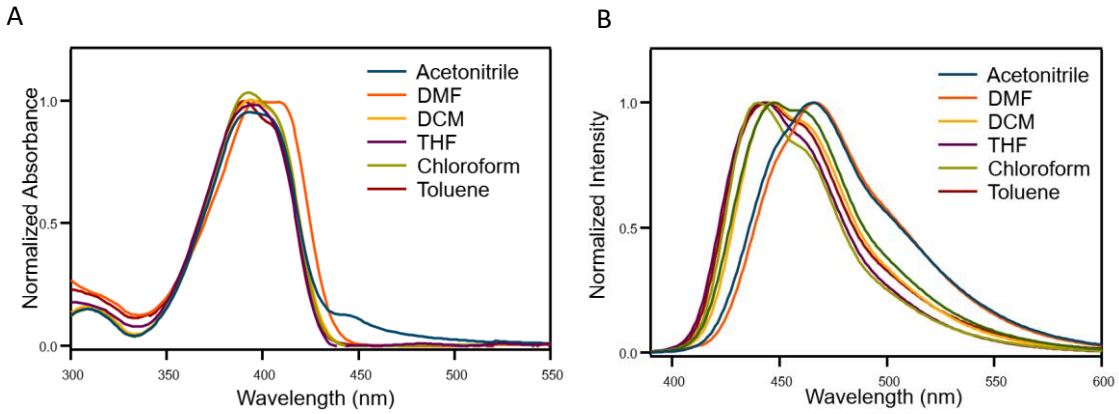

Figure 2.2 Absorbance (a) and emission (b) (λ_{exc}=390nm) of para-Cy DFB in acetonitrile, DMF, THF, DCM, chloroform, and toluene.

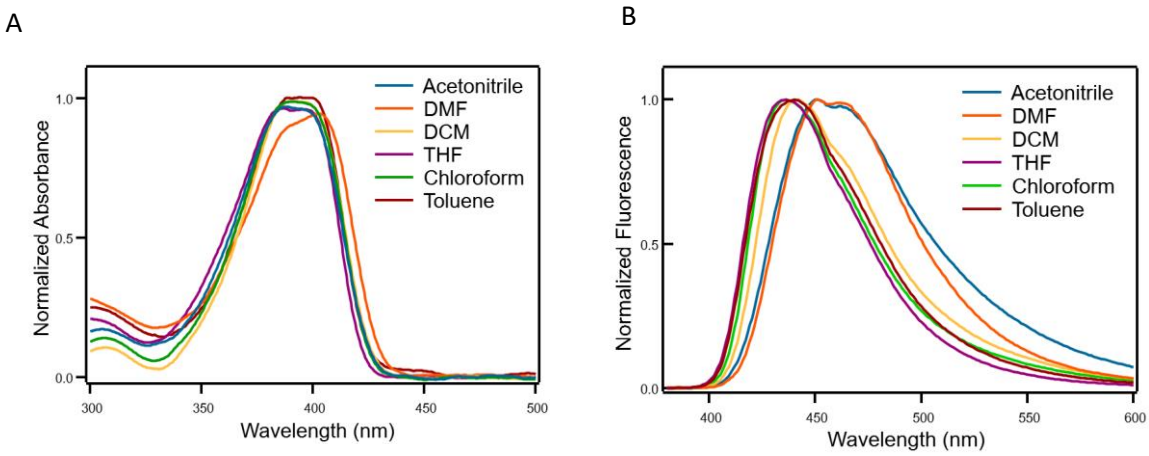

Figure 2.3 Absorbance (a) and emission (b) (λ_{exc}=390nm) of meta-Cy DFB in acetonitrile, DMF, THF, DCM, chloroform, and toluene.

Table 2.1 Characteristics of para-CyDFB at different solvent polarity

	ε[a]	η[b]	ƒ (ε, η)[c]	λ abs (nm)	λ em (nm)	Stokes shift (cm -1)
Acetonitrile	37.5	1.344	0.305	385	450	3751.81
DMF	37	1.427	0.276	393	451	3272.34
DCM	8.93	1.424	0.217	390	442	3016.60
THF	7.58	1.407	0.210	385	436	3038.25
Chloroform	4.81	1.446	0.148	388	436	2837.42
Toluene	2.38	1.497	0.013	387	440	3112.52

Table 2.2 Characteristics of meta-CyDFB at different solvent polarity

	ε[a]	η[b]	ƒ (ε, η)[c]	λ abs (nm)	λ em (nm)	Stokes shift (cm -1)
Acetonitrile	37.5	1.344	0.305	394	465	3875.33
DMF	37	1.427	0.276	398	466	3666.40
DCM	8.93	1.424	0.217	394	446	2959.19
THF	7.58	1.407	0.210	390	443	3067.67
Chloroform	4.81	1.446	0.148	393	440	2718.02
Toluene	2.38	1.497	0.013	389	444	3184.42

[a]*Dielectric constant*

[b]*Refractive index*

[c]*orientation polarizability of solvent calculated using the equation:* $\frac{\varepsilon-1}{2\varepsilon+1} - \frac{\eta^2-1}{2\eta^2+1}$

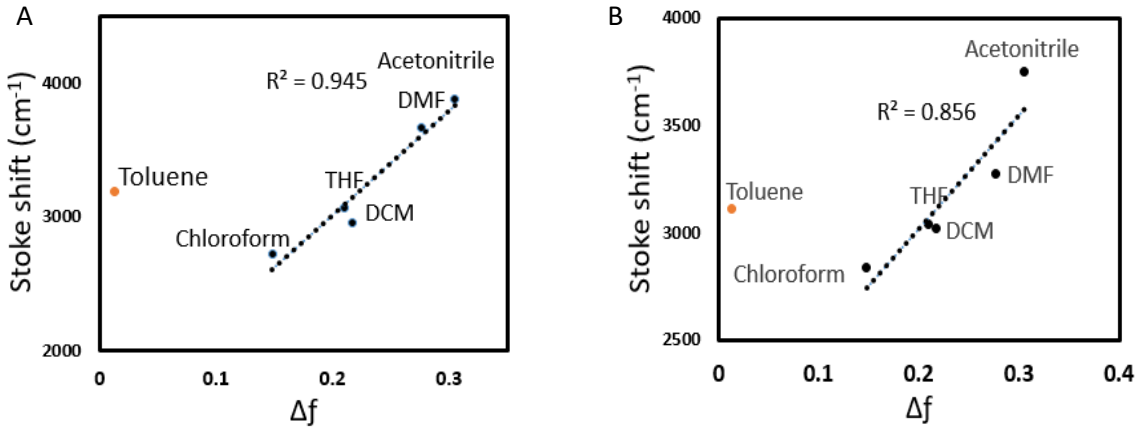

Figure 2.4 Lippert-Mataga plot of para-Cy DFB (a) and meta-Cy DFB (b) in different solvent.

Time-resolved spectroscopy measurements were conducted to gain insights to the emitting species in **para** and **meta (*S*)-CyDFB** in DCM solution. The decays were fitted with required satisfactory value of $X^2 < 1.2$ and the summary of decays are listed in Table 2.3 (see Chapter 6 for complete TCPSC plots). **Para (*S*)-CyDFB** exhibits a bi-exponential decay with decay time values τ_1= 12ns (a_1=0.01) and τ_2=2.0ns (a_2=0.99) while **meta (*S/R*)-CyDFB** exhibited tri-exponential decay with decay time values τ_1=7ns (a_1=0.02) and τ_2=2ns (a_2=0.70) and τ_3=0.7ns (a_3=0.27) measured at emission wavelength of 463nm (Table 2.2). For both compounds, the main contributions are from emitting species with decays around 2ns which may be attributed to the individual DFB unit by comparison with related monomeric compounds.[11] Long decay times 12ns for **para (*S*)-CyDFB** and 7ns for **meta (*S*)-CyDFB**) may be attributed to intramolecular exciton coupling between the two DFB units bridged by the cyclohexane diamine.

Table 2.3 Emission decay time constant (τ), pre-exponential factor (a) and fraction of intensity (f) of monomers in DCM of para and meta (S)-CyDFB (λ_{exc} = 390nm, λ_{em} = 463nm).

Sample	τ_1 (ns), (a_1, f_1)	τ_2 (ns), (a_2, f_2)	τ_3 (ns), (a_3, f_3)
para (*S*)-CyDFB (Monomers in DCM) (λ_{em} = 463nm)	12.2ns, (0.01, 0.03)	2.06ns, (0.99, 0.97)	-
meta (*S*)-CyDFB (Monomers in DCM) (λ_{em} = 463nm)	7.0ns, (0.02, 0.06)	2.4ns, (0.71, 0.84)	0.7ns, (0.27, 0.10)

Fraction of intensity was calculated from decay time constant (τ), pre-exponential factor (a) according to equation Iαiτi/∑αiτi.

2.2.2 Density Functional Theory (DFT) and Time-dependent DFT (TD-DFT) Calculations

To understand the molecular electronic properties of the compounds, density functional theory (DFT) and time-dependent DFT (TDDFT) calculations were performed in Gauss view 16 using the functional CAM-B3LYP and basis set (6-31+) G(d,p) with IEFPCM (DCM) solvation method. Optimized ground state geometry revealed that para (S)-CyDFB in DCM have two non-equivalents DFB units (Figure 2.5).

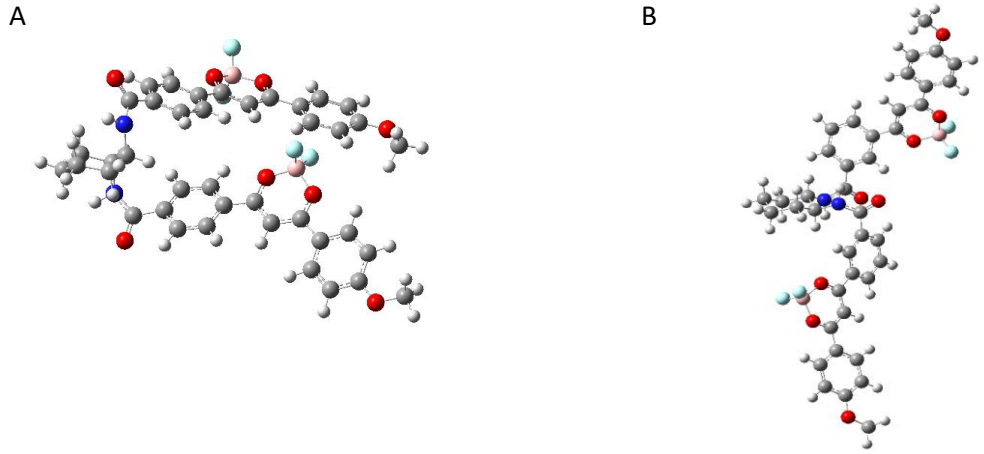

Figure 2.5 Optimized geometry of para-Cy DFB (a) and meta-Cy DFB (b) calculated with Gaussview 16 DFT calculation using CAM-B3LYP and basis set (6-31+) G(d,p) with IEFPCM (DCM) solvation method

In the first DFB, dihedral angle of phenyl group connected through amide bond has dihedral angle of 27.4° with respect to amide plane which is more twisted than the second DFB moiety with an angle -4.8°. Phenyl rings of the first DFB moiety has dihedral angle of 13.3° and -1.19° with respect to the difluoroboron β-diketonate plane while the phenyl rings of second DFB unit have dihedral angles of 24.9° and 6.97° respectively. The two DFB groups in para (*S*)-CyDFB were in proximity and overlapped their phenyl group attached in amide bonds. Single crystal analysis of para (*S*)-CyDFB showed a slight variation in arrangement of DFB moeities mainly because of presence of intermolecular interactions in crystals while the DFT was calculated in monomeric form (see Figure 2.6a).

On the other hand, optimized geometry of meta (*S*)-CyDFB showed that the DFB groups are in equatorial position where both are headed to the opposite sides. The phenyl rings connected to amide group has dihedral angle of -18.4° and -18.9° with respect to amide plane. In the first DFB moiety, phenyl rings have dihedral angle of -13.5° and -7.6° with respect to difluoro boron β-diketonate plane while in the second DFB moiety, phenyl rings have dihedral angle of -9.9° and 8.2° with respect to difluoro boron β-diketonate plane (see Figure 2.6b).

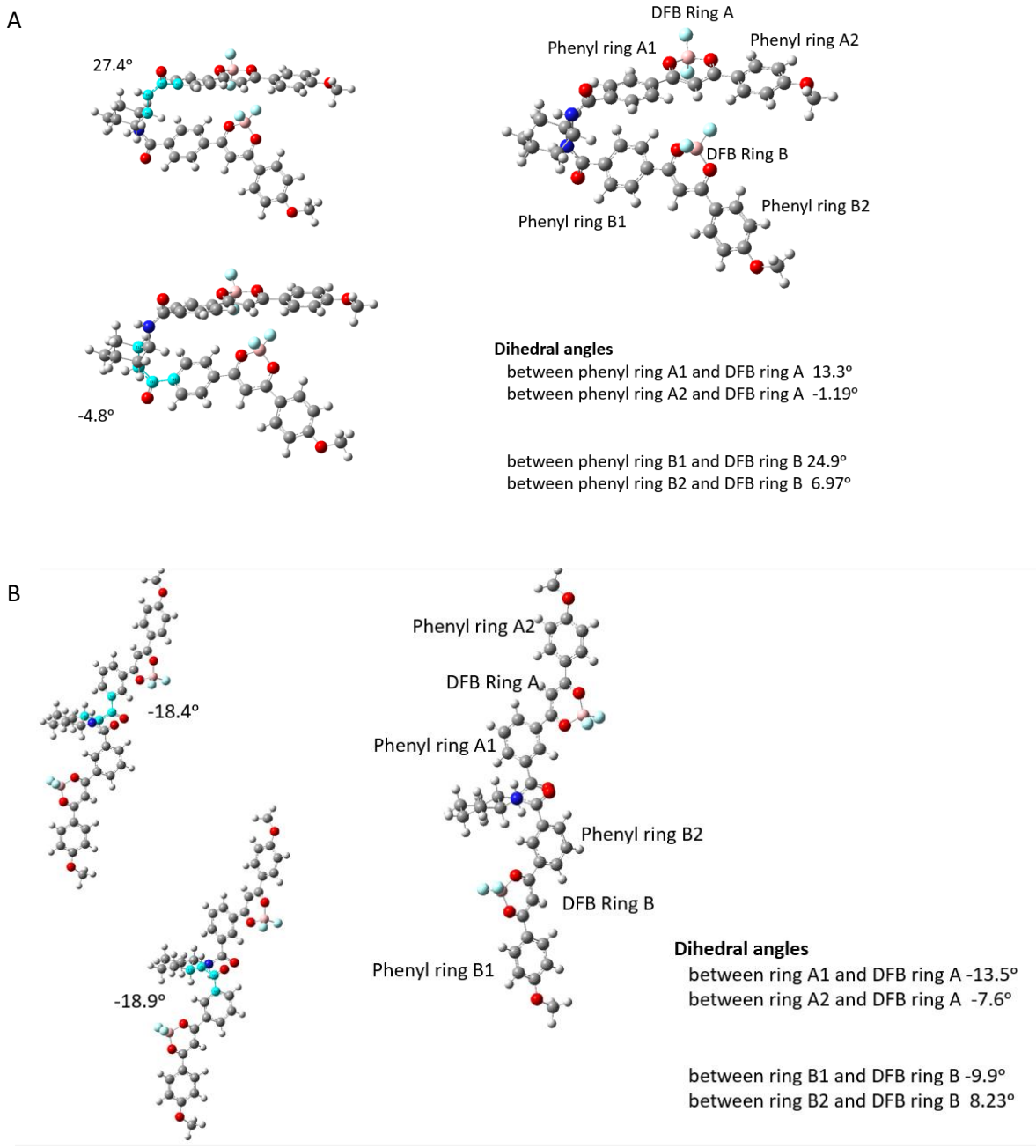

Figure 2.6. Optimized geometry showing dihedral angles of DFB moieties of para-Cy DFB (a) and meta-Cy DFB (b) calculated with Gaussview 16 DFT calculation using CAM-B3LYP and basis set (6-31+) G(d,p) with IEFPCM (DCM) solvation method.

The electronic transitions and corresponding involved molecular orbitals of para and meta (*S*)-CyDFB were calculated by time-dependent DFT (TD-DFT). The results showed that there are multiple molecular orbitals involved in each transition. Natural transition orbitals (NTO) were also calculated to clearly demonstrate the electronic

transitions involving multiple molecular orbitals. Both transitions showed a π-π* character with a slight shift of electron density from methoxy towards the β-diketonate group (see Figures 2.7 and Figure 2.8). This explains the weak solvatochromism property of both para and meta (*S/R*)-CyDFB (see Chapter 6 for list of molecular orbitals and oscillation strengths).

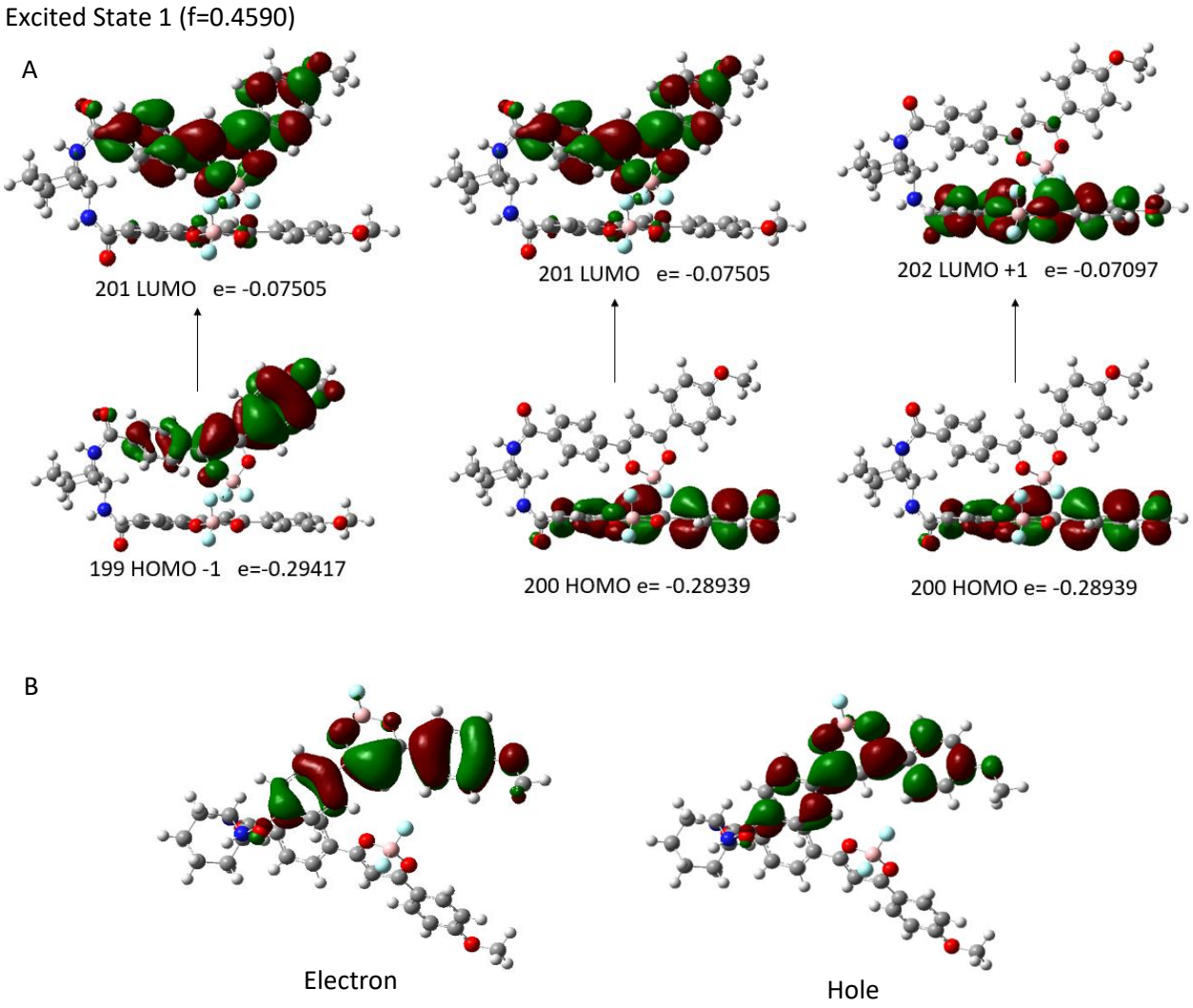

Figure 2.7. Molecular orbitals and electronic transitions of para (*S*)-CyDFB as calculated by TD-DFT using CAMB3LYP, 613+G (d,p), IEFPCM solvent DCM (a). Generated natural transition orbitals (NTOs) (b).

Excited State 1 (f=2.2677)

A

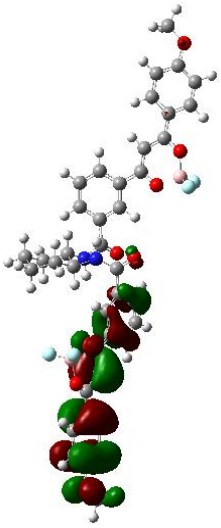

(201) LUMO e= -0.07168

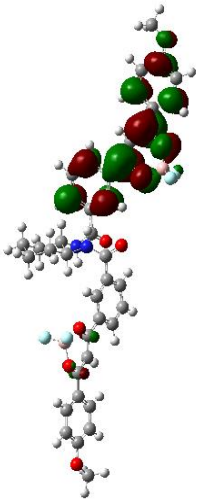

(202) LUMO+1 e= -0.070503

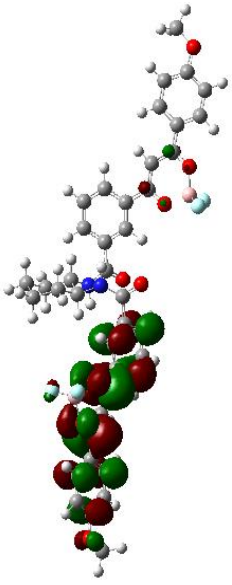

(199) HOMO-1 e= -0.29192

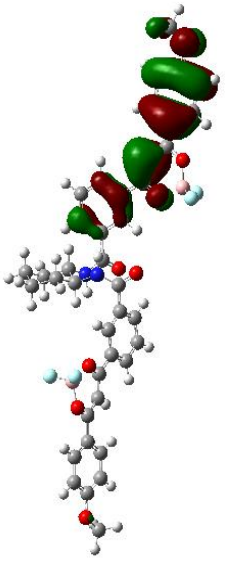

(200) HOMO e= -0.29186

B

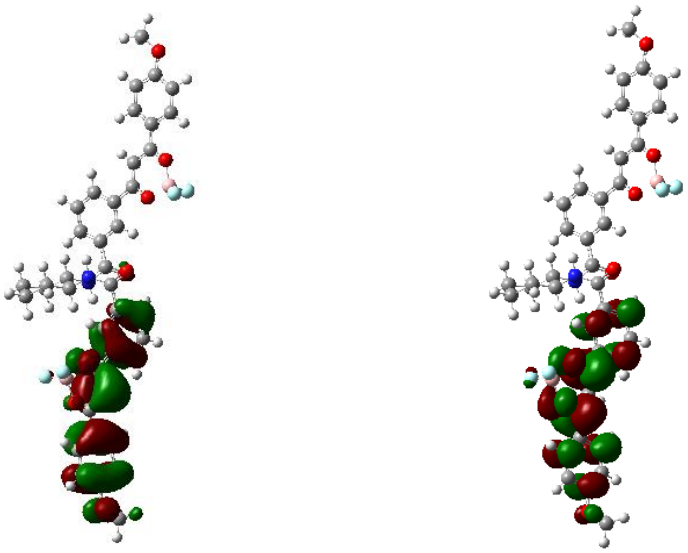

Electron Hole

Figure 2.8. Molecular orbitals and electronic transitions of meta (*S)*-CyDFB as calculated by TD-DFT using CAMB3LYP, 613+G (d,p), IEFPCM solvent DCM (a). Generated natural transition orbitals (NTOs) (b).

2.3 Chiroptical Properties of Monomeric and Aggregated Bichromophores

Chirality of monomeric compounds in the ground state were studied by circular dichroism (CD) measurement of both para and meta (*S/R*)-CyDFB compounds dissolved in DCM. CD spectra of para (*S/R*)-CyDFB enantiomers show mirror images with positive Cotton effect for S enantiomer while negative cotton effect for R enantiomer. Interestingly, meta (*S/R*) CyDFB display an opposite Cotton effect measured at the same wavelength as para (*S/R*)-CyDFB (see Figure 2.9). The observed Cotton effect signs for both para and meta-CyDFB are in good agreement with the theoretical CD spectra from TD-DFT (see Chapter 6 for ECD plots).

As shown in the DFT optimized geometry, variation in connectivity of para and meta leads to different spatial arrangement of DFB units. Para (*S/R*)-CyDFB units are in axial position and the DFB groups are more aligned and overlapped with one aromatic ring. In contrast, the meta derivative favors the equatorial position and rearranged the DFB groups towards the opposite sides preventing interactions of two DFB units. Notably, CD spectra of bichromophoric DFB in para position showed more intense CD response and displayed twice the dissymmetry factor with $|g_{abs}|$ value of $4x10^{-4}$ as compared with DFB in meta position with $|g_{abs}|$ value of $2x10^{-4}$ (Figure 2.9). Higher $|g_{abs}|$ value may be due to shorter distance of DFB units in para position causing excitonic coupling between the DFB units. Moreover, degree of overlap between the chromophores and the configurations of DFB units in DCM have directed the inversion of chirality.[17]

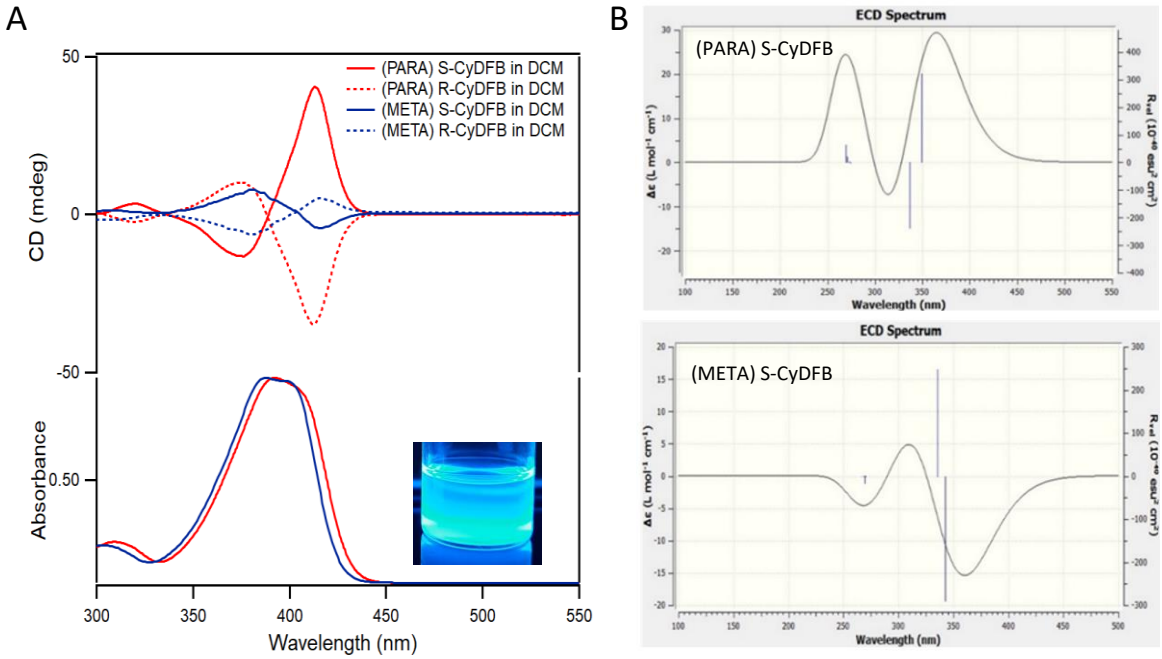

Figure 2.9. CD spectra and normalized absorbance of para CyDFB and meta CyDFB in DCM (3.5 x10^{-5}M) and insert image of the solution in DCM under 365nm UV source (a) and theoretical CD spectra from TD-DFT (b).

The measurements of photophysical properties were extended to self-assembled aggregates of para and meta (*S/R*)-CyDFB in a mixture of chloroform and methylcyclohexane (MCH) (29:1) at concentration 3.5x10^{-5} M. The solution turns from bright blue emission in monomeric form (DCM) to yellow emission (insert image in Figure 2.10a) in mixture of MCH and chloroform (29:1) under UV light. This is accompanied by broadening of absorbance as compared with the monomeric form. SEM images showed a randomly connected spherical aggregates both in para and meta derivatives (Figure. 2.10b). Like the monomeric form, CD spectra of para (*S/R*)-CyDFB aggregates displayed mirror images for (*R*) and (*S*) enantiomers with formation of new band at 430nm displaying an opposite sign of more intense band at 385nm (Figure 2.10a). These new bands correspond to the CD signals of newly formed absorbing species in aggregated form.

Interestingly, random aggregates formed by interacting units of para (*S/R*)-CyDFB showed an enhanced $|g_{abs}|$ values as compared to its monomeric form. Further increase in concentration from $3.5x10^{-5}$M to $1.0x10^{-4}$M displayed a decrease in dissymmetry factor from $|g_{abs}|$ value of $1.0x10^{-3}$ to $|g_{abs}|$ value of $3.0x10^{-4}$. This is due to formation of bigger aggregates forming precipitation in higher concentration, which suggests low reliability in the latter value. As compared with the aggregates formed with para (*R/S*)-CyDFB, CD spectra of meta (*R/S*)-CyDFB have broader but weaker bands between 360nm-460nm. Newly formed bands in aggregated form of para and meta displayed an opposite sign of Cotton effect to its corresponding monomeric form. In contrast to enhancement of $|g_{abs}|$ values of para, meta (*R/S*)-CyDFB did not show any significant enhancement in dissymmetry factor upon formation of aggregates which remains $|g_{abs}|$ value of ca. $2.0x10^{-4}$ at concentration of $3.5x10^{-5}$M.

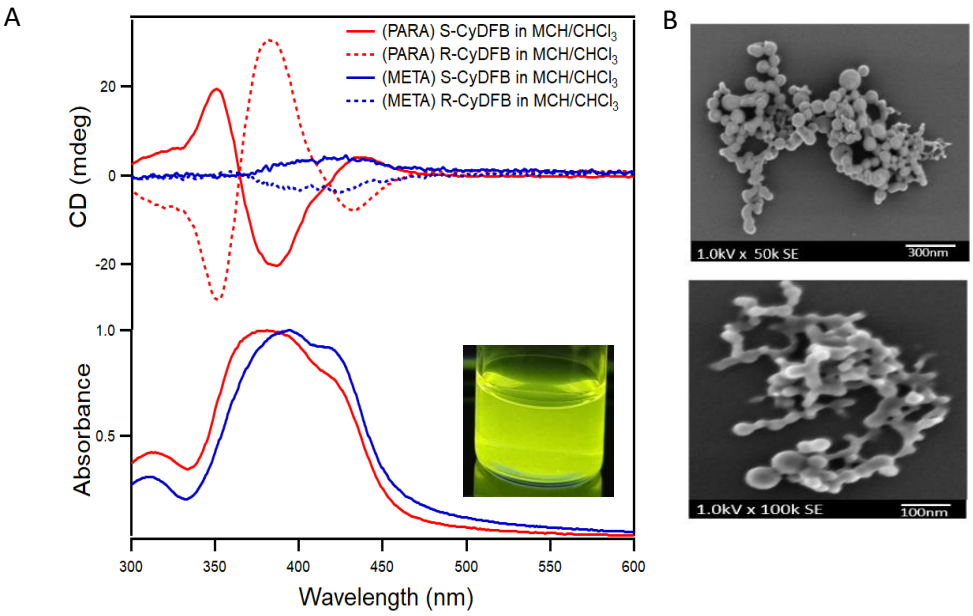

Figure 2.10. CD spectra and normalized absorbance of para CyDFB and meta CyDFB in (29:1) MCH:Chloroform ($3.5 x10^{-5}$M) and insert image of solution in MCH:Chloroform under 365nm source (A). SEM images of aggregates of para CyDFB (top) and meta CyDFB (bottom) (B).

Circularly polarized luminescence (CPL) measurements provided more evidence in chiroptical properties of meta and para (*R/S*)-CyDFB in their excited states. The $|g_{lum}|$ values of both para and meta isomers in monomeric form are too low to be reliably analyzed by the instrument (see Chapter 6). This seems reasonable as the lowest $|g_{lum}|$ of our lab-designed machine is about $1x10^{-3}$, which is not sufficient to characterize those as low as $2.0x10^{-4}$. Meanwhile, the aggregated form of para (*R/S*)-CyDFB compounds notably showed a mirror image of R and S enantiomers and has |glum| value of around $4.0x10^{-3}$ measured at 530nm which corresponds to the emission from aggregates shown in Figure 2.11. This clearly showed that the significant increase in $|g_{lum}|$ was attributed

to the intermolecular excitonic coupling between DFB units in chiral aggregates, which should operate over 4 or more DFB units.[17,18] In contrast, the meta-isomer displayed no significant CPL activity in both monomeric and the aggregated forms, which is attributable to less CPL activity to be detected in our system. These results clearly demonstrate significant difference in the intramolecular and intermolecular excitonic coupling between DFB units of two these isomers.

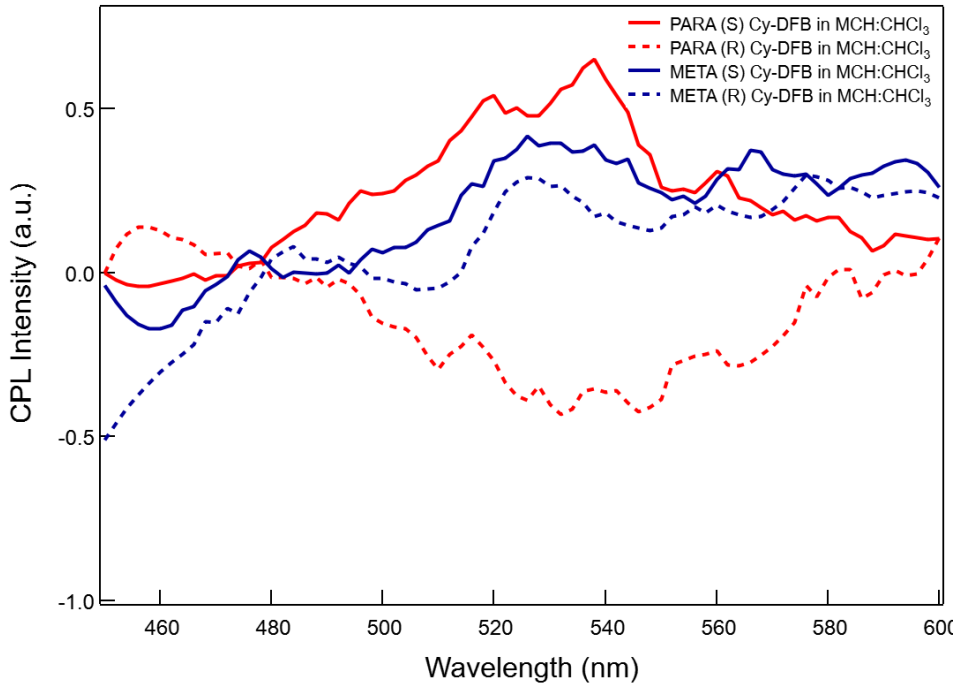

Figure 2.11. CPL spectra of para CyDFB and meta CyDFB in (29:1) MCH:Chloroform (3.5×10^{-5}M) λ_{exc} 375nm.

To further understand the changes in dissymmetry factors in MCH rich solution, fluorescence decays were measured by TCSPC at λ_{em} = 550nm for both para and meta (*S*)-CyDFB. Para (*S*)-CyDFB aggregates exhibited tri-exponential decay with decay times at τ_1=40.5ns (a_1=0.72), τ_2=14.7ns (a_2=0.21) and τ_3=1.6ns (a_3=0.07). Likewise, meta (*S*)-CyDFB aggregates also displayed a tri-exponential decays with decay times at τ_1=40.8ns (a_1=0.33), τ_2=16.9ns (a_2=0.27) and τ_3=2.7ns (a_3=0.40) (Table 2.4).

Table 2.4 Emission decay time constant (τ), pre-exponential factor (a) and fraction of intensity (f) aggregates in MCH/$CHCl_3$ of para and meta (S)-CyDFB (λ_{exc} = 390nm, λ_{em} = 550nm).

Sample	τ_1 (ns), (a_1, f_1)	τ_2 (ns), (a_2, f_2)	τ_3 (ns), (a_3, f_3)
para (*S*)-CyDFB (Aggregates MCH/$CHCl_3$) (λ_{em} = 550nm)	40.5ns, (0.72, 0.90)	14.7ns, (0.21, 0.10)	1.6ns, (0.07, <0.01)
meta (*S*)-CyDFB (Aggregates MCH/$CHCl_3$) (λ_{em} = 550nm)	40.9ns, (0.33, 0.70)	17.0ns, (0.27, 0.24)	2.7ns, (0.40, 0.06)

Noticeably, the pre-exponential factor of decays at 40ns in para-CyDFB is more than twice the pre-exponential in the meta isomer. This is in contrast with the short-lived species at around 2ns which has higher pre-exponential factors in meta- aggregates (40%) but has low pre-exponential factor in para (7%). The predominant decays of long-lived emitting species with decays at around 40ns and 15-17ns formed through intermolecular and intramolecular excitonic coupling may explain the enhanced chiroptical properties of para as compared with meta. These results also suggest rather minor and random bi- and multi-chromophoric coupling in the aggregated meta-isomers.

2.4 Supramolecular Assembly

Formation of para (*R/S*)-CyDFB organogels were observed in mixture of DCM and toluene (50:50) stimulated by ultrasonication followed by heating at 40°C for 10mins. The organogels were formed after 144 hours of slow evaporation of DCM at room temperature. Pure toluene assisted with ultra-sonication and heating formed a mixture of opaque aggregates and gels due to poor solubility of compounds in pure toluene. The presence of DCM in the solvent system balanced the solubility-precipitation of compounds and assisted the formation of thermodynamically stable organogels driven by π-π and hydrogen bonding [19]. The formation of gels is confirmed by stable inversion of test tube method and the emission while forming the gels were monitored as shown in Figure 2.12a. It was clearly shown that peak around 460nm was slowly decreasing

which is attributed to the monomeric form shown in Figure 2.12b. After 144 hours, majority of the bichromophoric units were self-assembled into nanowires.

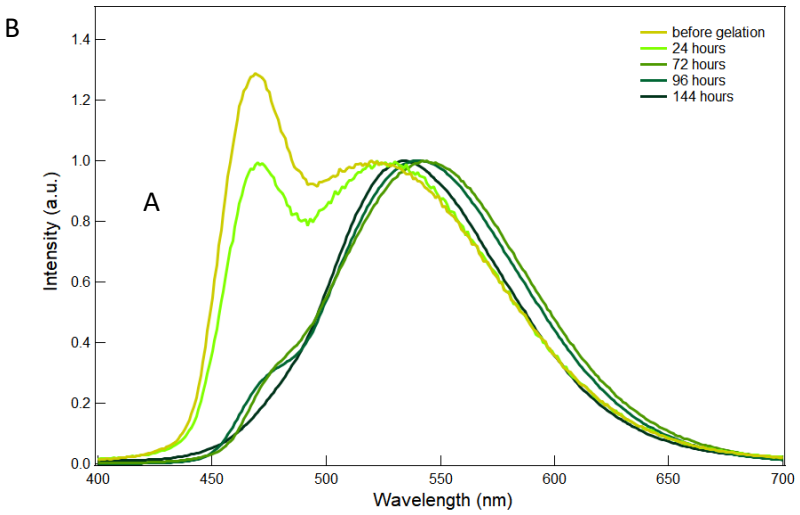

Figure 2.12. The gels formed in mixture of toluene and DCM (a) and the emissions of the solution while forming the gels (b).

Morphology of nanowires were observed after deposition and drying of organogels under vacuum (xerogels). SEM images of xerogels (Figure 2.13) shows the formation of extended nanofibers with thickness ranging from 5nm-15nm. The single para (*S*)-CyDFB unit has molecular length around 1.8nm as measured from the optimized structure calculated with DFT, hence it indicates that fibers formed are not one-dimensional but rather composed of multiple intertwined fibers which is evident in the images. To gain more insights in the molecular arrangement, single crystal structure of para (*S*)-CyDFB complex was determined from a crystal obtained by slow solvent evaporation using DCM as solvent.

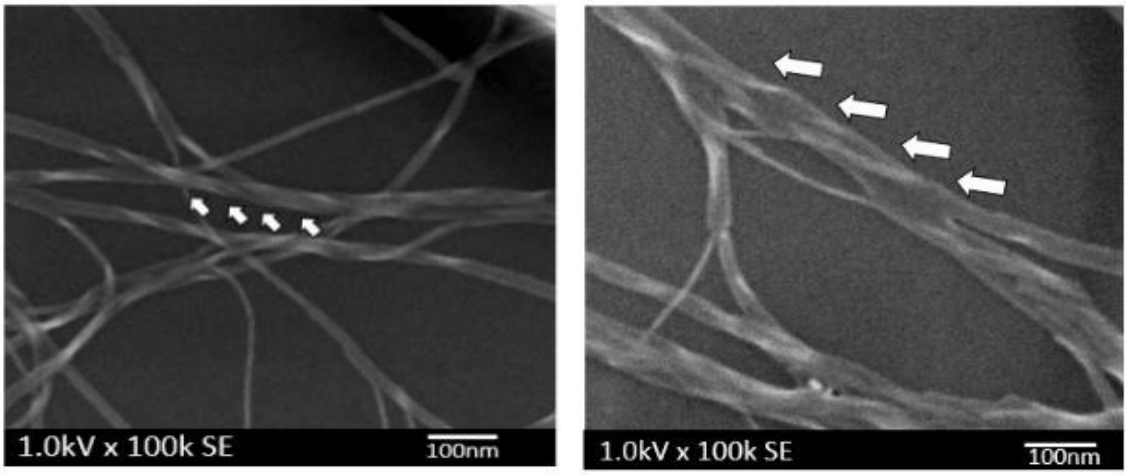

Figure 2.13. SEM images of nanowires **para (*S*)-** (left) and **(*R*)-** (right) **CyDFB** obtained from gels (D).

Crystal structure revealed that the bichromophoric units has various side-to-side interactions involving fluorine atoms to the methoxy as well as H-atom of the adjacent DFB units via CH/F hydrogen bonding as shown in Hirshfeld surface analysis (Figure 2.14b).[20] Moreover, extending the structures from top to bottom shows the π-π stacking between the extended fibers owing to H-bonding (Figure 2.14a). It was clearly shown that C=O and NH from amide were mainly involved in hydrogen bonding. Diffraction patterns of xerogels obtained from powder XRD coincided with the simulated patterns from CIF file, suggesting that the nanowires have similar stacking with the crystal structures as shown in Figure 2.15.

Simulated packing structures of bichromophoric units were obtained through Materials Studio 7.0 program using COMPASSII force field.[21] The hydrogen bonding observed in crystal structure through amide group is also present in simulated packing but differs mainly in twisting of DFB group (Figure 2.14c). Notably, the proposed calculated structures of nanowires displayed a periodical single and double hydrogen bonding every four bichromophoric units leading to twisting of one-dimension wires. DFB units were also bent downward as seen in the top DFB units and slightly reversing the bending towards the upward direction as seen in the last DFB unit located at the bottom part of the model.

This possibility of one-dimensional twisting based on the proposed packing may explain the intertwining of fibers as observed in SEM images. Moreover, formation of nanowires through amides and carbonyl hydrogen bonding is in good agreement with the previous studies of self- assembled nano- helical wires involving cyclohexane diamine as the chiral backbone moiety.[17,18,21,22]

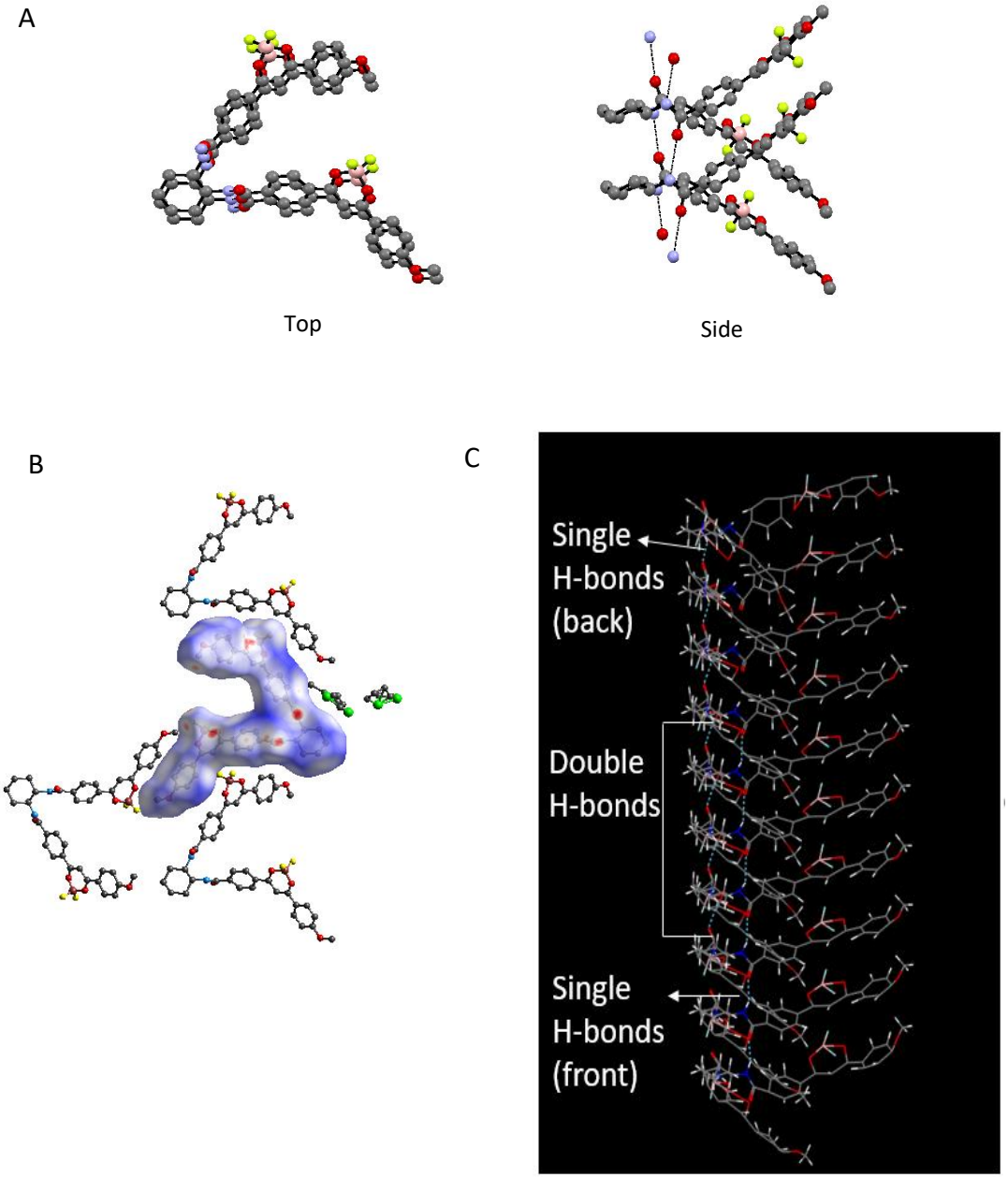

Figure 2.14. Top and side view of crystal packing induced by π-π stacking and hydrogen bonding of amide groups (A), Hirshfeld surface analysis showing intermolecular interactions (B). Simulated packing structures of using Materials Studio 7.0 (C).

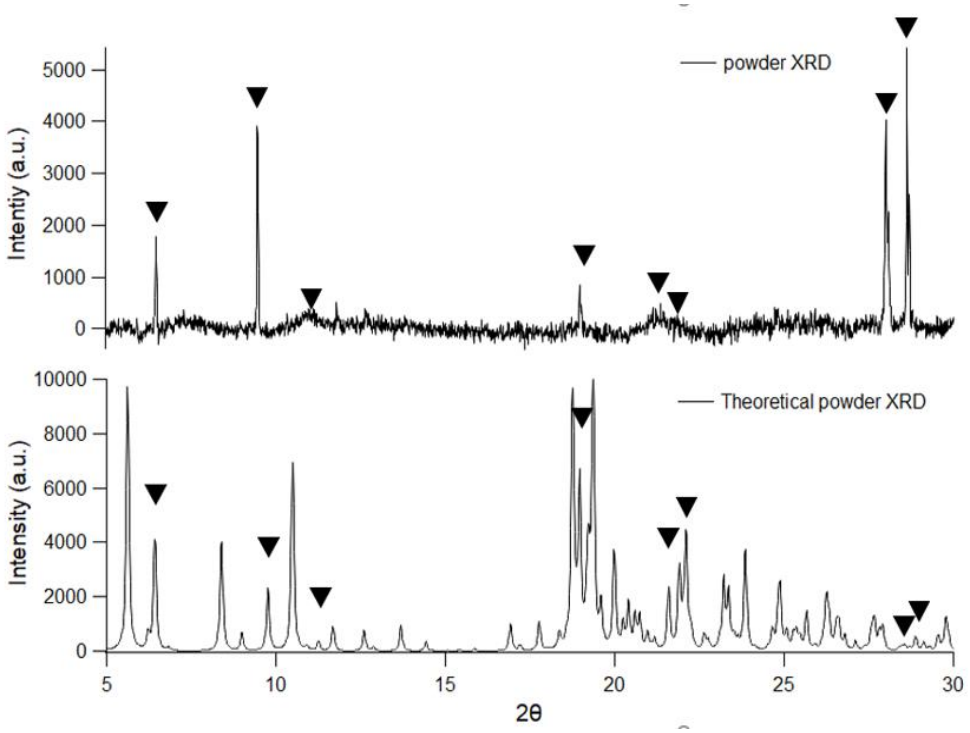

Figure 2.15. Experimental X-ray diffraction patterns of xerogels and simulated x-ray diffraction patterns obtained from CIF file of para (*S*)-cyclohexane diamine DFB.

The same method for the formation of organogels were tested for meta (*R/S*)-CyDFB using different solvents such as cyclohexane, hexane, toluene, acetonitrile, DCM, chloroform, and mixtures of polar and non-polar solvents. Unlike with the para-isomer, the meta isomer showed no organogels in any of these solvents but rather precipitations occurred in both non-polar and mixtures of solvents.

Molecular packing arrangements of nanowires in para-CyDFB compounds revealed that hydrogen bonding involving amide groups is crucial in the formation of chiral backbone in stacked bichromophoric units. Comparison of the orientation of meta and para in DFT optimized geometry showed that the orientation of DFB units of meta are causing hindrance or blocking to the amide group hence suppressing the formation hydrogen bonding between the adjacent DFB bichromophoric units. Introduction of long alkyl chain may help to form molecular wires and liquid crystalline states in future molecules.[23]

2.5 Photophysical Properties and Chiroptical Properties of Supramolecular Assembly

In section 2.4, it was shown the emission spectra of gels were initially displayed two emission bands at around 450nm and 550nm. The emission around 450nm was attributed to the monomeric form while the emission at 550nm is from the self-assembly which immediately formed after cooling down the solution at room temperature. Disappearance of emission at 430nm after 144 hours indicated that most of bichromophoric units were assembled into the helical nanowires (see Figure 2.12b).

TCSPC measurements of organogels provided more insights to the nature of emitters in nanowires. Table 2.5 shows that the long-live emitting species with decay-times τ_1=35ns (a_1=0.42) and τ_2=12.3ns (a_2=0.04) were prominent at longer wavelength but almost did not exist at 450nm. These decays along with the shift in emission to higher wavelength suggests the formation of new emitting species through intramolecular and intermolecular coupling of DFB units. Shorter decay was observed at 550nm (τ_3=2.3ns, a_3=0.35) but more prominent at 450nm (τ_2=2.1ns, a_2=0.72) which is attributed to the residual monomers in the toluene solution (see Chapter 6 for decay plots).

Table 2.5. Emission decay time constant (τ), pre-exponential factor (a) and fraction of intensity (f) of gels in toluene of para (*S*)-CyDFB measured (λ_{exc} = 390nm, λ_{em} = 450nm and 550nm).

Sample	τ_1 (ns), (a_1, f_1)	τ_2 (ns), (a_2, f_2)	τ_3 (ns), (a_3, f_3)	τ_4 (ns), (a_4, f_4)
para (*S*)-CyDFB (Gels in Toluene) (λ_{em} = 450nm)	11.5ns, (<0.01, 0.3)	2.1ns, (0.72, 0.89)	0.5ns, (0.27, 0.08)	
(λ_{em} = 550nm)	35.5ns, (0.42, 0.91)	12.3ns, (0.04, 0.03)	2.3ns, (0.35, 0.05)	0.6ns, (0.19, 0.01)

CPL measurements of para (*R/S*)-CyDFB organogels exhibited $|g_{lum}|$ value of about 0.015 which is not fully reproducible due to stability of gels with long exposure to UV source during CPL measurements but relatively high values for organic molecules that usually ranges from 10^{-2} to 10^{-5}.[13] High g_{CPL} values were observed at the range 530nm-550nm, which suggests that these CPL signals correspond to the newly formed emitting species in the self-assembled nanowires. This value has two orders of magnitude higher than its monomeric form and an order of magnitude higher than the random aggregates in MCH:$CHCl_3$ solution. Similarities in lifetimes and CPL signals observed at λ_{em} 500nm-550nm for aggregated form and organogels may indicate that emitting species with longer lifetimes are present for both assemblies formed through intermolecular interactions. Significantly intense CPL signal observed in the nanowires is probably due to the highly ordered arrangement of bichromophoric DFB units forming helical and

intertwined fibers. Such arrangement promotes the long range cooperative excitonic coupling between the chromophores causing enhanced CPL signals.[3,17,18]

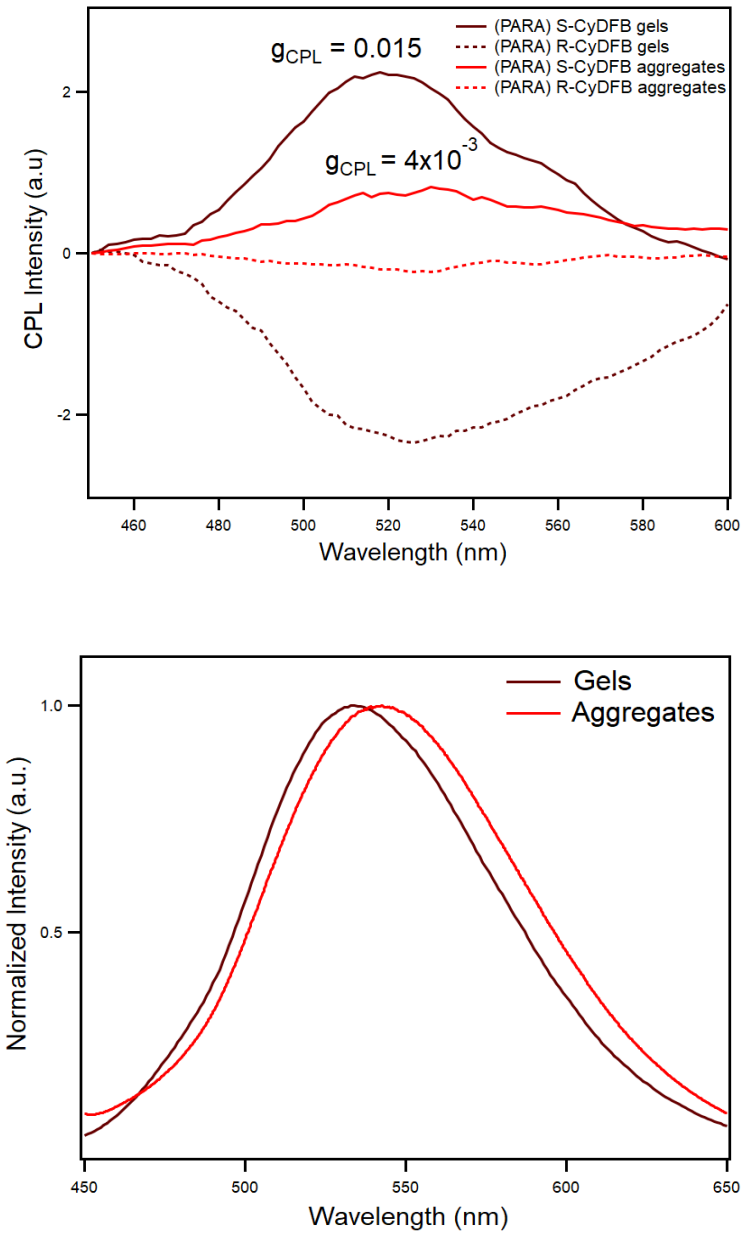

Figure 2.16. CPL Spectra of para (*R/S*) CyDFB gels formed in toluene (solid and broken dark red lines) and aggregates formed in MCH/$CHCl_3$ (solid and broken red lines) (A). Normalized emission of para (*R/S*)-CyDFB gels (solid dark red line) and aggregates in (29:1) MCH/$CHCl_3$ (solid red line) (B).

2.6 Conclusion

In this chapter we have synthesized two bichromophoric DFB complexes connected in para and meta position using cyclohexane diamine as chiral bridge moiety. We have shown that the difference in connectivity of para and meta has led to variation in spatial arrangement of DFB units, hence exhibited inversed sign of Cotton effect. DFB complex in para position appeared to have stronger CD and CPL signals owing to the overlap and shorter distance of DFB units which favored the intramolecular coupling.

CD and CPL signals in aggregated forms has increased as compared to the monomeric form accompanied by the existence of long-lived emitting species. This indicates prominent intermolecular and intramolecular excitonic coupling in the random aggregates. Moreover, para isomer formed nanowires in mixture of toluene and DCM solvent while the meta isomer failed to form nanowires showing that the spatial arrangements highly influenced the formation of π-π stacking and hydrogen bonding. Notably, the organogels displayed a $|g_{lum}|$ value of about 0.015. The results in this study may contribute to the future design of supramolecular assembled nanowires considering the influence of spatial arrangement of the supramolecular assembly formation and the tunability of the bichromophore units that induces the inversion of chirality.

2.7 References

(1) Ikeda, T.; Takayama, M.; Kumar, J.; Kawai, T.; Haino, T. Novel Helical Assembly of a Pt(II) Phenylbipyridine Complex Directed by Metal–Metal Interaction and Aggregation-Induced Circularly Polarized Emission. *Dalton Trans.* 2015, *44* (29), 13156–13162.

(2) Jintoku, H.; Kao, M.-T.; Del Guerzo, A.; Yoshigashima, Y.; Masunaga, T.; Takafuji, M.; Ihara, H. Tunable Stokes Shift and Circularly Polarized Luminescence by Supramolecular Gel. *J. Mater. Chem. C.* 2015, *3* (23), 5970–5975.

(3) Tempelaar, R.; Stradomska, A.; Knoester, J.; Spano, F. C. Circularly Polarized Luminescence as a Probe for Long-Range Interactions in Molecular Aggregates. *J. Phys. Chem. B.* 2011, *115* (36), 10592–10603.

(4) Ikeda, T.; Masuda, T.; Hirao, T.; Yuasa, J.; Tsumatori, H.; Kawai, T.; Haino, T. Circular Dichroism and Circularly Polarized Luminescence Triggered by Self-Assembly of Tris(Phenylisoxazolyl)Benzenes Possessing a Perylenebisimide Moiety. *Chem. Comm., B.* 2012, 48, 6025-6027.

(5) Kawai, T.; Kawamura, K.; Tsumatori, H.; Ishikawa, M.; Naito, M.; Fujiki, M.; Nakashima, T. Circularly Polarized Luminescence of a Fluorescent Chiral Binaphtylene–Perylenebiscarboxydiimide Dimer. *ChemPhysChem.* 2007, *8* (10), 1465–1468.

(6) Zhang, H.; Chen, P.-Z.; Niu, L.-Y.; Yang, Q.-Z. A Difluoroboron B-Diketonate-Based Luminescent Material with Tunable Solid-State Emission and Thermally Activated Delayed Fluorescence. *Mater. Chem. Front.* 2020, 4, 285.

(7) Zhang, D.-W.; Li, M.; Chen, C.-F. Recent Advances in Circularly Polarized Electroluminescence Based on Organic Light-Emitting Diodes. *Chem. Soc. Rev.* 2020, *49* (5), 1331–1343.

(8) Louis, M.; Brosseau, A.; Guillot, R.; Ito, F.; Allain, C.; Métivier, R. Polymorphism, Mechanofluorochromism, and Photophysical Characterization of a Carbonyl Substituted Difluoroboron-β-Diketone Derivative. *J. Phys. Chem. C.* 2017, *121* (29), 15897–15907.

(9) Nguyen, N. D.; Zhang, G.; Lu, J.; Sherman, A. E.; Fraser, C. L. Alkyl Chain Length Effects on Solid-State Difluoroboron β-Diketonate Mechanochromic Luminescence. *J. Mater. Chem.* 2011, 21, 8409.

(10) Zhai, L.; Liu, M.; Xue, P.; Sun, J.; Gong, P.; Zhang, Z.; Sun, J.; Lu, R. Nanofibers Generated from Nonclassical Organogelators Based on Difluoroboron β-Diketonate Complexes to Detect Aliphatic Primary Amine Vapors. *J. Mater. Chem. C.* 2016. 4,7939-7947.

(11) Louis, M.; Sethy, R.; Kumar, J.; Katao, S.; Guillot, R.; Nakashima, T.; Allain, C.; Kawai, T.; Métivier, R. Mechano-Responsive Circularly Polarized Luminescence of Organic Solid-State Chiral Emitters. *Chem. Sci.* 2019, *10* (3), 843–847.

(12) Wilbraham, L.; Louis, M.; Alberga, D.; Brosseau, A.; Guillot, R.; Ito, F.; Labat, F.; Métivier, R.; Allain, C.; Ciofini, I. Revealing the Origins of Mechanically Induced Fluorescence Changes in Organic Molecular Crystals. *Adv. Mater.* 2018, 30, 1800817.

(13) Kumar, J.; Nakashima, T.; Kawai, T. Circularly Polarized Luminescence in Chiral Molecules and Supramolecular Assemblies. *J. Phys. Chem. Lett.* 2015, *6* (17), 3445–3452.
(14) Galer, P.; Korošec, R. C.; Vidmar, M.; Šket, B. Crystal Structures and Emission Properties of the BF_2 Complex 1-Phenyl-3-(3,5-Dimethoxyphenyl)-Propane-1,3-Dione: Multiple Chromisms, Aggregation- or Crystallization-Induced Emission, and the Self-Assembly Effect. *J. Am. Chem. Soc.* 2014, *136* (20), 7383–7394.
(15) Chen, P.-Z.; Niu, L.-Y.; Chen, Y.-Z.; Yang, Q.-Z. Difluoroboron β-Diketonate Dyes: Spectroscopic Properties and Applications. *Coord. Chem. Rev.* 2017, *350*, 196–216.
(16) Živković, J. M.; Stanković, I. M.; Ninković, D. B.; Zarić, S. D. Phenol and Toluene Stacking Interactions, Including Interactions at Large Horizontal Displacements. Study of Crystal Structures and Calculation of Potential Energy Surfaces. *Cryst. Growth Des.* 2020, *20* (2), 1025–1034.
(17) Kumar, J.; Nakashima, T.; Kawai, T. Inversion of Supramolecular Chirality in Bichromophoric Perylene Bisimides: Influence of Temperature and Ultrasound. *Langmuir.* 2014, *30* (21), 6030–6037.
(18) Kumar, J.; Nakashima, T.; Tsumatori, H.; Mori, M.; Naito, M.; Kawai, T. Circularly Polarized Luminescence in Supramolecular Assemblies of Chiral Bichromophoric Perylene Bisimides. *Chem. Eur. J.* 2013, *19* (42), 14090–14097.
(19) Zhang, X.; Lu, R.; Jia, J.; Liu, X.; Xue, P.; Xu, D.; Zhou, H. Organogel Based on β-Diketone-Boron Difluoride without Alkyl Chain and H-Bonding Unit Directed by Optimally Balanced π–π Interaction. *Chem. Commun.* 2010, *46* (44), 8419.
(20) Spackman, M. A.; Jayatilaka, D. Hirshfeld Surface Analysis. *CrystEngComm.* 2009, *11* (1), 19–32.
(21) Sethy, R.; Métivier, R.; Brosseau, A.; Kawai, T.; Nakashima, T. Impact of Optical Purity on the Light Harvesting Property in Supramolecular Nanofibers. *J. Phys. Chem. Lett.* 2018, *9* (16), 4516–4521.
(22) Sethy, R.; Kumar, J.; Métivier, R.; Louis, M.; Nakatani, K.; Mecheri, N. M. T.; Subhakumari, A.; Thomas, K. G.; Kawai, T.; Nakashima, T. Enantioselective Light Harvesting with Perylenediimide Guests on Self-Assembled Chiral Naphthalenediimide Nanofibers. *Angew. Chem. Int. Ed.* 2017, *56* (47), 15053–15057.
(23) Yamamoto, H.; Inagaki, T.; Park, J.; Yoshida, S.; Kaneko, K.; Hanasaki, T.; Akagi, K. Helical Network Polymers Embodying High Dissymmetry Factors in Circularly Polarized Luminescence: Photocrosslinking Polymerization of Acrylate Derivatives in Chiral Smectic Liquid Crystals. *Macromolecules.* 2021, 54, 19, 8977–8986

CHAPTER 3

Energy Transfer and Sensitivity to UV Light of Supramolecular Nanowires based on Bichromophoric DFB compound

Synthetic light harvesting materials based on metal organic frameworks, dendrimers, polymers and supramolecular assemblies through arrays of chromophores have been utilized for device fabrications such as organic light emitting diodes, sensors and photovoltaic cells.[1–3] Supramolecular assembled compounds have advantages in device fabrication due to simplicity of each molecular units and less complicated synthesis as these supramolecular architectures are driven by spontaneous weak intermolecular interactions[4]. The efficiency of light harvesting properties originates from the intermolecular electronic interactions within the chromophores units that induce exciton migration.[1,5–7] Thus, it is equally important to evaluate the energy transfer in supramolecular assembly and its electronic communications in coupled chromophore with respect to its monomeric form for effective supramolecular molecular design for device fabrication.

The formation of supramolecular assembled nanowires in bichromophore DFB as well as its molecular stackings, electronic transitions, and enhanced chiroptical properties were discussed in the previous chapter. This chapter provides insights on the comparison of mono-substituted and di-substituted DFB (Figure 3.1) in terms of formation of supramolecular assembly and photophysical properties in monomeric form (Sections 3.2-3.4). The efficiency of energy transfer was evaluated with anisotropy measurements for mono and di-substituted DFB diluted in frozen matrices as well as in supramolecular assembly (Section 3.5). Lastly the sensitivity of the supramolecular assembly to exposure in high photon flux was evaluated (section 3.6).

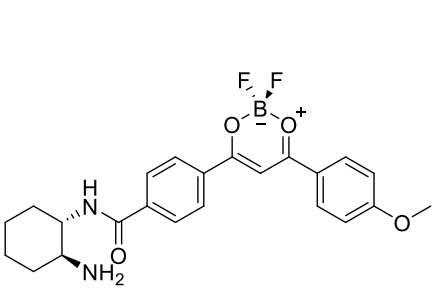

(*S*) Cydiamine mono-DFB

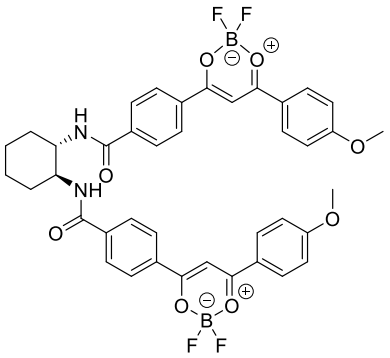

(*S*) Cydiamine di-DFB

Figure 3.1: Chemical structures of **cydiamine mono-DFB** and **cydiamine di-DFB**.

3.1 Synthesis

In this study we synthesized two compounds bearing one DFB unit (**cydiamine mono-DFB**) and two DFB units (**cydiamine di-DFB**) with pure (*S*) enantiomers (*S* is referring to 1*S*,2*S*). The target compounds **cydiamine mono-DFB** and **cydiamine di-DFB** were obtained by synthesizing first the intermediate **P-1**. This was already discussed in the previous chapter: **P-1** was synthesized through Claisen condensation reaction of 4-methoxy acetophenone and dimethyl terephthalate at 70°C for 12hours.[8] This was followed with reaction of LiOH to convert **P-1** to β-keto enol acid (**P-2**).[8,9] First step in synthesizing **cydiamine mono-DFB** is through protecting one amine group in 1*S*,2*S* cyclohexane diamine using tert-butoxycarbonyl (t-BOC) to obtain **Cydiamine-BOC** compound (scheme 3.1).[10] This was followed by peptidic coupling of **P-2** with **Cydiamine-BOC** using diethyl cyanophosphate (DECP) and triethylamine. After peptidic coupling, BOC protecting group was then removed using a mixture of trifluoroacetic acid (TFA) and dichloromethane (DCM) (2:1) to form the cyclohexane diamine mono-β-keto enol ligand.[11] Complexation with BF_2 was completed using $BF_3(OEt)_2$ and the target compound **cydiamine mono-DFB** was isolated through automatic column chromatography. Cyclohexane diamine difluoroboron-β-diketonate (**cydiamine di-DFB**) was synthesized using the previously reported scheme as discussed in Chapter 2. The reaction scheme is shown in 3.1 (see Chapter 6 for detailed synthesis).

BOC protection

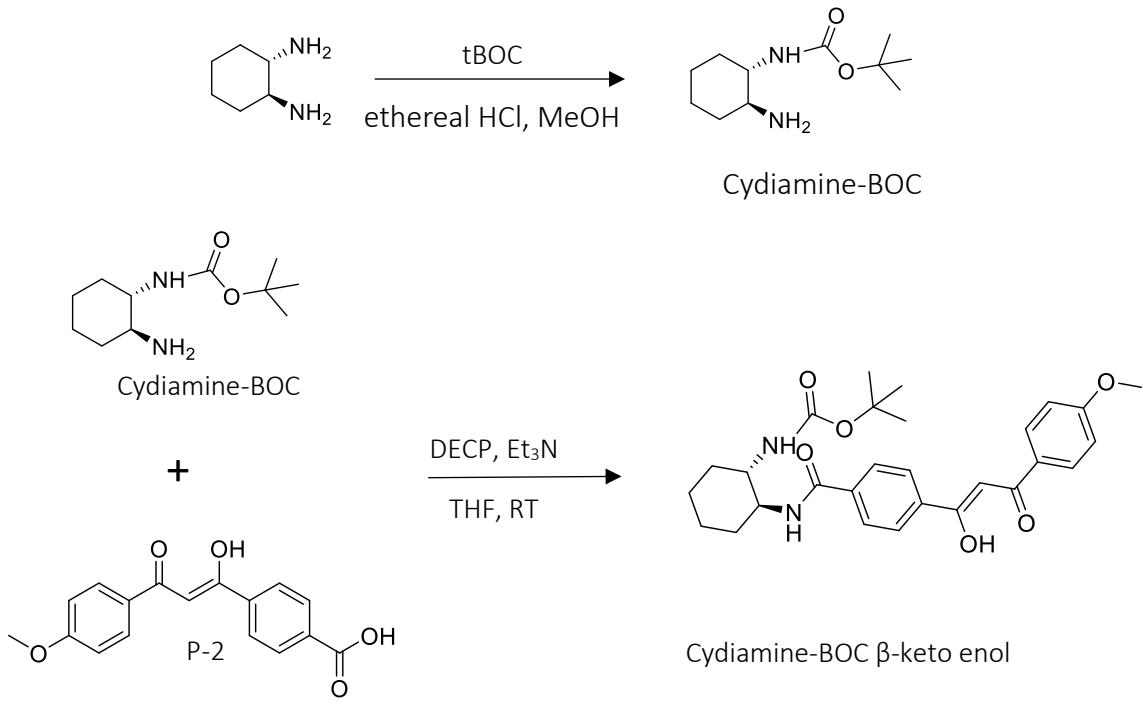

BOC deprotection

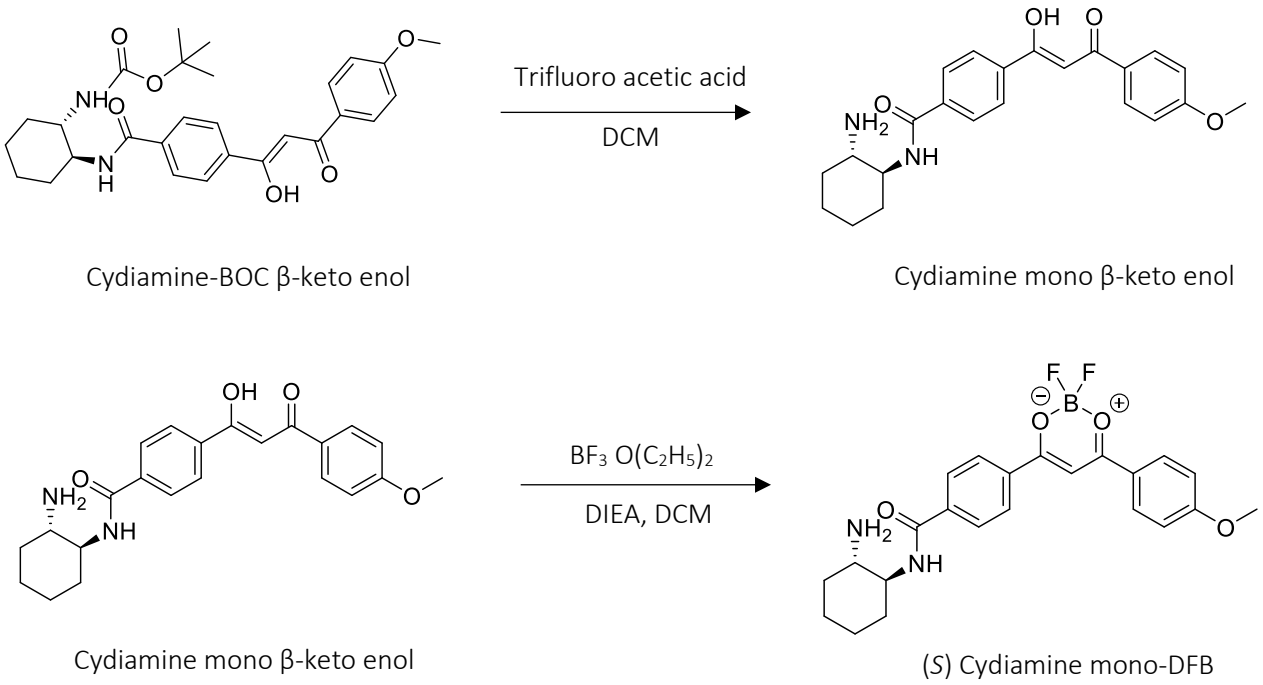

Scheme 3.1: Reaction scheme for synthesis of cydiamine mono-DFB

3.2 Photophysical Properties in Solution

The comparison of the photophysical properties of the two compounds in solution was done by measuring absorbance and emission of cydiamine mono-DFB and cydiamine di-DFB in different solvents as summarized in Table 3.1. As shown in Figure 3.2, both compounds display similar range of absorbance (387nm to 391nm for cydiamine mono-DFB and 390nm-394nm for cydiamine di-DFB) at different solvent polarity. The emission of di-substituted DFB are expected to display at longer wavelengths due to the intramolecular coupling of two chromophore units within one molecular unit.[12,13] However, emission spectra of cydiamine mono-DFB at different solvents polarity showed similar emission and solvatochromism as cydiamine di-DFB.

Table 3.1. Maximum absorbance (λ_{abs}) and emission (λ_{em}) of **cydiamine mono-DFB** and **cydiamine di-DFB** in different solvent (λ_{exc} 390nm).

Solvent	ε (static dielectric constant)	Cydiamine mono-DFB		Cydiamine di-DFB	
		λ_{abs}	λ_{em}	λ_{abs}	λ_{em}
Chloroform	4.81	388 nm	438 nm	393 nm	440 nm
THF	7.58	388 nm	444 nm	390 nm	443 nm
DCM	8.93	391 nm	455nm	394 nm	446 nm
Acetonitrile	37.5	387 nm	461 nm	394 nm	465 nm

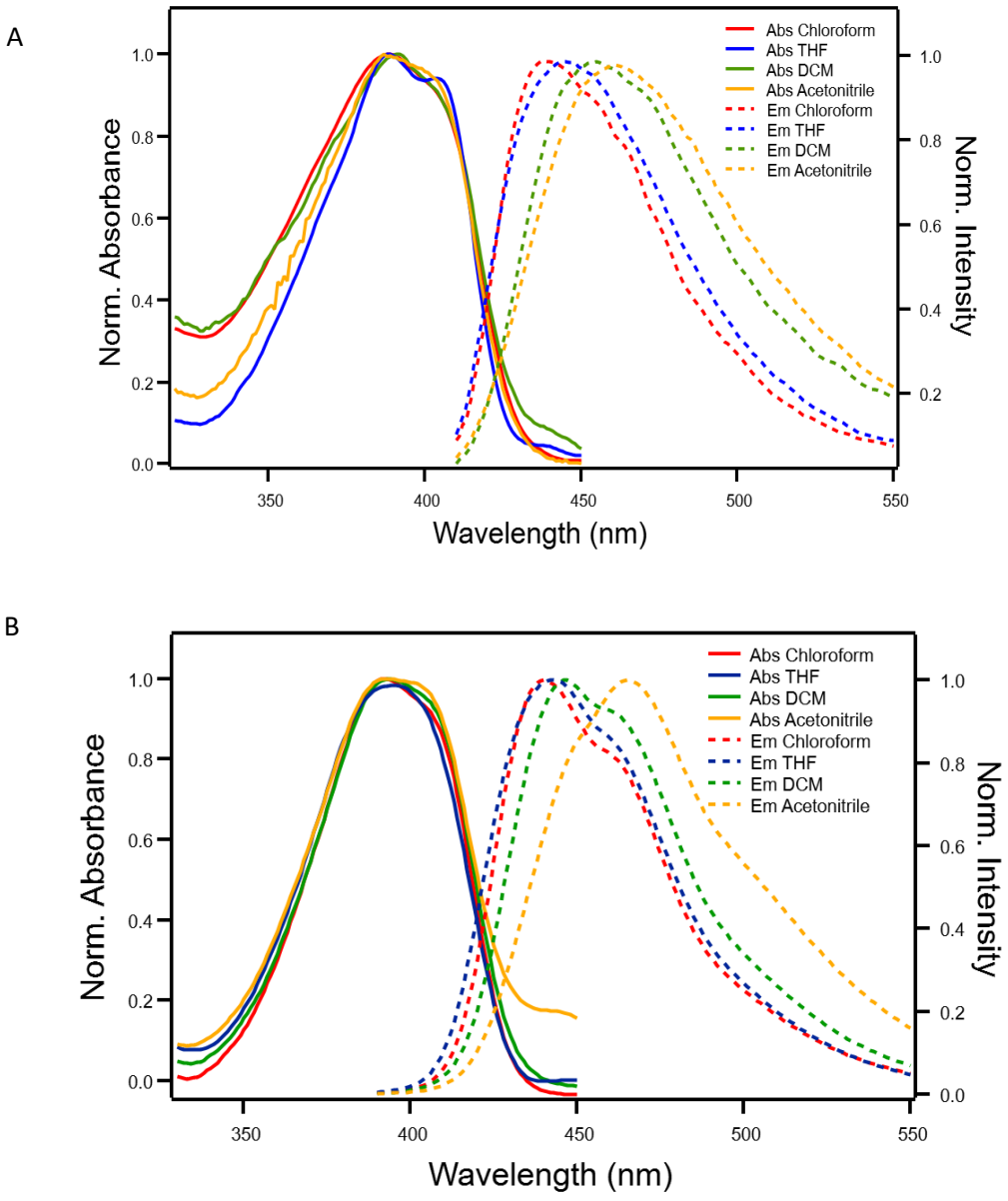

Figure 3.2. Absorbance and emissions of **cydiamine mono-DFB** (a) and **cydiamine di-DFB** (b) in chloroform, DCM, THF and acetonitrile (λ_{exc} 390nm).

Time-resolved fluorescence spectroscopy measurements were conducted to gain insights on the lifetimes in solution. The decays were fitted required satisfactory value of X^2 < 1.2 in global analysis and the summary of decays are listed in Table 3.2. Both compounds exhibit bi-exponential decay where **cydiamine mono-DFB** has decay time values τ1= 0.99ns (a1=0.08) and τ2=0.6ns (a2=0.92) while **cydiamine di-DFB** has τ1= 12.18 ns (a1=0.01) and τ2=2.06ns (a2=0.92). Although two decay times were observed, it is noticeable that one of them are with traceable contribution (τ1= 0.99ns for **cydiamine mono-DFB** and τ1= 12.18 ns for **cydiamine di-DFB**).

Similar with **cydiamine di-DFB**, quantum yield was calculated using quinine sulfate standard. The **cydiamine mono-DFB** in DCM has QY 0.31 while in the previous chapter, it was shown that **cydiamine di-DFB** in DCM has QY = 0.69. The red shift in emission spectra accompanied by positive solvatochromism and lower quantum yield was previously explained with the presence of electron donating group to the DFB molecules and intramolecular charge transfer (ICT) character.[14,15]

Table 3.2. Decay times of cydiamine mono-DFB (in acetonitrile) and cydiamine di-DFB (in DCM) using excitation wavelength of 390nm

	τ_1 (a_1, f_1) ns	τ_2(a_2, f_2) ns	$<\tau_{ave}>$ ns	Φ_f	K_{nr}, s^{-1}	K_r, s^{-1}
cydiamine mono-DFB	0.99 (0.08, 0.13)	0.60 (0.92, 0.87)	0.65	0.31	$1.06x10^9$	$4.77x10^8$
cydiamine di-DFB	12.18 (0.01, 0.02)	2.06 (0.99, 0.97)	2.41	0.69	$1.29x10^8$	$2.86x10^8$

where τ_n is decay time, a_n is pre-exponential factor and f_n is fraction of intensity, QY is fluorescence quantum yield K_{nr} and K_r are non-radiative and radiative rate constants.

3.3 Density Functional Theory (DFT) and Time-dependent DFT Calculations

To gain insights into the photophysical behavior of the two compounds and to determine the molecular orbitals involved as well as the electronic transitions, density functional theory (DFT) and time dependent DFT calculations were performed. In this calculation, functional CAMB3LYP, basis set 6-31+G (d,p), and IEFPCM solvation method using DCM were used. The optimized geometry of **cydiamine di-DFB** was previously discussed in Chapter 2, while the optimized geometry of **cydiamine mono-DFB** is included in supplementary documents (Chapter 6).

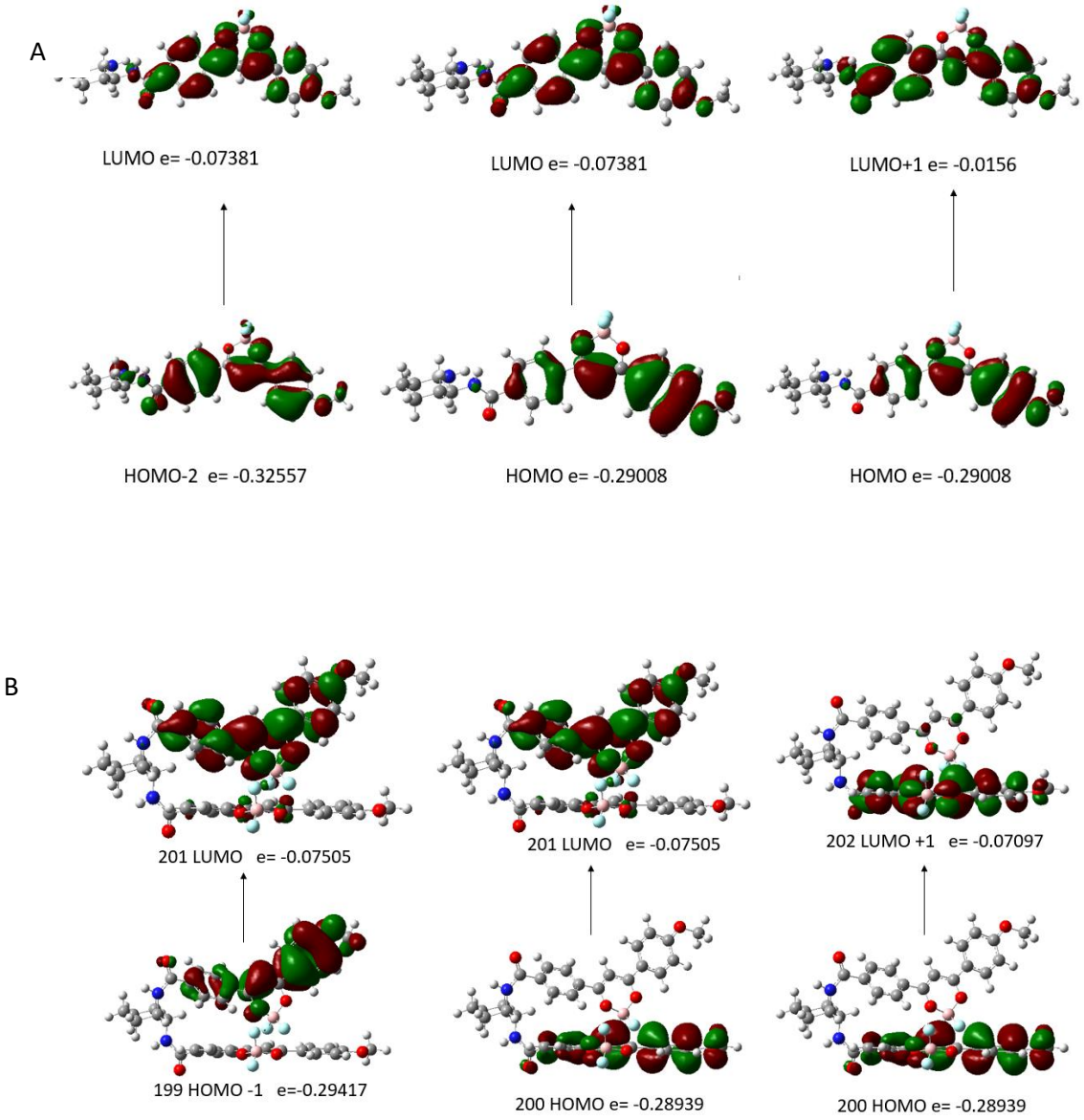

Figure 3.3. Molecular orbital surfaces involved in electronic transitions of **cydiamine mono-DFB** (refer to chapter 6 Table 6.6) (a) and **cydiamine di-DFB** (refer to chapter 6 table 6.4) (b) and their energies (Hartree), calculated using TDDFT with functional CAMB3LYP, basis set 6-31+G (d,p), and IEFPCM solvation method.

The TD-DFT calculations of **cydiamine mono-DFB** revealed that the electronic transitions from the lowest energy involve multiple molecular orbitals as shown in Figure 3.3. (See chapter 6 for tables of molecular orbitals and their contributions). Transitions from HOMO-2 to LUMO involves primary amine group which has contributed to the intramolecular charge transfer (ICT) from NH_2 to the electron withdrawing group DFB.

Other transitions such as HOMO to LUMO and HOMO to LUMO+1 display the typical π-π* and delocalized electrons within the DFB moiety (see Figure 3.2a).

In contrast, for cydiamine di-DFB, the molecular orbitals involved in the transitions show that the electrons are mainly delocalized to each β-diketonate moiety (see Figure 3.2b). Cydiamine di-DFB have the following transition: HOMO-1 to LUMO, HOMO to LUMO, and HOMO to LUMO+1. It was also noticeable that there is electron delocalization on the diketonate rings of opposite DFB unit shown in Figure 3.3b, indicating intramolecular coupling between the two DFB units of bichromophore.

3.4 Self-Assembled Nanowires

In the previous chapter, we have shown the formation of self-assembled nanowires of cydiamine di-DFB with mixture of toluene and DCM showing intertwined wires. Self-assembled nanowires formation was also attempted with cydiamine mono-DFB using different solvent systems and combinations of polar and non-polar solvents initiated with ultrasonication and heating. However, the compounds are either fully dissolved or precipitated in all the experimental conditions. First, failure to form a supramolecular assembly may result from the presence of a primary amine which may tend to form stronger hydrogen bonds causing precipitation of the compound. Secondly, it was clear from the calculated structures of nanowires from Materials Studio COMPASS II from the previous chapter that the presence of two amide groups is playing crucial part in supramolecular assembly. It is through the formation of H-bonds between the carbonyl and amide groups of the adjacent bichromophoric DFB units that the supramolecular backbone is formed. From these observations, it was suggested that single carbonyl and amide groups alongside with the presence of primary amine located at the cyclohexane moiety are not enough to form a stabilize the supramolecular backbone of nanowires.

3.4.1 Energy Transfer in Supramolecular Assembly

We then studied the comparison of energy transfer within mono substituted DFB to di-substituted DFB and its supramolecular assembly. The efficiency of energy migration was evaluated based on its anisotropy values. The steady-state fluorescence anisotropy measurements are based on the principle photo selective excitation of fluorophores wherein the absorbance of photons takes places if the fluorophores have parallel transition moments with the electric vectors of photons.[16,17]

The anisotropy was calculated with the following equation:

$$r = \frac{(I_{VV} - GI_{VH})}{(I_{VV} + 2GI_{VH})}$$

$$G = \frac{I_{HV}}{I_{HH}}$$

where:

r is anisotropy value

I_{VV} and I_{VH} are emission intensity measured at vertical and horizontal position when the polarizer is vertically oriented.

I_{HV} and I_{HH} are emission intensity measured at vertical and horizontal position when the polarizer is horizontally oriented.

G is gain factor

The measurements for monomeric forms of cydiamine mono-DFB and cydiamine di-DFB are done at -50°C with cryostat system using polypropylene glycol as solvent. The anisotropy values of cydiamine mono-DFB as a function of excitation and emission have similar average anisotropy values of r = 0.36 measured at range 390nm – 410nm and 440nm – 460nm respectively. On the other hand, cydiamine di-DFB exhibits anisotropy values of r = 0.18 as a function of excitation (390nm – 410nm) and r = 0.14 as function of emission (450nm – 470nm) as shown in Figures 3.4 and 3.5. High anisotropy values in cydiamine mono-DFB clearly shows that there is no exciton migration within the neighboring chromophore while the decrease in anisotropy values in cydiamine di-DFB clearly exhibits intra-molecular exciton migration between the two DFB units. This result is also parallel with the molecular orbitals calculated with TDDFT showing intramolecular interactions between the two DFB units of a bichromophore. The measurements were extended to the supramolecular assembly which displayed a dramatic decrease in anisotropy values to $r = 2\text{x}10^{-3}$ and a function of excitation (average at 410nm to 430nm) and $r = 5\text{x}10^{-3}$ as a function of emission (530nm-550nm). The depolarization is clear evidence of exciton migration in supramolecular assembly (see Figure 3.6).

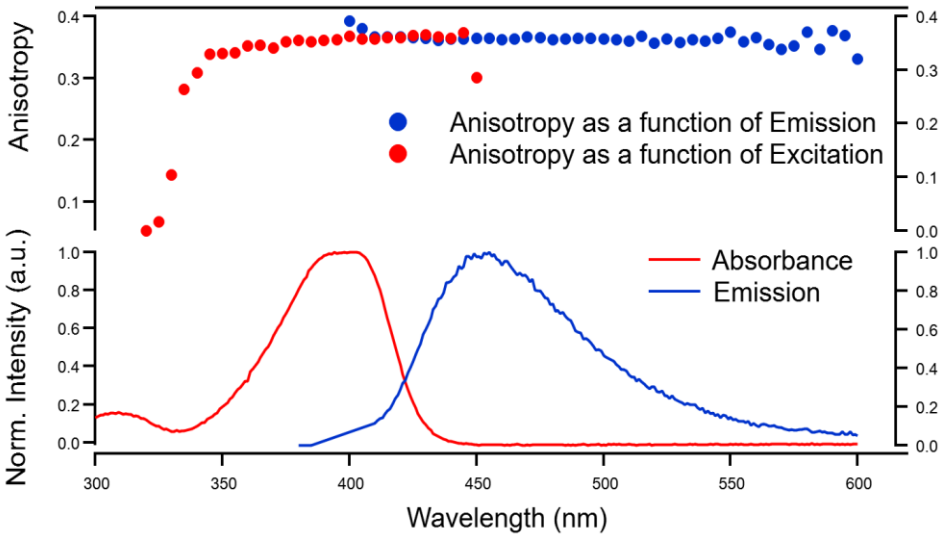

Figure 3.4. Anisotropy as a function of excitation (λ_{em}=480nm) and as a function of emission (λ_{exc}=380nm) of **cydiamine mono-DFB** in propylene glycol measured at -50°C.

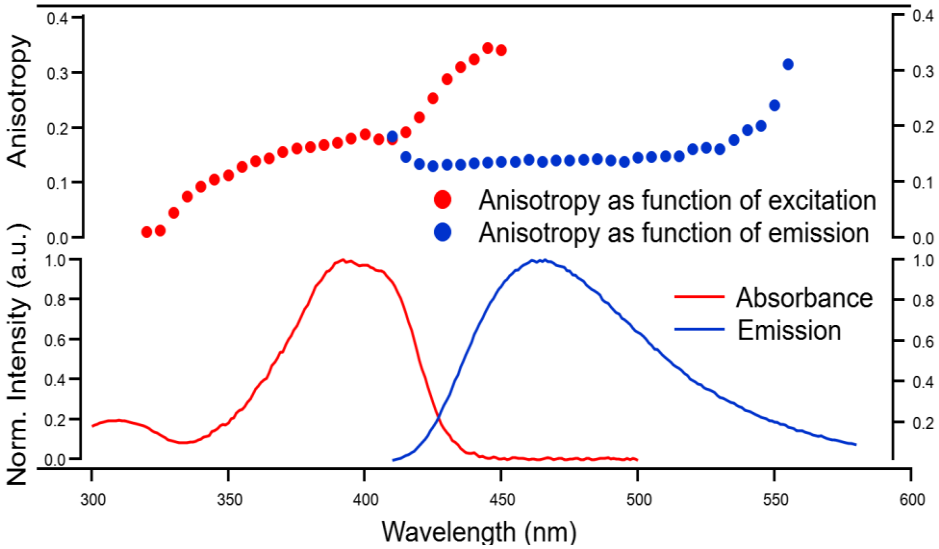

Figure 3.5. Anisotropy as a function of excitation (λ_{em}=480nm) and as a function of emission (λ_{exc}=380nm) of **cydiamine di-DFB** in propylene glycol measured at -50°C.

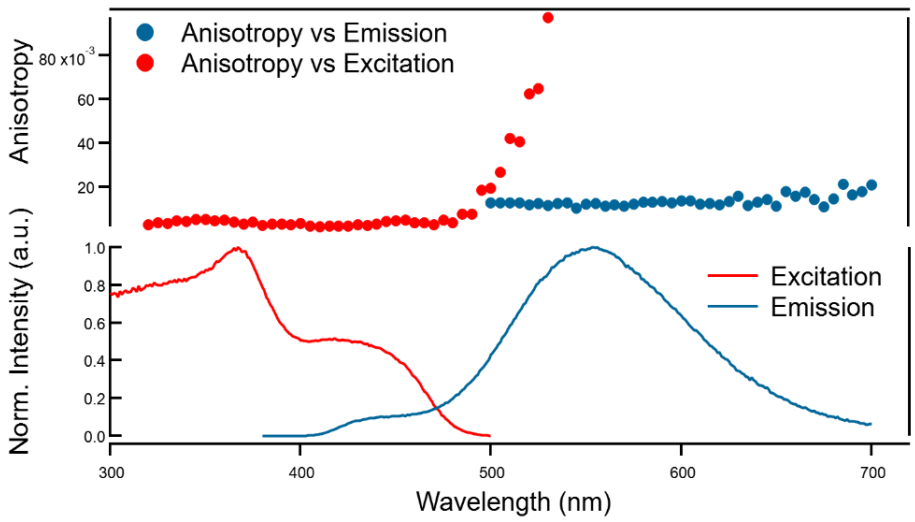

Figure 3.6. Anisotropy as a function of excitation (λ_{em}=550nm) and as a function of emission (λ_{exc}=450nm) of supramolecular assembly of cydiamine **di-DFB** measured at room temperature.

3.5 Responsiveness to UV Light

3.5.1 Photobleaching and Emission shift

The sensitivity of the nanowires to the UV light was first observed serendipitously using the specialized spectroscopic method wherein the atomic force microscope (AFM) was coupled with fluorescence microscopy equipped with EM-CCD camera and CCD spectrograph as shown in Figure 3.7.

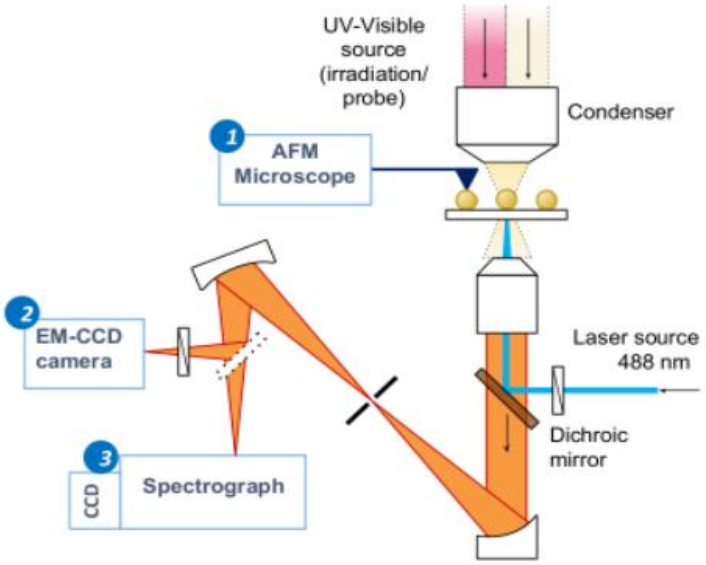

Figure 3.7: Experimental set-up of AFM coupled with fluorescence microscopy

Small amount of **cydiamine di-DFB** nanowires was deposited in a clean glass by sliding off a portion of organogels to the glass leaving a thin layer of nanowires on the surface. The glass was then placed under vacuum for at least 6 hours to remove the solvents. Isolated nanowires were subjected for emission measurements before and after exposure to UV. The UV source was set to excitation wavelength of 400nm with I=2% and total exposure time of 2 seconds. The measurement slit was set to 200 µm and the emission before and after exposure was measured in several areas along the measurement slit (see Figure 3.8a).

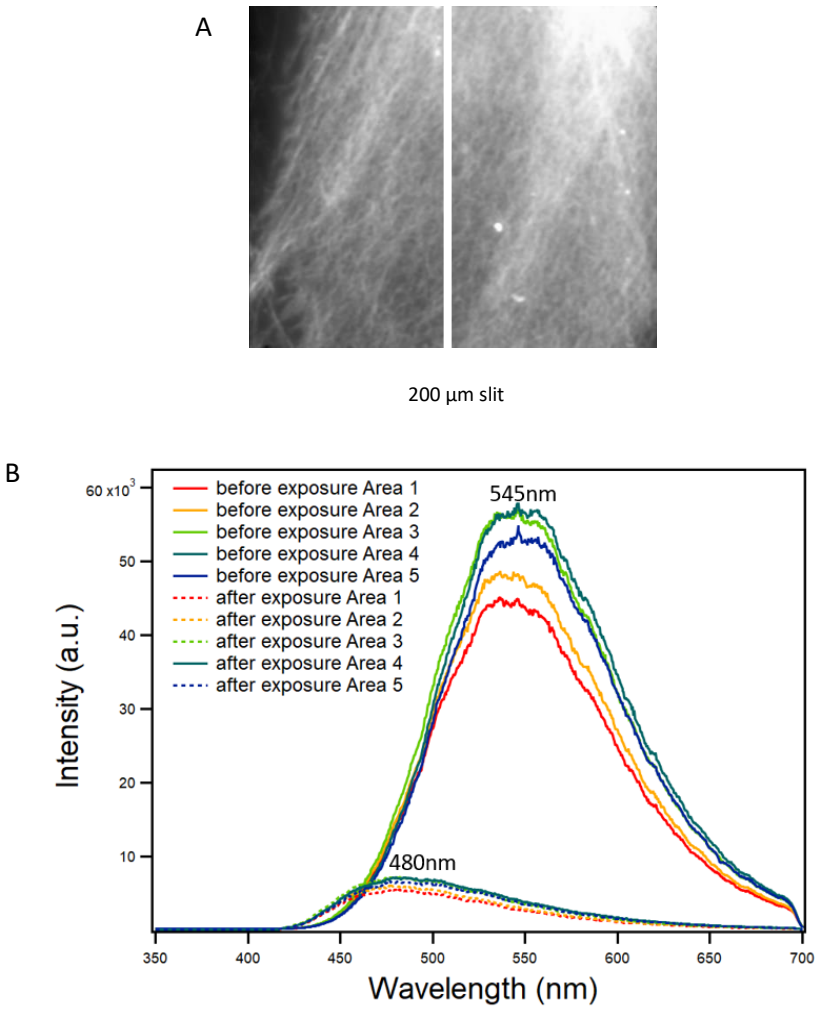

Figure 3.8. The fluorescence image of nanowires using CCD camera including the slit measurement area (a) and the emission before and after exposure 400 nm wavelength source (b).

It was observed that the emission has shifted to lower wavelength from 545nm to 480nm accompanied by a decrease in emission intensity as shown in Figure 3.8b. Photobleaching in nanowires was further investigated by monitoring the fluorescence intensity with exposure time. The same AFM coupled with fluorescence microscope was used but the exposure time was extended to 10mins while capturing the emission in 1 frame per second using the CCD camera. The decrease in emission intensity was monitored in several areas within the frame as shown in Figure 3.9a. The intensity vs time plotted for different areas under observation showed that there is ~75% decrease of intensity after 10minutes of exposure (see Figure 3.9b).

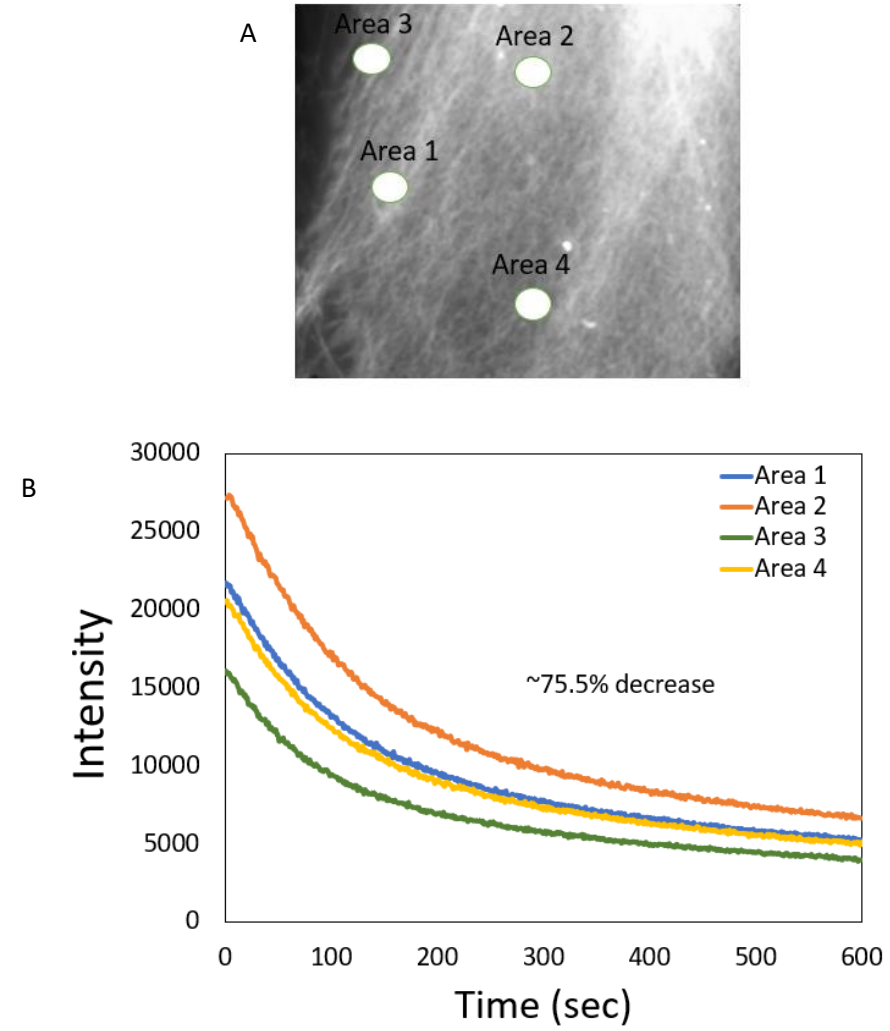

Figure 3.9. The fluorescence image of nanowires using CCD camera including the slit measurement area (a) and the emission before and after exposure 400 nm wavelength source (b).

To further understand the emission shift and decrease in the fluorescence intensity, the measurements were extended to macro-scale analysis. Organogel was exposed in UV source equipped with filters to select the wavelength around 380nm and was set to I=100%. The set-up was kept at 25°C to reduce the errors caused by accumulating heat from the source. The steady-state fluorescence emission was measured after exposure at different times while simultaneously measuring the time-resolved fluorescence emission to understand the nature of emitting species at both wavelengths shown in Figure 3.10a. The steady state fluorescence spectra showed that the overall emission intensity is decreasing which agreed with the photobleaching effect observed at microscale analysis. Apparently, emission peak at 450nm has gradually increased with respect to the emission peak at 550nm as shown in intensity ratio plot vs time (see Figure 3.10b). This is in contrast with the dramatic decrease in intensity at 550 nm after 15minutes of exposure time.

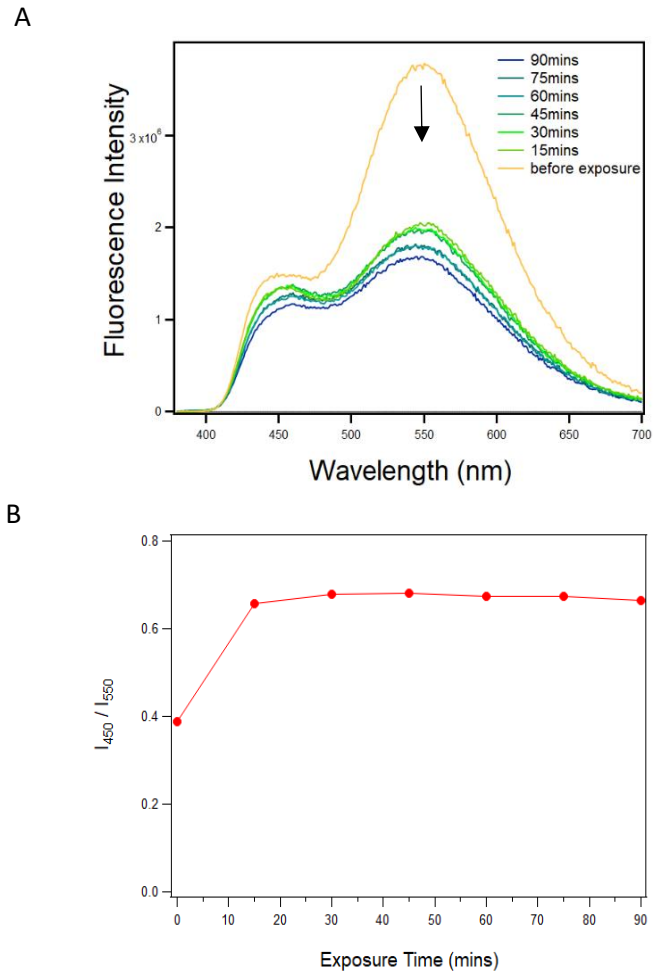

Figure 3.10: Steady-state fluorescence emission of organogels after exposure to UV (380nm) at different time (a) and the ratio of intensity at 450nm and 550nm at different exposure time (b).

Time-resolved spectroscopic measurements data obtained for wavelength peak 450nm at different exposure time was fitted with global analysis showing decay times τ_1 = 21.6ns, τ_2 = 2.13ns, τ_3 = 0.54 ns, and τ_4 = 0.05ns shown in Figure 3.11 and Table 1. The emitting species with decay time 21.6ns has very low pre-exponential factors which may be attributed to the residual aggregates from the long-lived emissive species. Meanwhile, the pre-exponential factors from the emitting species with decays τ_3 = 0.54 ns and τ_4 = 0.05ns are showing mirror images indicating that these are coming from one component (0.54ns) which eventually was converted to fast decays (0.05ns) after exposure to UV. The emitting species with decay at τ_2 = 2.13ns was gradually decreasing with exposure time which may be attributed to the monomeric form.

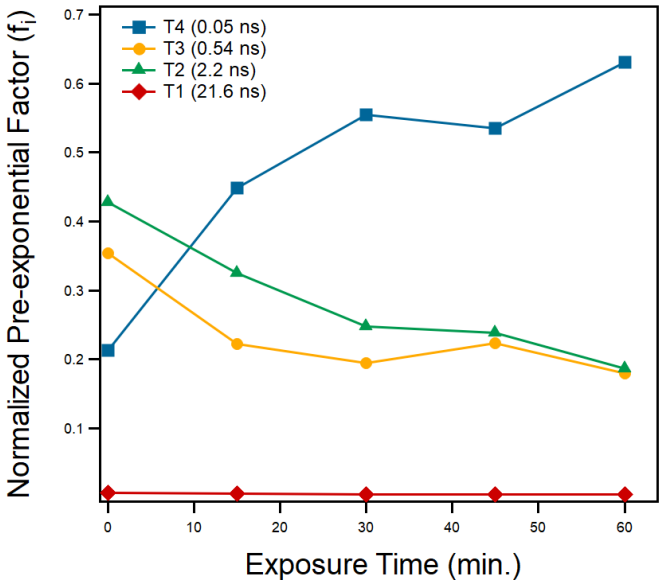

Figure 3.11: Time-resolved spectroscopic measurements of organogels exposed in UV (380nm) at different exposure time measured at 450nm.

Table 1. Pre-exponential factors (a_n) and fraction of intensity (f_n) of **cydiamine di-DFB** organogels at emission wavelength 450nm measured at different exposure time (excitation at 360nm).

	τ_1 (a, f_1)	τ_2 (a_2, f_2)	τ_3 (a_3, f_3)	τ_4 (a_4, f_4)
Before irradiation	21.5	2.13	0.54	0.06
	(0.01, 0.11)	(0.43,0.73)	(0.35, 0.15)	(0.21, 0.01)
15mins	21.5	2.13	0.54	0.06
	(<0.01 0.11)	(0.32,0.74)	(0.22, 0.13)	(0.45, 0.03)
30mins	21.5	2.13	0.54	0.06
	(<0.01, 0.12)	(0.25,0.70)	(0.19, 0.14)	(0.55, 0.04)
45mins	21.5	2.13	0.54	0.06
	(<0.01, 0.13)	(0.24,0.67)	(0.22, 0.16)	(0.53, 0.04)
60mins	21.5	2.13	0.54	0.06
	(<0.01, 0.14)	(0.19,0.64)	(0.18, 0.16)	(0.63, 0.06)

Similarly, time-resolved spectroscopic measurement data for wavelength peak 550nm was fitted with global analysis (see Figure 2.12 and Table 2). The decay times were found τ_1 = 38.4ns, τ_2 = 25.7ns, τ_3 = 5.74ns, and τ_4 = 0.71ns. The emitting species at longer decay times τ_1 = 38.4ns, τ_2 = 25.7ns, τ_3 = 5.74ns were from multimers formed through intermolecular interactions in the supramolecular assembly of nanowires and exhibit decay times which are far longer than the decay time of monomeric form (<2ns as discussed in chapter 2).

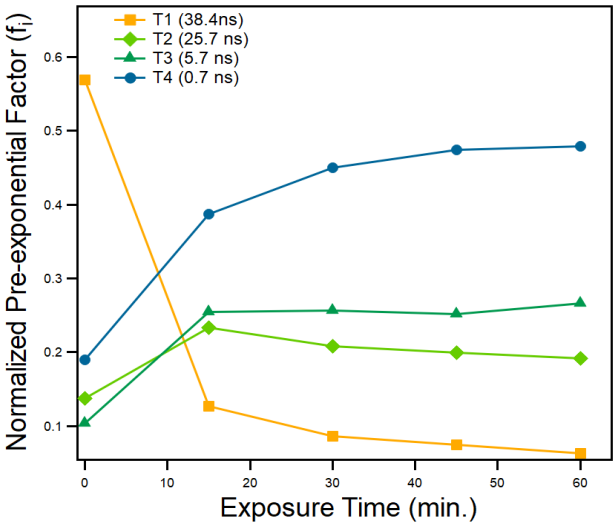

Figure 3.12: Time-resolved spectroscopic measurements of organogels exposed in UV (380nm) at different exposure time measured at 550nm.

Table 2. Pre-exponential factors (a_n) and fraction of intensity (f_n) of **cydiamine di-DFB** organogels at emission wavelength 550nm measured at different exposure time (excitation 360 nm).

	τ_1 (a, f_1)	τ_2 (a_2, f_2)	τ_3 (a_3, f_3)	τ_4 (a_4, f_4)
Before irradiation	38.40 (0.57, 0.84)	25.71 (0.14, 0.14)	5.74 (0.10, 0.02)	0.71 (0.19, 0.01)
15mins	38.40 (0.13, 0.39)	25.71 (0.23,0.48)	5.74 (0.25, 0.12)	0.71 (0.39, 0.02)
30mins	38.40 (0.09, 0.32)	25.71 (0.21,0.51)	5.74 (0.26, 0.14)	0.71 (0.45, 0.03)
45mins	38.40 (0.07, 0.29)	25.71 (0.20,0.53)	5.74 (0.25, 0.15)	0.71 (0.47, 0.03)
60mins	38.40 (0.06, 0.26)	25.71 (0.19,0.53)	5.74 (0.27, 0.17)	0.71 (0.48, 0.04)

The emission from long decay (38.4ns) exhibits the same mirror image as with short decay time (0.7ns), which also indicates these are emissions are from the same species. Noticeably there are emissive species with intermediate decays (25.7ns and 5.7ns) which further emerged after exposing the organogels to UV source. The shortest decay time are predominant for both emissions in 450nm and 550nm after exposure to UV. This may be attributed to the emission from bichromophore units without BF_2 which agree with the TCSPC analysis of this compound in solution showing a very short lifetime (< 0.01ns) (see Chapter 6 for supporting details).

The results obtained from the combination of time-resolved and steady state fluorescence spectroscopy, it was evident that the emissive components with long decays formed in 550nm wavelength was reduced in contribution after exposure of organogels in UV light. On the other hand, emissive species with intermediate and shorter decays gradually increase with UV exposure suggesting that there are possible distortion of long range multimers formed in supramolecular assembly.

3.5.2 AFM Image Analysis

The morphologies of the nanowires were compared before and after exposure to UV. The exposed nanowires were carefully collected and deposited in cleaned glass slides and dried under vacuum to remove the solvents prior to AFM analysis. AFM images showed fragments of nanowires and surprisingly radial aggregates were also found in the images in Figure 3.13.

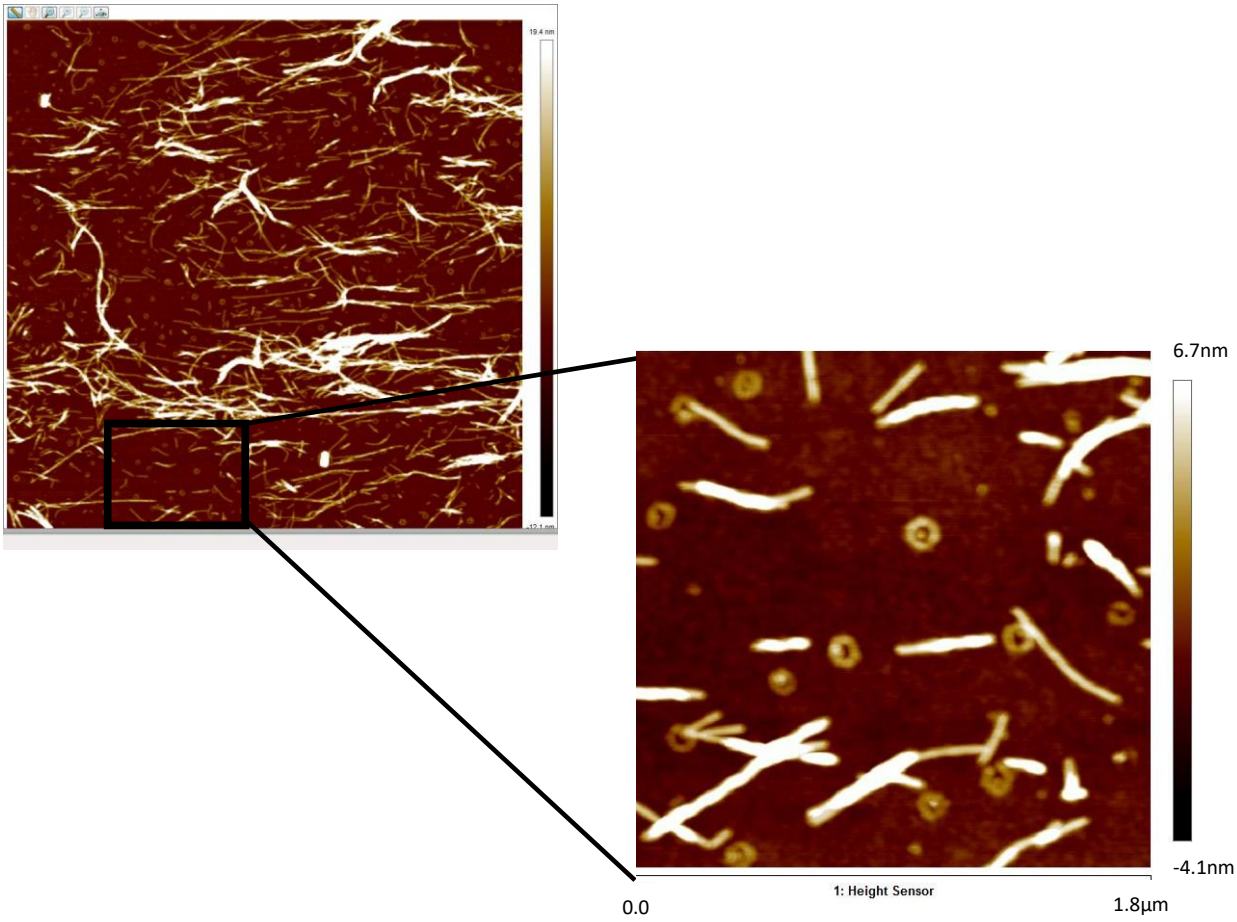

Figure 3.13. AFM images of nanowires after exposure to UV

The fragmented fibers as well as the radial aggregates were not observed in morphological analysis of isolated unexposed nanowires. This may indicate that high energy photons from the UV source may not only caused destructed BF_2 to carbonyl interactions, but also disruption of H-bonding of molecular backbone of nanowires. On the other hand, the radial deposits may be due to re-agglomeration of monomeric bichromophore units after dislodging from supramolecular assembly. It should also be noted that the solvent in organogels is toluene which is a poor solvent for cydiamine di-DFB which rationalizes the re-agglomeration into radial arrangement. Image analyses were conducted to determine the average length of fragments and the diameters of aggregates which gives the range of 200nm – 500nm for fragments (see Figure 3.14) and 150nm-200nm for diameters of radial aggregates as shown in Figure 3.15.

The time-resolved spectroscopic measurements for both 450nm and 550nm may then suggest that influx of photons to the organogels caused degradation of supramolecular assembly as evident with emerging decays with long exposure to UV.

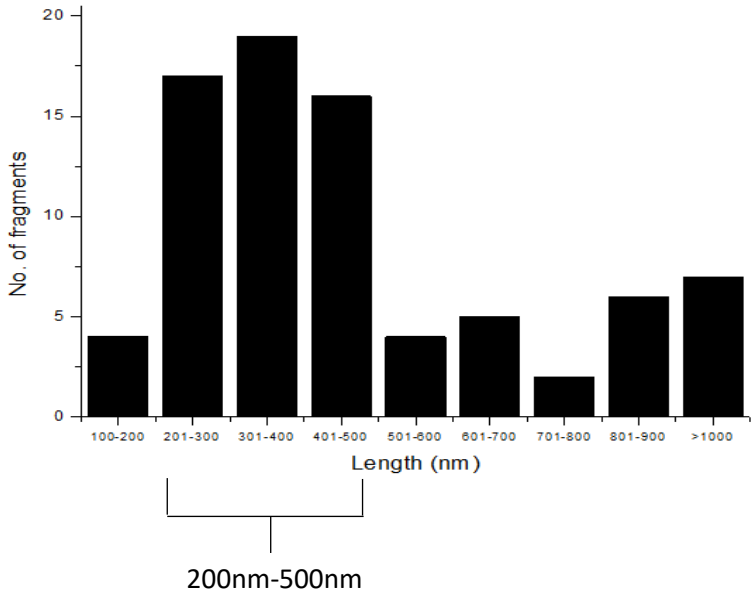

Figure 3.14: Histogram of the lengths of fragmented nanowires after exposure to UV analyzed using Gwyddion software.

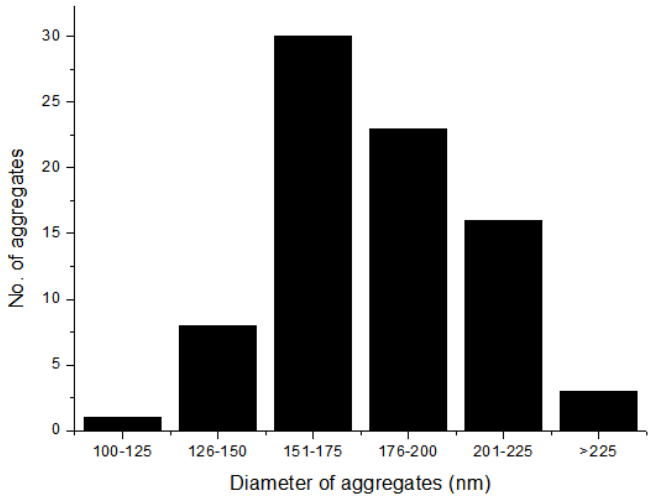

Figure 3.15: Distribution of diameter sizes of radial aggregate found in AFM image analyzed using Gwyddion software.

Finally, to demonstrate the emission shift after exposure to 380nm UV light source, we printed pattern in the surface of the organogels. It was shown that the exposed part has blue emission while the unexposed organogels emits yellow under visualized 365nm UV source shown in Figure 3.16.

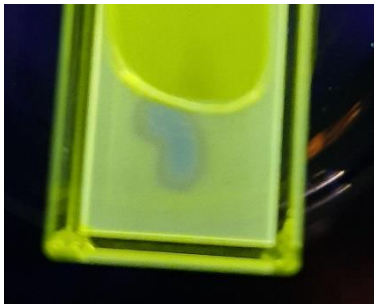

Figure 3.16: Image of printed pattern in organogels through UV light exposure at 380nm (blue emissive pattern) while the yellow emissive background are the non-exposed organogels visualized under 365nm light.

3.6 Conclusion

In this chapter, we discussed the photophysical properties of mono-substituted DFB (cydiamine-monoDFB) and di-substituted DFB (cydiamine-diDFB). Moreover, the DFT and TD-DFT calculations give an insight into the electronic transitions and electron delocalization within the DFB moiety of mono and di-substituted DFB. The supramolecular assembly formation was attempted for cydiamine-monoDFB and its failure justified the importance of two groups of carbonyls to amide H-bonding in stabilizing the molecular backbone as exhibited by cydiamine-diDFB in the previous chapter.

Energy transfer in monomeric form was evaluated through anisotropy measurements showing an efficient energy transfer within the two DFB units of isolated di-DFB, while the mono-DFB did not demonstrate such energy transfer. Meanwhile, the supramolecular assembly exhibits effective depolarization which proves the efficient exciton migration within the chromophores. This exhibits the potential applications in fabrication of light harvesting devices. Finally, the responsiveness of the nanowires to the UV exposure were explained by following the nature of emitting species in organogels at different exposure time. In accordance with the emerged short and intermediate lifetime emission, AFM image analysis provided evidence of disrupted H-bonding and re-agglomeration of monomeric forms which shifted the emission to lower wavelength. The responsiveness of the organogels with UV may suggest the potential use in sensors.

3.7 References

(1) Nelson, T.; Fernandez-Alberti, S.; Roitberg, A. E.; Tretiak, S. Electronic Delocalization, Vibrational Dynamics, and Energy Transfer in Organic Chromophores. *J. Phys. Chem. Lett.* 2017, *8* (13), 3020–3031.

(2) Andrews, D. L. Light Harvesting in Dendrimer Materials: Designer Photophysics and Electrodynamics. *J. Mater. Res.* 2012, *27* (4), 627–638.

(3) Bradshaw, D. S.; Andrews, D. L. Mechanisms of Light Energy Harvesting in Dendrimers and Hyperbranched Polymers. *Polymers* 2011, *3* (4), 2053–2077.

(4) Wong, K.-T.; Bassani, D. M. Energy Transfer in Supramolecular Materials for New Applications in Photonics and Electronics. *NPG Asia Mater* 2014, *6* (7), e116–e116.

(5) Lim, J. M.; Kim, P.; Yoon, M.-C.; Sung, J.; Dehm, V.; Chen, Z.; Würthner, F.; Kim, D. Exciton Delocalization and Dynamics in Helical π-Stacks of Self-Assembled Perylene Bisimides. *Chem. Sci.* 2013, *4* (1), 388–397.

(6) Sethy, R.; Métivier, R.; Brosseau, A.; Kawai, T.; Nakashima, T. Impact of Optical Purity on the Light Harvesting Property in Supramolecular Nanofibers. *J. Phys. Chem. Lett.* 2018, *9* (16), 4516–4521.

(7) Lefler, K. M.; Kim, C. H.; Wu, Y.-L.; Wasielewski, M. R. Self-Assembly of Supramolecular Light-Harvesting Arrays from Symmetric Perylene-3,4-Dicarboximide Trefoils. *J. Phys. Chem. Lett.* 2014, *5* (9), 1608–1615.

(8) Wilbraham, L.; Louis, M.; Alberga, D.; Brosseau, A.; Guillot, R.; Ito, F.; Labat, F.; Métivier, R.; Allain, C.; Ciofini, I. Revealing the Origins of Mechanically Induced Fluorescence Changes in Organic Molecular Crystals. *Adv. Mater.* 2018, *30* (28), 1800817.

(9) Louis, M.; Brosseau, A.; Guillot, R.; Ito, F.; Allain, C.; Métivier, R. Polymorphism, Mechanofluorochromism, and Photophysical Characterization of a Carbonyl Substituted Difluoroboron-β-Diketone Derivative. *J. Phys. Chem. C.* 2017, *121* (29), 15897–15907.

(10) Flores-Ferrándiz, J.; Fiser, B.; Gómez-Bengoa, E.; Chinchilla, R. Solvent-Induced Reversal of Enantioselectivity in the Synthesis of Succinimides by the Addition of Aldehydes to Maleimides Catalysed by Carbamate-Monoprotected 1,2-Diamines: Solvent-Induced Reversal of Enantioselectivity. *Eur. J. Org. Chem.* 2015, *2015* (6), 1218–1225.

(11) Lee, D. W.; Ha, H.; Lee, W. K. Selective Mono ‐ BOC Protection of Diamines. *Synth. Commun.* 2007, *37* (5), 737–742.

(12) Kumar, J.; Nakashima, T.; Kawai, T. Inversion of Supramolecular Chirality in Bichromophoric Perylene Bisimides: Influence of Temperature and Ultrasound. *Langmuir* 2014, *30* (21), 6030–6037.

(13) Ikeda, T.; Masuda, T.; Hirao, T.; Yuasa, J.; Tsumatori, H.; Kawai, T.; Haino, T. Circular Dichroism and Circularly Polarized Luminescence Triggered by Self-Assembly of Tris(Phenylisoxazolyl)Benzenes Possessing a Perylenebisimide Moiety. *Chem. Commun.*, 2012,48, 6025-6027.

(14) Yamaguchi, Y.; Matsubara, Y.; Ochi, T.; Wakamiya, T.; Yoshida, Z. How the π Conjugation Length Affects the Fluorescence Emission Efficiency. *J. Am. Chem. Soc.* 2008, *130* (42), 13867–13869.

(15) Chen, P.-Z.; Niu, L.-Y.; Chen, Y.-Z.; Yang, Q.-Z. Difluoroboron B-Diketonate Dyes: Spectroscopic Properties and Applications. *Coord. Chem. Rev.* 2017, 21.
(16) Lakowicz, J. R.; Masters, B. R. Principles of Fluorescence Spectroscopy, Third Edition. *J. Biomed. Opt.* 2008, *13* (2), 029901.
(17) Lakowicz, J. R.; Cherek, H.; Kuśba, J.; Gryczynski, I.; Johnson, M. L. Review of Fluorescence Anisotropy Decay Analysis by Frequency-Domain Fluorescence Spectroscopy. *J Fluoresc.* 1993, *3* (2), 103–116.

CHAPTER 4

Mechanofluorochromic Properties of Bichromophoric difluoroboron β-Diketonate

Several organic compounds display emission shift upon external stimuli such as force application, grinding and smearing which is known as mechanofluorochromism (MFC) or mechanochromic luminescence (MCL).[1] Highly mechano-responsive and emissive solid state organic materials are gaining interest for device fabrication such as OLEDs,[1,2] security tags[3,4], memory data storage[5] and microsensors.[6–8] Such responsiveness was explained through the molecular arrangements, formation of dimers and modulation of non-covalent intermolecular interactions such as H-bonding and π-π stacking after application of mechanical stress.[9–12] One of the most promising MFC organic compounds are difluoroboron β-diketonates (DFB) which display high quantum yield in both solution and solid state, high molar absorptivity, tunable and reversible MFC.[1–3,5,7,13] The mechanofluorochromic properties of difluoroboron β-diketonates and its reversibility have been intensively studied through variation of side chains[13,14] monitoring the dynamics of molecular arrangements[9,15] and in depth physico-chemical investigation with theoretical approach.[4,12]

Molecular interactions not only direct the mechanofluorochromic properties but also enhance optical properties in solutions and supramolecular assemblies. For example in the study of Kawai group, they synthesized bichromophore perylene-BINAP units which displayed enhanced chiroptical properties caused by intense intramolecular coupling as compared to mono-chromophore[16] and dramatically increase in supramolecular assembly.[17,18] Such molecular design which promotes excitonic coupling within molecular units has broaden the perspectives in future design and fabrication of small organic molecules.

In this chapter, we present the mechanofluorochromic properties of a small series of bichromophore DFB. We compare solid state photophysical properties of mono- and bi-chromophore units of difluoroboron β-diketonates (DFB) using cyclohexane diamine bridge. To better understand the different photophysical properties of the three compounds before and after mechanical stimulus, we analyze their structures obtained with X-Ray diffraction on single crystal, including the surface interaction using Hirschfeld surface analysis and net interaction energy in the crystal system using energy framework. Time-resolved fluorescence spectroscopy measurements allowed us to understand the mechanofluorochromic properties and the behavior of emitting species including their intermolecular interactions in crystal form, smeared, and thermal annealed samples. Finally, the impact of variation in spacers such as amide and ester to the molecular packing of bichromophoric DFB and their mechanofluorochromic behavior was studied.

4.1 Synthesis

The target compounds with pure (*R/S*) enantiomers (referring to *1S,2S* and *1R,2R*) of **cydiamine mono-DFB**, **cydiamine di-DFB** are synthesized using the scheme discussed in Chapters 2 and 3. Racemic cyclohexane diester difluoroboron-β-diketonate (**cydiester di-DFB**) was synthesized by coupling the intermediate **P-2** (see Chapter 6) to cyclohexane diol using NN'-Diisopropylcarbodiimide (*DCC*), and 4-Dimethylaminopyridine (*DMAP*) at 40°C for 12hours then purified with column chromatography using EtOAc:hexane (30:70) as eluent.[19] The cyclohexane β-diketo enol ligand was reacted with $BF_3 \cdot O(C_2H_5)_2$ to form the target compound **cydiester di-DFB.** Scheme 4.1 shows the synthetic route used in for synthesis (the detailed synthesis is discussed in Chapter 6).

Reaction Scheme:

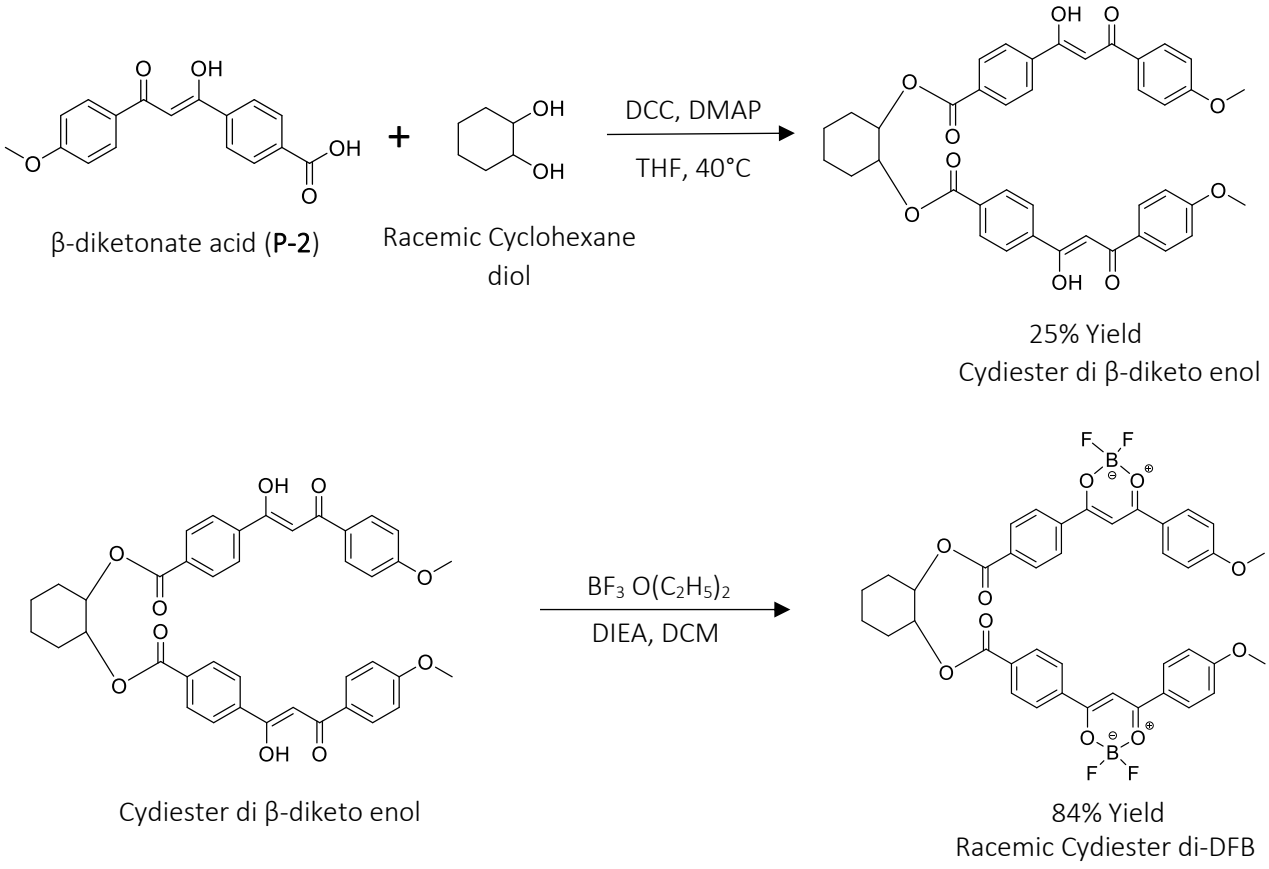

Scheme 4.1: Synthesis of **cydiester di-DFB**.

4.2 Photophysical Properties in Solution and Density functional theory (DFT) Calculations

The optimized geometry of **cydiamine mono-DFB, cydiamine di-DFB** and **cydiester di-DFB** were calculated with density functional theory (DFT) using the functional CAM-B3LYP and basis set 6-31G+(d,p) with IEFPCM (DCM) solvation method (Figure 4.1)

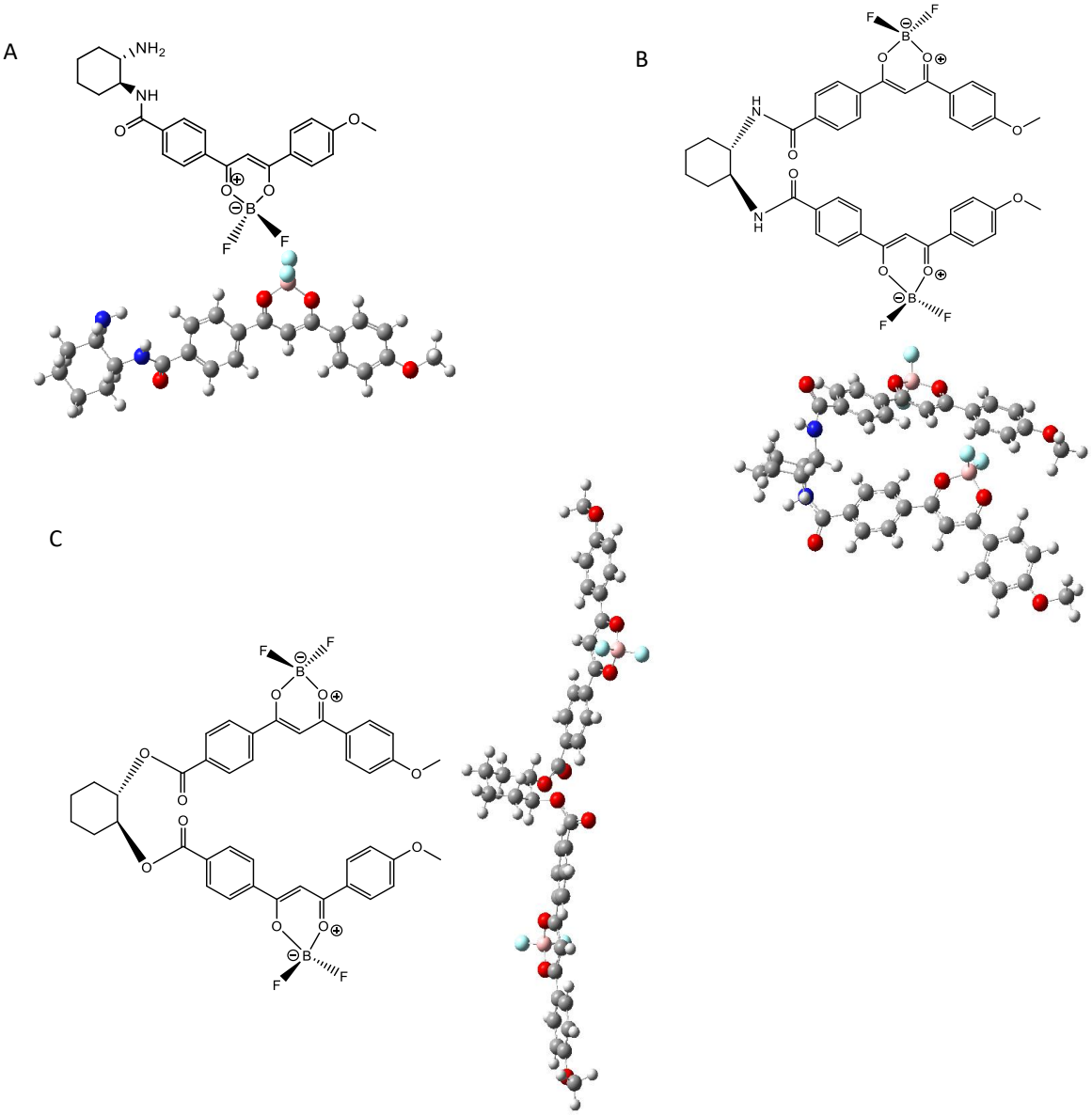

Figure 4.1. Chemical structure (top) and optimized geometry (bottom) of ***(S)*-cydiamine mono-DFB** (a) ***(S)*-cydiamine di-DFB** (b) and ***(R/S)*-cydiester di-DFB** (c) calculated with DFT using the functional CAM-B3LYP and basis set 6-31G+(d,p) with IEFPCM (DCM) solvation method.

The optimized geometry was shown in Figure 4.1a wherein the DFB moiety of **cydiamine mono-DFB** was slightly twisted with dihedral angles of phenyl rings 14.8° and -6.13° with respect with the diketonate plane. Both NH_2 and DFB moiety are in equatorial

position (see dihedral angles in Chapter 6). Optimized geometry of **cydiamine di-DFB** showed a similar arrangement but both DFB moieties are in axial position. The optimized geometry showed two unequal DFB moieties which are situated parallel to the cyclohexane ring and the corresponding dihedral angles are previously discussed in Chapter 2 (see Figure 4.1b). On the other hand, the optimized geometry of **cydiester di-DFB** showed that the two DFB units were situated at opposite direction and at equatorial position of cyclohexane ring (see Figure 4.1c). Corresponding dihedral angles for each DFB moiety with respect to β-diketonate plane are shown in Figure 4.2. The variation of spacer from amide to ester drastically changed the orientation of DFB moieties in **cydiamine di-DFB** and **cydiester di-DFB.**

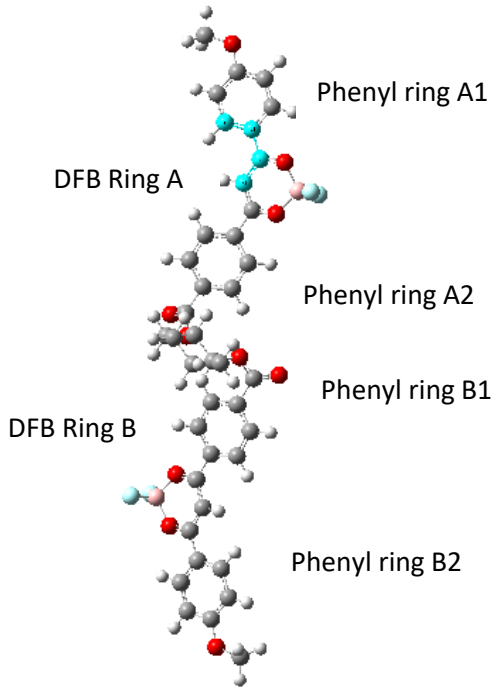

Dihedral angles:

Between ring A1 and DFB ring A 7.6
Between ring A2 and DFB ring A -17.5°

Between ring B1 and DFB ring B 14.9°
Between ring B2 and DFB ring B -7.9°

Figure 4.2. Optimized geometry of **cydiester di-DFB** with corresponding dihedral angles of DFB moieties.

The molecular orbitals involved in electronic transitions for **cydiamine mono-DFB, cydiamine di-DFB** and **cydiester di-DFB** were determined using time-dependent DFT (TD-DFT) calculations. The same functional CAM-B3LYP and basis set 6-31+ G(d,p) with IEFPCM (DCM) solvation method were used in this calculation. Electronic transitions from lowest energy calculated for the three compounds involve multiple molecular orbitals (see Tables 6.4 to 6.6 in Chapter 6), thus natural transition orbitals (NTO) calculations were performed for the lowest energy transitions. The NTO for **cydiamine di-DFB** was already discussed in Chapter 2. The NTO for **cydiamine mono-DFB and cydiester di-DFB** was shown in Figure 4.3. NTO calculations revealed that transitions of **cydiamine mono-**

DFB, cydiamine di-DFB and **cydiester di-DFB** clearly exhibits π-π* character localized in difluoro β-diketonate units with weak electron shift from methoxy group.

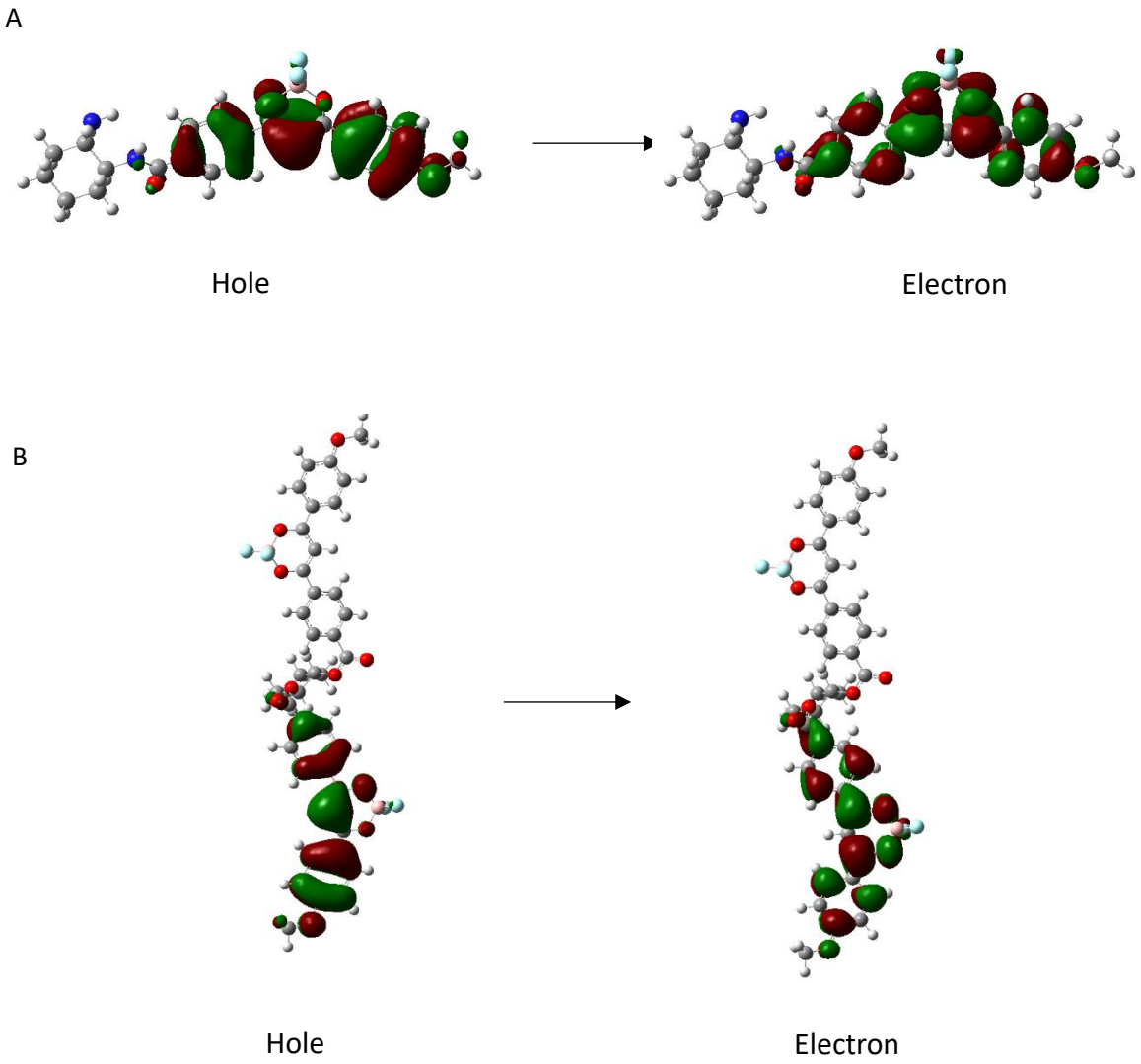

Figure 4.3. NTO of **cydiamine mono-DFB** (a) and **cydiester di-DFB** (b) from lowest energy transition calculated using the functional CAM-B3LYP and basis set 6-31G+(d,p) with IEFPCM (DCM) solvation methods (see chapter 6 for list of the transitions).

Steady state fluorescence and absorbance of the compounds were measured in DCM, and it was shown that **cydiamine mono-DFB**, **cydiamine di-DFB** and **cydiester di-DFB** display similar absorption and emission wavelengths (see Figure 4.4).

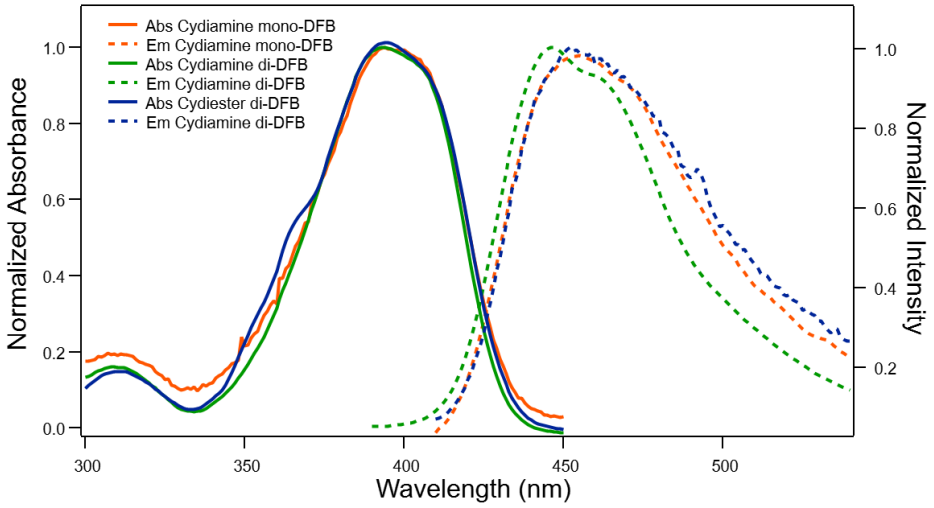

Figure 4.4. Absorbance and steady-state fluorescence spectra of **cydiamine mono-DFB**, **cydiamine di-DFB** and **cydiester di-DFB** (excitation at 390nm). Refer to chapter 6 for table of TDDFT vs experimental values.

Time-resolved fluorescence spectroscopy measurements were conducted to determine the decay time of emissive species in solutions. The decays were fitted with global analysis and all the compounds under observation displayed bi-exponential decays showed in Table 4.1. Higher concentrations of **cydiamine mono-DFB** in DCM formed aggregation, hence acetonitrile was used in decay measurements because of high solubility in acetonitrile.

Table 4.1. Decay time (τ_i), pre-exponential factors (a_i) and fraction of intensity (f_i) of **cydiamine mono-DFB** solution (in acetonitrile), **cydiamine di-DFB solution** (in DCM) and **cydiester di-DFB** (in DCM).

	τ_1 (a_1, f_1)	τ_2 (a_2, f_2)
Cydiamine mono-DFB	0.6ns (0.92, 0.87)	1ns (0.08, 0.13)
Cydiamine di-DFB	2ns (0.99, 0.96)	12ns (0.01, 0.03)
Cydiester di-DFB	1.8ns (0.78, 0.68)	3ns (0.22, 0.32)

*Cydiamine mono-DFB exc. = 390nm, em. =480nm, X^2 = 1.05
Cydiamine di-DFB exc. = 390nm, em. =463nm; X^2 = 1.09
Cydiester di-DFB exc. = 390nm, em. =480nm; X^2 = 1.13

4.3 Single Crystal Structures and Hirshfeld Surface Analysis

Needle-like crystals of **cydiamine mono-DFB** were formed in a mixture of ethyl acetate and hexane (30:70) at room temperature. These crystals emit yellow green fluorescence under UV excitation (365nm). Single crystal structure revealed that there are two distinct arrangements of **cydiamine mono-DFB** units that mainly differ in the twisted DFB around cyclohexane moiety. The single crystal structure is comparable to the calculated optimized geometry where both DFB and NH_2 are in equatorial position, but the DFB moiety is slightly twisted due to presence of intermolecular interactions. These units are alternately stacked with overlapping diketonate rings and distance of 3.8 Å which makes up the molecular column (see Figure 4.5a).

To gain insights on the intermolecular interactions in the crystal system, Hirshfeld surface was calculated. Hirshfeld surface analysis is a theoretical calculation based on F.L. Hirshfeld's stockholder partitioning which calculates the electron density of each atom to define the shape and occupied space in a molecular fragment as well as its interaction with neighboring atoms.[20,21] *Crystal Explorer21* software was used for calculations which provides visual illustration of intermolecular interactions and two-dimensional fingerprint plots of Hirshfeld surfaces.

Hirshfeld surface analysis and the finger print plots provides more extensive visual information on the interaction on molecular surfaces in a crystal.[20,22] Figure 4.5b shows that there is a strong interaction between the primary amine to the C=O of neighboring **cydiamine mono-DFB** and a solvent molecule. This was indicated by the red surface through H-bonds which made up the stacked molecular column. Moreover, a strong amide to BF_2 surface interactions also exists on the other side of **cydiamine mono-DFB** inducing the inter-columnar interactions. Fingerprint plots of Hirshfeld surface showed a C···C surface interactions consists of 6% (d_i-d_e at 1.8 Å) pertaining to the typical π-π stacking[11] while other atomic interactions such as C···H (13%), F···H (14%), and H···H (48%) comprised most of the molecular surface interaction in the **cydiamine mono-DFB** crystal. The fingerprint plots of all the atom-atom interactions were summarized in supporting details in Chapter 6. Crystal packing structures viewed along a-axis and its top view showing overlap of the diketonate rings were shown in Figure 4.6a. View along a-axis of extended structures of crystals revealed a columnar stacking corresponding to crystal packing motif **γ** which is characterized with angled face-to-face stacking (see Figure 4.6b).[23,24]

A

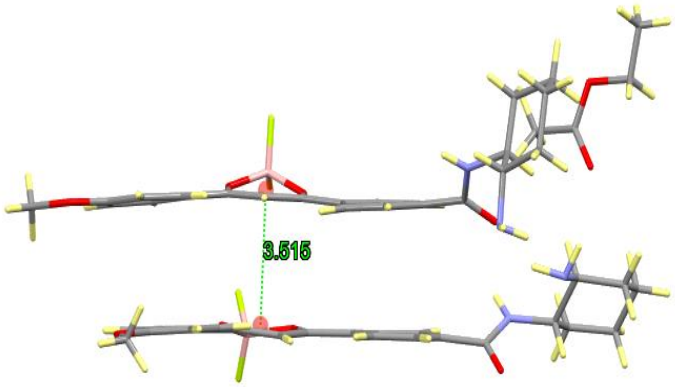

B

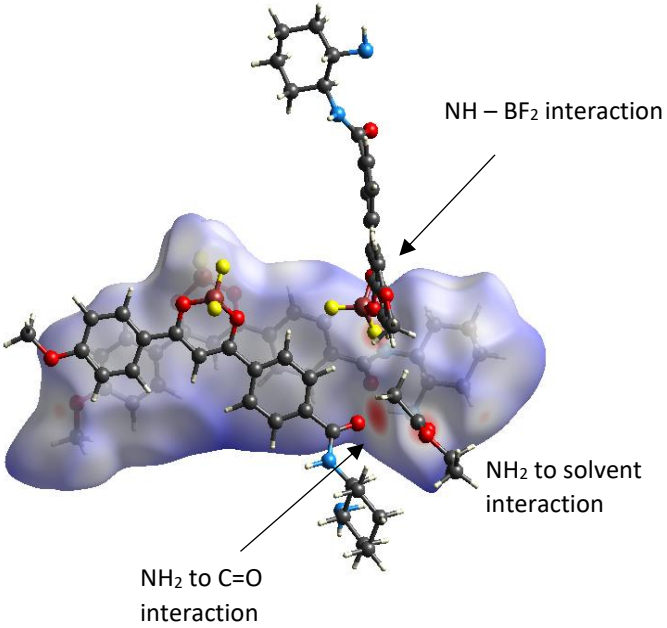

Figure 4.5. Crystal structure of cydiamine mono-DFB showing distinct arrangement of two units twisted in cyclohexane diamine moiety (a) and Hirshfeld surface analysis showing surface interactions to neighboring cydiamine mono-DFB units (b).

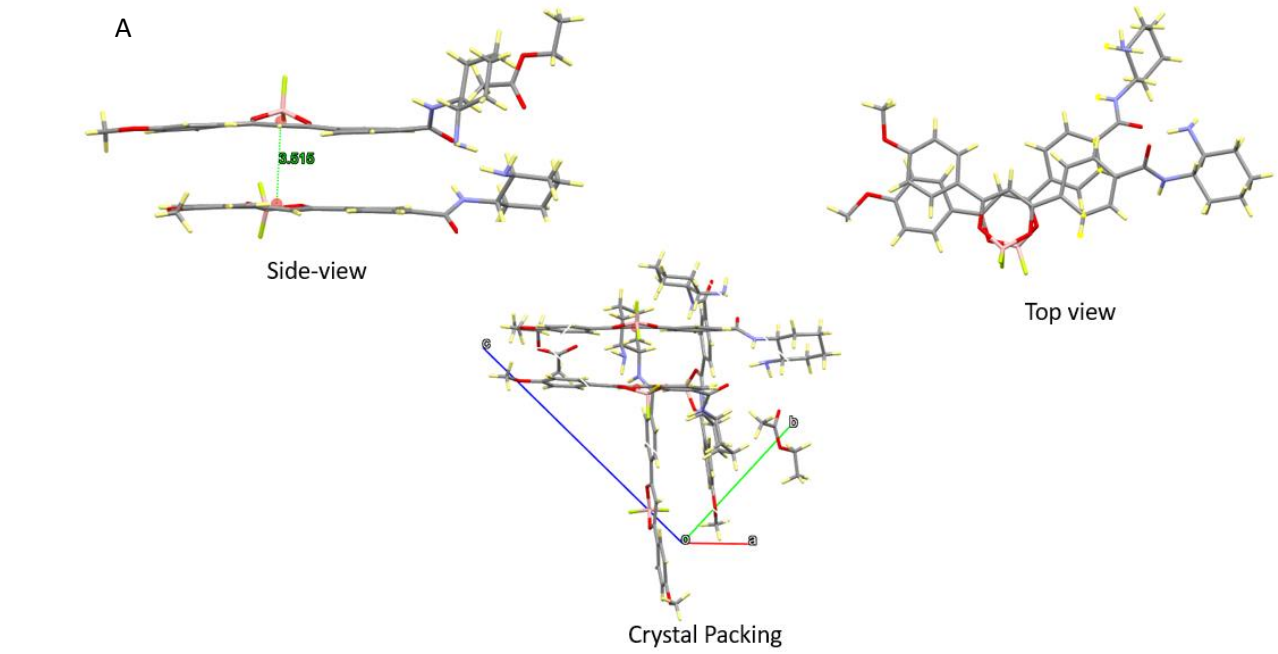

B

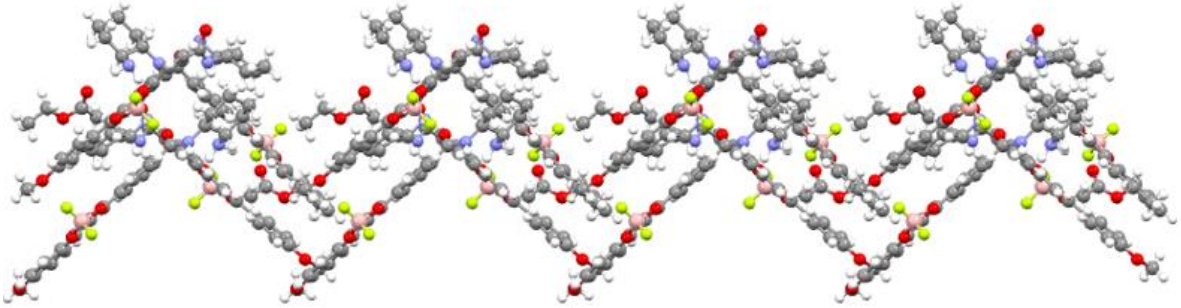

Figure 4.6. Crystal packing of **cydiamine mono-DFB** including top and side view (a) and the extended view along a-axis showing crystal packing motif γ (b).

Bichromophore units **cydiamine di-DFB** formed blue green emissive crystals by slow solvent evaporation using DCM at room temperature. Single crystal structures of **cydiamine di-DFB** revealed a uniform co-facial stacking with centroid distance of ca. 5.0 Å as shown in Figure 4.7. Hirshfeld surface analysis showed that C=O and amide group formed the stacked **cydiamine di-DFB** units through H-bonds. These are the main interactions responsible for the formation of columnar stacked **cydiamine di-DFB** units. On the other hand, BF_2···CH from diketonate of neighboring unit induced the inter-

columnar interactions in **cydiamine di-DFB** crystal (see Figure 4.8a). Extending the crystal structures revealed the herringbone crystal packing motif characterized by edge-to-face packing which tends to reduce steric hindrances between DFB moieties as illustrated in Figure 4.8b. Fingerprint plots showed that C···C surface interactions in **cydiamine di-DFB** crystal consists of 1.1% (d_i-d_e at 1.8 Å) which is lower as compared with **cydiamine mono-DFB.** Other surface interactions involving C···H (19.5%), H···F (17.2%), H···H (36.8%) and O···H (14.2%) comprised most interactions within the surface of **cydiamine di-DFB** (see Chapter 6).

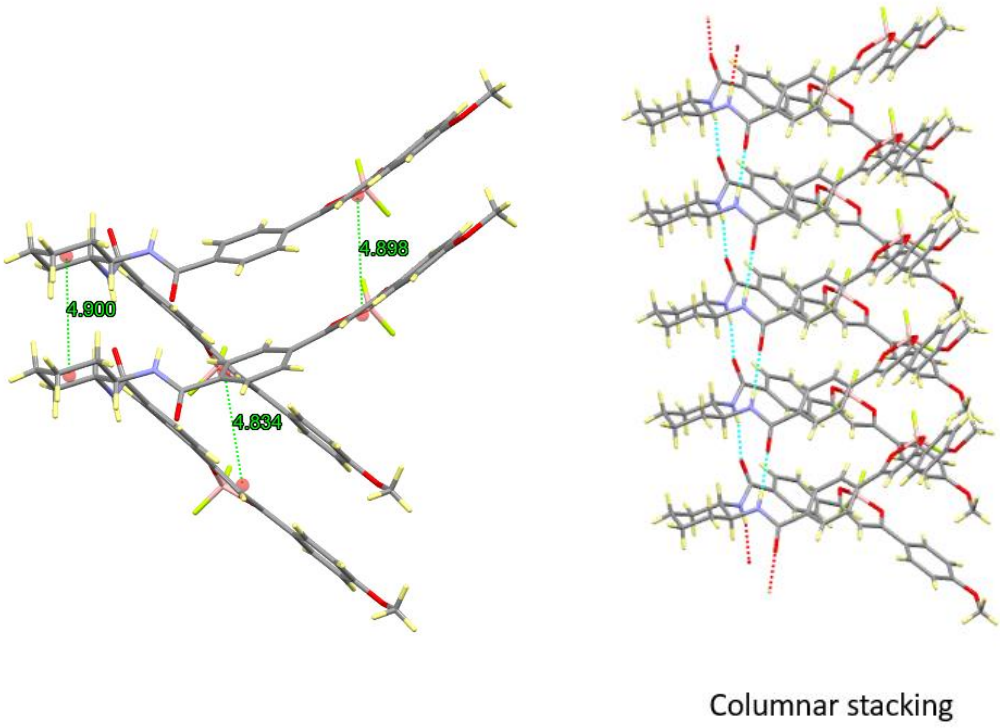

Figure 4.7. Crystal structure of **cydiamine di-DFB** showing inter-layer distance of ca. 4.9Å and columnar stacking showing amide to carbonyl H-bonding.

A

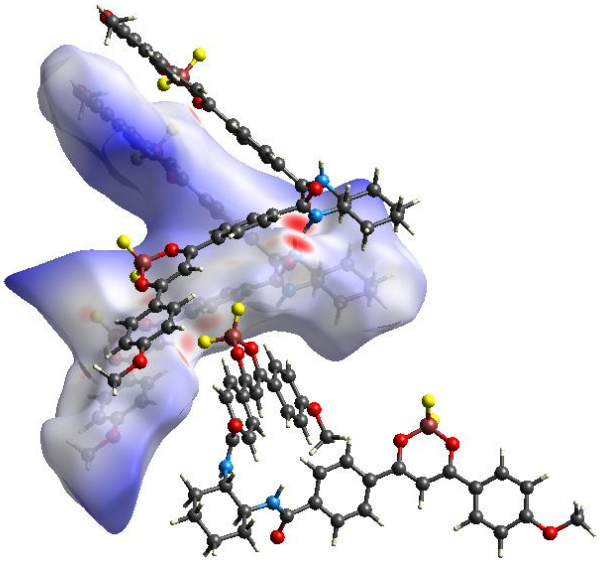

B

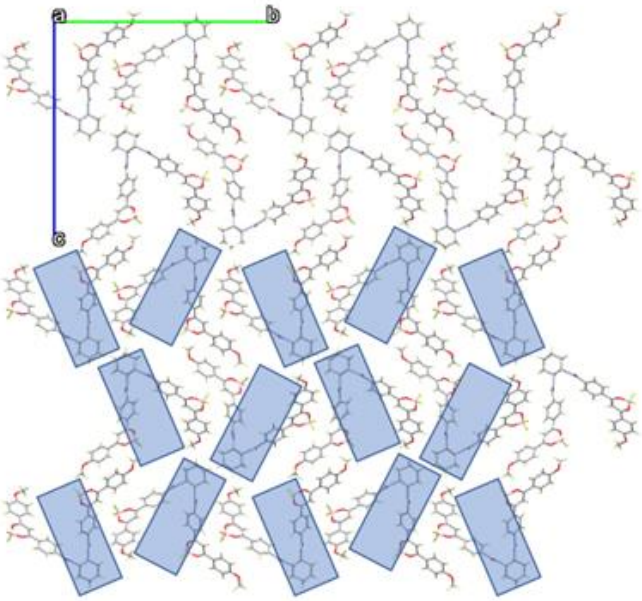

View along a-axis crystal packing motif: Herringbone characterized by edge-to-face packing.

Figure 4.8. Hirshfeld surface analysis (a) and extended structures showing herringbone crystal packing motif (b).

Another bichromophoric compound bearing ester group as spacer instead of amide (**cydiester di-DFB**) formed blue emissive crystals in mixture of chloroform and hexane (50:50) at room temperature. Single crystal analysis showed that the **cydiester di-DFB** crystals units were stacked in a brick-layer arrangement (see Figure 4.9a). Comparing the interlayer stacking in **cydiamine di-DFB** which was driven by close surface interaction of amide to C=O, **cydiester di-DFB** was driven by the C=O group interacting with BF_2 group of the adjacent unit forming a row of **cydiester di-DFB** with interlayer distance of ca. 5.7 Å (see Figure 4.9b).

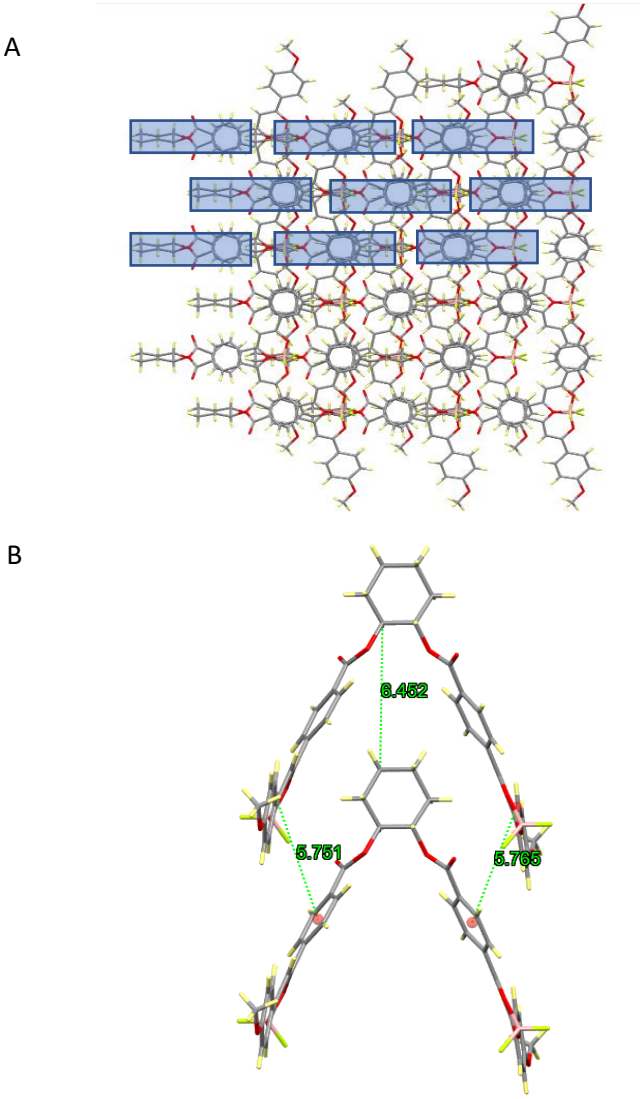

Figure 4.9. Extended crystal packing of **cydiester di-DFB** view along b-axis showing brick-layered arrangement (a) layers of **cydiester di-DFB** as viewed from top showing interlayer distance of 5.7 Å (b).

This close surface interaction was shown in Hirshfeld surface analysis and the π-π stacking interlayer distance was measured with ca. 5.7 Å from the centroids of the diketonate rings (Figure 4.10b). The second layer was stacked in a brick-layer arrangement through interaction of BF_2 (top unit) to the aromatic -CH (bottom unit) and C···C interactions while the other diketonate moiety shows overlapping aromatic groups shown in Figure 4.10b. This overlapping DFB unit forms π-π stacking (ca. 4.1 Å) of the top and bottom layer of **cydiester di-DFB** as revealed in the crystal structure. The other DFB moiety of inter-layer stacked did not show overlapping and π-π aromatic interaction, but rather BF_2··· CH was observed. The brick layers of stacked **cydiester di-DFB** have made up the molecular column of crystals.

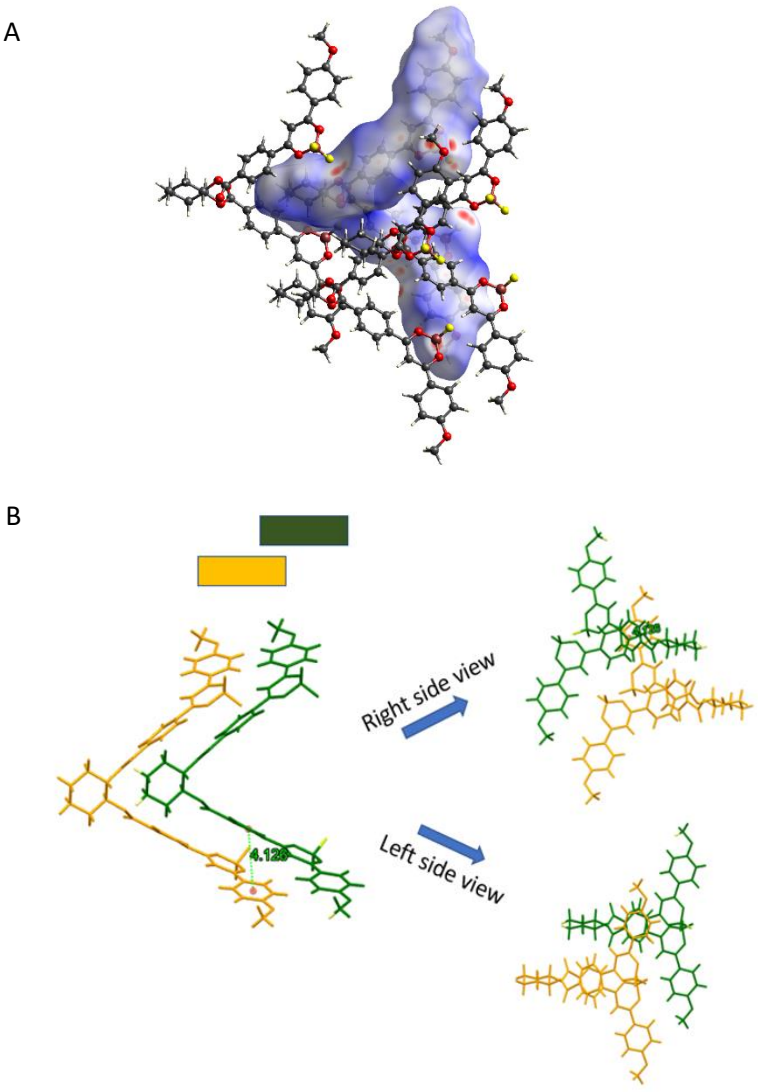

Figure 4.10. Hirshfeld surface analysis showing surface interactions to neighbor **cydiester di-DFB** units (a) and top to bottom interactions **cydiester di-DFB** as viewed from right (non-overlapping DFB moiety) and left (overlapping DFB moiety) (b).

The observed crystals structure in single XRD analysis totally differs from the optimized geometry in monomeric state mainly due to the intermolecular interactions in crystal packing. Fingerprint plots showed that C···C surface interactions in **cydiester di-DFB** crystal consists of 7.1% (d_i-d_e at 1.8-2.4 Å) of the atom-atom surface interactions attributed to π-π interactions as shown in finger plot Hirshfeld surface analysis. Other atom-atom surface interactions which dominates the crystals are C···H (15%), C···F (3.6%), F···H (17.5%), H···H (35.6%), and H···O (17.9%) (see Chapter 6). It is noticeable that among the Hirshfeld surfaces of three compounds, **cydiester di-DFB** crystals display with most red surfaces indicating close contacts with neighboring bichromophore unit as well as the highest C···C interaction (7.1%) corresponding the π-π stacking. Summary of the atom-atom interactions based on fingerprint plots for **cydiamine mono-DFB, cydiamine di-DFB** and **cydiester di-DFB** were summarized in Figure 4.11.

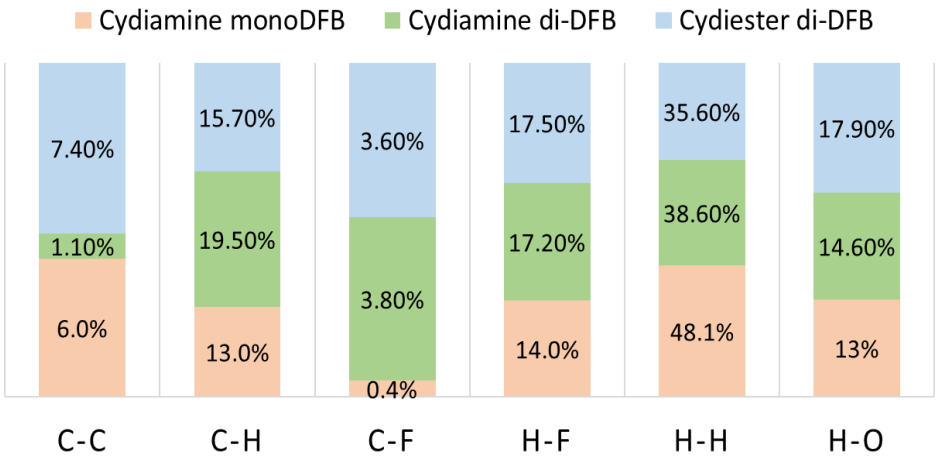

Figure 4.11. Summary of the atom-atom interaction in fingerprint plot of Hirshfeld surface analysis of cydiamine mono-DFB (orange), cydiamine di-DFB (green) and cydiester di-DFB (blue).

4.4 Mechanofluorochromic Property

The emissions of crystals of **cydiamine mono-DFB**, **cydiamine di-DFB** and **cydiester di-DFB** are shown in Figure 4.12a using excitation wavelength of 350nm. These crystals are grinded using mortar and pestle and the powdered samples are collected on a quartz plate then measured for emission (see Figure 4.12b). The emissions of all the compounds shifted to higher wavelength after smearing and are also evident in the images of crystals and smeared samples shown in Figure 4.13.

A

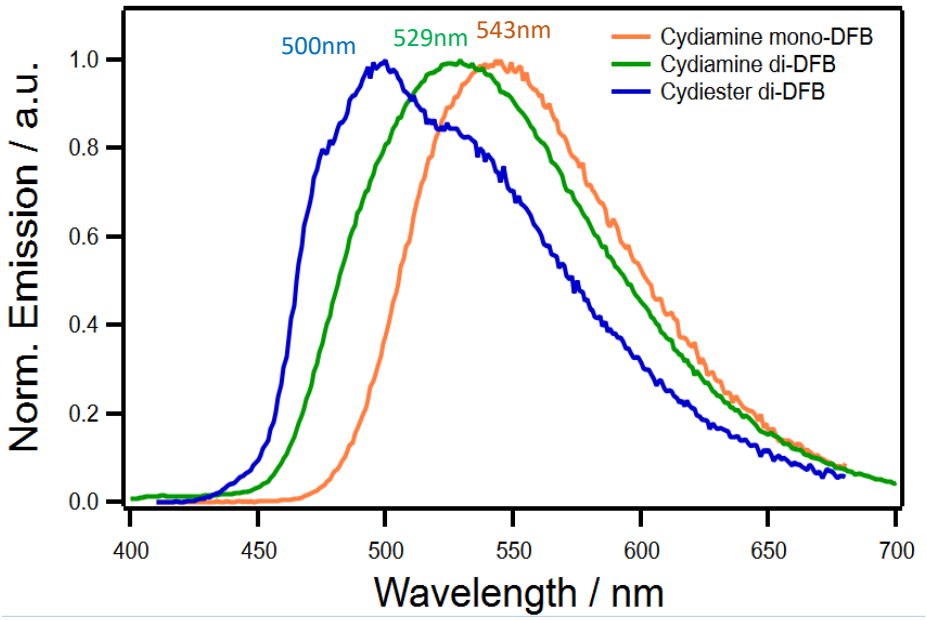

B

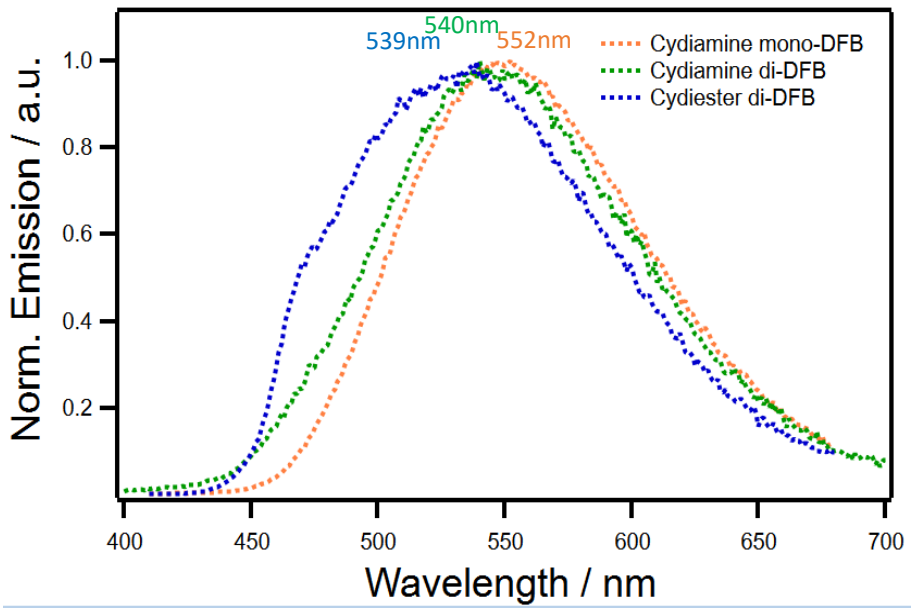

Figure 4.12. Fluorescence emissions of **cydiamine mono-DFB**, **cydiamine di-DFB** and **cydiester di-DFB** crystals (a) and smeared (b) (excitation at 350nm).

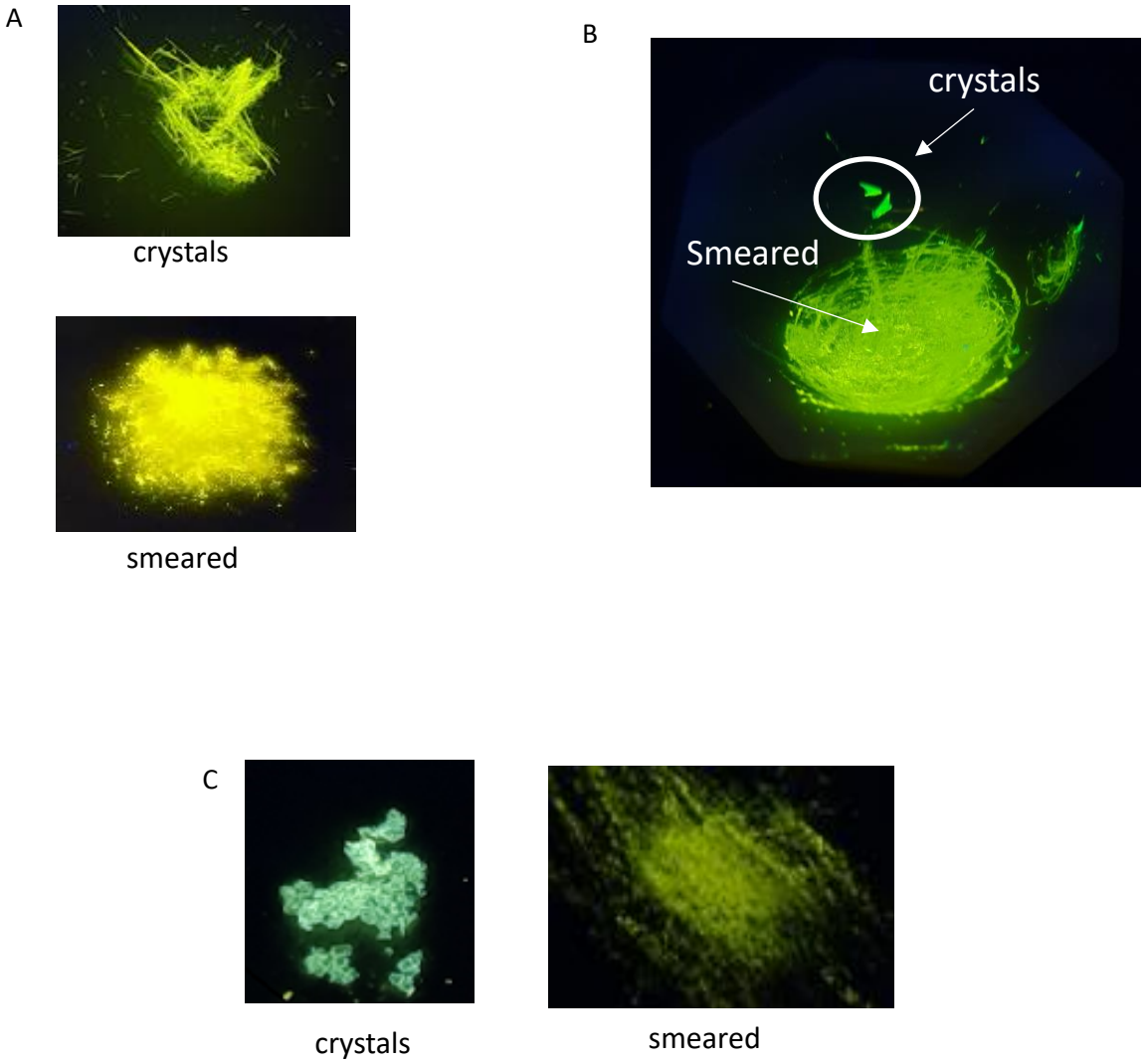

Figure 4.13. Crystals and smeared samples of cydiamine mono-DFB (a), cydiamine di-DFB (b) and cydiester di-DFB (c).

4.4.1 Mechanofluorochromism of Cydiamine mono-DFB

The needle-like crystals of cydiamine mono-DFB display a maximum fluorescence emission at λ_{em} = 543nm. The comparison of emissions of the three compounds under study revealed that cydiamine mono-DFB crystals emission is the most red-shifted (Figure 4.12a). After smearing using mortar and pestle, it further shifts to higher wavelength λ_{em} at 552nm as shown in Figure 4.12b. To understand the mechanofluorochromic behavior as well as the molecular interactions in crystal, time-resolved spectroscopy measurements at different wavelengths were conducted to the samples. The decays of emitting species in crystalline, smeared, and thermal annealed samples were measured

at different emission wavelengths using excitation wavelength of 350nm. The results were fitted using global analysis and the decay times (τ_i), pre-exponential factors (a_i) and fraction of intensites (f_i) obtained after fitting are summarized in Chapter 6. The plots of fraction of intensities of crystals, smeared, thermal annealed and pristine powders (as collected powder after synthesis) are shown in Figure 4.14. The tables decays, fraction of intensity and pre-exponentials factors are listed in supporting documents (Chapter 6).

Cydiamine mono-DFB crystals exhibit exponential decays with decay time τ_1= 15.6ns, τ_2= 7.5ns, τ_3= 1.5ns, and τ_4= 0.5ns at different wavelengths (see Figure. 4.14a). Shorter decay times (<2ns) are attributed to the residual emission from monomeric species as these decay times are similar to the decays observed in monomeric form in solution (see Table 4.1) while the longer decays at τ_1= 15.6ns and τ_2= 7.5ns may be attributed to preformed excimers within the crystals. This also agree with the crystal structure showing a π-π interactions and close distance stacking of cydiamine mono-DFB units ca. 3.5 Å which favors intermolecular interactions thus red-shifted emission (λ_{em} = 543nm) was observed as shown in Figure 4.12a. After smearing the cydiamine mono-DFB crystals, a new emissive species with longer decay time τ_1= 22ns was observed (see Figure 4.14b). Smearing induced a shift in longer wavelength (λ_{em} = 552nm) caused by the destruction of intra-columnar molecular stacking leading to a closer π-π interaction as characterized by broader and bathochromic shift in emission.[3,10,25] The emerged emitting species with longer decays time in smeared samples may indicate the formation of new dimers or aggregates formed through intermolecular interaction induced after smearing.[4,11] This was evident with the time-resolved spectroscopy showing a higher fraction of intensity from longest decays τ_1= 22ns (f_1=0.41) and τ_2= 8.6ns (f_2=0.48) measured at 550nm shown in Figure 4.14b.

Thermal annealing did not show any significant changes in emission wavelength at 80°C for 3hours, however time-resolved fluorescence spectroscopy measured at 550nm showed that the contribution from longer emissive species τ_1= 22ns (f_1=0.58) gradually increased indicating that thermal annealing favors the formation of closed packed arrangement of cydiamine mono-DFB units (see Figure 4.14c). Powder XRD also showed that after smearing, few XRD peaks are still visible suggesting that there are residual crystals even after applying of mechanical stress (see Figure 4.15).

A

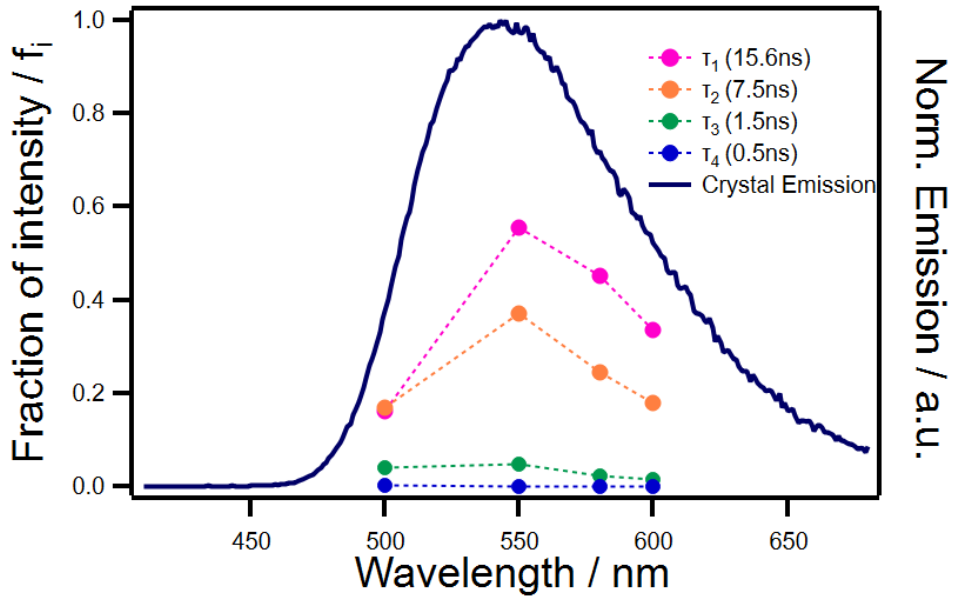
Fraction of intensity / f_i
1.0
0.8
0.6
0.4
0.2
0.0
450
500
550
600
650
Wavelength / nm
τ_1 (15.6ns)
τ_2 (7.5ns)
τ_3 (1.5ns)
τ_4 (0.5ns)
Crystal Emission
Norm. Emission / a.u.

B

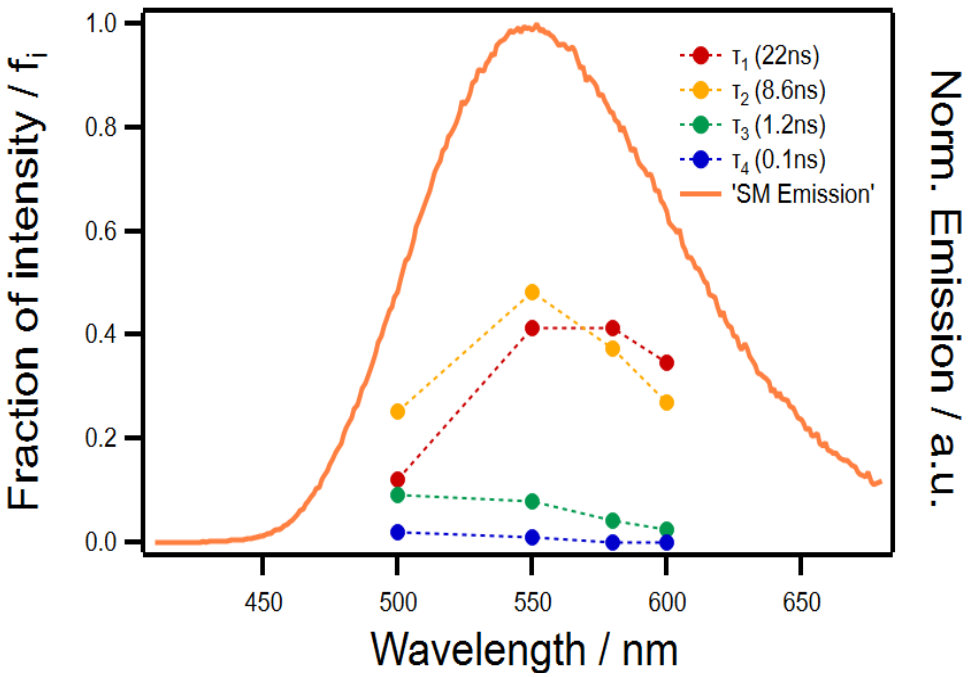
Fraction of intensity / f_i
1.0
0.8
0.6
0.4
0.2
0.0
450
500
550
600
650
Wavelength / nm
τ_1 (22ns)
τ_2 (8.6ns)
τ_3 (1.2ns)
τ_4 (0.1ns)
'SM Emission'
Norm. Emission / a.u.

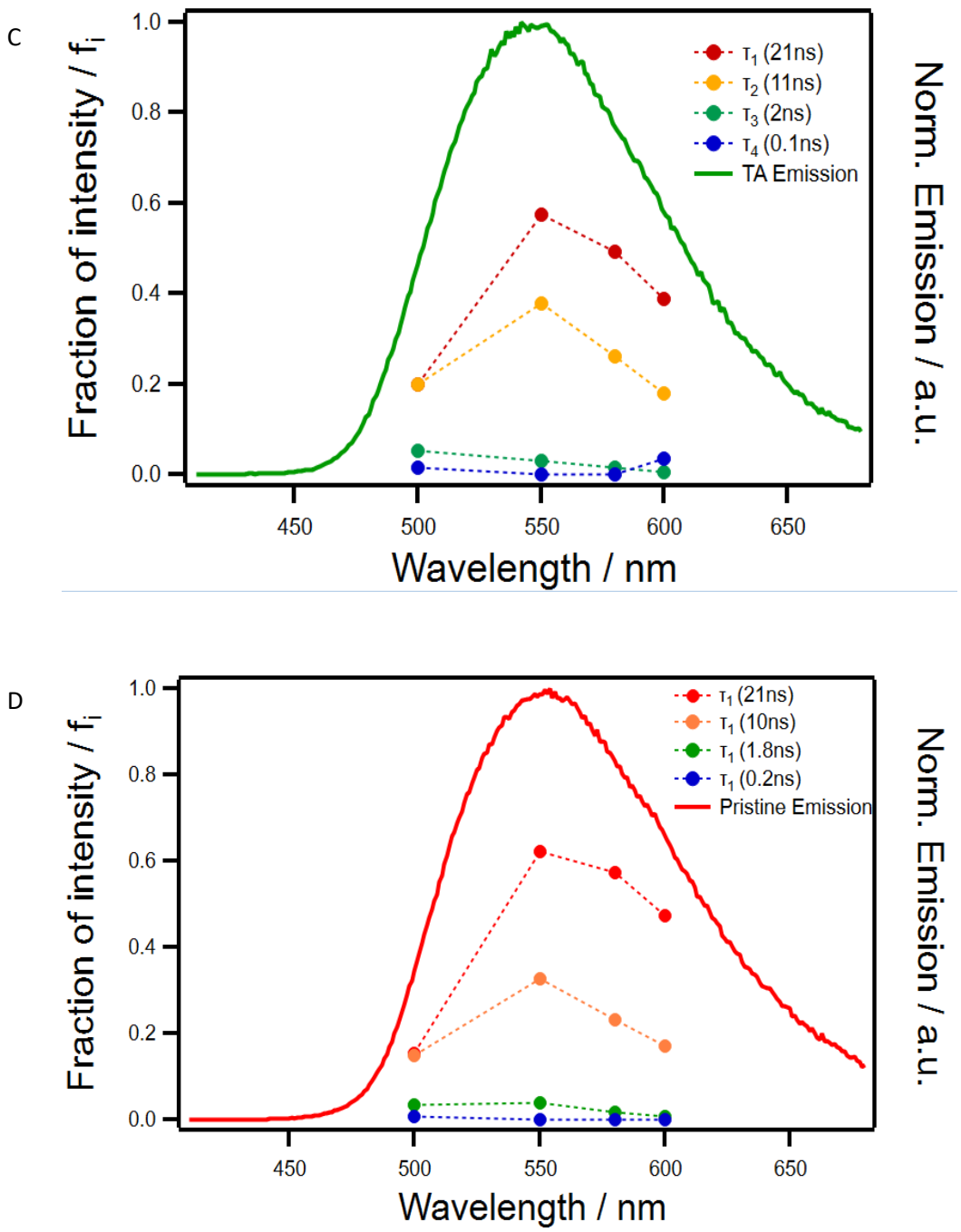

Figure 4.14. Plots of fraction of intensity obtained from time-resolved spectroscopy measurements of **cydiamine mono-DFB** crystals (a), smeared (b), thermal annealed (c), and pristine powders (d) measured at difference wavelengths (500nm to 600nm) using excitation at 350nm.

After thermal annealing at 80°C for 2 hours, the XRD patterns remains the same as with smeared samples shown (Figure 4.15). Single visible peak at 2θ = 5.2° and several broad peaks beyond 2θ= 5.5° suggest low crystallinity even after thermal annealing.[26]

Increasing the annealing temperature higher than 80°C decreased the fluorescence intensity of smeared powder showing thermal instability and degradation at higher temperature. The decays profile of thermal annealed and as-collected powder after synthesis (pristine powders) shown in Figures 4.14c and 4.14d is almost identical which implies that thermal annealing induced molecular packing similar with pristine powder. This may indicate a meta-stable state since the compounds did not display any further changes in emission even after prolonged heating.

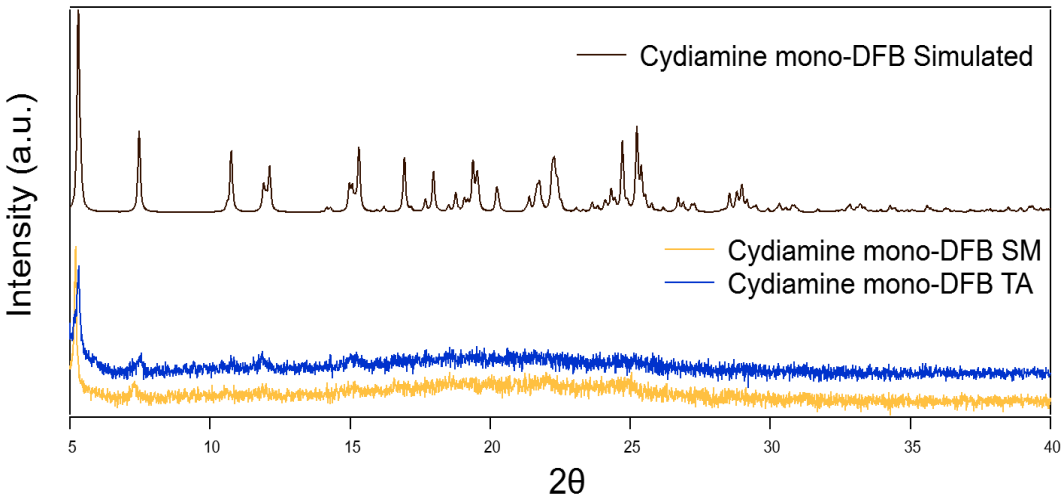

Figure 4.15. Simulated powder XRD of crystal from CIF file, powder XRD of smeared, thermal annealed samples of **cydiamine mono-DFB** annealed at 80°C.

4.4.2 Mechanofluorochromism of Cydiamine di-DFB

Blue green emissive crystals of **cydiamine di-DFB** formed by slow solvent evaporation using DCM displayed a maximum emission (λ_{em}) at 529nm (see Figure 4.11b). Surprisingly, the emission of crystals is blue shifted as compared to the emission observed in **cydiamine mono-DFB** crystals. Since **cydiamine di-DFB** was covalently bridge by cyclohexane moiety, it was expected to form emissive species with longer emission wavelength as compared to mono substituted DFB due to intra-molecular coupling as what was previously observed in bichromophores.[16,27,28] The crystals were smeared with mortar and pestle and the fully grinded powder were deposited on a quartz plate. Upon smearing, yellow green emissive powder with λ_{em}=540nm was observed (see Figure 4.11b). Time-resolved fluorescence spectroscopy measurements were conducted to follow the behavior of emitting species in crystal and smeared form. **Cydiamine di-DFB** crystals display exponential decays with decay times τ_1= 23ns, τ_2= 7ns, τ_3= 2ns and τ_3= 0.2ns (see Figure 4.16a). Similar with **cydiamine mono-DFB** crystals, the shorter lifetimes

<2ns were attributed to the monomeric components while intermediate (τ_2= 7ns) and longer lifetime (τ_1= 23ns) are due to formation of dimers. Pre-exponential factor from short-lived (2ns) and intermediate components (7ns) have the largest values at 550nm while highest fraction of intensity was observed from intermediate component τ_2= 7ns (f_2=0.57). Moreover, emissive species with longer decay (τ_1= 23ns) was initially observed in crystals but with low fraction of intensity (<0.2) as shown in Figure 4.16a.

A

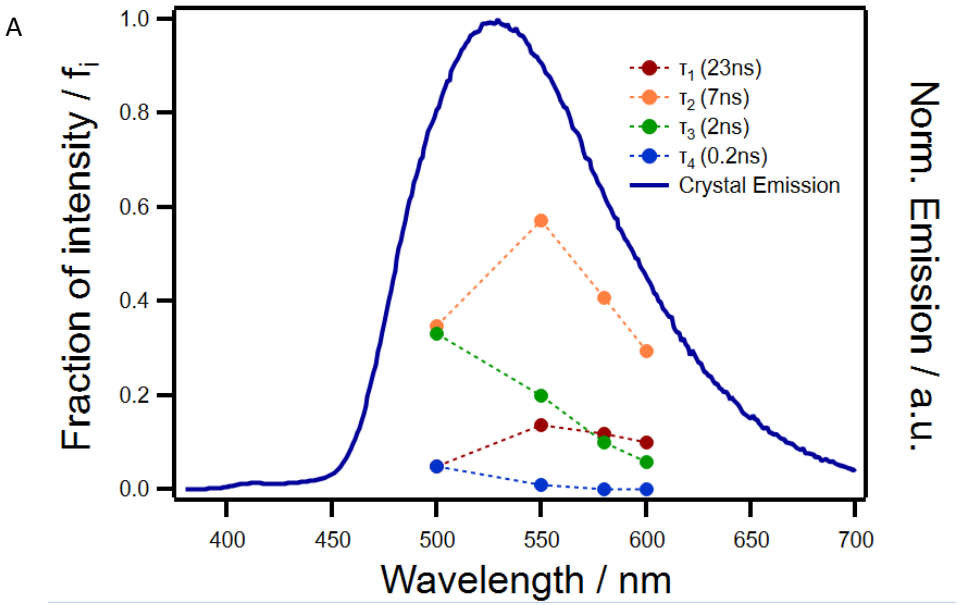

B

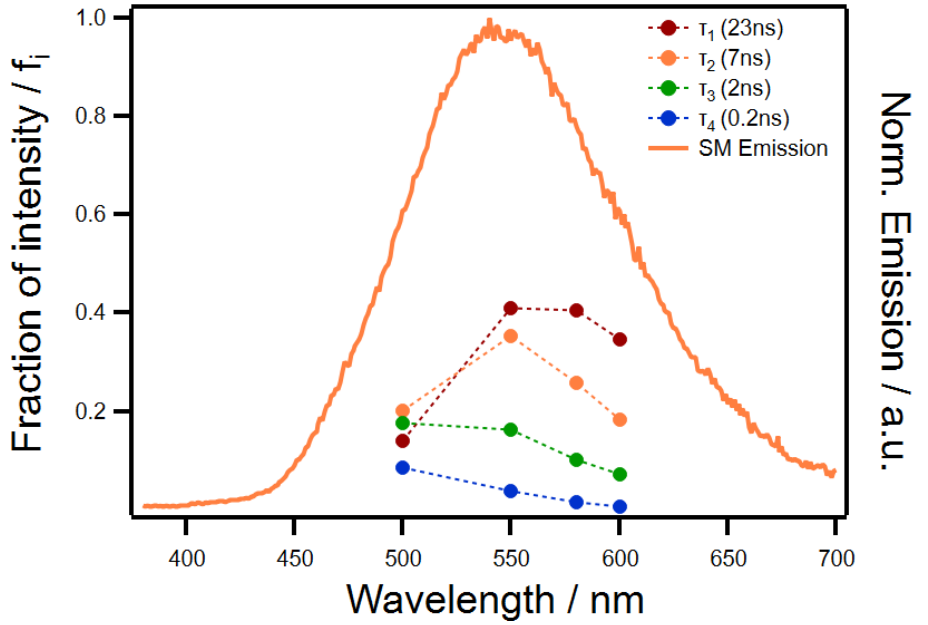

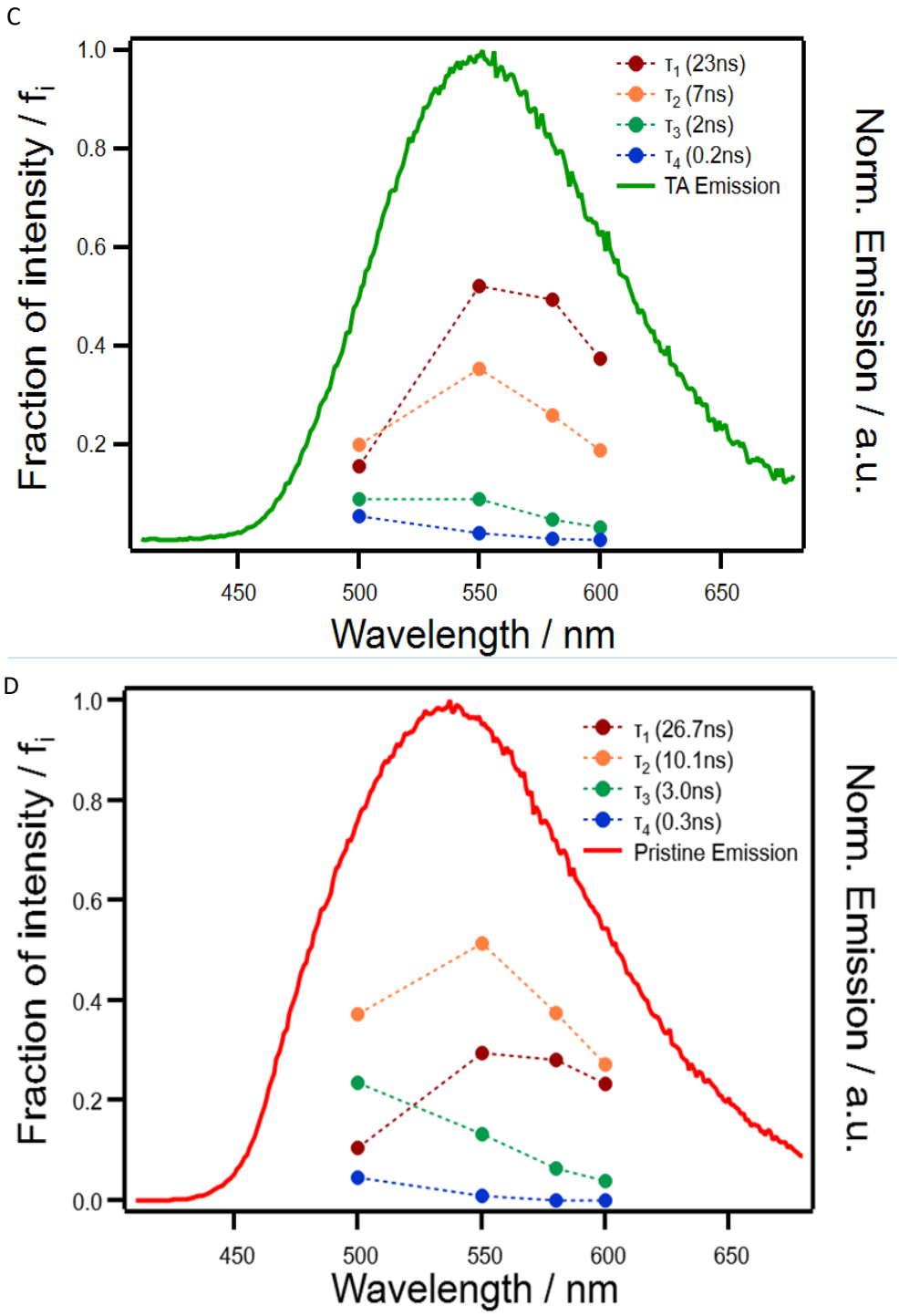

Figure 4.16. Plots of fraction of intensity obtained from time-resolved spectroscopy measurements of **cydiamine di-DFB** crystals (a), smeared (b), thermal annealed (c), and pristine powders (d) measured at difference wavelengths (500nm to 600nm) using excitation at 350nm.

Single crystal structure of **cydiamine di-DFB** has a good overlap between each bichromophoric units, but the amide group (NH···C=O) provides the shortest surface

interactions while minimal π-π interaction resulted to columnar stacking distance of ca. 5.0 Å as previously discussed in crystal structures (see Figure 4.7). The observed stacking distance is longer than the distance in **cydiamine mono-DFB** units (ca. 3.8 Å) which have resulted in low intermolecular interactions. This is parallel with the time-resolved fluorescence spectroscopy measurements displaying low fraction of intensity from long decay components (23ns) and blue shifted emission of **cydiamine di-DFB** crystals (λ_{em}=529nm) as compared with **cydiamine mono-DFB** crystals (λ_{em}=543nm). It is also noticeable that despite the larger interlayer distance and low C···C interactions, the **cydiamine di-DFB** crystal emits at longer emission wavelength (λ_{em}=529nm) as compared to its monomeric form in solution (λ_{em}=453nm). The red-shift emission may indicate that long-range coupling among identical DFB chromophores in **cydiamine di-DFB** still occur with its neighboring DFB within the molecular column.[29,30] This is evident by prominent intermediate decay time (7ns) which is longer than the decays for monomeric form with decay time 2ns.

Smeared crystals exhibited bathochromic shift and broadened emission peaks caused by the destructed columnar packing. The bathochromic shift in smeared samples may be caused by favored formation of long-lived dimers or aggregates.[4,11,25] This was evident by the prominent fraction of intensity of long emissive components τ_1= 23ns (f_1=0.41) measured at 550nm in smeared samples while the intermediate decays (τ_2= 7ns) remarkably decreased (Figure 4.16b).

On the other hand, Figure 4.16c shows that thermal annealing at 80°C for 2hours further increase the fraction of intensity of long emissive components (τ_1= 23ns) suggesting that annealing induces the close distance stacking of **cydiamine di-DFB**, however XRD patterns did not significantly change showing low crystallinity (see Figure 4.17). The maximum emission peak of **cydiamine di-DFB** remains constant after thermal annealing at 80°C and even at higher annealing temperature (130°C) (see Figure 4.18). Smeared and thermal annealed samples shown in Figures 4.16b and 4.16c have similar decay profiles indicating that the compound reached a meta-stable state even before annealing.

The decay profiles of smeared and thermal annealed are also similar with pristine powders measured at 550nm-600nm, however higher fraction of intensity in intermediate decays τ_2= 11ns (f_1=0.31) was observed at shorter wavelength (500nm). The dominating emission from intermediate decay component (τ_2= 11ns) at 500nm and broader emission peaks of pristine powders (Figure 4.16d).

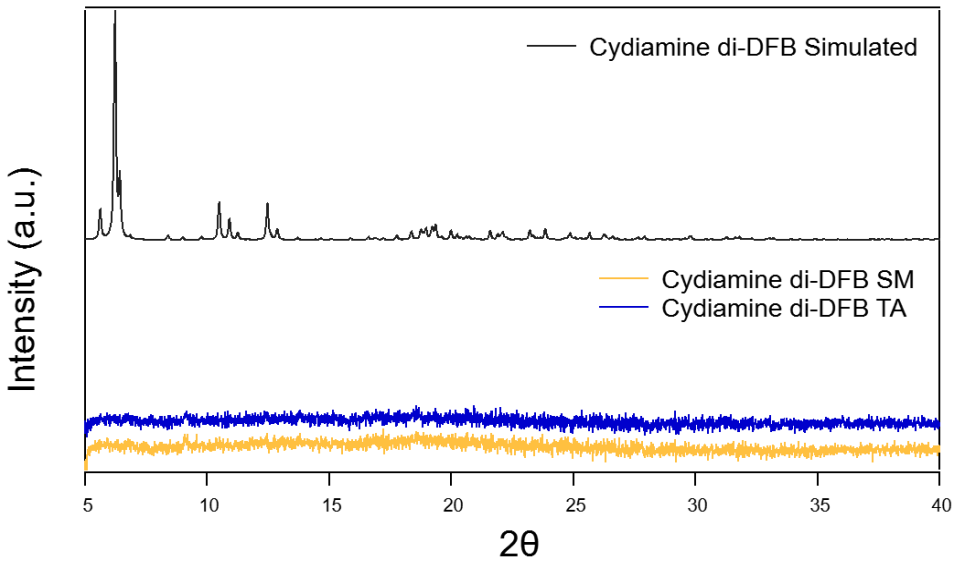

Figure 4.17. Simulated powder XRD of crystal from CIF file, powder XRD of smeared, thermal annealed samples of **cydiamine di-DFB** annealed at 130°C.

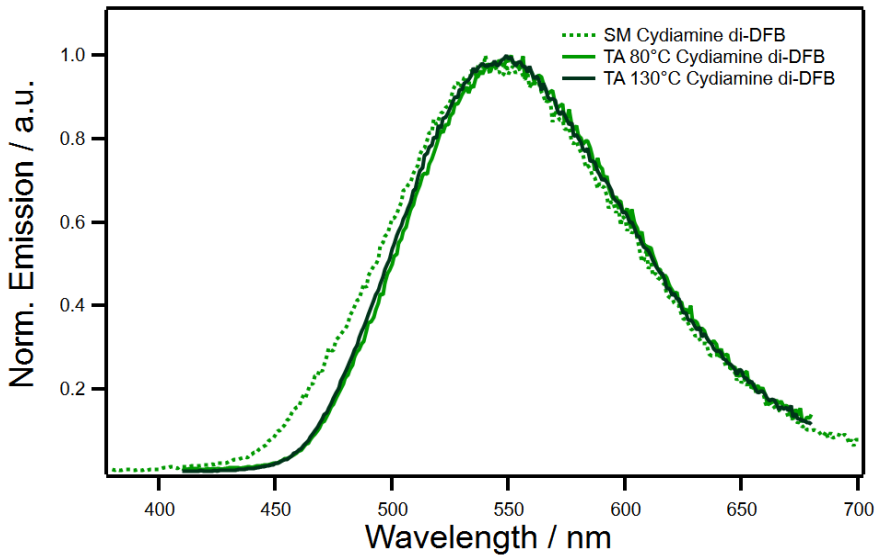

Figure 4.18. Emission spectra of smeared and thermal annealed samples of cydiamine di-DFB.

4.4.3 Mechanofluorochromism of Cydiester di-DFB

Cydiester di-DFB crystals display maximum emission (λ_{em}) at 500nm which is the shortest emission wavelength among the three crystals under study (see Figure 4.12a). Time-resolved fluorescence spectroscopy measurement at different wavelengths were

also fitted using global analysis and showed decay times τ_1= 9.2ns, τ_2= 2.9ns, τ_3= 0.9ns and τ_3= 0.26ns. Noticeably the longest decay time in **cydiester di-DFB** crystals (9.2ns) is shorter than the longest decay times observed in **cydiamine mono-DFB** crystals (15ns) and **cydiamine di-DFB** crystals (23ns) as shown in Figure 4.19a. The fraction of intensity from short decay time (τ_2= 2.9ns) is the most prominent while the longest decay time (τ_1= 9.2ns) has lowest fraction throughout the measured wavelength (500nm to 600nm). It was also observed in the single crystal structure that **cydiester di-DFB** has longer interlayer distance of ca. 5.7Å between each unit than the stacking distances observed in **cydiamine mono-DFB** and **cydiamine di-DFB** implying less intermolecular interactions. This agrees with time-resolved fluorescence plot showing a dominant short decay time (2.9ns).

A

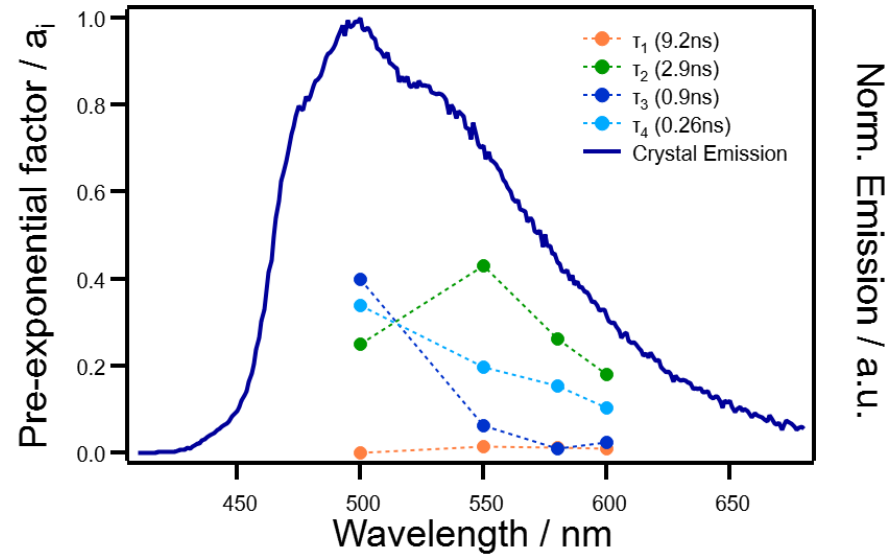

B

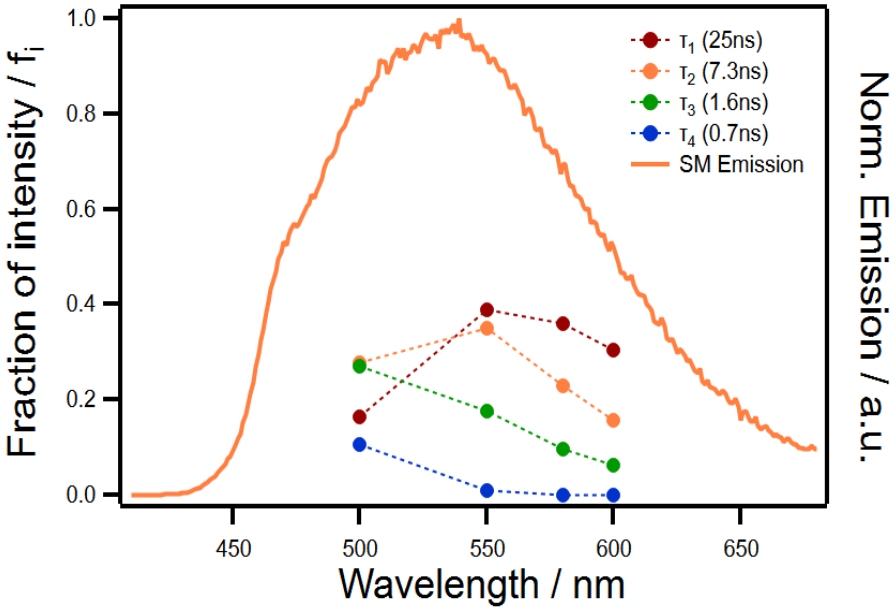

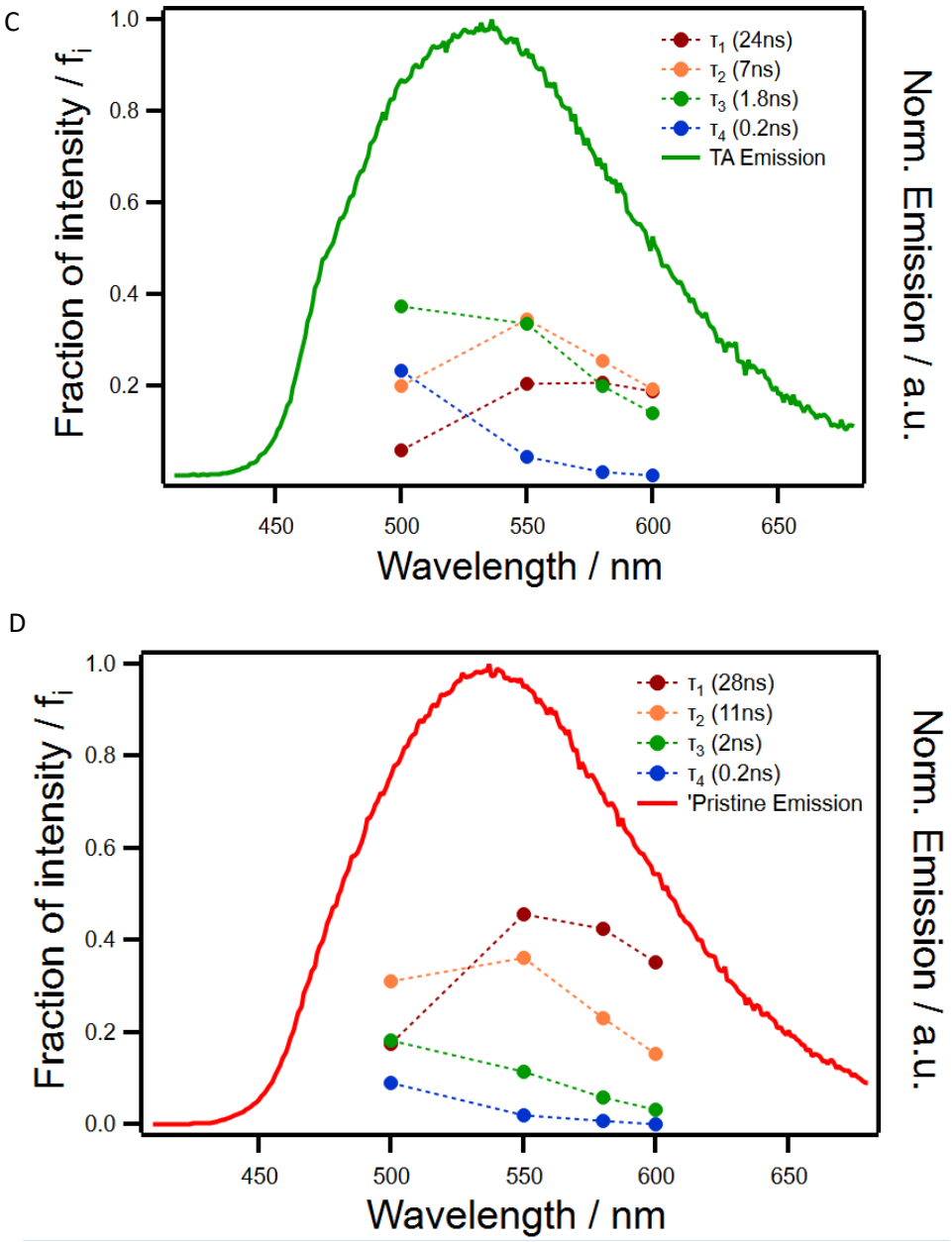

Figure 4.19. Plots of fraction of intensity obtained from time-resolved spectroscopy measurements of **cydiester di-DFB** crystals (a), smeared (b), thermal annealed (c) and pristine powders (d) measured at difference wavelengths (500nm to 600nm) using excitation at 350nm.

After smearing, a new emissive component with long decay time (τ_1= 25ns) is observed which contributes with the highest fraction of intensity for long wavelengths from 550nm to 600nm (see Figure 4.19b). Noticeably, emission spectrum after smearing displays a shouldering peak around 500nm as observed in Figure 4.11b. Time-resolved fluorescence spectroscopy measurements revealed that emissive species with intermediate decay time (τ_2= 7.3ns) and shorter decay time (τ_3= 1.6ns) were prominent and sharing an equal contribution at shorter wavelength (500nm). This may indicate that

smearing did not totally destruct the initial intermolecular interaction in crystals. This also agree with powder XRD showing few diffraction patterns after smearing (see Figure 4.20).

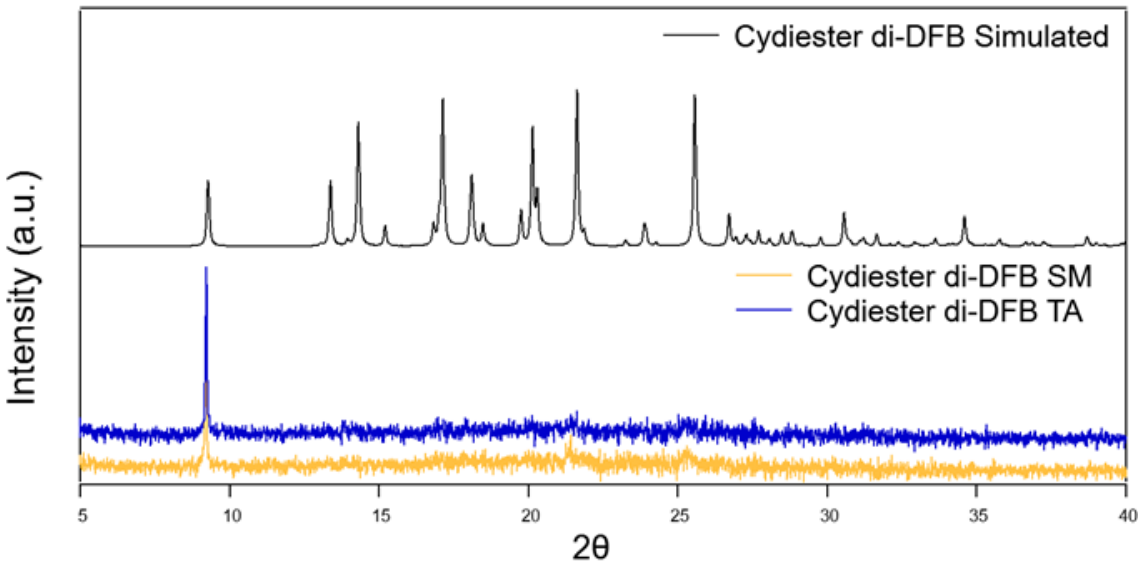

Figure 4.20. Simulated powder XRD of crystal from CIF file, powder XRD of smeared, thermal annealed samples of cydiester di-DFB annealed at 130°C.

Smearing shifted the maximum emission to higher wavelength induced by closer π-π stacking bought by destructed crystal structure and this was evident by broader emission and existence of longer decay time (τ_1= 25ns) as shown in the fraction of intensity plot in Figure 4.19b. Pristine powders showed similar decay profile with smeared samples except for shouldering peak at 500nm, which may also indicate a meta-stable state after smearing (see Figure 4.19d).

Thermal annealing at 80°C for 2 hours shows partial recovery of emission as shown in the increased intensity in 500nm (see Figure 4.21) accompanied by increase in components with short decay time (τ_3= 1.8ns) as shown in Figure 4.19c. Higher annealing temperature (130°C) has caused further increase in the shouldering peak at 500nm as shown in Figure 4.21, moreover powder XRD displayed an increased intensity in 2θ=9.2° indicating higher crystallinity due to recovery of the molecular packing. Annealing at higher temperature (130°C) did not induce degradation as shown in thermogravimetric analysis (see Chapter 6). Steric hindrance and bulkiness of some organic molecules affect the thermal back reaction by hindered reversion to the initial molecular stacking.[10] Interestingly, partial emission recovery was only observed in **cydiester di-DFB** crystals and did not occur in **cydiamine mono-DFB** and **cydiamine di-DFB**. To understand this, we compare the intermolecular interaction energies of the crystals through calculations.

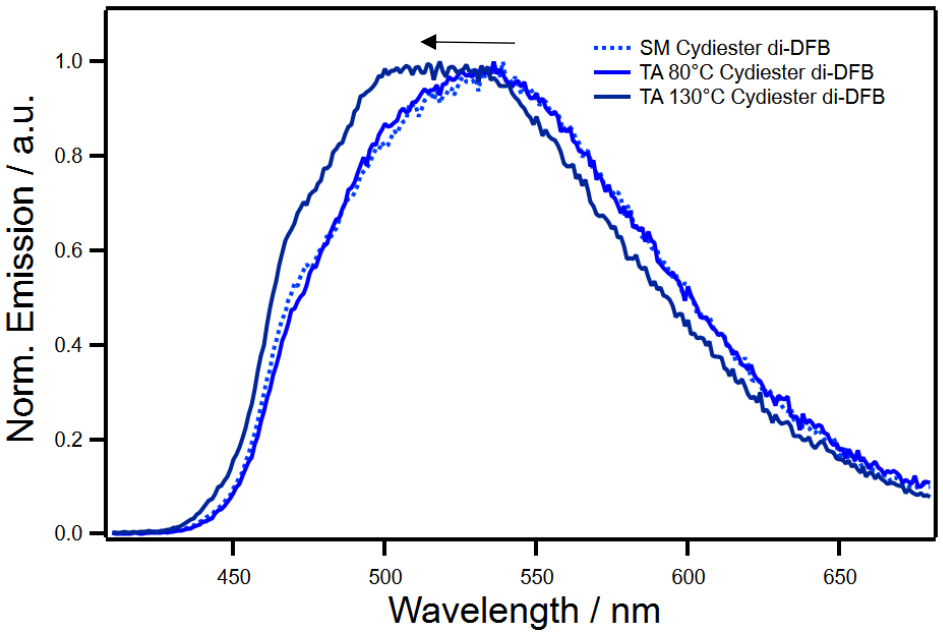

Figure 4.21. Emission spectra of smeared and thermal annealed samples of cydiester di-DFB.

4.5 Intermolecular Interaction Energy in Crystals: Energy Framework

Energy framework was calculated to gain more insights not only to the close surface contact but also to the overall intermolecular interaction energy within the crystal. This computational approach was previously used by Spackman *et al.* to study the intermolecular energy and explain the mechanical properties of crystals at molecular level.[31,32] In this calculation, total energy was reported as the summation of all the intermolecular interactions such as polarization, dispersion, repulsion, and dispersion energies (kJ). The calculation was performed for the interaction of all molecules within the 3.8Å distance from the central molecule. The calculations were performed using CE HF/3-21G electron densities model. The Figure 4.22a shows the total interaction energy framework viewed along a-axis of **cydiamine mono-DFB** represented by interconnected blue cylinders which are proportional to the intermolecular interaction energy. The calculated intermolecular energy values in kJ were indicated in annotated energy diagrams shown in Figure 4.22b.

A

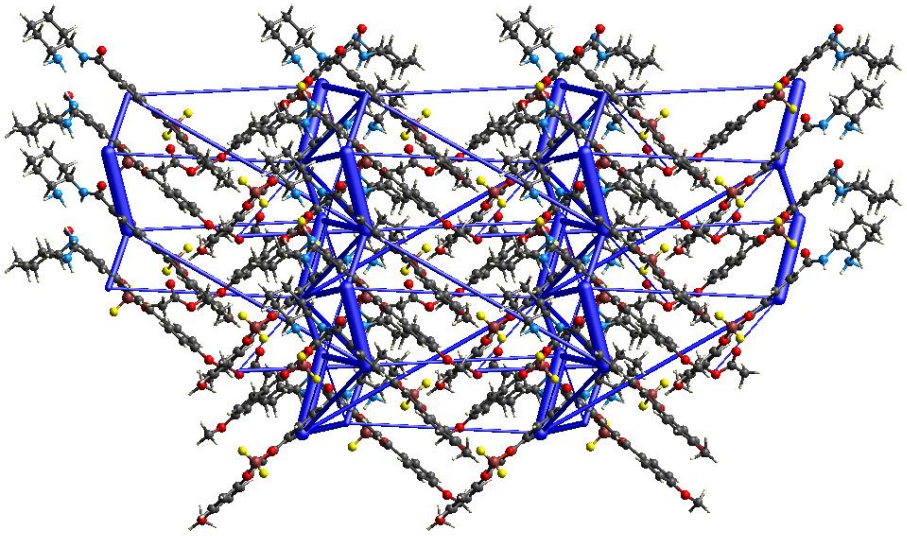

B

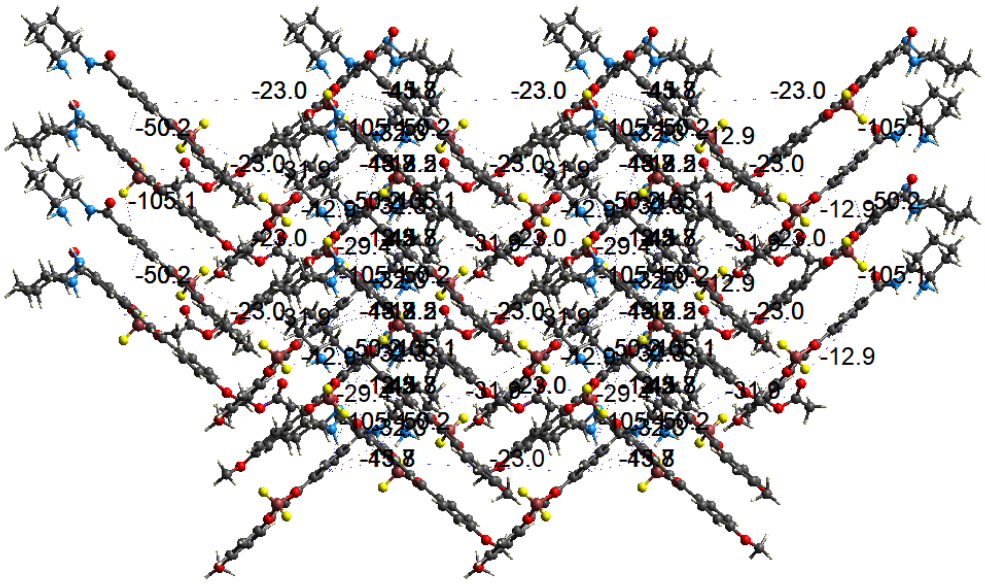

Figure 4.22. Total energy framework of cydiamine mono-DFB (a) and annotated energy diagram viewed along a-axis (b).

It was shown that in cydiamine mono-DFB, the highest energies (largest cylinder diameter) were observed within the molecular column (-105.1kJ) and weaker inter-columnar energies (-50.2kJ, and -32.3kJ). Moreover, there are noticeable smaller radius cylinders indicating weaker but significant long distance inter-columnar interaction energies (-23 kJ).

Same parameters were used to calculate the total interaction energy **cydiamine di-DFB** and Figure 4.23 shows the total energy framework and the annotated energy diagram for the crystal structure.

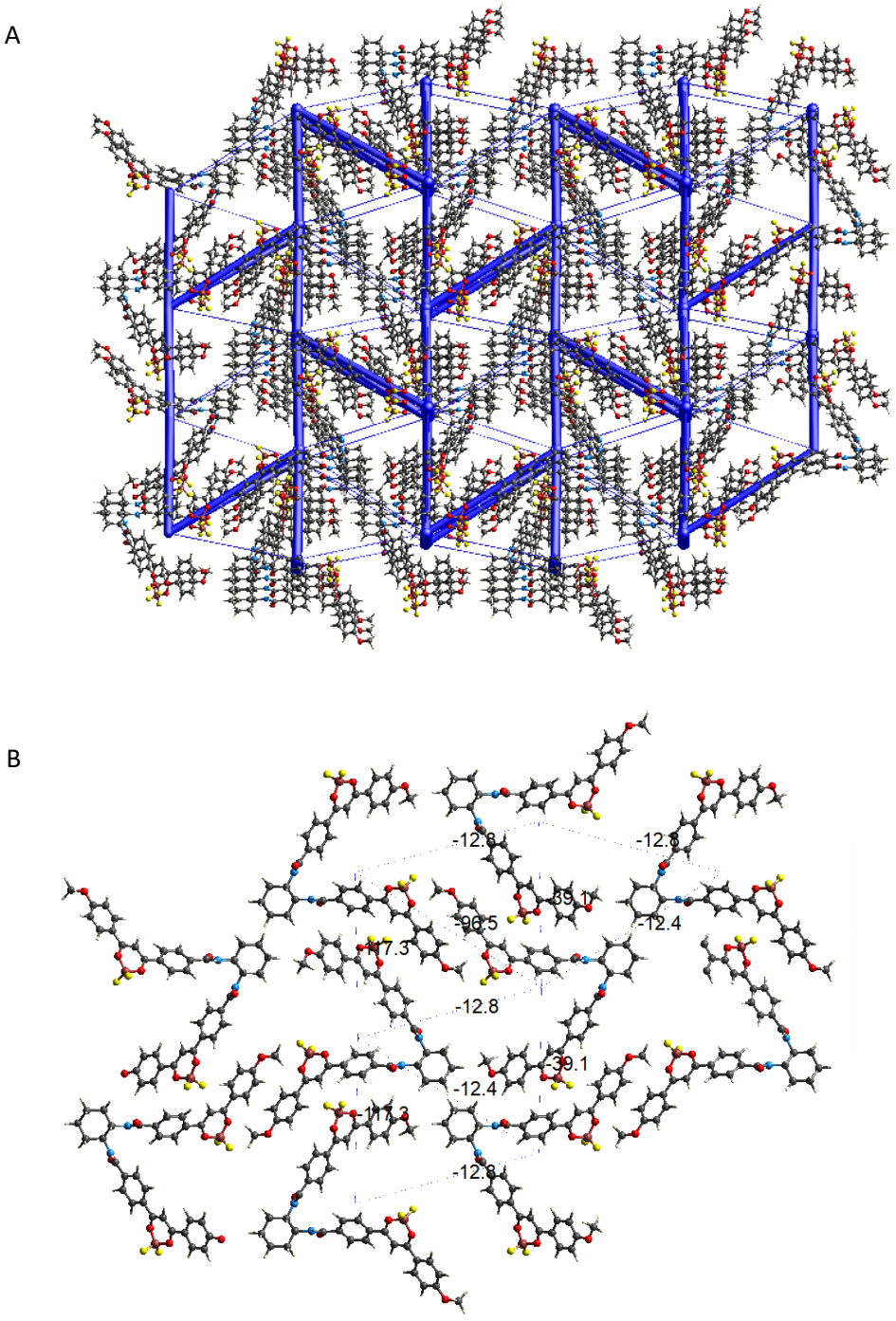

Figure 4.23. Total energy framework of **cydiamine di-DFB** (a) and annotated energy diagram viewed along a-axis (b).

Similar with the mono-DFB, there are strong intermolecular energies with the top to bottom stacking of bichromophore units (-154kJ) as well as interactions within the adjacent columns (-117.3kJ, -96.5kJ and -39.5kJ). It is also noticeable that there is smaller radius cylinder from long distance inter-columnar interaction (-12.8kJ) which are weaker than what was observed in cydiamine mono-DFB.

Lastly, the total energy framework for cydiester di-DFB showed that most of the thick cylinders are concentrated within the column (-101.9 kJ, -52.8 kJ and -25.7 kJ) while very weak long distance inter-columnar interaction was demonstrated with small radius cylinder (-3.9 kJ) shown in Figures 4.24a and 4.24b.

A

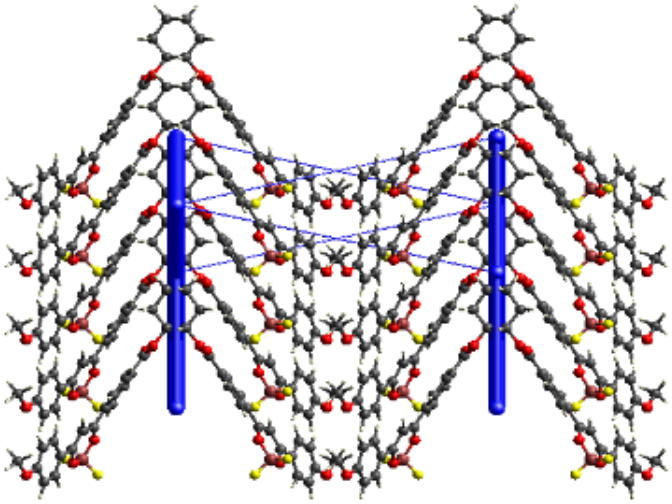

B

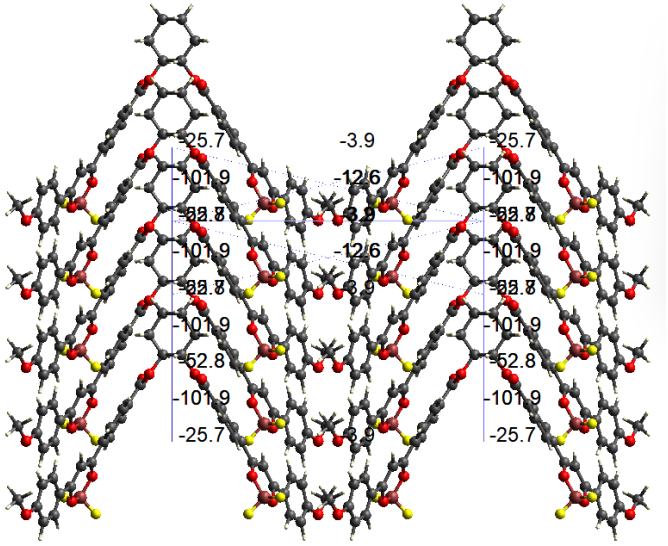

Figure 4.24. Total energy framework of cydiamine di-DFB (a) and annotated energy diagram viewed along a-axis (b).

To gain more understanding of the weaker net inter-columnar interaction energy within the **cydiester di-DFB**, we investigated the coulombic energy and dispersive energy frameworks shown in Figure 4.25.

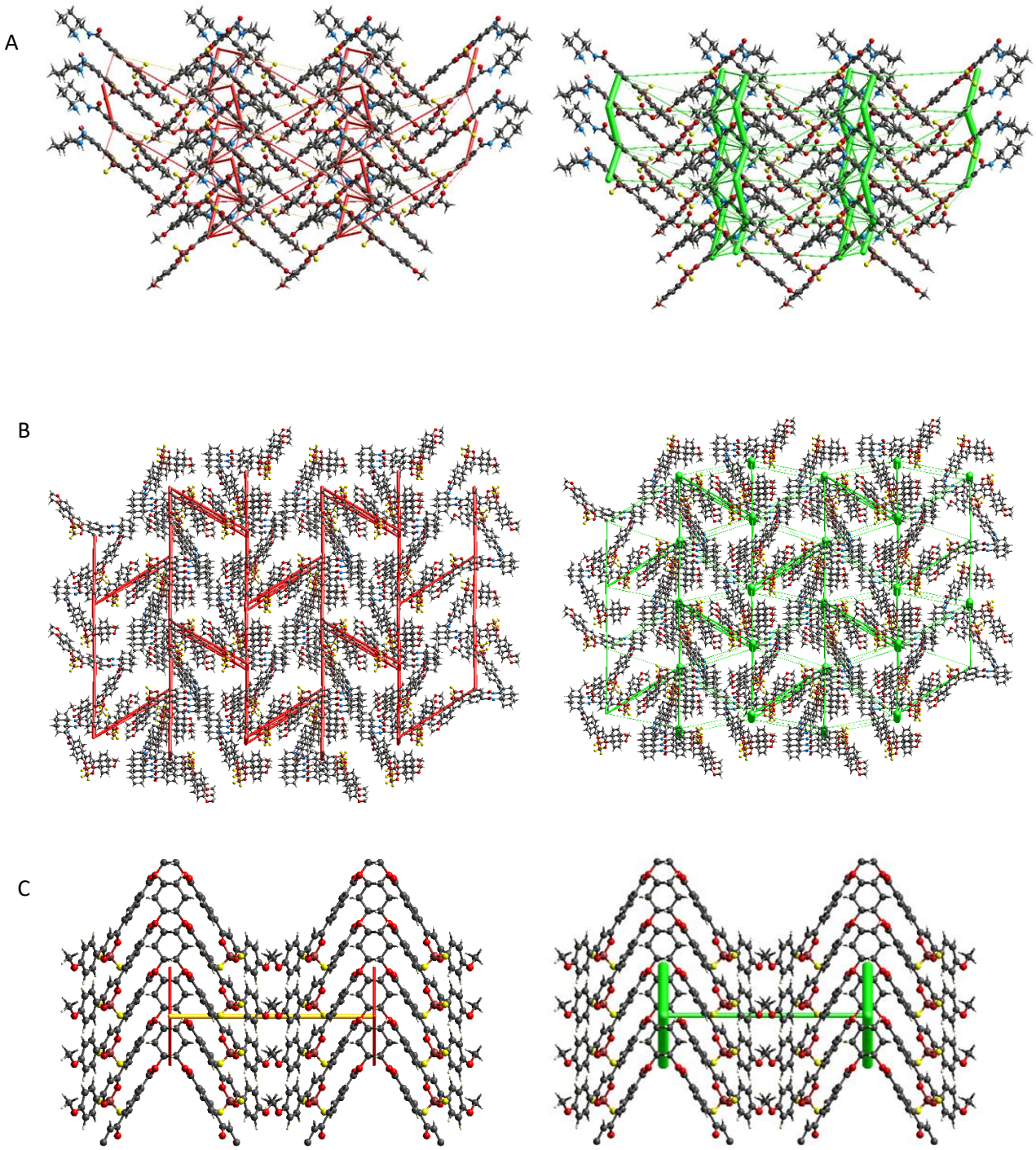

Figure 4.25. Electrostatic (red and yellow) and dispersive (green) components **of cydiamine mono-DFB** (a) **cydiamine di-DFB** (b) and **cydiester di-DFB** (c) viewed along a-axis.

It is noticeable that there is a large yellow cylinder which corresponds to positive Coulomb energy (repulsive) and red cylinder inter-columnar indicating negative coulomb energy (attractive) shown in Figure 4.25c. Although the repulsive energy is significantly large in crystal unit of cydiester di-DFB, dispersive forces counteract the Coulomb energy which is enough to stabilize the structure in crystal as shown in small blue cylinders in total energy framework.

Comparison of the Coulomb energies within the crystal system of cydiester di-DFB to the cydiamine mono-DFB and cydiamine di-DFB revealed that there are no significant inter-columnar repulsive forces (see Figures 4.25and 4.25b). The combined total interaction energy, strong atom-atom, and surface interactions of cydiamine mono-DFB and cydiamine di-DFB may explain the favored formation of close packing structures after smearing. These energies may stabilize the new conformations preventing the back reaction even after thermal annealing. These observations agreed with time-resolved spectroscopy measurements showing similar decay profiles in smeared and thermal annealed samples. In contrast with cydiester di-DFB, total energy framework shows a weak long-range distance interaction because of repulsive forces, however strong intra-columnar interactions energy forces have stabilized the structure. Smearing the crystals did not fully destruct the initial stacking of the molecules which may be brought by strong intra-columnar stacking. This is evidenced by the emission spectra of smeared samples showing shouldering peaks at emission wavelength 500nm and retained diffraction peaks in powder XRD of smeared powder. Thermal annealing induced the back reaction which may be due to combination of repulsive forces and weaker atom-atom interaction that made it easier to recover the initial state of the cydiester di-DFB crystal. This agrees with time-resolved spectroscopy measurements of thermal annealed samples showing a significant increase in fractions of intensity from short decay times accompanied by the decrease in fraction of intensity from dimers with long decay times.

The comparison of these three compounds showed that cydiester di-DFB has the most promising mechanofluorochromic property as well as the partial reversibility. The observed weak intercolumnar and atom-atom interactions by cydiester di-DFB as compared with cydiamine mono-DFB and cydiamine di-DFB played a significant role in the mechanofluorochromic property. This result is in good agreement with the previous study of Krishna et al. showing that easy-to-deform crystals displayed better mechanofluorochromic property due to presence of slip planes formed by weak interactions of functional groups.[33,34]

4.6 Conclusion

The mechanofluorochromic properties of three compounds, consisting of mono-chromophore DFB (**cydiamine mono-DFB**), bichromophore with amide spacer (**cydiamine di-DFB**) and bichromophore with ester spacer (**cydiester di-DFB**), were studied. It was revealed that **cydiamine mono-DFB** crystals displayed the longest emission wavelength while the bichromophore with ester spacer **cydiester di-DFB** crystals emit at the shortest wavelength. The presence of amine (NH_2) in **cydiamine mono-DFB** and amide (-NH) **cydiamine di-DFB** favors the atom-atom interactions with carbonyl group of neighboring bichromophore unit with closer interlayer distances indicating stronger intermolecular interactions. On the other hand, **cydiester di-DFB** favors the carbonyl to BF_2 interactions displaying brick-layering and longer intermolecular stacking distance leading to a blue shifted emission comparing to bichromophore with -NH and -NH_2 spacers. Bathochromic shifts were observed for the three compounds after smearing while **cydiester di-DFB** displayed the largest emission shift with increased intermolecular interaction as confirmed by time-resolved spectroscopy measurements. This proves that the spacers amine and ester highly influenced the mechanofluorochromic properties of bichromophore DFB crystals through its atom-atom interactions and molecular stacking. Finally, only **cydiester di-DFB** displayed back reaction after thermal annealing and showed large positive coulomb energy (repulsive) as observed in the energy framework. The thermal back reaction as well as the significant positive coulomb energy was not observed in **cydiamine mono-DFB** and **cydamine di-DFB** which suggested that weaker atom-atom interactions and net repulsive forces favors back reaction **cydiester di-DFB** crystals. As demonstrated in this study, the small differences in the functional groups (amides and esters) with different interaction strengths highly influence the mechanofluorochromic properties as well as the thermal back reaction. The understanding of the molecular behavior of both mono and bichromophore DFB crystals will broaden the perspective in molecular design of reversible MFC materials for application in security and sensing devices.

4.7 References

(1) Chen, P.-Z.; Niu, L.-Y.; Chen, Y.-Z.; Yang, Q.-Z. Difluoroboron B-Diketonate Dyes: Spectroscopic Properties and Applications. *Coord. Chem. Rev.* 2017, 196-216.

(2) Zhang, H.; Chen, P.-Z.; Niu, L.-Y.; Yang, Q.-Z. A Difluoroboron B-Diketonate-Based Luminescent Material with Tunable Solid-State Emission and Thermally Activated Delayed Fluorescence. *Mater. Chem. Front.* 2020, 4, 285.

(3) Louis, M.; Sethy, R.; Kumar, J.; Katao, S.; Guillot, R.; Nakashima, T.; Allain, C.; Kawai, T.; Métivier, R. Mechano-Responsive Circularly Polarized Luminescence of Organic Solid-State Chiral Emitters. *Chem. Sci.* 2019, *10* (3), 843–847.

(4) Wilbraham, L.; Louis, M.; Alberga, D.; Brosseau, A.; Guillot, R.; Ito, F.; Labat, F.; Métivier, R.; Allain, C.; Ciofini, I. Revealing the Origins of Mechanically Induced Fluorescence Changes in Organic Molecular Crystals. *Adv. Mater.* 2018, *30* (28), 1800817

(5) Zhao, J. Mechanofluorochromism of Difluoroboron β-Ketoiminate Boron Complexes Functionalized with Benzoxazole and Benzothiazole. *Dyes Pigm. 149* 2018, 276-283.

(6) Calupitan, J. P.; Brosseau, A.; Josse, P.; Cabanetos, C.; Roncali, J.; Métivier, R.; Allain, C. Mechanofluorochromic Material toward a Recoverable Microscale Force Sensor. *Adv. Mater. Interfaces.* 2022, 9, 2102246.

(7) Zhuang, M.; Joshi, S.; Sun, H.; Batabyal, T.; Fraser, C. L.; Kapur, J. Difluoroboron β-Diketonate Polylactic Acid Oxygen Nanosensors for Intracellular Neuronal Imaging. *Sci. Rep.* 2021, *11* (1), 1076.

(8) Louis, M.; Piñero García, C.; Brosseau, A.; Allain, C.; Métivier, R. Mechanofluorochromism of a Difluoroboron-β-Diketonate Derivative at the Nanoscale. *J. Phys. Chem. Lett.* 2019, *10* (16), 4758–4762.

(9) Katsumi, S.; Saigusa, M.; Ito, F. Molecular Aggregation Dynamics via a Liquid-like Cluster Intermediate during Heterogeneous Evaporation as Revealed by Hyperspectral Camera Fluorescence Imaging. *J. Phys. Chem. B.* 2022, *126* (4), 976–984.

(10) Hirai, Y. Mechanofluorochromism of Pyrenyl Acrylates with Different Substitutional Position and Steric Hindrance. *J. Photochem. Photobiol. A.* 405, 2021, 112972

(11) Hirai, Y.; Laize-Générat, L.; Wrona-Piotrowicz, A.; Zakrzewski, J.; Makal, A.; Brosseau, A.; Michely, L.; Versace, D.; Allain, C.; Métivier, R. Multi-Directional Mechanofluorochromism of Acetyl Pyrenes and Pyrenyl Ynones. *ChemPhysChem.* 2021, *22* (15), 1638–1644.

(12) Louis, M.; Brosseau, A.; Guillot, R.; Ito, F.; Allain, C.; Métivier, R. Polymorphism, Mechanofluorochromism, and Photophysical Characterization of a Carbonyl Substituted Difluoroboron-β-Diketone Derivative. *J. Phys. Chem. C* 2017, *121* (29), 15897–15907.

(13) Nguyen, N. D.; Zhang, G.; Lu, J.; Sherman, A. E.; Fraser, C. L. Alkyl Chain Length Effects on Solid-State Difluoroboron b-Diketonate Mechanochromic Luminescence. *J. Mater. Chem.* 2011, 21, 8409.

(14) Xu, S.; Evans, R. E.; Liu, T.; Zhang, G.; Demas, J. N.; Trindle, C. O.; Fraser, C. L. Aromatic Difluoroboron β-Diketonate Complexes: Effects of π-Conjugation and Media on Optical Properties. *Inorg. Chem.* 2013, *52* (7), 3597–3610.
(15) Ito, F.; Naganawa, R.; Fujimoto, Y.; Takimoto, M.; Mochiduki, Y.; Katsumi, S. Real-Time Fluorescence Visualization of Nanoparticle Aggregation and the Polymorph-Transition Process of a Mechanofluorochromic Difluoroboron-β-Diketone Derivative. *ChemPhysChem.* 2021, 22, 1662–166.
(16) Kawai, T.; Kawamura, K.; Tsumatori, H.; Ishikawa, M.; Naito, M.; Fujiki, M.; Nakashima, T. Circularly Polarized Luminescence of a Fluorescent Chiral Binaphtylene–Perylenebiscarboxydiimide Dimer. *ChemPhysChem.* 2007, *8* (10), 1465–1468.
(17) Sethy, R.; Métivier, R.; Brosseau, A.; Kawai, T.; Nakashima, T. Impact of Optical Purity on the Light Harvesting Property in Supramolecular Nanofibers. *J. Phys. Chem. Lett.* 2018, *9* (16), 4516–4521.
(18) Kumar, J.; Nakashima, T.; Tsumatori, H.; Kawai, T. Circularly Polarized Luminescence in Chiral Aggregates: Dependence of Morphology on Luminescence Dissymmetry. *J. Phys. Chem. Lett.* 2014, 5, 316-321.
(19) Rauf, A.; Parveen, H. Direct Esterification of Fatty Acids with Phenylalkanols by Using Dicyclohexylcarbodiimide. *Eur. J. Lipid Sci. Technol.* 2004, *106* (2), 97–100.
(20) Spackman, M. A.; Jayatilaka, D. Hirshfeld Surface Analysis. *CrystEngComm.* 2009, *11* (1), 19–32.
(21) Sharfalddin, A.; Davaasuren, B.; Emwas, A.-H.; Jaremko, M.; Jaremko, Ł.; Hussien, M. Single Crystal, Hirshfeld Surface and Theoretical Analysis of Methyl 4-Hydroxybenzoate, a Common Cosmetic, Drug and Food Preservative—Experiment versus Theory. *PLoS. ONE.* 2020, *15* (10), e0239200.
(22) Spackman, P. R.; Turner, M. J.; McKinnon, J. J.; Wolff, S. K.; Grimwood, D. J.; Jayatilaka, D.; Spackman, M. A. *CrystalExplorer* : A Program for Hirshfeld Surface Analysis, Visualization and Quantitative Analysis of Molecular Crystals. *J. Appl. Crystallogr.* 2021, *54* (3), 1006–1011.
(23) Loveland, D.; Kailkhura, B.; Karande, P.; Hiszpanski, A. M.; Han, T. Y.-J. Automated Identification of Molecular Crystals' Packing Motifs. *J. Chem. Inf. Model.* 2020, *60* (12), 6147–6154.
(24) Loots, L.; Barbour, L. J. A Simple and Robust Method for the Identification of π–π Packing Motifs of Aromatic Compounds. *CrystEngComm* 2012, *14* (1), 300–304.
(25) Morris, W. A.; Liu, T.; Fraser, C. L. Mechanochromic Luminescence of Halide-Substituted Difluoroboron β-Diketonate Dyes. *J. Mater. Chem. C* 2015, *3* (2), 352–363.
(26) Ungár, T. Microstructural Parameters from X-Ray Diffraction Peak Broadening. *Scr. Mater.* 2004, *51* (8), 777–781.
(27) Kumar, J.; Nakashima, T.; Tsumatori, H.; Mori, M.; Naito, M.; Kawai, T. Circularly Polarized Luminescence in Supramolecular Assemblies of Chiral Bichromophoric Perylene Bisimides. *Chem. Eur. J.* 2013, *19* (42), 14090–14097.

(28) Kumar, J.; Nakashima, T.; Kawai, T. Circularly Polarized Luminescence in Chiral Molecules and Supramolecular Assemblies. *J. Phys. Chem. Lett.* 2015, *6* (17), 3445–3452.
(29) Aragó, J.; Troisi, A. Dynamics of the Excitonic Coupling in Organic Crystals. *Phys. Rev. Lett.* 2015, *114* (2), 026402.
(30) Windischbacher, A.; Steiner, L.; Haldar, R.; Wöll, C.; Zojer, E.; Kelterer, A.-M. Exciton Coupling and Conformational Changes Impacting the Excited State Properties of Metal Organic Frameworks. *Molecules.* 2020, *25* (18), 4230.
(31) Dey, D.; Bhandary, S.; Thomas, S. P.; Spackman, M. A.; Chopra, D. Energy Frameworks and a Topological Analysis of the Supramolecular Features in in Situ Cryocrystallized Liquids: Tuning the Weak Interaction Landscape via Fluorination. *Phys. Chem. Chem. Phys.* 2016, *18* (46), 31811–31820.
(32) Turner, M. J.; Thomas, S. P.; Shi, M. W.; Jayatilaka, D.; Spackman, M. A. Energy Frameworks: Insights into Interaction Anisotropy and the Mechanical Properties of Molecular Crystals. *Chem. Commun.* 2015, *51* (18), 3735–3738.
(33) Krishna, G. R.; Devarapalli, R.; Prusty, R.; Liu, T.; Fraser, C. L.; Ramamurty, U.; Reddy, C. M. Structure–Mechanical Property Correlations in Mechanochromic Luminescent Crystals of Boron Difluoride Dibenzoylmethane Derivatives. *IUCrJ.* 2015, *2* (6), 611–619.
(34) Krishna, G. R.; Kiran, M. S. R. N.; Fraser, C. L.; Ramamurty, U.; Reddy, C. M. The Relationship of Solid-State Plasticity to Mechanochromic Luminescence in Difluoroboron Avobenzone Polymorphs. *Adv. Funct. Mater.* 2013, *23* (11), 1422–1430.

CHAPTER 5

Conclusion and Prospects

This work was divided into three main parts: chiroptical properties of bichromophore difluoroboron β-diketonate (DFB), energy transfer and responsiveness to UV and mechanofluorochromic properties of bichromophore DFB. The discussion in each chapter mainly covers the combination of theoretical calculations and photophysical properties to understand the fundamental reasons for the behavior and responses of the molecules with light and mechanical stress.

We first introduce the concept of circularly polarized luminescence (CPL) and the overview of instrument as well as the early studies of CPL active compounds such as lanthanide complexes and small organic compounds (SOMs). We discussed the advantages of SOMs such as their tunability, simple synthetic route and biocompatibility. One of the challenges with CPL active SOMs is the low g_{CPL} values hence, recent studies were focusing on enhancement of CPL of SOMs using self-assembly. In this study, we used difluoroboron β-diketonate (DFB) as our chromophore because of high QY both in solution and solid state. This compound is known to display mechanofluorochromic property. In the recent paper of Louis *et al.* they designed DFB linked with chiral amide group which exhibits both CPL and mechanofluorochromic properties. However, enhancement through self-assembly was not yet explored. We aimed to synthesize similar DFB based CPL active and mechanofluorochromic SOMs with enhance the chiroptical properties. Bichromophoric compound was already reported to enhance CPL through intramolecular coupling. Moreover, the chiral bridge and chromophore surface interaction may induce formation of supramolecular assembly.

In the first part of this study, we synthesized a series of bichromophoric DFB using cyclohexane diamine as chiral bridge (*R/S* para and meta cydiamine DFB). The effect of connectivity in para and meta positions in DFB moieties to the orientation of chromophores as well as to the chiroptical properties of the bichromophore DFB was explored. Through theoretical calculations (DFT and TD-DFT) we show that the variation in connectivity from para to meta position of DFB displayed a totally different direction of chromophores. This has led to inversion of chirality in monomeric form. Moreover, the orientation of DFB influenced the intramolecular coupling of chromophore leading to higher g_{CPL} values for para as compared to meta. The formation of supramolecular assembly of para cydiamine di-DFB was confirmed to enhance the g_{CPL} values wherein we obtained 0.015. We also divulged the effect of chromophore orientation on the formation or hindrance of H-bonding among the carbonyl and amides functional group leading to long range supramolecular assembly.

Supramolecular assemblies of organic compounds can be utilized in device fabrications and artificial light harvesting materials.[1–3] Therefore, in the second part of

the study we investigated the energy transfer between the two DFB units within the isolated bichromophore as compared to mono-DFB and supramolecular self-assembled nanowires. In this study we have shown that in mono-DFB, isolated molecules do not have any interactions with neighboring mono-DFB units. On the contrary with bichromophore DFB, we have proven that the two DFB units bridged with cyclohexane diamine have intramolecular coupling as evident by low anisotropy values. Lastly, supramolecular assembly has very efficient energy transfer which agree with the work of Spano et al. (2011) showing that long range excitonic coupling exist between the chromophore units in supramolecular assembly.[4,5] We have also investigated the response of the nanowires to UV irradiation, wherein the exposure has caused emission shift to lower wavelength accompanied by decreased in emission intensity. Through the combination of atomic force microscopy analysis and time-resolved fluorescence measurements, we have proved that the UV exposure destruct the BF_2 to oxygen bonding in DFB moieties, also the H-bonding in supramolecular assembly which has caused the fragmentations of nanowires thus, emission shift was observed. The sensitivity of the supramolecular assembly to UV was demonstrated by printing patterns on the surface of gels.

In the previous parts of the study, we have discussed the intermolecular coupling of DFB in bichromophore units and how it has influenced the properties in solution and gel states. In the last part of the study, we therefore extend the measurements of bichromophore units in solid state wherein we compared the mechanofluorochromic property of cydiamine mono-DFB to cydiamine di-DFB. We uncover the effect of amine and DFB units to the molecular packing distance and strength of atom-to-atom interactions through single crystal analysis and Hirshfeld surface analysis.[6,7] We showed that the cydiamine mono-DFB has shorter molecular stacking distance as compared to the cydiamine di-DFB which is mainly due to stronger H-bonding attributed to the presence of amine. Meanwhile, cydiamine di-DFB has longer molecular packing distance in crystals resulting to low π-π interactions. These explains the red-shifted emission of mono-DFB as compared with di-DFB. Moreover, we also show that the variation in spacer from amide to ester highly influenced the molecular stacking in crystal. The weaker H-bonding in cydiester di-DFB leads to longer interlayer brick arrangement hence, displayed the shortest wavelength emission among the three compounds. Through the combination of time-resolved fluorescence measurements, Hirshfeld surface analysis and energy frameworks,[7–9] we reveal the role of atom-to-atom interactions, stacking of molecules as well as repulsive forces to mechanofluorochromism and its thermal reversibility.

Recent research for CPL active small organic compounds based on axial chirality involved chiral bridges such as BINOL, BINAP and cyclohexane.[5,10,11] While some of these compounds exhibits tunable CPL through external stimulation, solvent effect or presence of guest molecules,[12–15] our study divulged the significance of molecular design in

inversion of chirality in monomeric form. We also highlighted the effect of the orientation of chromophores in hindered formation of supramolecular assembly. These findings may be supplemental for future molecular design of CPL active supramolecular assembly. One of the emerging applications of supramolecular assembled SOMs are the CPL switches wherein CPL signals can be turned "on" and "off" as a response to stimuli such as light. Incorporation of chromic molecules to a chiral compound or supramolecular assembly has made this CPL switching possible. We have shown in this study that supramolecular assembled DFB display g_{CPL} values comparable to other SOMs and has efficient energy transfer thus, a potential chiral molecular backbone for CPL switches. Design of chromic molecules which can directly interact with supramolecular assembled DFB can be a subject for further studies in such a way that energy transfer (FRET) may induce the turning "on" or "off" the CPL signals.

Through molecular modification of spacers, we also revealed the role of intermolecular stacking and strength of atom-to-atom interactions to solid state photophysical properties of bichromophore DFB. From these, we revealed that ester has the most promising emission shift after smearing as well as thermal back reaction. However, these are limited to methoxy as side chain in DFB moiety. Variation of side chains such as longer alkyl or bulky groups may be subjected for study as these has previously reported in some chromophore. To the best of our knowledge these are not explored yet for bichromophoric DFB. These findings may direct the molecular design of mechanofluorochromic compounds for mechano-sensing device fabrication.

The discussed results and conclusions from these three-part studies may contribute to the field of photochemistry specifically in supramolecular assembly, chirality and mechanofluorochromism. Combined efforts in study of molecular design, theoretical calculations, and utilization of specialized photophysical measuring instruments have made it feasible to understand the connection between macroscopic photophysical properties to molecular-level arrangements and behavior of the compounds. These are the fundamental building block for efficient molecular design for future fabrication of sensing and opto-electronic devices.

5.1 References

(1) Sethy, R.; Kumar, J.; Métivier, R.; Louis, M.; Nakatani, K.; Mecheri, N. M. T.; Subhakumari, A.; Thomas, K. G.; Kawai, T.; Nakashima, T. Enantioselective Light Harvesting with Perylenediimide Guests on Self-Assembled Chiral Naphthalenediimide Nanofibers. *Angew. Chem. Int. Ed.* 2017, *56* (47), 15053–15057.

(2) Wong, K.-T.; Bassani, D. M. Energy Transfer in Supramolecular Materials for New Applications in Photonics and Electronics. *NPG Asia Mater.* 2014, *6* (7), e116–e116.

(3) Lim, J. M.; Kim, P.; Yoon, M.-C.; Sung, J.; Dehm, V.; Chen, Z.; Würthner, F.; Kim, D. Exciton Delocalization and Dynamics in Helical π-Stacks of Self-Assembled Perylene Bisimides. *Chem. Sci.* 2013, *4* (1), 388–397.

(4) Tempelaar, R.; Stradomska, A.; Knoester, J.; Spano, F. C. Circularly Polarized Luminescence as a Probe for Long-Range Interactions in Molecular Aggregates. *J. Phys. Chem. B.* 2011, *115* (36), 10592–10603.

(5) Kumar, J.; Nakashima, T.; Tsumatori, H.; Mori, M.; Naito, M.; Kawai, T. Circularly Polarized Luminescence in Supramolecular Assemblies of Chiral Bichromophoric Perylene Bisimides. *Chem. Eur. J.* 2013, *19* (42), 14090–14097.

(6) Sharfalddin, A.; Davaasuren, B.; Emwas, A.-H.; Jaremko, M.; Jaremko, Ł.; Hussien, M. Single Crystal, Hirshfeld Surface and Theoretical Analysis of Methyl 4-Hydroxybenzoate, a Common Cosmetic, Drug and Food Preservative—Experiment versus Theory. *PLoS. ONE.* 2020, *15* (10), e0239200.

(7) Spackman, M. A.; Jayatilaka, D. Hirshfeld Surface Analysis. *CrystEngComm.* 2009, *11* (1), 19–32.

(8) Turner, M. J.; Thomas, S. P.; Shi, M. W.; Jayatilaka, D.; Spackman, M. A. Energy Frameworks: Insights into Interaction Anisotropy and the Mechanical Properties of Molecular Crystals. *Chem. Commun.* 2015, *51* (18), 3735–3738.

(9) Dey, D.; Bhandary, S.; Thomas, S. P.; Spackman, M. A.; Chopra, D. Energy Frameworks and a Topological Analysis of the Supramolecular Features in in Situ Cryocrystallized Liquids: Tuning the Weak Interaction Landscape via Fluorination. *Phys. Chem. Chem. Phys.* 2016, *18* (46), 31811–31820.

(10) Wan, S.-P.; Lu, H.-Y.; Li, M.; Chen, C.-F. Advances in Circularly Polarized Luminescent Materials Based on Axially Chiral Compounds. *J. Photochem. Photobiol. C.* 2022, *50*, 100500.

(11) Imai, Y. Non-Classical Circularly Polarized Luminescence of Organic and Organometallic Luminophores. *Chem. Lett.* 2021, *50* (6), 1131–1141.

(12) Wang, F.; Ji, W.; Yang, P.; Feng, C.-L. Inversion of Circularly Polarized Luminescence of Nanofibrous Hydrogels through Co-Assembly with Achiral Coumarin Derivatives. *ACS Nano*. 2019, 13, 6, 7281–7290

(13) Maeda, H.; Bando, Y.; Shimomura, K.; Yamada, I.; Naito, M.; Nobusawa, K.; Tsumatori, H.; Kawai, T. Chemical-Stimuli-Controllable Circularly Polarized Luminescence from Anion-Responsive π-Conjugated Molecules. *J. Am. Chem. Soc.* 2011, *133* (24), 9266–9269.

(14) Maity, S.; Das, P.; Reches, M. Inversion of Supramolecular Chirality by Sonication-Induced Organogelation. *Sci. Rep.* 5, 16365 (2015).

(15) Kumar, J.; Nakashima, T.; Tsumatori, H.; Kawai, T. Circularly Polarized Luminescence in Chiral Aggregates: Dependence of Morphology on Luminescence Dissymmetry. *J. Phys. Chem. Lett.* 2014*,* 5, 2, 316–321

CHAPTER 6

Methods and Supplementary Information

6.1 General Synthesis and Characterizations

Analytical reagents were purchased from Tokyo Chemical Industry Co., Ltd (TCI) and Sigma Aldrich and were used without further purification. The reactions were monitored using Merck TLC silica gel 60 F_{254} and visualized using UV lamp with wavelength 254nm and 365nm. ^{1}H, ^{13}C, ^{19}F and ^{11}B NMR analyses were recorded using 400MHz, 500MHz NMR JEOL JNM-ECX-500 and 600MHz NMR JEOL JNM-ECA600. The reference used for the ^{19}F and ^{11}B NMR analyses is BF_3 $O(C_2H_5)_2$ in $CDCl_3$. Mass was analyzed using high Bruker Autoflex II MALDI-TOF and JEOL MALDI Spiral-TOF high resolution mass spectrometer.

6.1.1 Synthesis of Compounds in Chapter 2

Synthesis of P-1
methyl (Z)-4-(1-hydroxy-3-(4-methoxyphenyl)-3-oxoprop-1-en-1-yl)benzoate

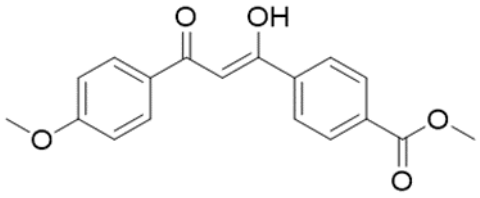

Synthesis of P-1 and P-2 were already reported from the previous manuscript of Wilbraham, Louis et al.[1] Sodium hydride (1.04 g, 1.3eq) was loaded in flamed dried flask and dissolved in 100mL of dry THF under nitrogen atmosphere. In separate flask, 4-methoxyacetophenone (5 g, 1.0 eq) was dissolved in dry 30mL THF under nitrogen atmosphere then loaded dropwise to the sodium hydride suspension. The solution was heated to 45°C with continuous stirring for 30 mins. In another flask, dimethyl terephthalate (7.98 g, 1.23 eq) was dissolved in 50 mL THF and slowly loaded to the reaction medium. The reaction was put under reflux for 12 hours. Reaction was cooled down to 30°C and quenched by adding 1.35mL concentrated HCl. Excess THF solvent was removed in vacuum, and the compound was extracted with 200mL DCM then washed with water (100mL) for three times. The organic moiety was washed with brine (50mL) two times then dried with $MgSO_4$. The crude product was purified by silica gel column chromatography using EtOAc/Hexane (30/70) as eluent. The target compound was obtained with 67% yield. ^{1}H-NMR (500MHz, $CDCl_3$): δ (ppm) 17.10 (s, 1H), 8.13 (d, *J*=8.Hz, 2H), 8.01 (dd, *J*=8.5Hz, 4H), 6.99 (d, *J*=8.5Hz, 2H), 6.83 (s,1H) 3.96(s, 3H) and 3.89 (s,3H).

MALDI-TOF mass spectrometry $C_{18}H_{16}O_5$ $[M + H]^+$: m/z =313.134 (calculated: 313.100).

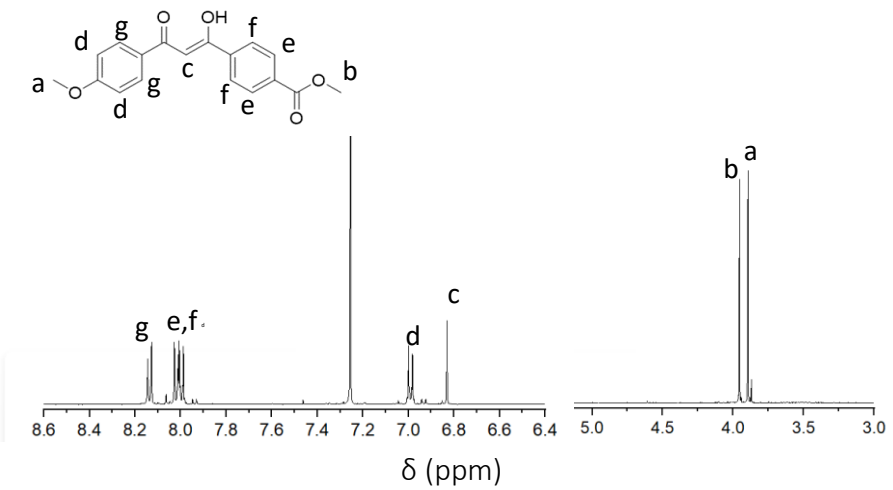

Synthesis of P-2
(Z)-4-(1-hydroxy-3-(4-methoxyphenyl)-3-oxoprop-1-en-1-yl)benzoic acid

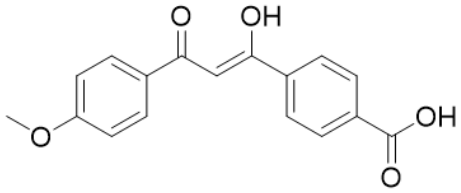

P-2 was synthesized using the same method used by Wilbraham, Louis et al. Compound P-1 (0.5 g, 1.0 eq.) was dissolved in 8 mL of THF. The medium was cooled down to 0°C. In separated flask, LiOH (0.34 g, 9.0 eq.) was pre-dissolved in 7.5 mL distilled water then slowly added to compound P-1. The medium was stirred for 24 hours at room temperature. Afterwards, the solution was poured in distilled water and washed with DCM (50mL) thrice. The aqueous phase was collected, the compound was precipitated by adding 1M HCl and isolated by filtration. No further purification was needed1. ^{1}H-NMR (500MHz, DMSO): δ (ppm) 17.19 (s, 1H), 13.29 (s, 1H), 8.22 (d, *J*=6.4 Hz, 2H), 8.17(d, *J*=7.2 Hz, 2H), 8.04 (d, *J*=6.8 Hz, 2H), 7.34 (s, 1H), 7.08 (d, *J*=6.0 Hz, 2H), 3.85 (s, 3H).

MALDI-TOF mass spectrometry $C_{17}H_{14}O_5$ $[M + H]^+$: m/z =299.138 (calculated: 299.084).

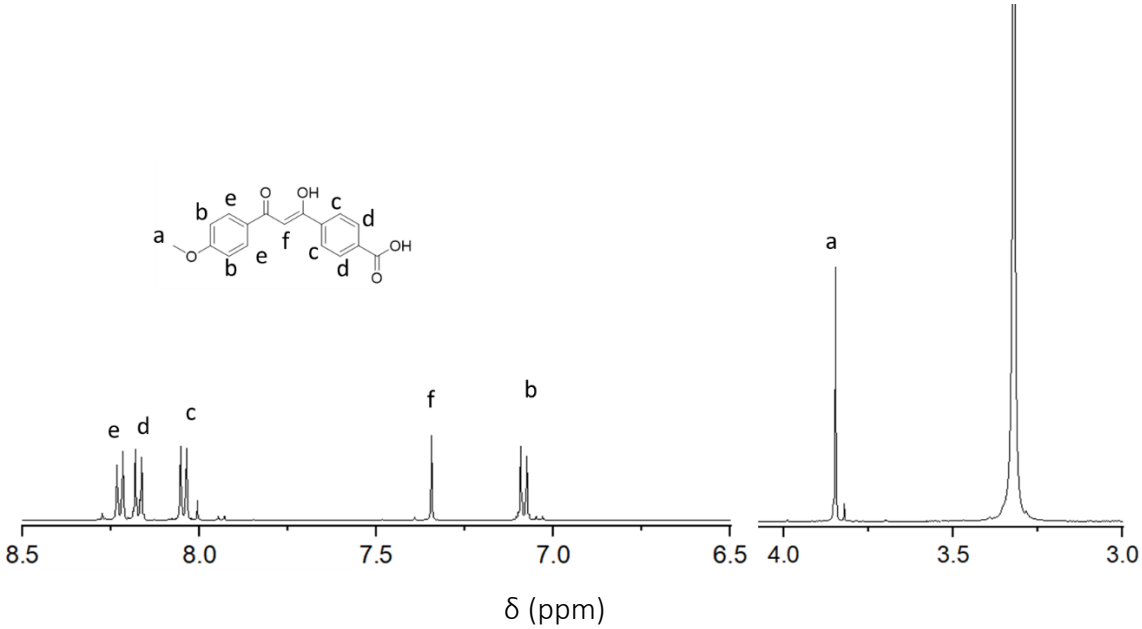

Synthesis of P-3 N,N'-((1S,2S)-cyclohexane-1,2-diyl)bis(4-((Z)-1-hydroxy-3-(4-methoxyphenyl)-3-oxoprop-1-en-1-yl)benzamide) and N,N'-((1R,2R)-cyclohexane-1,2-diyl)bis(4-((Z)-1-hydroxy-3-(4-methoxyphenyl)-3-oxoprop-1-en-1-yl)benzamide)

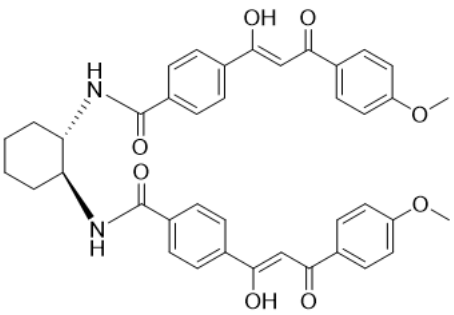

Compound P-2 (600mg, 2.2 eq.) was loaded in flame dried flask and dissolved in 5ml of dry THF under nitrogen atmosphere. Diethylcyanophosphate (DECP) (300 µL, 2.2 eq.) and Et_3N (297µL, 2.2 eq.) were added dropwise, and the solution was stirred for 15mins [2]. In a separate flask, (*R/S*) Cyclohexane diamine (104.5mg, 1eq) was dissolved in 3mL of dry THF and added dropwise to reaction vessel. The medium was stirred for 48 hours at room temperature. Excess solvent was removed in vacuo and the crude was extracted with DCM (100mL). The compound was washed with distilled water (100mL, twice) and dried with $MgSO_4$. Crude solution was purified with silica gel column chromatography using EtOAc/Hexane (40/60) as eluent. The desired compound was obtained with 47% yield (S) and 21% yield (R).

^{1}H-NMR (400MHz, $CDCl_3$): δ (ppm) 16.87 (s, 2H), 7.96 (d, J=8.0 Hz, 8H), 7.82 (d, J=8.0 Hz, 4H), 6.97 (d, J=8.0 Hz, 4H), 6.86 (d, J=4.0 Hz, 2H), 6.77 (s, 2H), 4.05 (m, 2H), 3.88 (s, 6H), 2.26(m, 2H), 1.89 (m, 2H), 1.46 (m, 4H).

^{13}C-NMR (150MHz, $CDCl_3$/TMS): 187.1, 182.0, 167.5, 163.6, 138.3, 137.1, 129.6, 128.1, 127.3, 127.2, 114.1, 93.0, 55.6, 54.9, 32.4, 24.9. MALDI-TOF mass spectrometry $C_{40}H_{38}N_2O_8$ $[M+Na]^+$: m/z =697.258 (calculated: 697.253).

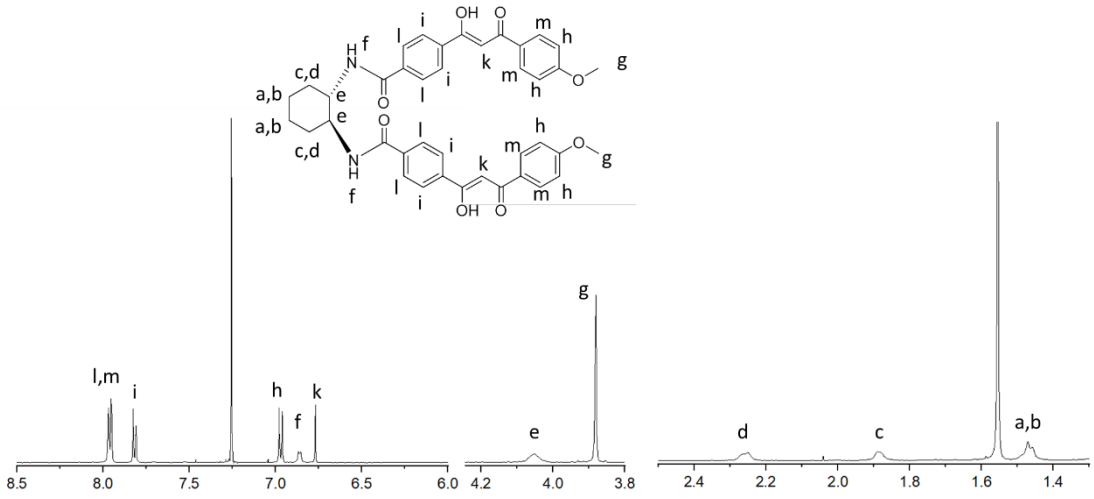

Synthesis of Para (S/R)-Cy DFB 4-(2,2-difluoro-6-(4-methoxyphenyl)-2H-1l3,3,2l4-dioxaborinin-4-yl)-N-((1R,2R)-2-(4-(2,2-difluoro-6-(4-methoxyphenyl)-2H-1l3,3,2l4-dioxaborinin-4-yl)benzamido)cyclohexyl)benzamide and 4-(2,2-difluoro-6-(4-methoxyphenyl)-2H-1l3,3,2l4-dioxaborinin-4-yl)-N-((1S,2S)-2-(4-(2,2-difluoro-6-(4-methoxyphenyl)-2H-1l3,3,2l4-dioxaborinin-4-yl)benzamido)cyclohexyl)benzamide

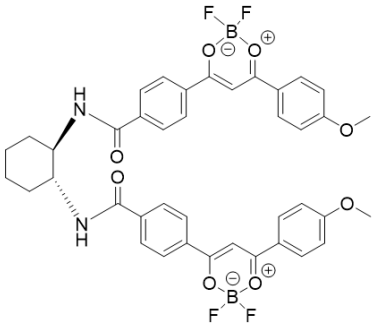

(R/S) P-3 (50mg, 1 eq.) and DIEA (51.6 µL, 4 eq.) were dissolved in dry DCM (5ml) in a flame dried flask and under nitrogen atmosphere. $BF_3 \cdot O(C_2H_5)_2$ in DCM (55µL, 6 eq.) was added dropwise to the flask and the reaction was monitored using TLC. After completion, excess DCM was removed in vacuo and the crude sample was purified with silica gel column chromatography using EtOAc/Hexane (50/50) as eluent. Pure enantiomers (R/S) refer to (1S,2S) -(+)-1,2-diamino cyclohexane and (1R,2R) -(+)-1,2-diamino cyclohexane moiety. The target compound was obtained with 63% yield (S) and 60% yield (R).

Para (S/R)-Cy DFB Analysis: R and S enantiomers shows identical NMR and HRMS.

^{1}H-NMR (600MHz $CDCl_3$/TMS): δ (ppm) 8.03 (d, *J*=9.2 Hz, 4H), 7.82 (d, *J*=8.8 Hz, 4H), 7.72 (d, *J*=8.8 Hz, 4H), 7.43 (m, 2H), 7.08 (s, 2H), 6.92 (d, *J*=8.8 Hz, 4H), 4.19 (m, 2H), 3.90 (s, 6H), 2.27 (m, 2H), 1.96 (m, 2H), 1.49 (m, 4H).

^{13}C-NMR (150MHz $CDCl_3$/TMS) 182.9, 179.3,167.2, 166.1, 139.1, 134.7, 132.1, 128.7, 127.5, 123.9, 114.7, 93.2, 55.9, 54.9, 32.1, 29.8, 25.1.

^{11}B NMR (190MHz, δ ppm ref. 0 ppm), (s): δ (ppm) 0.28 (s).

^{19}F NMR (600MHz, ppm ref. -161.6) δ (ppm) -139.1 (s), -139.2 (s).

HRMS (Spiral-TOF): $C_{40}H_{36}B_2F_4N_2O_8$ $[M+Na]^+$: m/z = 793.2502 (calculated 793.2499).

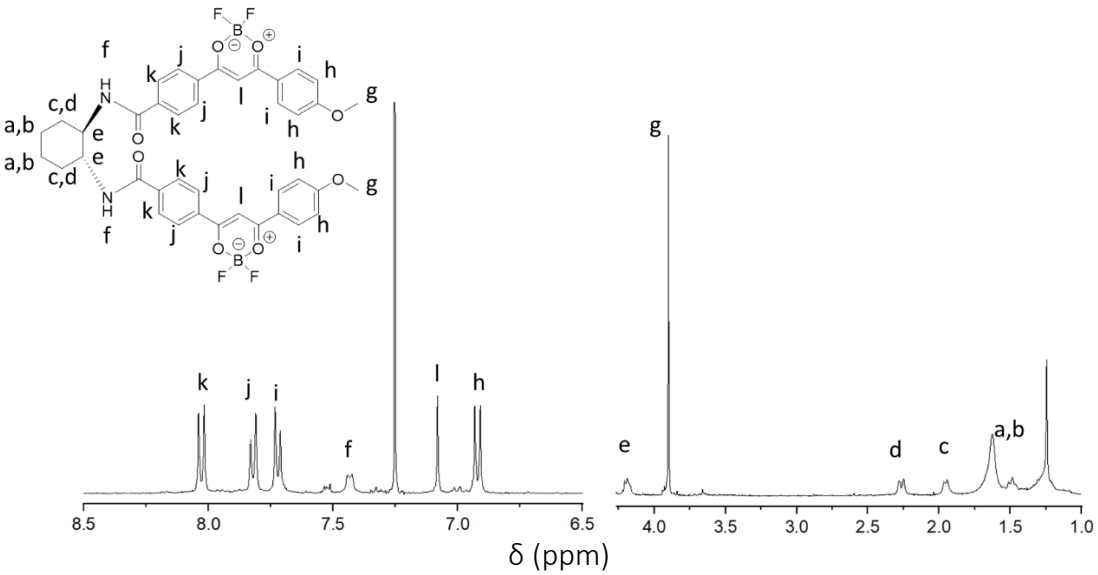

Synthesis of meta (*S/R)*-Cy DFB

methyl (Z)-3-(1-hydroxy-3-(4-methoxyphenyl)-3-oxoprop-1-en-1-yl)benzoate

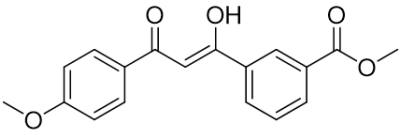

The synthesis of (*R/S*) meta-cyclohexane diamine 2-DFB was synthesized using the same steps as for (*R/S*) para cyclohexane diamine 2-DFB. Dimethyl isophthalate was used instead of dimethyl terephthalate to synthesize pre-cursor M1 with the yield of 78%.

^{1}H-NMR (500MHz, $CDCl_3$): 16.98 (s,1H), 8.60 (s,1H), 8.19 (t, *J*=8.0, 2H), 8.00 (d, *J*=8.0, 2H), 7.58 (t, *J*=8.0, 1H), 7.00 (d, *J*=8.0, 2H), 6.84 (s, 1H), 3.97 (s, 3H), 3.90 (s, 3H).

^{13}C-NMR (150MHz, $CDCl_3$/TMS): 186.66, 182.81, 166.55, 163.53, 136.05, 133.00, 131.37, 130.75, 129.57, 129.01, 128.14, 128.03, 114.13, 92.65, 55.62, 55.52.

MALDI-TOF mass spectrometry $C_{18}H_{16}O_5$ $[M+H]^+$: m/z =313.124 (calculated: 313.100).

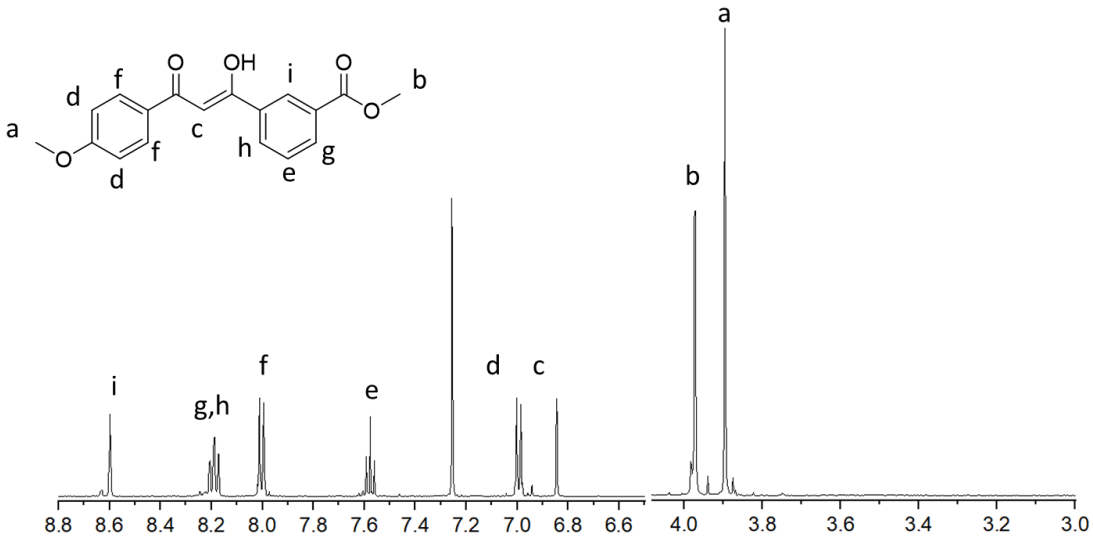

δ (ppm)

Synthesis of M-2
(Z)-3-(1-hydroxy-3-(4-methoxyphenyl)-3-oxoprop-1-en-1-yl)benzoic acid

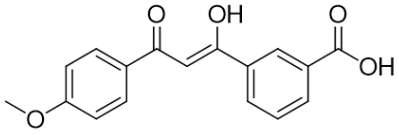

Crude powder of M1 was used for saponification forming M2. The desired compound was obtained after saponification with 50.4% yield. ^{1}H-NMR (400MHz, DMSO): δ (ppm) 17.28 (s,1H), 13.25 (s, 1H), 8.57 (s, 1H), 8.44 (s, 1H), 8.39 (d, *J*=6.4, 1H), 8.17 (d, *J*=6.4, 1H), 8.13 (d, *J*=6.4, 1H), 7.66 (t, *J*=6.4, 1H), 7.61 (t, *J*=6.4, 1H), 7.31 (s,1H), 7.07 (d, *J*=6.4, 1H), 3.84 (s, 3H).

MALDI-TOF mass spectrometry $C_{17}H_{14}O_5$ $[M+H]^+$: m/z =299.128 (calculated: 299.084).

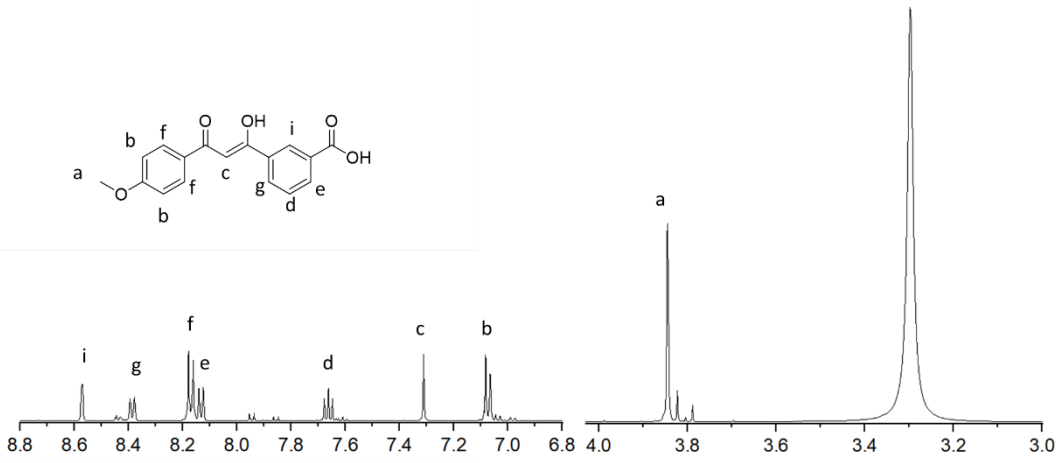

δ (ppm)

Synthesis of M-3

N,N'-((1S,2S)-cyclohexane-1,2-diyl)bis(3-((Z)-3-hydroxy-3-(4-methoxyphenyl)acryloyl)benzamide) and N,N'-((1R,2R)-cyclohexane-1,2-diyl)bis(3-((Z)-3-hydroxy-3-(4-methoxyphenyl)acryloyl)benzamide)

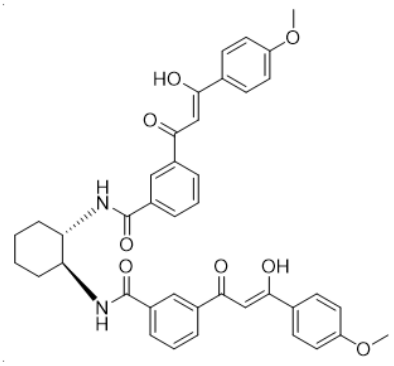

The precursor M-3 was obtained with 17% yield (S) and 20% yield (R):

^{1}H-NMR (400MHz, $CDCl_3$): δ (ppm) 16.93 (s, 2H), 8.32 (s, 2H), 8.04 (d, *J*=6.4, 2H), 7.98 (d, *J*=8.0, 4H), 7.92 (d, *J*=6.4, d), 7.47 (t, *J*=6.4, 2H), 6.98 (m, 2H), 6.93 (d, *J*=6.4, 4H), 6.87 (s,2H), 4.06 (m,2H), 3.86 (s, 6H), 2.29 (m, 2H), 1.88 (m, 2H), 1.47 (4H, m).

^{13}C-NMR (150MHz, $CDCl_3$/TMS): 186.5, 182.8, 163.5, 136.1, 130.8, 130.0, 129.6, 129.2, 127.9, 125.4, 114.1, 92.7, 55.6, 55.0, 32.4, 24.9.

MALDI-TOF mass spectrometry $C_{40}H_{38}N_2O_8$ $[M + Na]^+$: m/z =697.257 (calculated: 697.253)

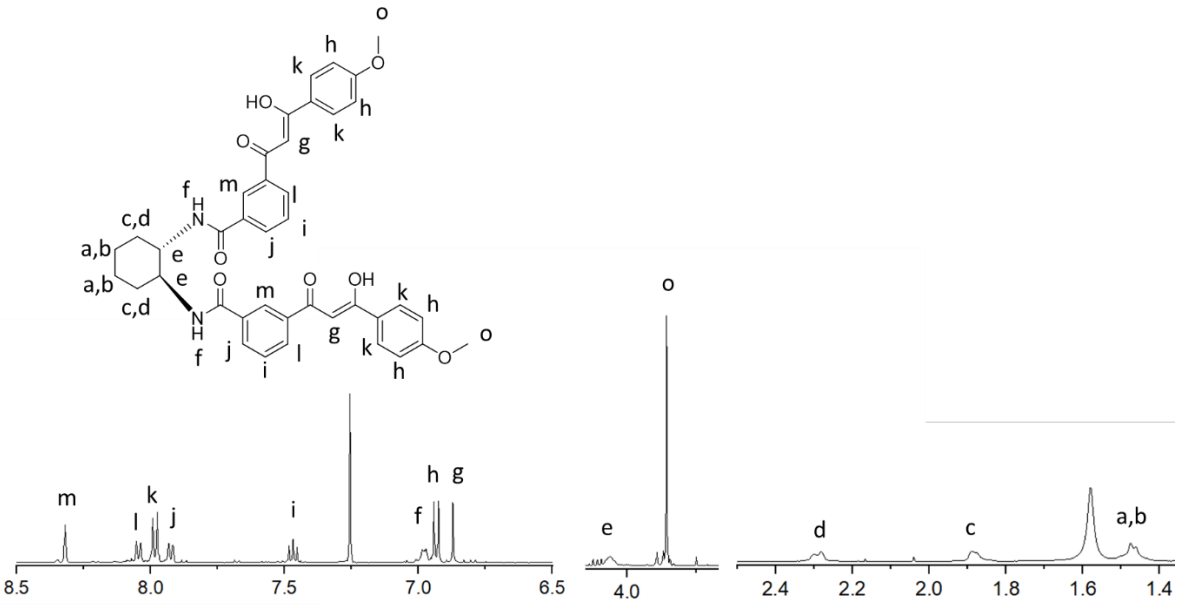

δ (ppm)

Meta (*S/R)*-CyDFB Analysis:

N,N'-((1R,2R)-cyclohexane-1,2-diyl)bis(3-(2,2-difluoro-6-(4-methoxyphenyl)-2H-1,3l3,2l4-dioxaborinin-4-yl)benzamide) and N,N'-((1S,2S)-cyclohexane-1,2-diyl)bis(3-(2,2-difluoro-6-(4-methoxyphenyl)-2H-1,3l3,2l4-dioxaborinin-4-yl)benzamide)

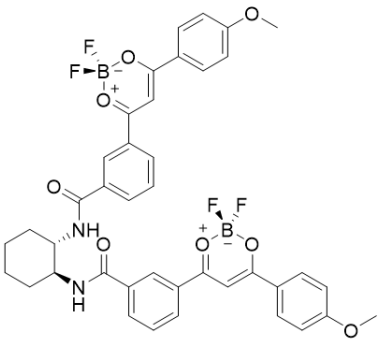

Meta (R/S) cyclohexane DFB were obtained using the same synthetic method as for para. R and S enantiomers shows identical results for NMR and HRMS.

^{1}H-NMR (600MHz, $CDCl_3$/TMS): δ (ppm) 8.41 (s, 2H), 8.15 (d, *J*=12.0, 6H), 8.00 (d, *J*=12, 6H), 7.50 (t, *J*=7.2, 2H), 7.22 (s, 2H), 7.10(m, 2H), 6.95 (d, *J*=6.0, 4H), 4.06 (m, 2H), 3.90 (s, 6H), 2.28 (m, 2H), 1.87 (m, 2H), 1.43 (m, 2H), 1.22 (m, 2H).

^{13}C-NMR (150MHz, $CDCl_3$/TMS): 183.0, 179.9, 167.1, 166.2, 135.1, 133.1, 132.7, 132.2, 131.4, 129.8, 126.7, 123.9, 114.8, 92.9, 55.9, 55.2, 32.3, 24.9.

^{11}B NMR (190MHz, δ ppm ref. 0 ppm), (s): δ (ppm) 0.28(s).

^{19}F NMR (600MHz, ppm ref. -161.6) δ (ppm) -139.4 (s), -139.5 (s).

HRMS (Spiral-TOF): $C_{40}H_{36}B_2F_4N_2O_8$ $[M + Na]^+$: m/z =793.2505 (calculated 793.2499).

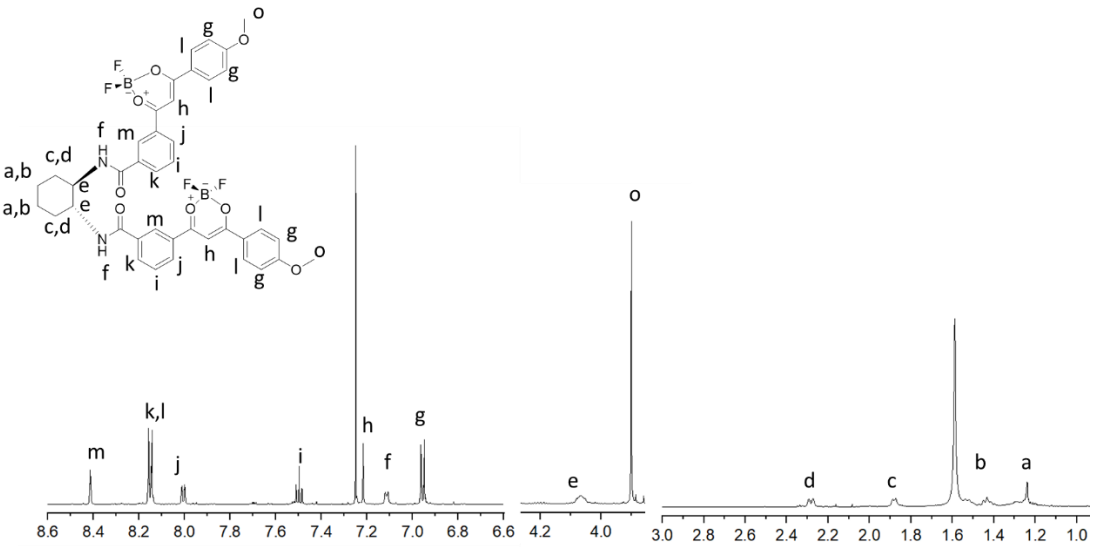

δ (ppm)

6.1.2 Synthesis of Compounds in Chapter 3

Synthesis of Cydiamine-BOC (BOC protection):
tert-butyl ((1S,2S)-2-aminocyclohexyl)carbamate

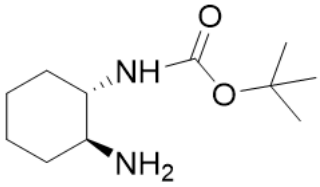

Cyclohexane diamine (2.4g, 1 eq.) was dissolved in 6.3mL methanol and stirred until dissolved. Ethereal HCl was added dropwise (2M, 10.5mL) to the solution and stirred for 15 minutes. Deionized water (2mL) was added to the solution and extended the mixing for another 30 minutes. In a separate flask, tert-butyloxycarbonyl protecting group (tBOC) was dissolved in 10 mL MeOH and slowly added to the cyclohexane diamine solution and stirred at room temeprature for 2 hours. Excess amount of diethyl ether was added until white precipitate forms. The precipitate was collected and washed with diethyl ether (10 mL three times) to remove unreacted cylohexane diamine. The precipitate suspended in 2M NaOH (20mL) then extracted with 30mL DCM. The solution was washed with DI water for three times (30 mL) and dried over magnesium sulfate. Excess solvents were removed under vacuum. Off-white powder was collected with 49% yield.[3]

^{1}H-NMR (500MHz, $CDCl_3$/TMS): δ (ppm) 1.08, (m, 2H), 1.23, (m, 2H), 1.43 (s, 9H), 1.55 (s, 2H), 1.69 (m, *J*=11.5 2H), 1.97 (m, *J*=12.5, 2H), 2.30 (m, 1H), 3.12 (m, 1H), 4.42 (s, 1H).
13C-NMR (150MHz, CDCl3/TMS): δ (ppm) 156.24ppm, 79.41ppm, 57.70ppm, 55.82ppm, 35.29ppm, 33.02ppm, 28.49ppm, 25.29ppm, 25.16ppm
MALDI-TOF mass spectrometry $C_{11}H_{22}N_2O_2$[M + Na]$^+$: m/z = 237.138 (calculated: 237.158)

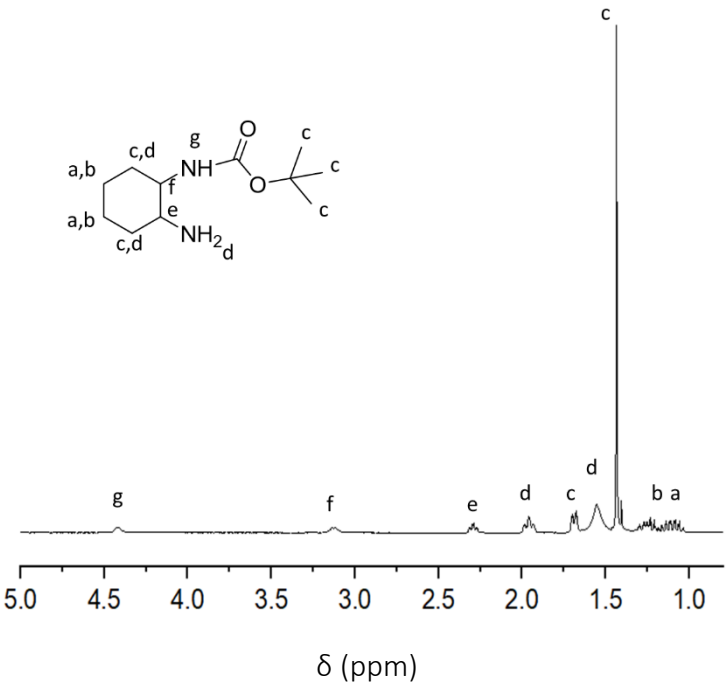

Synthesis of Cydiamine-BOC β-keto enol:
tert-butyl((1S,2S)-2-(4-((Z)-1-hydroxy-3-(4-methoxyphenyl)-3-oxoprop-1-en-1-yl)benzamido)cyclohexyl)carbamate

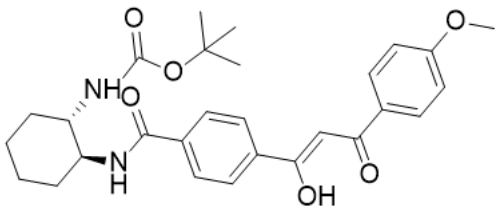

The intermediate cydiamine-BOC (2.15g, 1.1 eq.) was loaded in flame dried flask and dissolved in 8mL of dry THF under nitrogen atmosphere. Diethylcyanophosphate (DECP) (1.6mL, 1.3 eq.) and Et_3N (1.7mL, 1.3 eq.) were added dropwise, and the solution was stirred for 15minutes at room temperature. In another flask, P-1 intermediate was dissolved (2.72g, 1 eq.) in 8mL dry THF and added dropwise to the cydiamine-BOC medium.[4] The medium was stirred for 48 hours at room temperature. Excess solvent was removed in vacuum and the crude was extracted with DCM (100mL). The compound was washed with distilled water (100mL, twice) and dried over $MgSO_4$. Crude solution was purified with silica gel column chromatography using EtOAc/Hexane (40/60) as eluent. The solvent was dried under vacuum with 32% yield.

^{1}H-NMR (500MHz, $CDCl_3$/TMS): δ (ppm) 1.25 (m, 4H), 1.43 (s, 9H),1.76 (m, 1H), 1.82 (m, 1H), 2.01 (m, 1H), 2.33 (m, 1H), 3.55 (m, 1H), 3.74 (m, 1H), 3.89 (s, 3H), 4.65 (d, *J*=9.0 1H), 7.04 (d, *J*=9.0 2H), 7.11 (s, 1H), 7.48 (d, *J*=7.5 1H), 7.99 (d, *J*=9.0, 2H), 8.13 (d, *J*=9.0 2H), 8.16 (d, *J*=9.0 2H)

13C-NMR (150MHz, CDCl3/TMS): δ (ppm) 187.05, 182.41, 166.26, 163.52, 157.40, 137.95, 137.39, 129.57, 128.20, 127.49, 127.02, 114.12, 92.98, 80.16, 57.05, 55.62, 53.32, 32.51 28.38, 25.26, 24.48, 18.54.

MALDI-TOF mass spectrometry $C_{28}H_{34}N_2O_6$[M + Na] $^+$: m/z = 517.220 (calculated: 517.231)

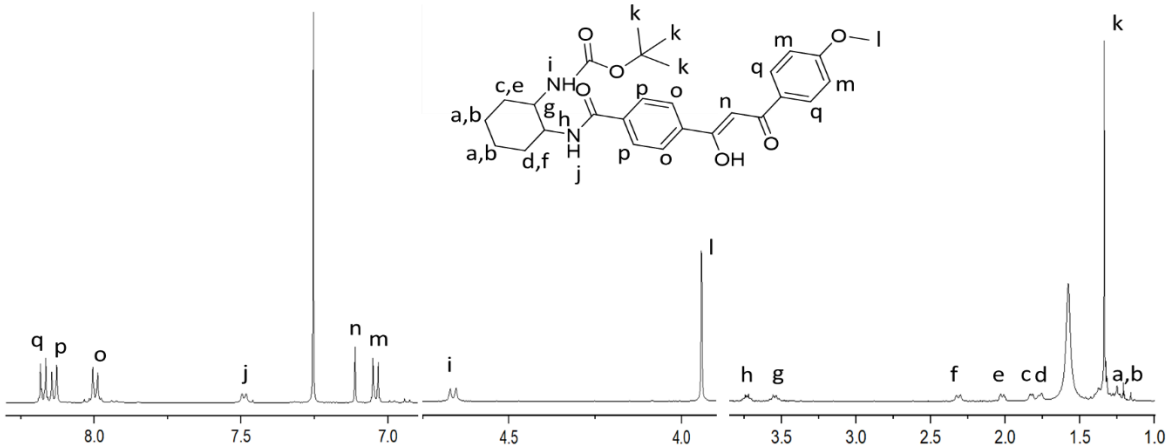

δ (ppm)

Synthesis of Cydiamine mono β-keto enol (BOC de-protection):
N-((1S,2S)-2-aminocyclohexyl)-4-((Z)-1-hydroxy-3-(4-methoxyphenyl)-3-oxoprop-1-en-1-yl)benzamide

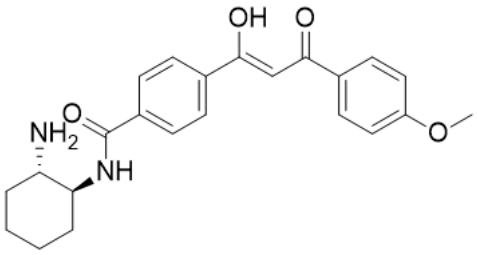

The protecting group (BOC) in intermediate was removed by dissolving the cydiamine-BOC β-diketonate (400mg) in 8mL of trifluoroacetic acid:DCM solution (1:2) and stirring at room temperature for 2hours. [5] The solution was neutralized with ammonium hydroxide solution until pH reached 9-10. The compound was extracted with DCM (50mL) and washed with deionized water (100mL) for three times then dried over magnesium sulfate. The excess solvent was removed under vacuum with 81% yield.

^{1}H-NMR (500MHz, Acetonitrile-D3/TMS): δ (ppm) 1.25 (m, 4H), 1.39 (m, 1H), 1.78 (m, 2H), 2.02 (m, 1H), 2.17 (m, 1H), 2.56 (m, 1H), 3.74 (m, 2H), 3.88 (m, 3H), 6.26 (s, 1H), 6.83 (s, 1H), 6.98 (d, *J*=9, 2H), 7.87 (d, *J*=9, 2H), 7.99 (dd, *J*=9, 2H),

^{13}C-NMR (150MHz, Acetonitrile-D3/TMS) : δ(ppm) 187.12, 182.15, 166.99, 163.57, 138.22, 137.74, 129.59, 128.12, 127.36, 127.23, 114.14, 93.01, 56.69, 55.62, 35.93, 32.57, 25.08.

MALDI-TOF mass spectrometry $C_{23}H_{26}N_2O_4[M+Na]^+$: m/z = 417.176 (calculated: 417.179).

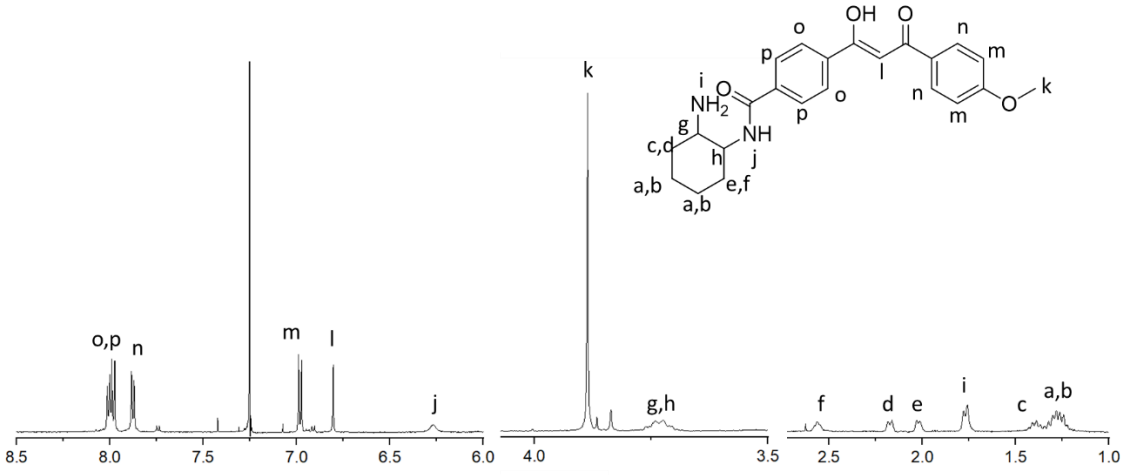

Synthesis of Cydiamine mono-DFB

N-((1S,2S)-2-aminocyclohexyl)-4-(2,2-difluoro-6-(4-methoxyphenyl)-2H-1l3,3,2l4-dioxaborinin-4-yl)benzamide

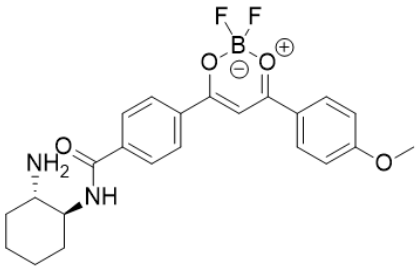

Cydiamine mono β-diketonate (250mg, 1 eq.) and DIEA (0.22 mL, 2 eq.) were dissolved in dry DCM (8mL) in a flame dried flask and under nitrogen atmosphere. $BF_3 \cdot O(C_2H_5)_2$ in DCM (0.31 mL, 4 eq.) was added dropwise to the flask and the reaction and was stirred at room temperature for 12 hours. Excess DCM was removed in vacuo and the crude sample was purified with silica gel flash column chromatography using EtOAc/petroleum ether (50/50) as eluent. The solvent was dried under vacuum and the target compound was collected with 44% yield.[6]

^{1}H-NMR (500MHz, Acetonitrile-D3/TMS): δ (ppm) 1.35 (m, 4H), 1.53 (m, 4H), 1.80 (m, 3H), 3.13 (m, 1H), 3.87 (s, 3H), 3.92 (m, 1H), 7.14 (d, 2H), 7.32 (d, *J*=11, 1H), 7.43 (s, 1H), 8.01 (d, *J*=9, 2H), 8.27 (dd, *J*=9, 4H).

13C-NMR (150MHz, Acetonitrile-D3/TMS) 187.12, 182.15, 167.02, 163.57, 138.22, 129.59, 128.12, 127.36, 127.36, 127.23, 114.22, 114.14, 113.41, 93.52, 90.03, 56.69, 55.62, 32.61, 25.18, 25.09

HRMS Spiral-TOF mass spectrometry $C_{23}H_{25}BF_2N_2O_4$ $[M+Na]^+$:m/z =465.171 (calculated: 465.177)

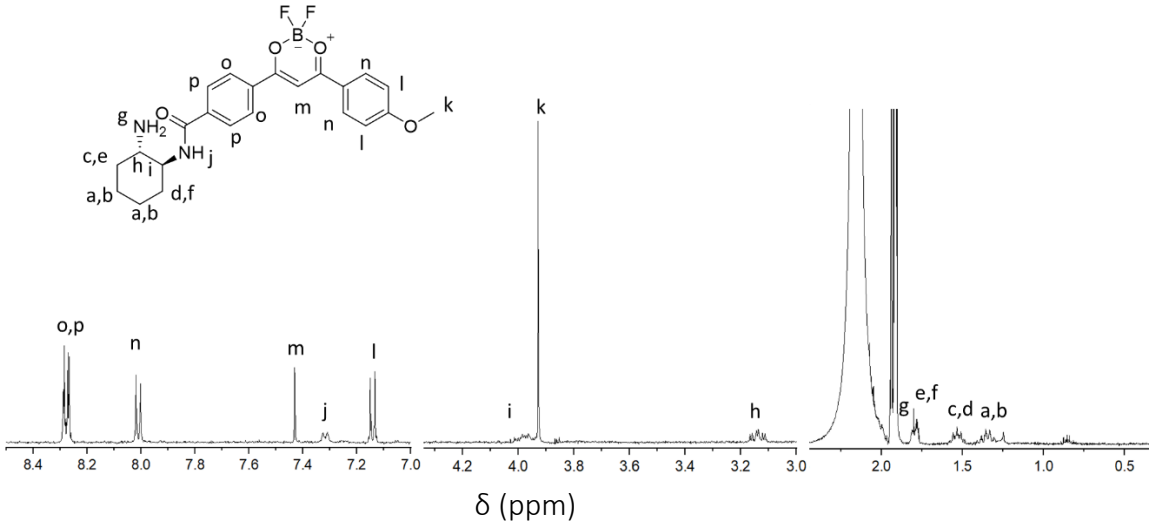

6.1.3 Synthesis of Compounds in Chapter 4

Synthesis of Cydiester β-keto enol: cyclohexane-1,2-diyl bis(4-((Z)-1-hydroxy-3-(4-methoxyphenyl)-3-oxoprop-1-en-1-yl)benzoate)

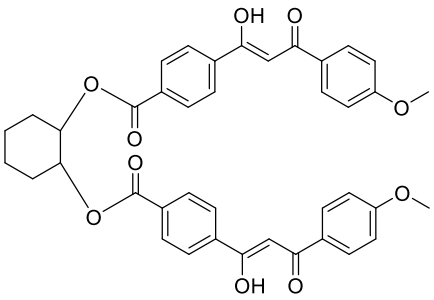

Racemic cydiester di β-keto enol was synthesized by esterification of P-1 intermediate with 1,2-cyclohexane diol.[7] 1,2-cyclohexane diol (51.9 mg, 1 eq.) and β-keto enol acid (400mg, 3 eq.) was loaded in pre-dried flask under atmospheric condition and dissolve in dry THF (10ml). After dissolving the cyclohexane diol, 4-dimethylaminopyridine (DMAP) (70mg, 1.2eq) and N, N-Dicyclohexylcarbodiimide (DCC) (0.21 mL, 3 eq.) was added to the flask and heat the solution to 40°C for 12hours with stirring.[7] The solution was cooled down to room temperature and the compound was extracted with DCM and washed with DI water for three times. The organic phase was collected and dried over magnesium sulfate. The compound was purified by column chromatography using hexane and ethyl acetate as eluent (30:70). Yellowish powder was collected with 32% yield.

^{1}H-NMR (500MHz, $CDCl_3$/TMS): δ (ppm) 1.25 (m, 2H), 1.69 (m, 2H), 1.86 (m, 2H), 2.27 (d, *J*=13, 2H), 3.89 (s, 6H), 5.28 (m, 2H), 6.77 (s, 2H), 6.96 (d, *J*=9, 2H), 7.93 (d, *J*=9, 2H), 7.97 (d, *J*=9, 2H), 8.02 (d, *J*=9, 2H), 16.86 (s, 2H).

^{13}C-NMR (150MHz, $CDCl_3$/TMS): 187.42, 181.74, 165.41, 163.59, 139.48, 132.98, 129.90, 129.62, 128.14, 126.92, 114.13, 93.27, 74.92, 55.61, 30.37, 23.64.

MALDI-TOF mass spectrometry $C_{40}H_{36}O_{10}$ $[M + Na]^+$: m/z =699.208 (calculated: 699.211).

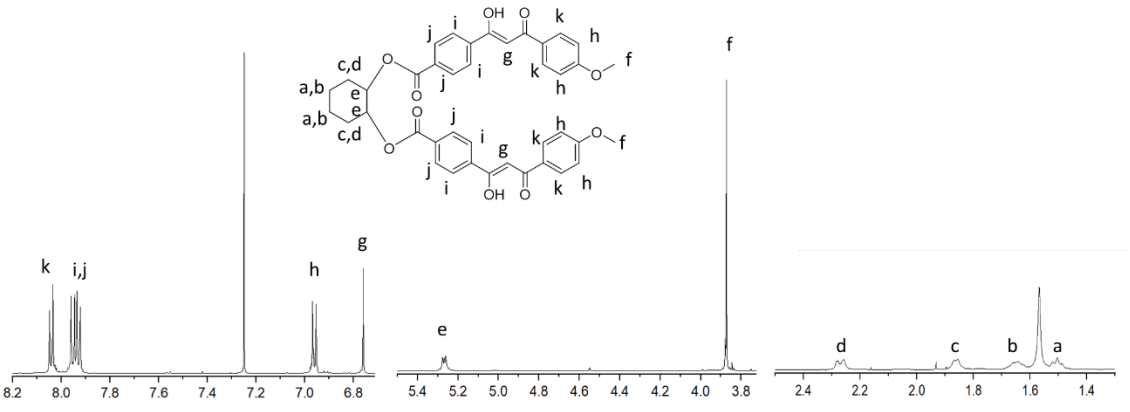

Synthesis of Cydiester di-DFB

2-((4-(2,2-difluoro-6-(4-methoxyphenyl)-2H-1l3,3,2l4-dioxaborinin-4-yl)benzoyl)oxy)cyclohexyl4-(2,2-difluoro-6-(4-methoxyphenyl)-2H-1l3,3,2l4-dioxaborinin-4-yl)benzoate

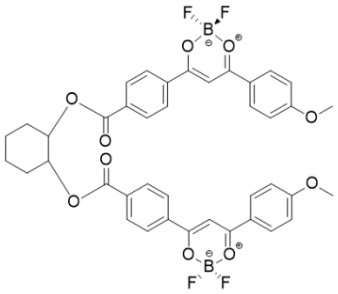

Racemic cydiester di β-diketonate (50mg, 1 eq.) and DIEA (51.6 µL, 4 eq.) were dissolved in dry DCM (5ml) in a flame dried flask and under nitrogen atmosphere. $BF_3 \cdot O(C_2H_5)_2$ in DCM (55µL, 6 eq.) was added dropwise to the flask and the reaction and was stirred at room temperature for 12 hours. Excess DCM was removed in vacuo and the crude sample was purified with silica gel column chromatography using EtOAc/Hexane (50/50) as eluent. The target compound was obtained with 74% yield.

^{1}H-NMR (500MHz, $CDCl_3$/TMS): δ (ppm) 1.67 (m, 2H), 1.88 (m, 2H), 2.01 (m, 2H), 2.27 (m, 2H), 3.93 (s, 6H), 5.29 (m, 2H), 7.02 (d, 4H), 7.07 (s, 2H), 8.08 (s, 8H), 8.12 (d, 4H).

^{13}C-NMR (150MHz, $CDCl_3$/TMS) 187.7,181.25, 163.39,132.36,132.14,131.02, 130.12, 129.89, 129.61, 128.44, 126.92, 114.93, 114.13, 113.84, 93.27, 60.48, 58.60, 55.62, 44.29, 32.02, 22.78, 18.53, 14.29, 12.23.

HRMS Spiral-TOF mass spectrometry $C_{40}H_{34}B_2F_4O_{10}$ $[M + Na]^+$: m/z =795.2178 (calculated: 795.2172).

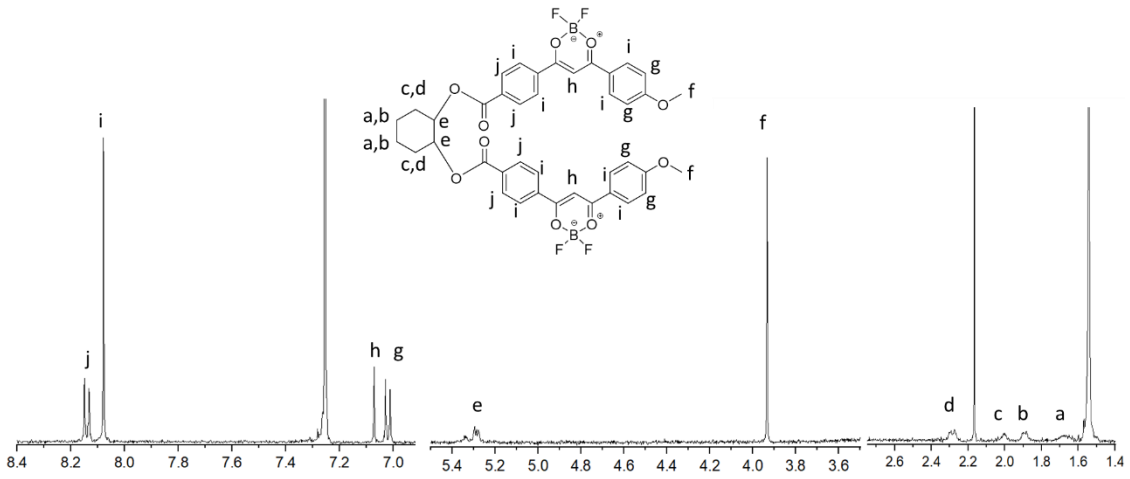

δ (ppm)

6.2 Fluorescence Measurements

Steady-State Photophysical Measurements

All absorbance and emission measurements were conducted using spectroscopy grade solvent purchased from Fujifilm Wako Pure Chemicals Industries Ltd. without any purification. The absorbances were obtained using double beam UV-Vis Jasco V-760 and double beam spectrometers Cary 100. The emissions were measured using Jasco FP-8500, Horiba Jobin-Yvon spectrofluorometers Fluoromax FM3 and Fluorolog FL3-221 while the PLQY of aggregates were measured using integrating sphere made by Hamamatsu and calculated using system software U6039-05 ver.3.2.1.

Time-Resolved Fluorescence Measurements

Fluorescence decay curves were obtained by the time-correlated single-photon counting (TCSPC) method. The setup is composed of a titanium sapphire Ti:Sa oscillator (Spectra Physics, Maï Taï HP) emitting pulses of 100 fs duration at 780nm, 80MHz frequency. The laser pulses then pass through a pulse picker which implements acousto-optic modulator to pick up specific pulse to reduce the repetition rate at 4MHz. Then the signal was doubled at 390nm (solutions) and 350nm (solids/crystals) by focalizing the laser in a non-linear SHG crystal (GWU Lasertechnik, UHG-23-PSK). Then the beam passes through the sample solution after adjusting the excitation power with an intensity attenuator filter wheel. Fluorescence photons were detected at 90° through a monochromator and slit of 0.3mm (CVI Laser Corporation, Digikröm CM110) and a polarizer at magic angle by means of a micro channel plate photomultiplier (Hamamatsu, MCP-PMT R3809U-50), connected to a TCSPC module (Becker & Hickl, SPC-130-EMN). The instrumental response function was recorded before each decay measurement with a fwhm (full width at half-maximum) of ~25 ps. Time-correlated fluorescence decay data is finally processed and analyzed with the help of a software which implements the non-linear square method (Globals, Laboratory for Fluorescence Dynamics at the University of Illinois at Urbana-Champaign). Output for decays (τ_i) and pre-exponential factor (α_i) were obtained after Global analysis, while the fraction of intensity (f_i) was calculated based on the equation: $I\alpha_i\tau_i / \sum \alpha_i\tau_i$.

6.2.1 TCSPC Plots of Compounds in Chapter 2

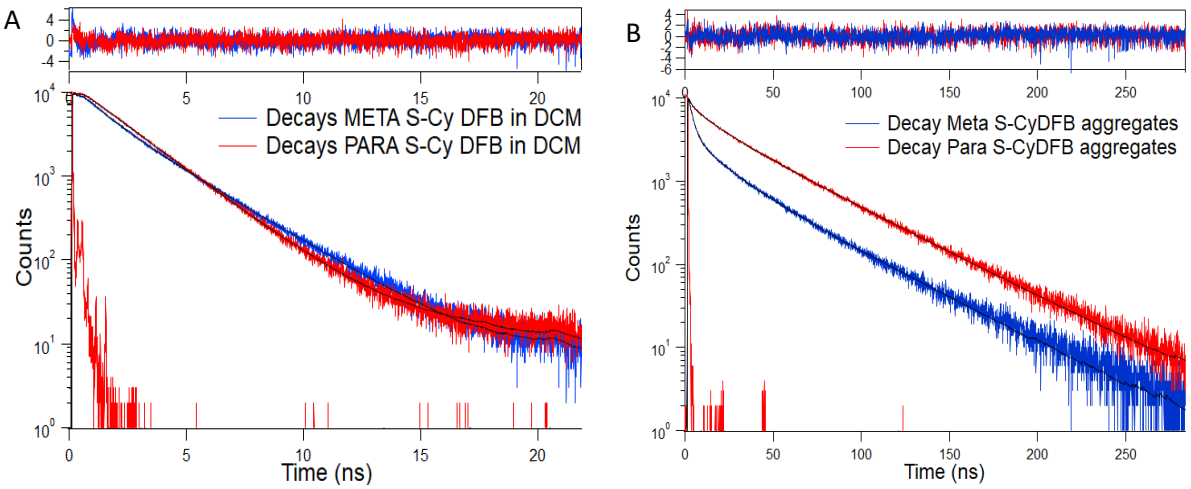

Figure 6.1. Time-resolved fluorescence decay of para and meta (*S*)-Cy DFB monomers measured with λ_{exc}=390nm/ λ_{em}=463nm (A) and para and meta (*S*)-Cy DFB aggregates measured with λ_{exc}=390nm/λ_{em}=550nm including the residuals (upper panel). The decays were fitted with satisfactory $X^2 < 1.2$.

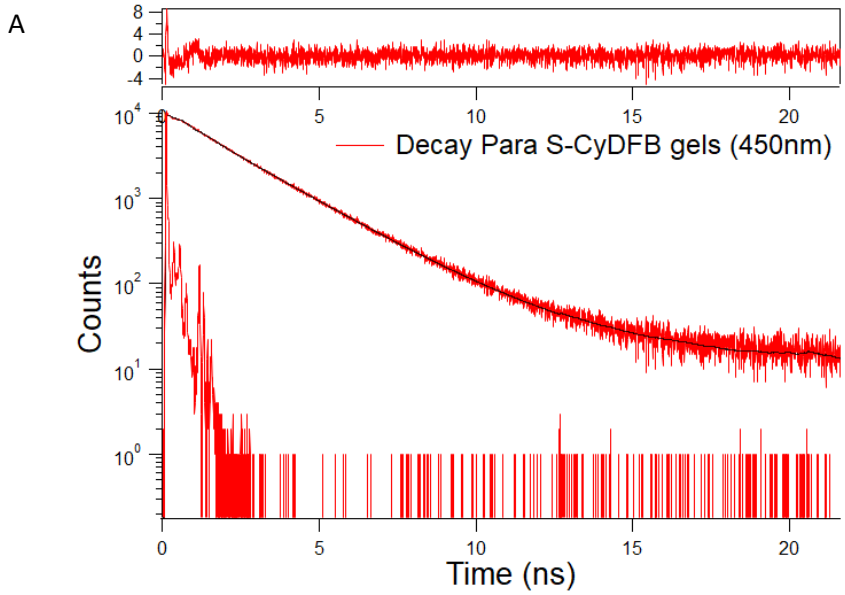

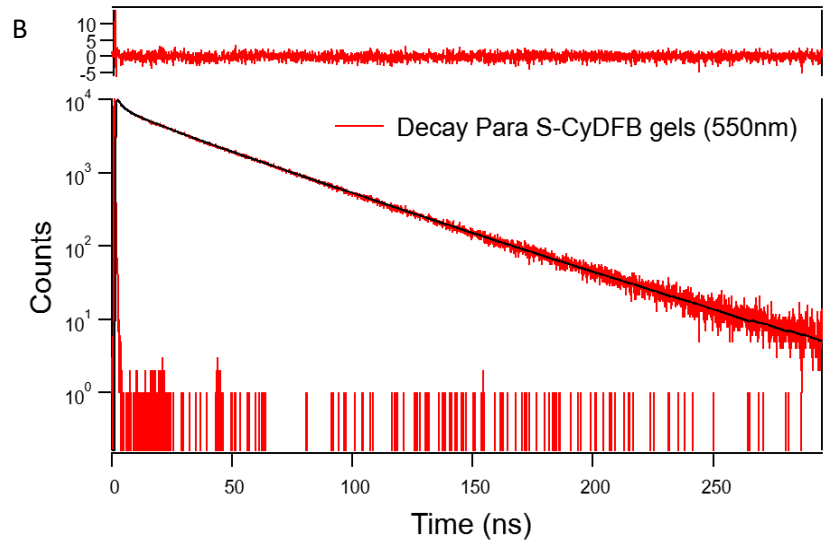

Figure 6.2. Time-resolved flurorescence decay of para (*S*)-Cy DFB gels measured at λ_{exc}=390nm/ λ_{em}=450nm with X^2 = 1.01 (A) and λ_{exc}=390nm/λ_{em}=550nm with X^2 =1.22 (B) and corresponding residuals (upper panel).

6.2.2. TCSPC Plots of Compounds in Chapter 3

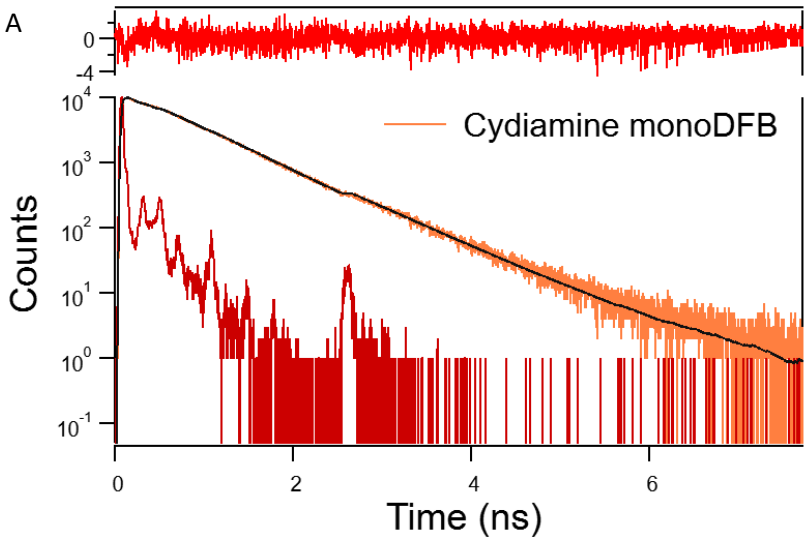

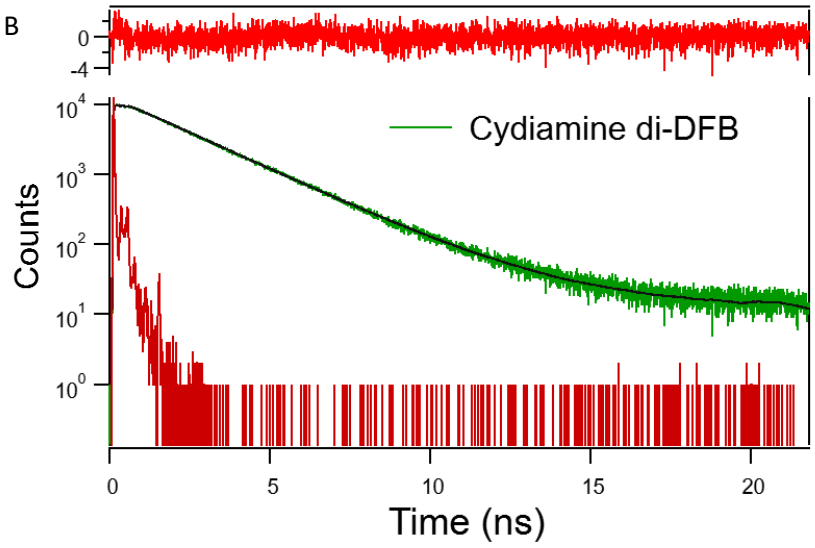

Figure 6.3 Time-resolved spectroscopy measurement plots of cydiamine mono-DFB solution in acetonitrile (λ_{exc}=390nm; λ_{em}=480nm; X^2 = 1.05) (a) and cydiamine di-DFB solution in DCM (λ_{exc}=390nm; λ_{exc}=463nm; X^2 = 1.09) (b). Residuals are shown in upper panel.

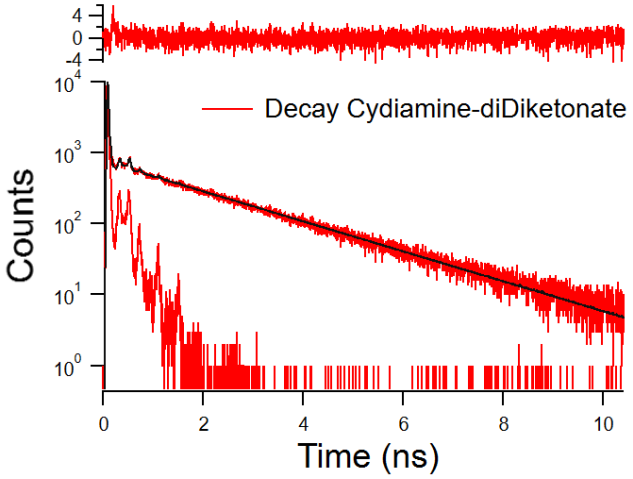

	τ_1 (a, f_1)	τ_2 (a_2, f_2)
Emission at 480nm	2.05	0.006
	(0.02, 0.87)	(0.98, 0.13)

Figure 6.4. Time-resolved flurorescence decay of para (*S*)-Cydiamine β-diketonate measured at λ_{em}=480nm; λ_{exc}=390nm) with X^2 = 1.24 with residuals shown in upper panel.

6.2.2. TCSPC Plots of Compounds in Chapter 4

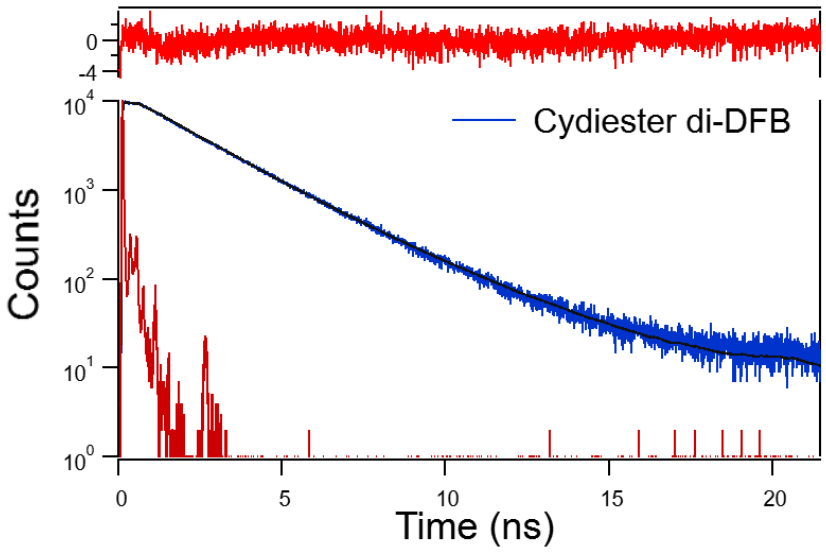

Figure 6.5 Time-resolved spectroscopy measurement plots of cydiester di-DFB solution (in DCM) λ_{exc}=390nm, λ_{em}=480nm, X^2= 1.13 with residual shown in upper panel.

Table 6.1. Normalized pre-exponential factors (a_n) and fraction of intensity (f_n) of cydiamine mono-DFB measured at different wavelength.

a. Crystals

Wavelength	τ_1 (a_1, f_1)	τ_2 (a_2, f_2)	τ_3 (a_3, f_3)	τ_4 (a_4, f_4)
500	15 (0.03,0.16)	7.5 (0.06, 0.17)	1.5 (0.08, 0.04)	0.5 (0.21, <0.01)
550	15 (0.23,0.56)	7.5 (0.33, 0.37)	1.5 (0.20, 0.05)	0.5 (0.21, <0.01)
580	15 (0.24, 0.45)	7.5 (0.28, 0.24)	1.5 (0.12, 0.02)	0.5 (0.07, <0.01)
600	15 (0.20, 0.34)	7.5 (0.22, 0.18)	1.5 (0.08, 0.02)	0.5 (0.02, <0.01)

τ_n decay time
a_n pre-exponential factor
f_n fraction of intensity
Excitation: 350nm; χ^2_R = 1.24

b. Smeared

Wavelength	τ_1 (a_1, f_1)	τ_2 (a_2, f_2)	τ_3 (a_3, f_3)	τ_4 (a_4, f_4)
500	22 (0.01, 0.12)	8.6 (0.05, 0.25)	1.2 (0.12, 0.09)	0.1 (0.30, 0.02)
550	22 (0.10, 0.41)	8.6 (0.31, 0.38)	1.2 (0.33, 0.08)	0.1 (0.26, 0.02)
580	22 (0.14, 0.41)	8.6 (0.40, 0.37)	1.2 (0.32,0.04)	0.1 (0.11, <0.01)
600	22 (0.13, 0.35)	8.6 (0.29, 0.27)	1.2 (0.20, 0.03)	0.1 (0.01, <0.01)

τ_n decay time
a_n pre-exponential factor
f_n fraction of intensity
Excitation: 350nm; χ^2_R = 1.25

c. Thermal annealed

Wavelength	τ_1 (a_1, f_1)	τ_2 (a_2, f_2)	τ_3 (a_3, f_3)	τ_4 (a_4, f_4)
500	21 (0.03, 0.20	11 (0.05, 0.20)	2.1 (0.09, 0.05)	0.1 (0.29, 0.01)
550	21 (0.25, 0.58	11 (0.31, 0.38)	2.1 (0.19, 0.03)	0.1 (0.25, <0.01)
580	21 (0.30, 0.49	11 (0.30, 0.26)	2.1(0.12, 0.02)	0.1 (0.05, <0.01)
600	21 (0.27, 0.39	11 (0.24, 0.18)	2.1 (0.06, 0.01)	0.1 (0.02, 0.03)

τ_n decay time
a_n pre-exponential factor
f_n fraction of intensity
Excitation: 350nm; χ^2_R = 1.11

d. Pristine powder

Wavelength	τ_1 (a_1, f_1)	τ_2 (a_2, f_2)	τ_3 (a_3, f_3)	τ_4 (a_4, f_4)
500	21 (0.03, 0.15)	10 (0.05, 0.15)	1.8 (0.07, 0.03)	0.2 (0.19, 0.01)
550	21 (0.26, 0.62)	10 (0.29, 0.33)	1.8 (0.18, 0.04)	0.2 (0.27, <0.01)
580	21 (0.32, 0.57)	10 (0.28, 0.23)	1.8 (0.12, 0.02)	0.2 (0.11, <0.01)
600	21 (0.30, 0.47)	10 (0.24, 0.17)	1.8 (0.07, 0.01)	0.2 (0.05, <0.01)

τ_n decay time
a_n pre-exponential factor
f_n fraction of intensity
Excitation: 350nm; χ^2_R = 1.08

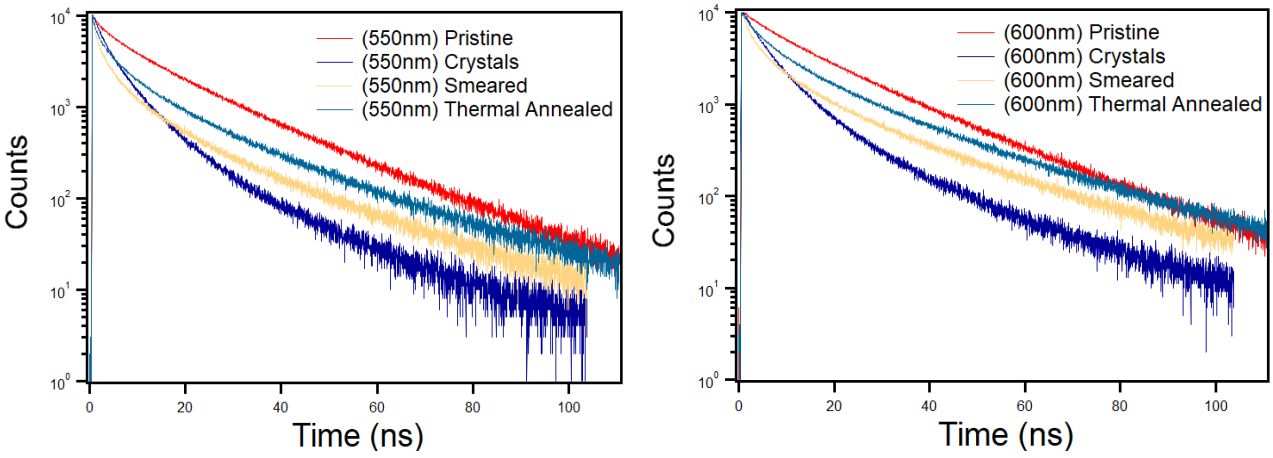

Figure 6.6. Time-resolved spectroscopy measurement plots of cydiamine mono-DFB crystals, smeared, thermal annealed and pristine powder measured at 550nm and 600nm (λ_{exc}=350nm).

Table 6.2. Normalized pre-exponential factors (a_n) and fraction of intensity (f_n) of cydiamine di-DFB measured at different wavelength.

a. Crystals

Wavelength	$\tau_1(a_1, f_1)$	$\tau_2(a_2, f_2)$	$\tau_3(a_3, f_3)$	$\tau_4(a_4, f_4)$
500	23 (0.01, 0.05)	7.1 (0.11, 0.35)	2.0 (0.32, 0.33)	0.2 (0.37, 0.05)
550	23 (0.03, 0.14)	7.1 (0.34, 0.57)	2.0 (0.42, 0.20)	0.2 (0.13, 0.01)
580	23 (0.03, 0.12)	7.1 (0.32, 0.41)	2.0 (0.28, 0.10)	0.2 (<0.01, <0.01)
600	23 (0.03, 0.10)	7.1 (0.27, 0.21)	2.0 (0.19, 0.06)	0.2 (0.08, <0.01)

τ_n decay time
a_n pre-exponential factor
f_n fraction of intensity
Excitation: 350nm; χ^2_R = 1.24

b. Smeared

Wavelength	$\tau_1(a_1, f_1)$	$\tau_2(a_2, f_2)$	$\tau_3(a_3, f_3)$	$\tau_4(a_4, f_4)$
500	23 (0.01, 0.14)	7.1 (0.04, 0.20)	2.0 (0.12, 0.18)	0.2 (0.45, 0.09)
550	23 (0.06, 0.41)	7.1 (0.16, 0.35)	2.0 (0.28, 0.16)	0.2 (0.45, 0.04)
580	23 (0.09, 0.41)	7.1 (0.18, 0.26)	2.0 (0.24, 0.10)	0.2 (0.27, 0.02)
600	23 (0.08, 0.35)	7.1 (0.15, 0.18)	2.0 (0.20, 0.07)	0.2 (0.18, 0.01)

τ_n decay time
a_n pre-exponential factor
f_n fraction of intensity
Excitation: 350nm; χ^2_R = 1.24

c. Thermal annealed

Wavelength	$\tau_1(a_1, f_1)$	$\tau_2(a_2, f_2)$	$\tau_3(a_3, f_3)$	$\tau_4(a_4, f_4)$
500	23 (0.01, 0.15)	7.1 (0.04, 0.20)	2.0 (0.07, 0.09)	0.2 (0.36, 0.05)
550	23 (0.11, 0.52)	7.1 (0.25, 0.35)	2.0 (0.21, 0.09)	0.2 (0.41, 0.02)
580	23 (0.15, 0.49)	7.1 (0.26, 0.26)	2.0 (0.16, 0.05)	0.2 (0.25, 0.01)
600	23 (0.14, 0.38)	7.1 (0.19, 0.19)	2.0 (0.12, 0.03)	0.2 (0.14, 0.01)

τ_n decay time
a_n pre-exponential factor
f_n fraction of intensity
Excitation: 350nm; χ^2_R = 1.24

d. Pristine powder

Wavelength	$\tau_1(a_1, f_1)$	$\tau_2(a_2, f_2)$	$\tau_3(a_3, f_3)$	$\tau_4(a_4, f_4)$
500	26 (0.01, 0.11)	10 (0.11, 0.37)	3.0 (1.36, 0.24)	0.3 (0.41, 0.05)
550	26 (0.08, 0.29)	10 (0.34, 0.51)	3.0 (0.30, 0.13)	0.3 (0.23, 0.01)
580	26 (0.09, 0.28)	10 (0.35, 0.37)	3.0 (0.19, 0.06)	0.3 (0.08, <0.01)
600	26 (0.10, 0.23)	10 (0.29, 0.27)	3.0 (0.14, 0.04)	0.3 (0.02, <0.01)

τ_n decay time
a_n pre-exponential factor
f_n fraction of intensity
Excitation: 350nm; χ^2_R = 1.10

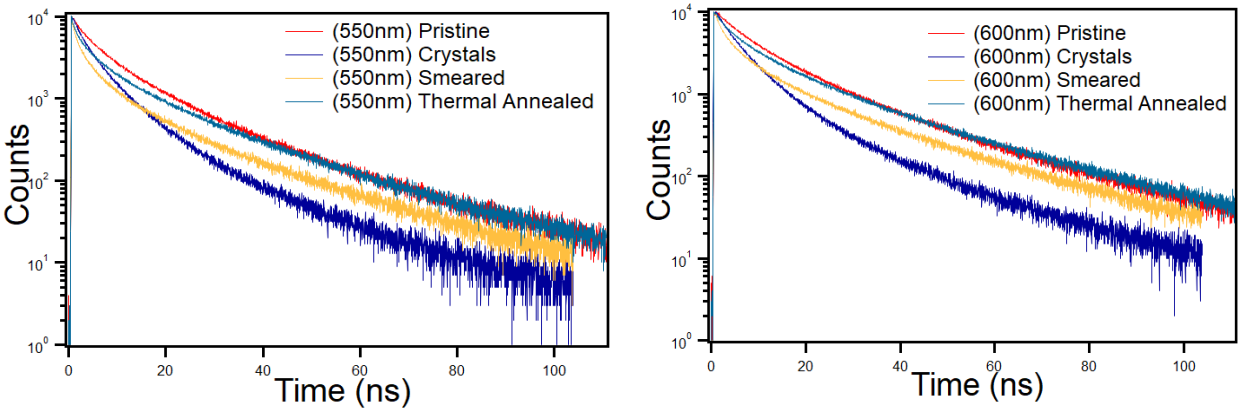

Figure 6.7. Time-resolved spectroscopy measurement plots of cydiamine di-DFB crystals, smeared, thermal annealed and pristine powder measured at 550nm and 600nm (excitation at 350nm).

Table 6.3. Normalized pre-exponential factors (a_n) and fraction of intensity (f_n) of cydiester di-DFB measured at different wavelength.

a. Crystals

Wavelength	$\tau_1 (a_1, f_1)$	$\tau_2 (a_2, f_2)$	$\tau_3 (a_3, f_3)$	$\tau_4 (a_4, f_4)$
500	9.2(<0.01, 0.03)	3.0 (0.25, 0.60)	0.95(0.40, 0.30)	0.3 (0.34, 0.07)
550	9.2 (0.01, 0.06)	3.0 (0.43, 0.59)	0.95 (0.06, 0.03)	0.3 (0.20, 0.02)
580	9.2 (0.01, 0.05)	3.0 (0.26, 0.36)	0.95 (0.01, 0.00)	0.3 (0.15, 0.02)
600	9.2 (0.01, 0.04)	3.0 (0.18, 0.25)	0.95 (0.03, 0.01)	0.3 (0.10, 0.01)

τ_n decay time
a_n pre-exponential factor
f_n fraction of intensity
Excitation: 350nm; χ^2_R = 1.17

b. Smeared

Wavelength	$\tau_1 (a_1, f_1)$	$\tau_2 (a_2, f_2)$	$\tau_3 (a_3, f_3)$	$\tau_4 (a_4, f_4)$
500	25 (0.01, 0.16)	7.3 (0.04, 0.28)	1.6 (0.16, 0.27)	0.2 (0.61, 0.11)
550	25 (0.06, 0.39)	7.3 (0.18, 0.35)	1.6 (0.41, 0.18)	0.2 (0.29, 0.01)
580	25 (0.09, 0.36)	7.3 (0.20, 0.23)	1.6 (0.39, 0.10)	0.2 (0.01, <0.01)
600	25 (0.07, 0.30)	7.3 (0.14, 0.26)	1.6 (0.25, 0.06)	0.2 (0.06, <0.01)

τ_n decay time
a_n pre-exponential factor
f_n fraction of intensity
Excitation: 350nm; χ^2_R = 1.39

c. Thermal annealed

Wavelength	τ_1 (a_1, f_1)	τ_2 (a_2, f_2)	τ_3 (a_3, f_3)	τ_4 (a_4, f_4)
500	24 (<0.01, 0.06)	6.9 (0.02, 0.20)	1.8 (0.14, 0.37)	0.2 (0.70, 0.23)
550	24 (0.02, 0.21)	6.9 (0.11, 0.35)	1.8 (0.40, 0.34)	0.2 (0.40, 0.05)
580	24 (0.03, 0.21)	6.9 (0.13, 0.26)	1.8 (0.37, 0.20)	0.2 (0.15, 0.01)
600	24 (0.03, 0.19)	6.9 (0.12, 0.19)	1.8 (0.32, 0.14)	0.2 (0.06, 0.01)

τ_n decay time
a_n pre-exponential factor
f_n fraction of intensity
Excitation: 350nm; χ^2_R = 1.12

d. Pristine powder

Wavelength	τ_1 (a_1, f_1)	τ_2 (a_2, f_2)	τ_3 (a_3, f_3)	τ_4 (a_4, f_4)
500	28 (0.01, 0.17)	11 (0.04, 0.31)	2.2 (0.12, 0.18)	0.2 (0.58, 0.09)
550	28 (0.09, 0.46)	11 (0.18, 0.36)	2.2 (0.29, 0.11)	0.2 (0.39, 0.02)
580	28 (0.14, 0.42)	11 (0.19, 0.23)	2.2 (0.24, 0.06)	0.2 (0.15, 0.01)
600	28 (0.14, 0.35)	11 (0.16, 0.15)	2.2 (0.18, 0.03)	0.2 (0.07, 0.06)

τ_n decay time
a_n pre-exponential factor
f_n fraction of intensity
Excitation: 350nm; χ^2_R = 1.23

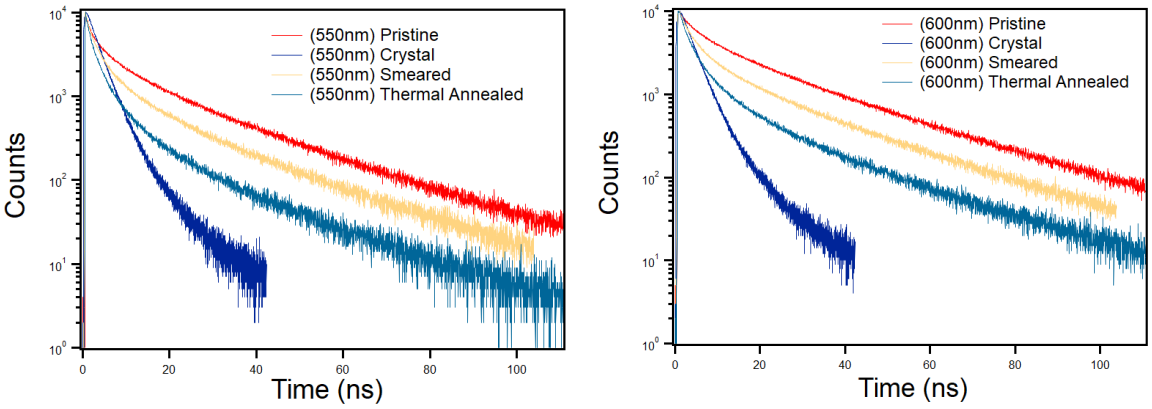

Figure 6.8. Time-resolved spectroscopy measurement plots of cydiester di-DFB crystals, smeared, thermal annealed and pristine powder measured at 550nm and 600nm (excitation at 350nm).

6.3 Calculations

Optimized geometry were calculated using CAM-B3LYP functional and 6-31+ g (d,p) basis set including IEFPCM (DCM) solvation model. The energy transitions, molecular orbitals, simulated ECD, absorbance and oscillator strengths were calculated with TD-DFT using the same basis sets solvent models as the optimization.[11] The calculation was conducted using Mésocentre" computing center of CentraleSupélec and École Normale Supérieure Paris-Saclay supported by CNRS and Région Île-deFrance.

6.3.1 DFT and TD-DFT Calculations of Compounds in Chapter 2

Table 6.4. Excitation energies, oscillator strength and molecular orbitals involved in electronic transitions of para (*S)*-CyDFB.

Excitation Energies			Oscillator strengths
Excited state 1		3.3963 eV	f = 0.4590
199 -> 201	-0.33191		
200 -> 201	-0.11826		
200 -> 202	0.55683		
Excited state 2		3.4381 eV	f = 2.3259
199 -> 201	0.56511		
200 -> 202	0.34066		
Excited state 3		4.4419 eV	f = 0.0867
192 -> 201	-0.13183		
194 -> 201	-0.11054		
196 -> 201	-0.11765		
197 -> 201	0.55644		
198 -> 201	-0.18489		
199 -> 201	-0.12985		
199 -> 203	-0.14562		

Table 6.5. Excitation energies, oscillator strength and molecular orbitals involved in electronic transitions of meta (*S)*-CyDFB.

Excitation Energies			Oscillator strengths
Excited state 1		3.5396 eV	f = 2.2677
199 -> 201	0.58567		
200 -> 202	-0.31017		
Excited state 2		3.5848 eV	
195 -> 202	-0.13231		f = 0.3006
199 -> 201	0.28965		
199 -> 202	0.12087		
200 -> 201	-0.13204		
200 -> 202	0.57155		
Excited state 3		4.5682 eV	f = 0.0623
190 -> 201	0.13689		
191 -> 201	-0.20020		
194 -> 201	-0.10792		
194 -> 204	-0.15080		
196 -> 201	-0.10763		
196 -> 202	-0.19216		
197 -> 201	0.38171		
198 -> 201	0.32634		

A

B

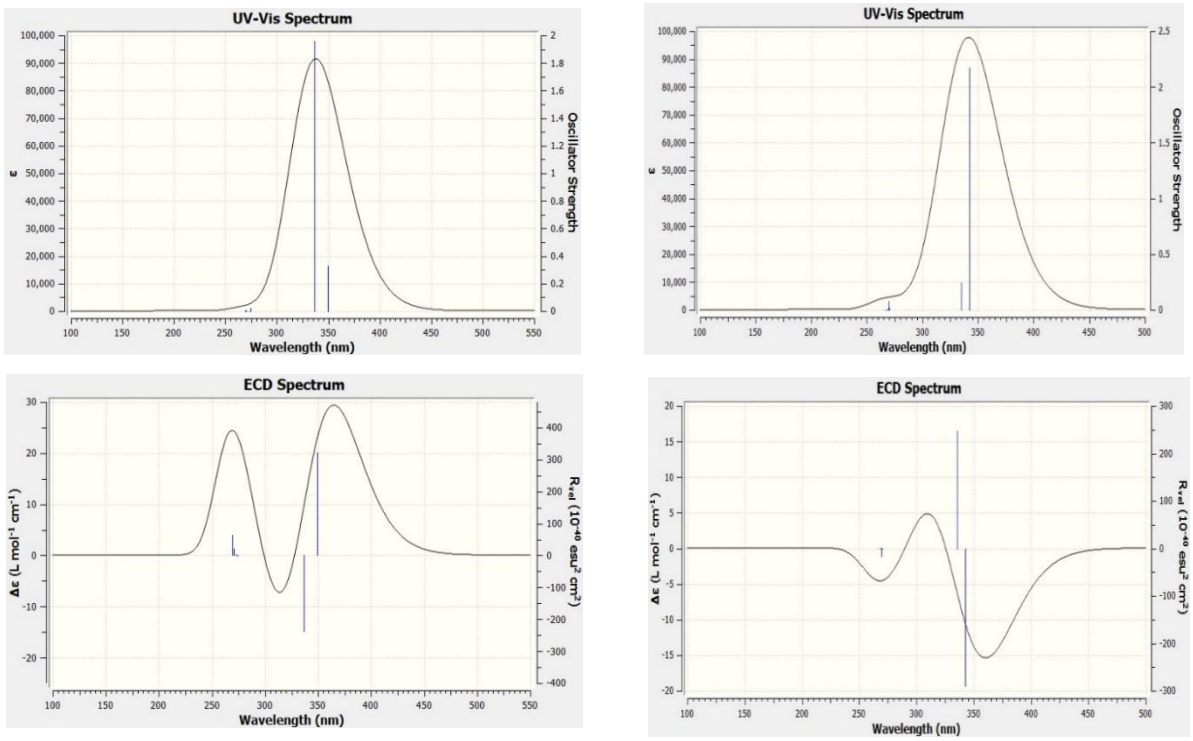

Figure 6.9. Simulated UV-Vis and ECD spectra of para *S*-cyclohexane diamine DFB (A) meta *S*-cyclohexane diamine DFB (B) as calculated by TD-DFT with CAMB3LYP, 613+G (d,p) basis set and IEFPCM using DCM as solvent.

6.3.2 DFT and TD-DFT Calculations of Compounds in Chapter 3

Table 6.6. Excitation energies, oscillator strength and molecular orbitals involved in electronic transitions of (*S*) cydiamine mono-DFB (in DCM)

Excitation Energies			Oscillator strengths
Excited state 1		3.4124 eV	f = 1.440
114 -> 117	0.16249		
116 -> 117	0.65844		
116 -> 118	0.10317		
Excited state 2		4.4390 eV	f = 0.1100
114 -> 117	0.62151		
115 -> 117	-0.13671		
116 -> 117	-0.14019		
116 -> 118	-0.15976		
Excited state 3		4.5457 eV	f = 0.0650
111 -> 117	0.23908		
111 -> 118	-0.12023		
112 -> 117	-0.35107		
113 -> 117	0.45699		
113 -> 118	-0.15627		
114 -> 118	-0.10442		
114 -> 119	-0.11169		

6.3.3 DFT and TD-DFT Calculations of Compounds in Chapter 4

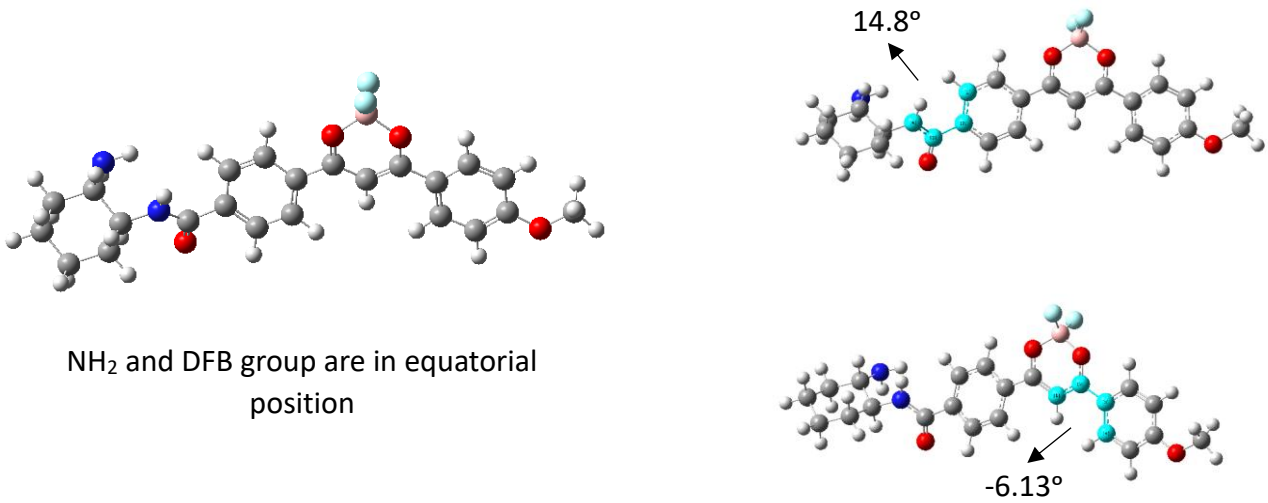

Figure 6.10. Optimized geometry of cydiamine mono-DFB calculated using the functional CAM-B3LYP and basis set (6-31+) G(d,p) with IEFPCM (DCM) solvation method and the corresponding dihedral angles of DFB moiety (a) and theoretical vs experimental absorption of three compounds in DCM (b).

Table 6.7. Excitation energies, oscillator strength and molecular orbitals involved in electronic transitions of Cydiester di-DFB

Excitation Energies			Oscillator strengths
Excited state 1		3.5118 eV	f = 2.5604
197 → 202	0.10792		
198 → 201	-0.12340		
199 → 201	0.38258		
199 → 202	0.30169		
200 → 201	-0.33401		
200 → 202	0.28597		
Excited state 2		3.5497 eV	f = 0.0453
198 → 202	0.10072		
199 → 201	-0.40537		
199 → 202	0.17185		
200 → 201	0.10224		
200 → 202	0.47928		

Excited state 3		4.5591 eV	f = 0.0748
193 → 201	-0.33372		
193 → 202	-0.17339		
193 → 204	-0.13446		
194 → 201	0.40272		
194 → 203	-0.11223		
197 → 201	-0.15143		
197 → 202	-0.14894		
198 → 201	0.20891		

Table 6.8. Excitation energies, oscillator strength calculated using the functional CAM-B3LYP and basis set (6-31+) G(d,p) with IEFPCM (DCM) solvation method and the corresponding theoretical values obtained with UV-Vis.

	Theoretical (eV)		Experimental (eV)
Cydiamine mono-DFB	ES 1: 3.4124 eV	(f = 1.4440)	Max. 3.16 eV (392nm)
	ES 2: 4.4390 eV	(f=0.1100)	
	ES 3: 4.5457 eV	(f=0.0650)	
Cydiamine di-DFB	ES 1: 3.3963 eV	(f = 0.4590)	Max. 3.15 eV (394nm)
	ES 2: 3.4381 eV	(f=2.3259)	
	ES 3: 4.5682 eV	(f= 0.0867)	
Cydiamine di-DFB	ES 1: 3.5118 eV	(f = 2.5604)	Max. 3.15 eV (393nm)
	ES 2: 3.5497 eV	(f=0.0453)	
	ES 3: 4.5591 eV	(f=0.0748)	

*where ES is excited states and f is oscillator strengths.

6.4 Crystal Analysis

The powder XRD patterns were recorded using Rigaku Smartlab9kW using CuKα1 monochormatization Ge220crystals. Suitable single crystal was isolated and mounted in sample holder. X-ray diffractions were recorded using Rigaku Varimax Rapid RA Micro7 equipped with imaging plate detector monochromated Mo Kα radiation at 103.15K. The crystal structure and calculations were done using the system software Rigaku Crystal structure 3.8.1.

6.4.1 Crystal Analysis of Cydiamine mono-DFB

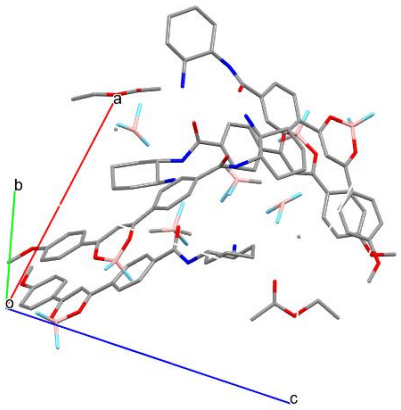

Figure 6.11. Single Crystal structure of Cydiamine mono-DFB

Table 6.9. Crystallographic parameters of Cydiamine mono-DFB single crystals.

Properties of Cydiamine mono-DFB	
Formula weight	442.27
Crystal system	monoclinic
calculated density	1.137
a (Å)	16.405 (3)
b (Å)	9.4466 (19)
C (Å)	16.671 (4)
α (deg)	90.000
β (deg)	91.305 (3)
γ(deg)	90.000
Z value	4

6.4.2 Crystal Analysis of Cydiamine di-DFB

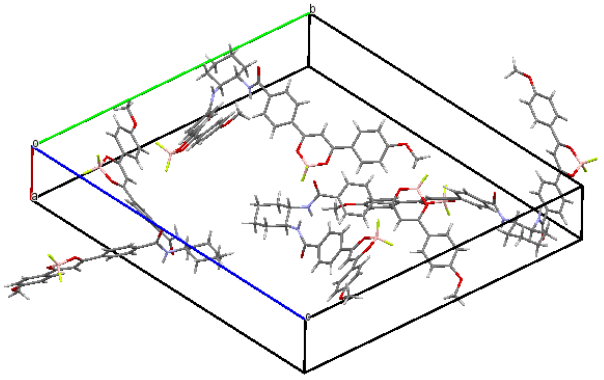

Figure 6.12. Single Crystal structure of Cydiamine di-DFB

Table 6.10 Crystallographic parameters of Cydiamine-DFB single crystals.

Properties of Cydiamine di-DFB	
Formula weight	770.35
Crystal system	orthorhombic
calculated density	1.1772
a (Å)	4.8980 (5)
b (Å)	28.365 (3)
C (Å)	31.422 (4)
α (deg)	90.0
β (deg)	90.0
γ(deg)	90.0
Z value	4

6.4.3 Crystal Analysis of Cydiester di-DFB

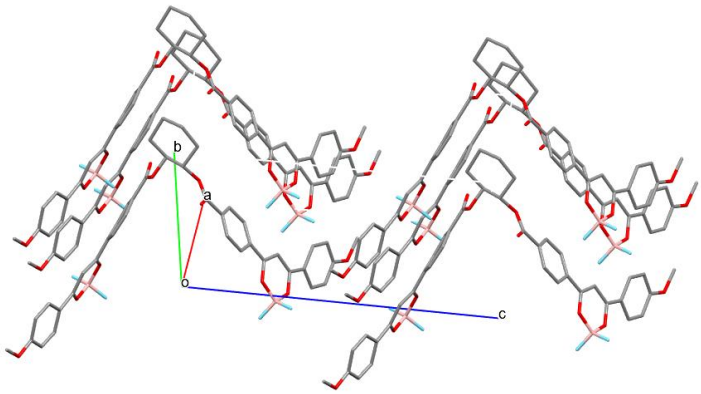

Figure 6.13. Single Crystal structure of Cydiester di-DFB

Table 6.11 Crystallographic parameters of Cydiester-DFB single crystals.

Properties of Cydiester di-DFB	
Formula weight	772.32
Crystal system	monoclinic
calculated density	1.432
a (Å)	10.479 (3)
b (Å)	8.980 (2)
C (Å)	19.289 (6)
α (deg)	90.000
β (deg)	99.312 (7)
γ(deg)	90.000
Z value	2

6.5 Thermogravimetric Analysis

Thermogravimetric analyses were conducted using Shimadzu DTG-60 (DTA-TGA apparatus) using aluminum crimp pan (max. 600°C). Analyses were performed from 45°C to 300°C with constant rate temperature of 10°C/min. under atmospheric condition.

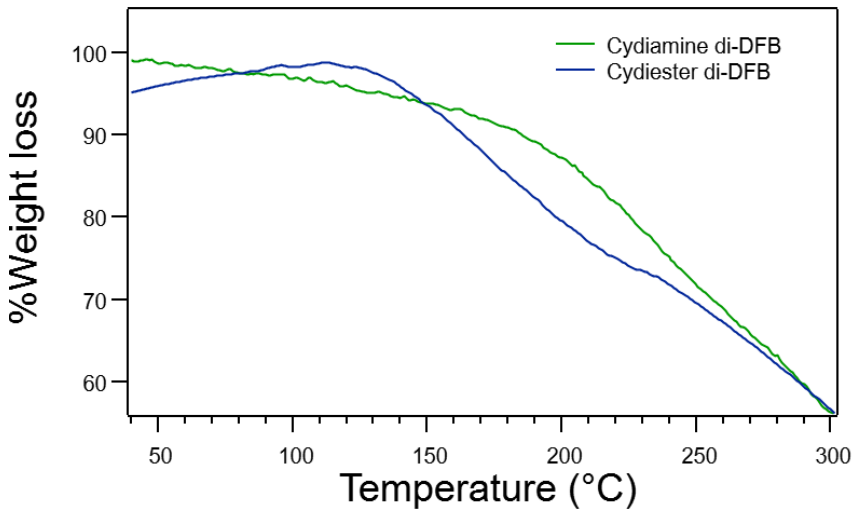

Figure 6.14. Thermogravimetric analysis of cydiamine di-DFB and cydiester di-DFB.

6.6 Hirshfeld Surface Analysis

Hirshfeld surface analyses were performed using Crystal Explorer 21 software using the .cif file from single crystal analysis.[8,9] The fingerprint plots each atom-to-atom interaction in each crystal were shown in Figures 6.14 to Figure 6.16.

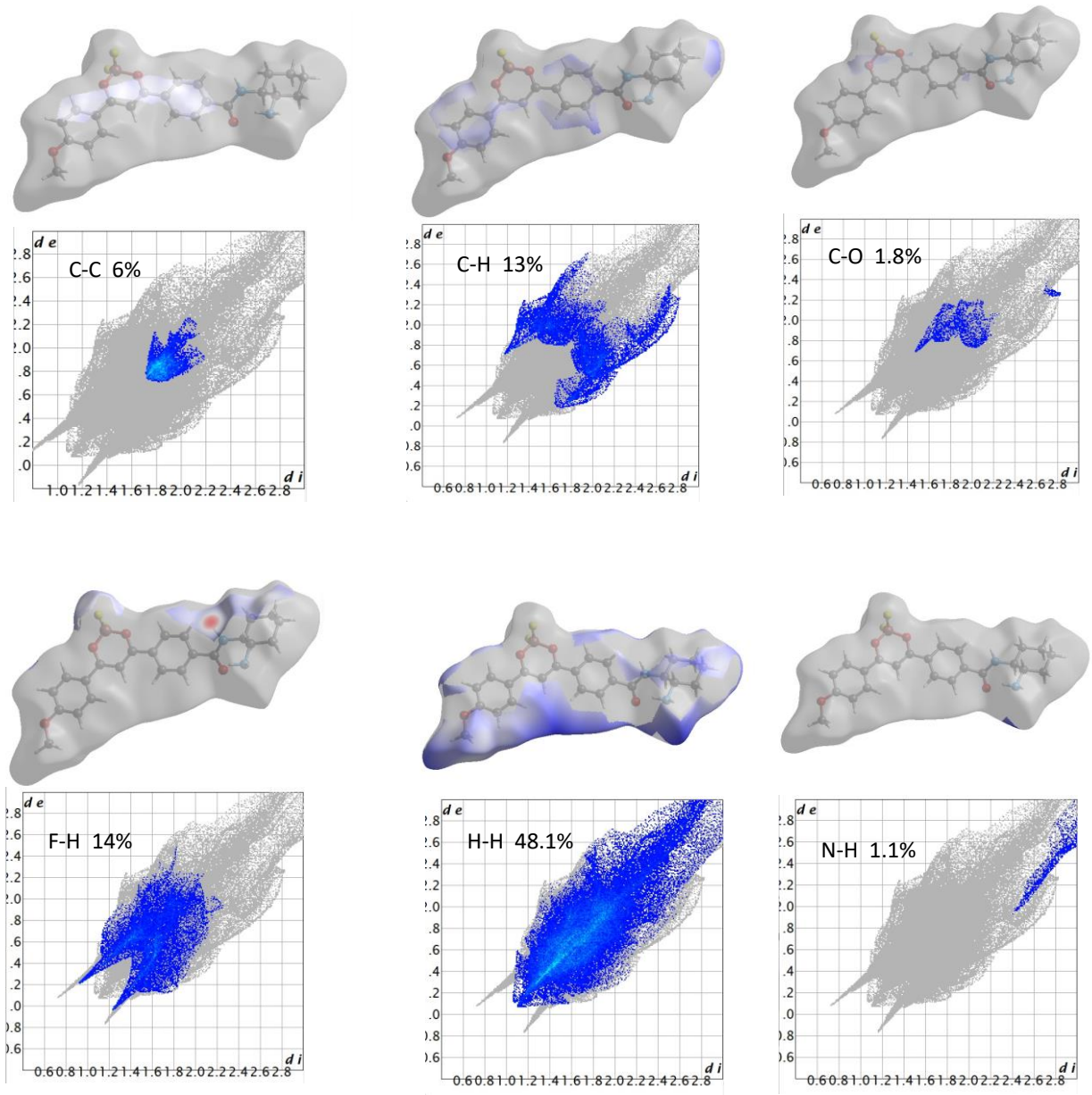

Figure 6.15. Fingerprint plots of cydiamine mono-DFB calculated from Hirshfeld surface analysis.

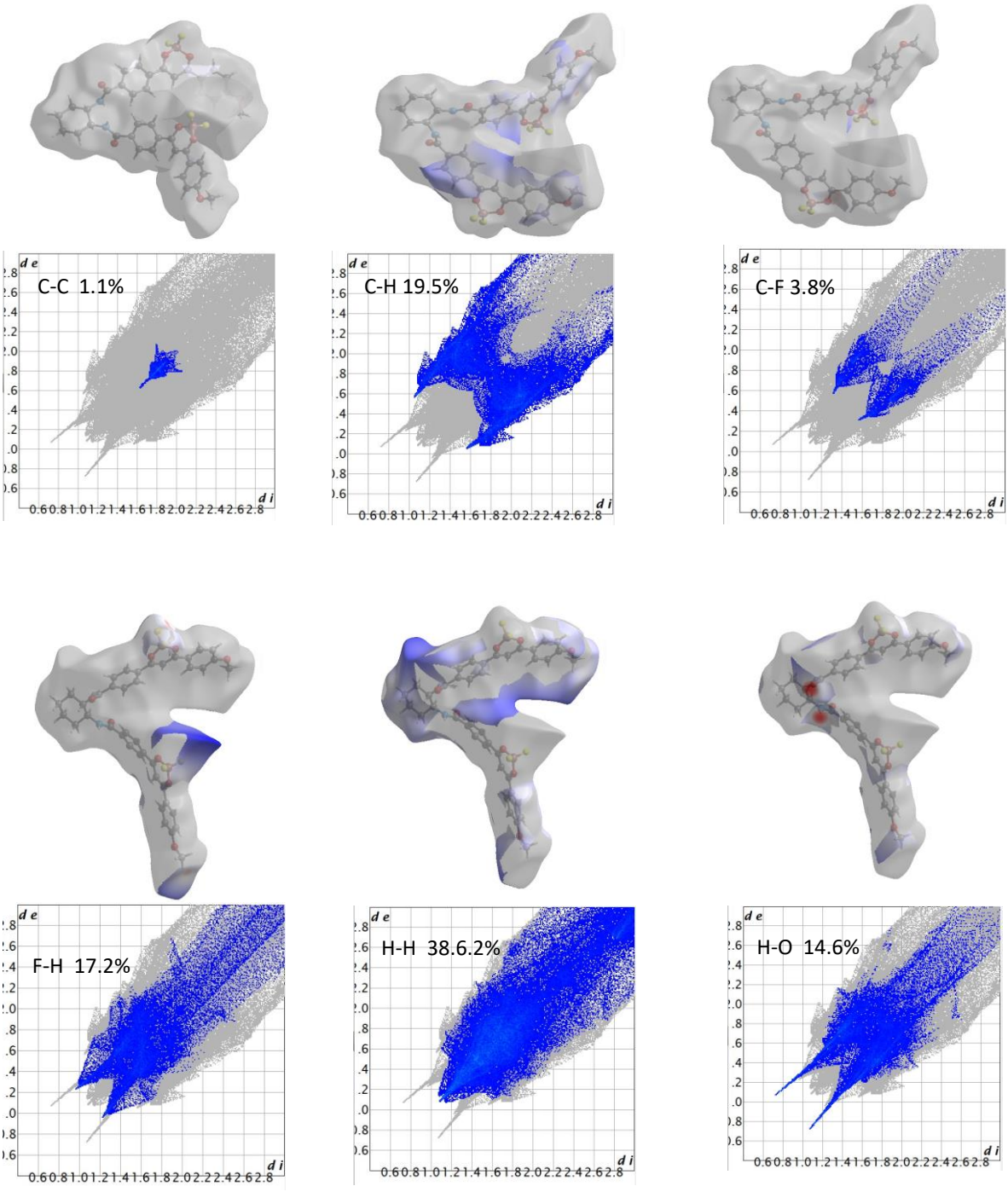

Figure 6.16. Fingerprint plots of cydiamine di-DFB calculated from Hirshfeld surface analysis.

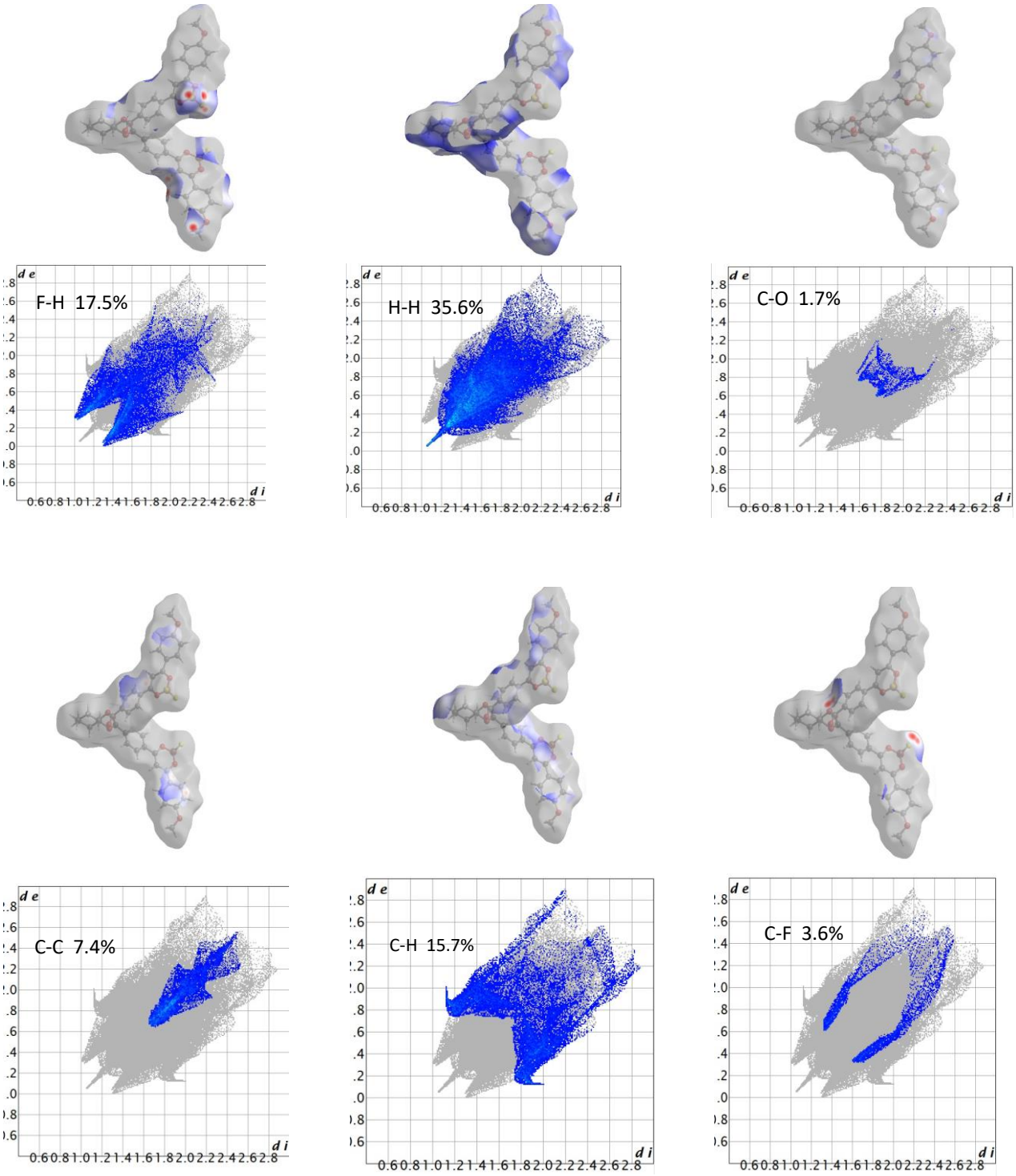

Figure 6.17. Fingerprint plots of cydiester di-DFB calculated from Hirshfeld surface analysis.

6.7 Circularly Polarized Luminescence (CPL)

The CPL were measured using the lab-designed CPL system consisting of excitation laser at 375nm, Hinds PEM-90 photoelastic modulator with frequency of 50KHz, Hamamatsu H7732 photomultiplier tube with signal amplifier, polarizing prism, and Shimadzu monochromator (10cm, single grating).[10]

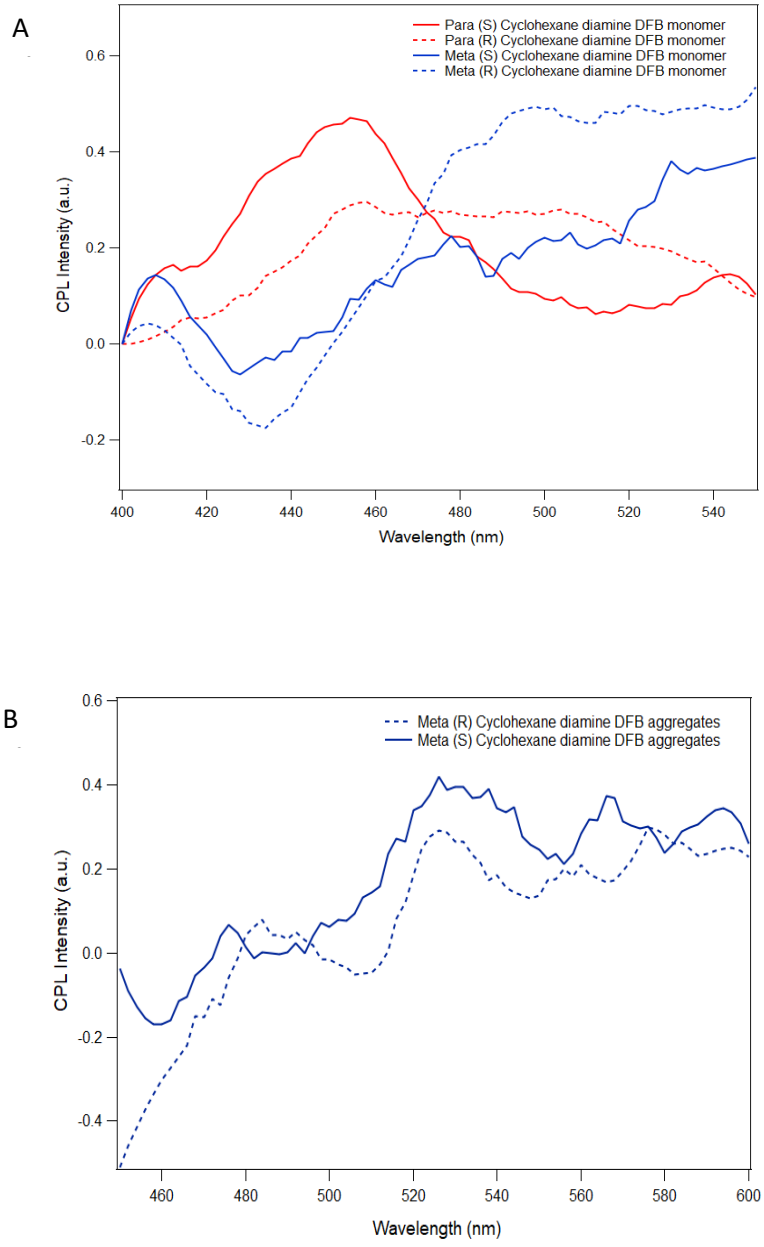

Figure 6.18. CPL spectra of para and meta (*R/S*)-CyDFB monomeric form in chloroform (A) and meta (S)-CyDFB aggregates in MCH: CHCl3 (29:1) (B). The concentration was kept at 3.0 x10-5M.

References

(1) Wilbraham, L.; Louis, M.; Alberga, D.; Brosseau, A.; Guillot, R.; Ito, F.; Labat, F.; Métivier, R.; Allain, C.; Ciofini, I. Revealing the Origins of Mechanically Induced Fluorescence Changes in Organic Molecular Crystals. *Adv. Mater.* 2018, *30* (28), 1800817.

(2) Kumar, J.; Nakashima, T.; Kawai, T. Inversion of Supramolecular Chirality in Bichromophoric Perylene Bisimides: Influence of Temperature and Ultrasound. *Langmuir* 2014, *30* (21), 6030–6037.

(3) Flores-Ferrándiz, J.; Fiser, B.; Gómez-Bengoa, E.; Chinchilla, R. Solvent-Induced Reversal of Enantioselectivity in the Synthesis of Succinimides by the Addition of Aldehydes to Maleimides Catalysed by Carbamate-Monoprotected 1,2-Diamines: Solvent-Induced Reversal of Enantioselectivity. *Eur. J. Org. Chem.* 2015, *2015* (6), 1218–1225.

(4) Kumar, J.; Nakashima, T.; Tsumatori, H.; Mori, M.; Naito, M.; Kawai, T. Circularly Polarized Luminescence in Supramolecular Assemblies of Chiral Bichromophoric Perylene Bisimides. *Chem. Eur. J.* 2013, *19* (42), 14090–14097.

(5) Han, G.; Tamaki, M.; Hruby, V. J. Fast, Effecient and Selective Deprotection of the Tert-Butoxycarbonyl (Boc) Group Using HCl/Dioxane. *J.Peptide Res.* 2001, *58*, 338–341.

(6) Louis, M.; Brosseau, A.; Guillot, R.; Ito, F.; Allain, C.; Métivier, R. Polymorphism, Mechanofluorochromism, and Photophysical Characterization of a Carbonyl Substituted Difluoroboron-β-Diketone Derivative. *J. Phys. Chem. C.* 2017, *121* (29), 15897–15907.

(7) Rauf, A.; Parveen, H. Direct Esterification of Fatty Acids with Phenylalkanols by Using Dicyclohexylcarbodiimide. *Eur. J. Lipid Sci. Technol.* 2004, *106* (2), 97–100.

(8) Spackman, M. A.; Jayatilaka, D. Hirshfeld Surface Analysis. *CrystEngComm* 2009, *11* (1), 19–32.

(9) Sharfalddin, A.; Davaasuren, B.; Emwas, A.-H.; Jaremko, M.; Jaremko, Ł.; Hussien, M. Single Crystal, Hirshfeld Surface and Theoretical Analysis of Methyl 4-Hydroxybenzoate, a Common Cosmetic, Drug and Food Preservative—Experiment versus Theory. *PLoS ONE* 2020, *15* (10), e0239200.

(10) Yuasa, J.; Ohno, T.; Miyata, K.; Tsumatori, H.; Hasegawa, Y.; Kawai, T. Noncovalent Ligand-to-Ligand Interactions Alter Sense of Optical Chirality in Luminescent Tris(β-Diketonate) Lanthanide(III) Complexes Containing a Chiral Bis(Oxazolinyl) Pyridine Ligand. *J. Am. Chem. Soc.* 2011, *133* (25), 9892–9902.

(11) Gaussian 16, Revision B.01, Frisch, M.J., Trucks, G.W., Schlegel, H.B., Scuseria, G.E., Robb, M.A., Cheeseman, J.R.; Scalmani, G.; Barone, V.; Petersson, G.A.; Nakatsuji, H.; Li, X.; Caricato, M.; Marenich, A.V.; Bloino, J., Janesko, B.G., Gomperts, R., Mennucci, B., Hratchian, H.P., Ortiz, J.V., Izmaylov, A.F., Sonnenberg, J.L., Williams-Young, D., Ding, F., Lipparini, F., Egidi, F., Goings, J., Peng, B., Petrone, A., Henderson, T., Ranasinghe, D., Zakrzewski, V.G., Gao, J., Rega, N., Zheng, G., Liang, W., Hada, M., Ehara, M., Toyota, K., Fukuda, R., Hasegawa, J., Ishida, M., Nakajima, T., Honda, Y., Kitao, O., Nakai, H., Vreven, T., Throssell, K., Montgomery Jr., J.A., Peralta, J.E., Ogliaro, F., Bearpark, M.J., Heyd, J.J., Brothers, E.N., Kudin, K.N., Staroverov, V.N., Keith, T.A., Kobayashi, R., Normand, J., Raghavachari, K., Rendell, A.P., Burant, J.C., Iyengar, S.S., Tomasi, J., Cossi, M., Millam, J.M., Klene, M., Adamo, C., Cammi, R., Ochterski, J.W., Martin, R.L., Morokuma, K., Farkas, O., Foresman, J.B., Fox, D.J. Gaussian, Inc., Wallingford CT (2016) GaussView 5.0. Wallingford, E.U.A.

Acknowledgements

I would like to acknowledge my supervisors Prof. Tsuyoshi Kawai (NAIST) and Dr. Clémence Allain (ENS-Paris Saclay) for their support and guidance throughout my PhD journey. To NAIST and ENS-Paris Saclay for the financial support as well and the scholarship grants. I am also very thankful to Dr. Rémi Métivier and Assistant Prof. Marine Louis for their guidance and for sharing their expertise to help me with the experimental set-up and made the necessary measurements possible. Their directions and guidance shaped me to become a better student and future researcher. I also would like to express my sincerest gratitude to the jury members: Prof. Gwénaël Rappene, Prof. Jeanne Crassous, Prof. Michel Sliwa, Prof. Shun Hirota and Prof. Takuya Nakashima for giving part of their time to read, suggest and help me improve my manuscript and research.

I am very thankful to the new and previous members of Photonics and Reactive Molecular Science Laboratory especially to my senpai and tutors Dr. Yoshida, Dr. Mizutsu, Dr. Kuno, and Dr. Asato who helped me a lot during my first year of stay in NAIST. Also, to all the members under Marine sensei's team for all the fun memories especially to Katsumi-san. To Dr. Pablo Reiné for sharing his expertise and time, also to my colleagues in PPSM especially Dr. Poggi, Dr. Sethy, and Dr. Hirai who imparted their knowledge in solid state chemistry and became my support group while I was in France. To Dr. Calupitan for his support and encouragement to apply for double-degree Doctoral Program of NAIST and ENS-Paris Saclay, I am not here without his advice. Also, to all the technical staffs in NAIST and ENS-Paris Saclay especially to Arnaud Brosseau who I spent most of my time doing solid-state measurements; to Katao-san, Asanoma-san and Nishikawa-san for patiently analyzing and characterizing my samples.

To the Filipino community in NAIST especially Candell, James, Virgil, Mark, Nicko, JC, Dianne, Paul, Ken, Chi, Peki, Enzo, Magin and Josh for being my support group and making my PhD life fun and memorable. Also, I am expressing gratitude to all the friendly international students of NAIST and ENS-Paris Saclay.

To my mentor Dr. Diaz and all my professors in Ateneo de Manila University and Polytechnic University of the Philippines, and Department of Science and Technology thank you so much. I will not acquire all the basic skills and knowledge needed to pursue my doctoral studies without the scholarship, guidance, and teachings from you.

To my family and extended family, Mama, Papa, Ate, Cherry, Jay, Joseph, Jheel and Mairene thank you so much for taking care of things while I was away, also for the for the support and encouragement.

Scientific Production

Published paper

1. Circularly Polarized Luminescence and Circular Dichroism of Bichromophoric Difluoroboron-β-diketonates: Inversion and Enhanced Chirality based on Spatial Arrangements and Self-assembly

   Joy Ann Panis, Marine Louis, Arnaud Brosseau, Shouhei Katao, Florencio de los Reyes, Takuya Nakashima, Rémi Métivier, Clémence Allain and Tsuyoshi Kawai

   Chem. Eur. J.2022, e202201012
   https://doi.org/10.1002/chem.202201012

2. Influence of Amide and Ester Spacers to the Mechanofluorochromic Property of Difluoroboron β-diketonates (DFB) Bichromophore

   Joy Ann Panis, Marine Louis, Arnaud Brosseau, Shouhei Katao, Rémi Métivier, Clémence Allain and Tsuyoshi Kawai
   (for submission in *Chemistry: An Asian Journal*)

3. Energy Transfer and Photosensitivity of Bichromophoric Difluoroboron-β-diketonates.

   Joy Ann Panis, Marine Louis, Arnaud Brosseau, Shouhei Katao, Rémi Métivier, Clémence Allain and Tsuyoshi Kawai
   (Manuscript writing for *Photochemical & Photobiological Sciences*)

Conferences and Presentations

- Japan Photochemistry Association Annual Conference 2020
  (Sept 9-11, 2020) Web poster presentation
  Synthesis and Chiroptical Nature of Bichromophore Difluoroboron β-Diketonates and Their Chiral Aggregates.

- 5th Japan-France Nanosynergestics Workshop
  (November 13, 2020) Oral presentation
  Mechanofluorochromism and Chiroptical Nature of Bichromophoric Difluoroboron β-Diketonates and Their Chiral Aggregates

- 11th Asian Photochemistry conference
  (October 31-November 4, 2021) Short Oral and Web Poster presentation.
  Synthesis and Chiroptical Nature of Bichromophore Difluoroboron β-Diketonates and Their Chiral Aggregates.

- 6th Japan-France Nanosynergestic Conference
  (November 9, 2021) Oral presentation
  Chiroptical Nature of Bichromophore Difluoroboron β-Diketonates and Their Supramolecular Assemblies